Development of electrochemical tip-enhanced Raman spectroscopy : towards the characterization of electroactive molecular architectures

Alice Fiocco

Sorbonne Université

Ecole doctorale 388
Chimie Physique et Chimie Analytique
Laboratoire Interfaces et Systèmes Electrochimiques (LISE), UMR CNRS 8235

Development of electrochemical tip-enhanced Raman spectroscopy

Towards the characterization of electroactive molecular architectures

Par Alice Fiocco

Thèse de doctorat de chimie physique

Dirigée par Ivan T Lucas

Co-encadrée par Jean-Marc Noël

Pour une soutenance publique prévue le 20 janvier 2022

Devant un jury composé de :

M[me] Tréguer-Delapierre Mona	Prof., Université de Bordeaux	Rapporteure
M. Leroux Yann	CR-HDR CNRS, Université de Rennes	Rapporteur
M[me] Domke Katrin F	Dr., Max Planck Inst. for Polymer Research	Examinatrice
M. Breton Tony	Prof., Université d'Angers	Examinateur
M[me] Courty Alexa	Prof., Sorbonne Université	Examinatrice
M. Maisonhaute Emmanuel	Prof., Sorbonne Université	Examinateur
M. Noël Jean-Marc	CR CNRS, Université de Paris	Co-encadrant
M. Lucas Ivan T	MCF HDR, Sorbonne Université	Directeur de thèse

Summary

Introduction

Functional (nano)materials constituted by thin molecular layers and or micro/nano molecular patterns on supporting surfaces (metals, semi-conductors, insulators) are gaining interest in numerous research fields for a wide series of applications, such as catalysis, batteries, (bio)sensors, or even biomedicine. Indeed, the fine tuning of the molecular layer properties allows optimizing the performance of the final device toward targeted uses. For the specific case of hybrid structures made of metallic supports functionalized by molecules, richer (electro)chemical functionalities can be reached through the design of complex electroactive molecular architectures, with respect to classic devices based on macro inorganic structure. Ultimately, the great potentialities and virtually limitless possibility of modulation of functional molecular materials encourage today the research towards more and more fine developments and successive integration in operational devices.

The elaboration of new functional (nano)materials and the understanding of complex (bio)interfaces**,** useful for instance in electrocatalysis, requires the development of analytical tools with a sufficient sensitivity, which can operate at the nanoscale and under the condition**s** of operation of these materials (*in situ*, *operando*, *in vitro*). Ultimately, establishing structure-reactivity relationships would allow directing the design of functionalized substrates towards specific and targeted applications.

Compositional and structural analysis of low cross-section material like molecular films can be achieved *via* a myriad of microscopic and spectroscopic techniques, although often their operation conditions can strongly limit/compromise *in situ* applications (e.g. use of ultrahigh vacuum, signal screening by the solvent or by the atmosphere). Scanning Probe Microscopies SPMs stand as great alternatives to X-ray and electron microscopies to access the structure of functional surfaces at the (sub)nanoscale in the ambient and in liquids, with minimal interference of the probe with the system under study (no beam damages). Among benchtop spectroscopies, instead, the Raman technique has shown spectacular characterization abilities especially since the introduction, in the early 70's, of Surface-Enhanced Raman Spectroscopy (SERS), which circumvented its classical issue of poor sensitivity and brought the detection threshold down to the molecular level.

Tip-Enhanced Raman Spectroscopy (TERS, or nanoRaman), which combines SPMs with enhanced-Raman microscopy, was introduced in the late 90s, but almost remained at the

conceptual stage of its development for many years, being the privilege of only a handful of research groups worldwide. The exceptional sensitivity of TERS and the wealth of information contained in its vibrational signatures was demonstrated in 2013 [1] through the imaging under vacuum of the vibration modes of a single porphyrin molecule on an Ag(111) surface, and in 2014 [2] through the composition imaging in the ambient of a single carbon nanotube with a 1.7 nm resolution. The demonstration of its implementation in water in 2009 [3] and under electrochemical conditions (EC) a few years later [4] has paved the road to the characterization of functional (nano)materials in their operating conditions.

This work has been dedicated to the characterization of electroactive molecular layers through important developments and optimizations of EC-TERS measurements, using a scanning tunnelling microscope (STM-TERS) for the precise control of the TERS tip-sample distance. On one side, our efforts were focused on the study of molecular structures involving different classes of compounds carrying redox active entities (thiol-based self-assembled monolayers SAMs and 2D-3D molecular architectures built via the electroreduction of diazonium derivatives). On the other side, we attempted the development of real-time measurements to characterize the chemical transformation pathways occurring during electrochemical redox processes of the electroactive layer. Moreover, to get a better understanding of the structure-reactivity relationships of molecular-based devices, the reactivity of well-organized 2D monolayers and randomly organized 3D structures were cross-compared through the screening of their potential-dependent composition by EC-STM-TERS.

This work around the development of electrochemical tip-enhanced Raman spectroscopy and the characterization of SAM and diazonium-based electroactive molecular architectures is divided into 4 independent chapters, organized as follows.

Chapter 1 will describe in detail the characteristics of thiol- and diazonium-derived substrates, expose their fabrication procedures and discuss the influence of their structures on the overall system reactivity. Therefore, a series of *in situ* and *operando* methods, which have been employed for the characterization of the aforementioned molecular structures (both at the micro- and nano-scale) will be reviewed. Finally, an *excursus* about the EC-TERS technique, from the first prototypes to the last innovations, will be presented, along with a final note regarding the challenges that are actually faced by the TERS community.

Chapter 2 will be dedicated to the experimental and technical developments that were carried out in this work to optimize the performances of EC-STM-TERS analyses, including

the fabrication of metal probes used as Raman signal plasmonic amplifiers, the design and optimization of electrochemical tools and methods suitable for reliable *in situ* TERS measurements.

Chapter 3 will present the first proof-of-concept of dynamic nanospectroscopic investigations under electrochemical conditions. This was achieved by using EC-TERS to monitor in real time the composition evolution of a model thiol SAM (4-nitrobenzyl mercaptan 4-NBM) subjected to reductive conditions. The insights on the reaction mechanism of nitro-based molecular compounds, deduced from 4-NBM analyses, will serve as a base to Chapter 4.

Chapter 4 aims at screening the structure-reactivity relationships in more complex molecular architectures, i.e. 4-nitrobenzene (4-NB) layers at different thicknesses, obtained by reduction of the corresponding diazonium salt.

In conclusion, we will summarize the most important results achieved through this work and present the envisaged future perspectives.

Chapter 1 State of the art

1.1. Introduction

Nowadays the massive request of novel technological devices, with specifically designed characteristic and minimal size, leads several research fields to turn towards the realization of nano-functionalized (bio)interfaces and, on the other side, towards the development of feasible measurement techniques for the analysis of the final systems in their working conditions. Ideally, the characterization methods should have a great sensitivity, so that to obtain signals even from single thin molecular layers or isolated nano-objects, and an extraordinary resolution, in order to distinguish among adjacent structures on the surface and not to get just an overall averaged information. Besides, getting insights in the reaction mechanisms that involve these nanostructures requires for the characterization method to be compatible with the operating conditions of the functionalized devices (in terms of instrumental setup, environment, time resolution, and so on).

In the following paragraphs we will first discuss about the chemistry of surface functionalization, focusing in particular on two kinds of molecular species. Later on, we will review a few characterization methods that have been so far implemented with the aim of analysing *operando* functional materials at the macro/micro and nano scale. Finally, we will present the electrochemical tip-enhanced Raman spectroscopy (EC-TERS) technique, which is so far one of the best developments for carrying out *in situ* chemical characterization at the nanoscale and on which this thesis work is based.

1.2. Surface modification

Patterning a surface with chemical species, nano-objects or even proteins presents numerous advantages: first, upon decreasing the size of chemically active regions, molecular mass transfer limitations can be overcome, meaning that the intrinsic chemical activity can be fully exploited. This is particularly interesting in the field of catalysis, where the efficiency and selectivity for certain kinds of reaction (as oxygen reduction reaction [5], water splitting [6], or CO_2 conversion [7]) can be specifically tuned.

Moreover, nanoscale motifs can provide the underlying substrate with new properties, as hydrophobicity [8], adhesion [9], electric conductivity or insulation [10], and can also work as precursors for click-chemistry reactions that immobilize specific objects on top of the original substrate (as nanoparticles [11], biosensors [12] or cubes for memory storage [13]). Besides, patterned

surfaces seem promising for the development of safer and more efficient electrocatalytic materials for energy storage [14] or conversion [15].

Structuring an organic layer on a surface requires a precise knowledge of the type of interactions formed between the molecules and the substrate atoms. In general, strongly attached layers are obtained if chemical bonds are formed, while simple physisorption occurs when the molecules establish weaker interactions (e.g. Van der Waals or hydrogen bonds) with the substrate. The presence of either or both kind of bonds is mostly related to the nature of the organic compound, but also the experimental conditions adopted for the layer formation can play a role (as solvent or temperature, which can push the process rather towards the thermodynamic or the kinetic deposition product) and on the substrate (nature, crystalline structure, presence of surface defects, etc.).

More specifically, in the following paragraphs we will focus on two classes of organic compounds (thiols and diazonium salts), which represent good candidates for surface functionalization, and will discuss about their structuration over a substrate.

1.2.1 Thiols

Alkyl and aryl thiols are organosulfur compounds characterized by a –SH head-group, whose high affinity for metals promotes thiols adsorption on both crystalline and semi-crystalline surfaces, where they spontaneously arrange in self-assembled monolayers (SAMs) [16] (**Figure 1.1**).

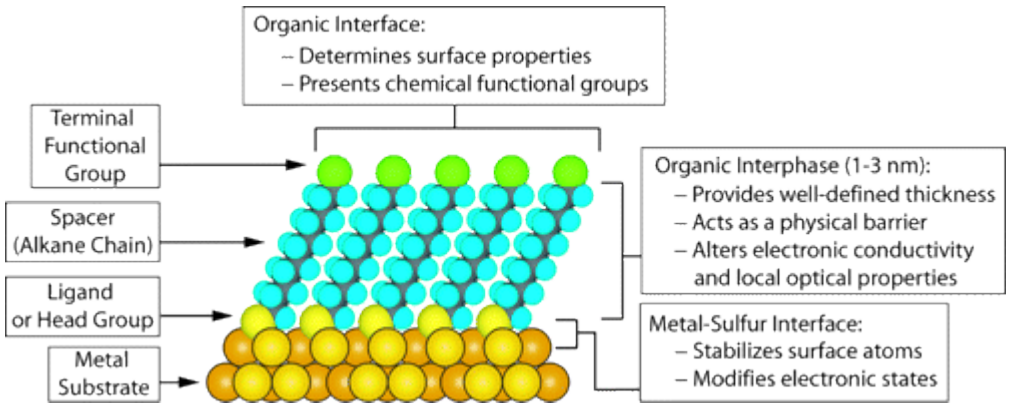

Figure 1.1. Schematic diagram of an ideal, single-crystalline SAM of alkanethiolates supported on a gold surface with a (111) texture. The anatomy and characteristics of the SAM are highlighted. Adapted from [16].

The assembling process depends only on the environment at the interface between liquid (or gas) and metal and does not need any guidance from an external source [17]. The final

structure is defined by a specific molecular orientation (with respect to the surface and between adjacent species) and a surface coverage rate, which determines also the overall compactness of the layer. Thiol-based SAMs can be prepared either by electrochemically induced adsorption [18] or by electroless deposition from gas [19] or from liquid phase; the latter method is the most employed and consists simply in incubating the desired substrate in the precursor thiol solution for a certain time [16].

1.2.1.1. Structure of the film

The SAM structuration is influenced by many parameters, starting from the concentration of the thiol species in solution. For instance, AFM images recorded on 4-nitrothiophenol (4-NTP) SAMs exhibited a dramatic decrease in the surface coverage when the concentration of the functionalizing solution was decreased from 7 (**Figure 1.2**a) to 3.5 $mmol.L^{-1}$ (**Figure 1.2**b) [20]. Besides, the incubation time was shown to have an effect on the stability and orientation of the molecular species within the SAM. Investigations of the bonding strength of cysteamine SAMs on gold *via* single-molecule force spectroscopy evidenced the reaching of a maximum in the binding force with the substrate within 30 minutes from immersion in the precursor solution, (without any significant variations in the following 24 hours), followed by a decrease in the next 5 days due to thiol re-dissolution [21]. Moreover, evolutions in the orientation of alkanethiolate chains from lying-down to standing-up arrangements with time (**Figure 1.2**c) have been evidenced during the deposition process in both gas [22] and liquid phase [17,23].

The structure of the film is also greatly influenced by the nature and the morphology of the underlying substrate. Comparative XPS and STM studies, performed along with DFT calculations, have shown different SAM orientations and coverage on Au, Ag, Cu, Pt, Pd and Ni substrates, influenced, among others, by the S-metal bond strength, the presence of defects or impurities on the reconstructed surfaces, and the surface geometry (planar, nanoparticle or nanocluster) [17]. In particular, DFT calculations modelled the absorption of SAMs on different Au crystal phases and showed different S-Au binding geometries and strengths depending on the reciprocal arrangement of the gold atoms and on the presence of adatoms defects [24]. More specifically, as **Figure 1.2**d shows, close-packed Au(111) surfaces preferentially form staple-motif bonds (where the S atom is linked to a superficial Au and an Au adatom), while more "open" Au(100) and (110) faces privileges bridging bonds (S connecting two superficial Au atoms).

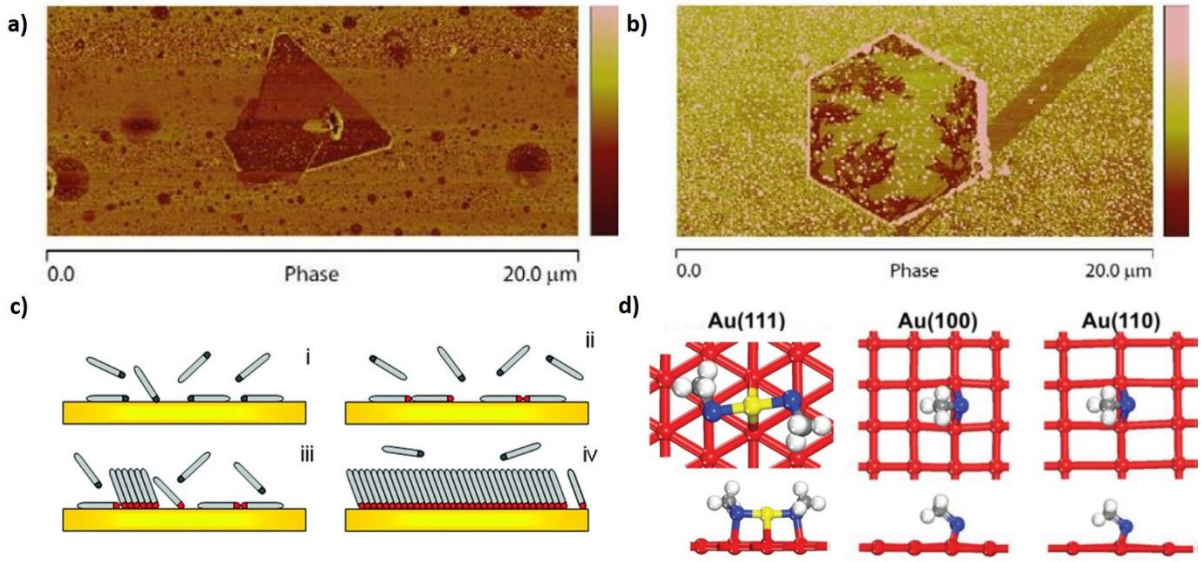

Figure 1.2. Effects of incubation parameters on SAM structure - Thiol precursor concentration: AFM phase images (**a**, color scale: -27 – 29°, and **b**, color scale: 0 - 15°) of Au nanoplates covered with 4-NTP after 12h immersion in a 7.0 mmol.L^{-1} solution (**a**, full coverage evidenced from phase color of the gold nanotriangle, different from the underlying substrate) and 3 mmol.L^{-1} solution (**b**, partial coverage evidenced by few darker zones on the nanohexagone). Adapted from [20]; **Incubation time: c)** Schematic view of an alkanethiol geometrical arrangement evolution with time on an Au(111) substrate during deposition from gas phase: (i) initial physisorption; (ii) adsorption in lying-down arrangement; (iii) partial stand-up rearrangement; (iv) final stand-up close-packed arrangement. Adapted from [22]; **Substrate crystalline structure: d)** Top view (upper panel) and side view (lower panel) of the optimized structures for methylthiolate on Au(111) surface (packed structure, favoring staple motifs *via* Au adatom), and on Au(100) and Au(110) surfaces (open structures, favoring thiol bridges). Only the topmost surface layer is shown. Au, red; Au adatom, yellow; S, blue; C, grey; H, white. Adapted from [24].

Last but not least, the nature itself of the thiol species influences the interactions established with the substrate and between adjacent tethered species, thus influencing the structure of the film. For instance, infrared, contact angle and STM analyses evidenced that the higher polarity of rigid 4'-substituted-4-mercaptobiphenyls, with respect to their alkanethiolate analogues, confer them lower tilting angles from the metal surface normal [25,26], thus increasing the spacing between adjacent molecules. This is why, thanks to the higher flexibility in their bonding angles, alkanethiolates establish stronger intermolecular interactions, thus yielding SAMs with higher surface coverages and denser structures, as it was shown by STM mapping [27] (**Figure 1.3**a).

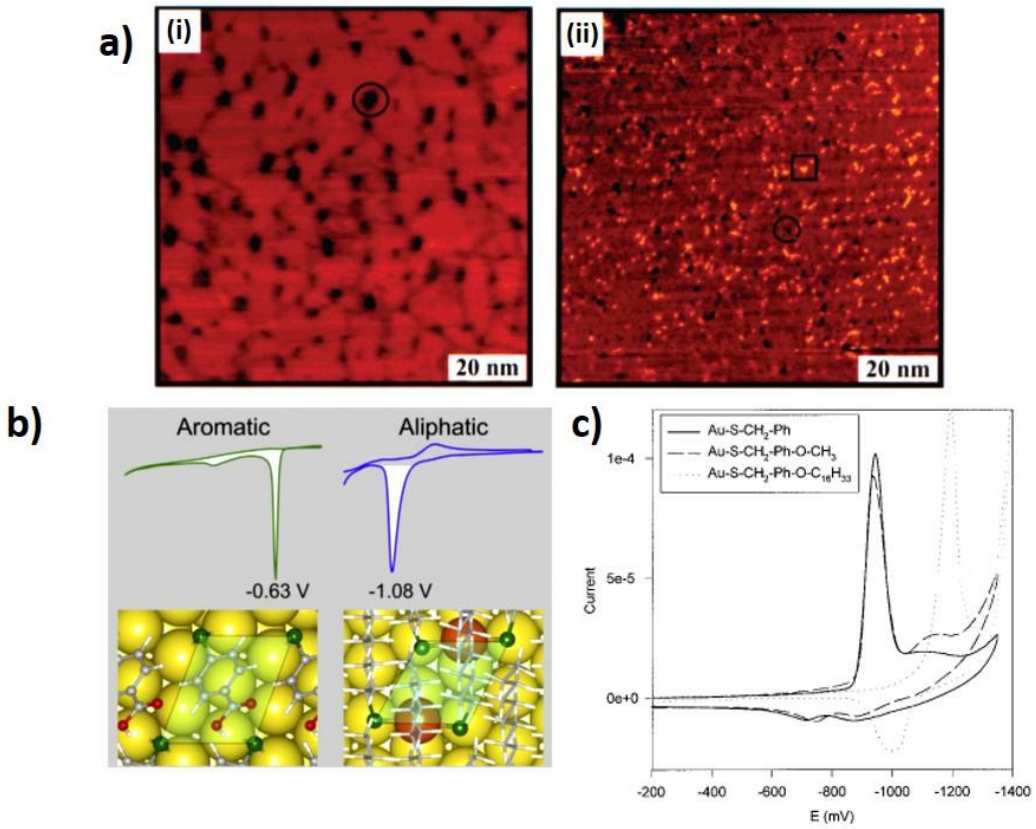

Figure 1.3. Influence of the thiol species on the SAM structure and stability – a) Morphologies of (i) decanethiol and (ii) benzenethiol SAMs on Au(111). Examples of gold vacancy and adatom islands are highlighted by circles and squares, respectively. In (i) the SAM is formed by large, densely packed domain separated by vacancy islands, while in (ii) the molecules form more separated domains, intercalated by a series of small vacancy islands and gold adatoms (induced by the aromatic thiols during the deposition process). Adapted from [27]; **b)** Upper: Typical reductive desorption voltammograms for an aromatic and an aliphatic thiols on Au(111). The peak potential value (Ep) and the charge involved in the peaks (white areas) are indicated. Lower: representation of the models used for DFT calculations: adsorbed thiols for aromatic and staples moieties for aliphatic thiols. Golden: Au surface atoms, orange: Au adatoms, green: S atoms, gray: C atoms, white: H atoms, red: O atom. Adapted from [28]; **c**) Cyclic voltammetry curves for Au-S-CH2-C6H5, Au-S-CH2-C6H4-O-CH3,and Au-S-CH2-C6H4-O-C16H33 monolayers. The cathodic peak reveals the reductive desorption of the studied layer. Adapted from [29].

1.2.1.2. Stability of the SAMs

Probably the major drawback of thiol-based SAMs relies on the weakness of the S-metal bond that leads to easy desorption processes, thus compromising the stability of the modified surface. However, this limitation can be controlled in different manners. For instance, the organisation of the SAMs at the surface was shown to influence the stability of the whole layer. Indeed, close-packed structures were found to be more resistant to electrochemical desorption with respect to less dense layers, as it was evidenced by DFT calculations performed on model aliphatic and aromatic SAMs [28] (**Figure 1.3**b). This effect was remarked also by comparing packing density and electrochemical stability, evaluated from cyclic voltammetry (CV)

experiments, of thiophenols and benzyl mercaptan derivatives [29]. Thanks to the presence of a methyl group between the benzene ring and the SH groups, benzyl mercaptans are more flexible and form denser structures, with stronger intermolecular interactions. These are furtherly stabilized when the length of the *para* substituents increases [29,30] (**Figure 1.3**c).

The effect of the thiol adsorption on the bond strength between the superficial Au adatom and the bulk Au was also evaluated. Single-molecule force microscopy measurements showed that stronger Au-S interactions were established when incubating partially oxidized gold surfaces on functionalizing solutions at high pH [21]. These conclusions suggested that thiol deposition occurs by chemisoprtion, which should indeed be facilitated by the cleavage of the S-H bond in alkaline conditions and the condensation of the H^+ with the shallow –OH groups (which leave as water). However, more recent studies, carried out by scanning tunnelling microscope-break junction, compared the values of conductance in solution and in the air between two gold contacts through a SAM. From the results it was concluded that, despite chemisorption actually occurs during the incubation process (high conductance in liquid), the S-H bond eventually forms again upon sample drying (low conductance in air) and is retained in the final structure, thus leading to a bare SAM physisorption onto the substrate [31].

1.2.1.3. Reactivity of the SAMs

The reactivity of the SAMs is mainly controlled by their structure. Typically, the surface coverage of the layer, controlled by the incubation time, the concentration in solution and the co-presence on the surface of different thiol species, has an important impact on the properties and reactivity of the whole metal-layer system. For instance, absorption spectro-electrochemical experiments on perylenediimide-derived SAMs evidenced the influence of the molecular surface coverage over the sample optical properties [32]. A non-linear shift in the absorbance maxima was indeed recorded (**Figure 1.4**a) when the pure perylenediimide layer was "diluted" by co-adsorbing shorter hexanethiol chains, which altered the original intermolecular interactions and generated higher tilting angles inside the layer.

The nature of the thiols itself can strongly affect the electronic property of the grafted substrate. Indeed, CV experiments, carried out in a ferrocene solution on gold electrodes modified with benzothiophenol and benzyl mercaptan, showed that the higher short-range order in the SAM of the second compound facilitated the electron transfer process across the layer and therefore did not isolate completely the conductive substrate [33] (**Figure 1.4**b).

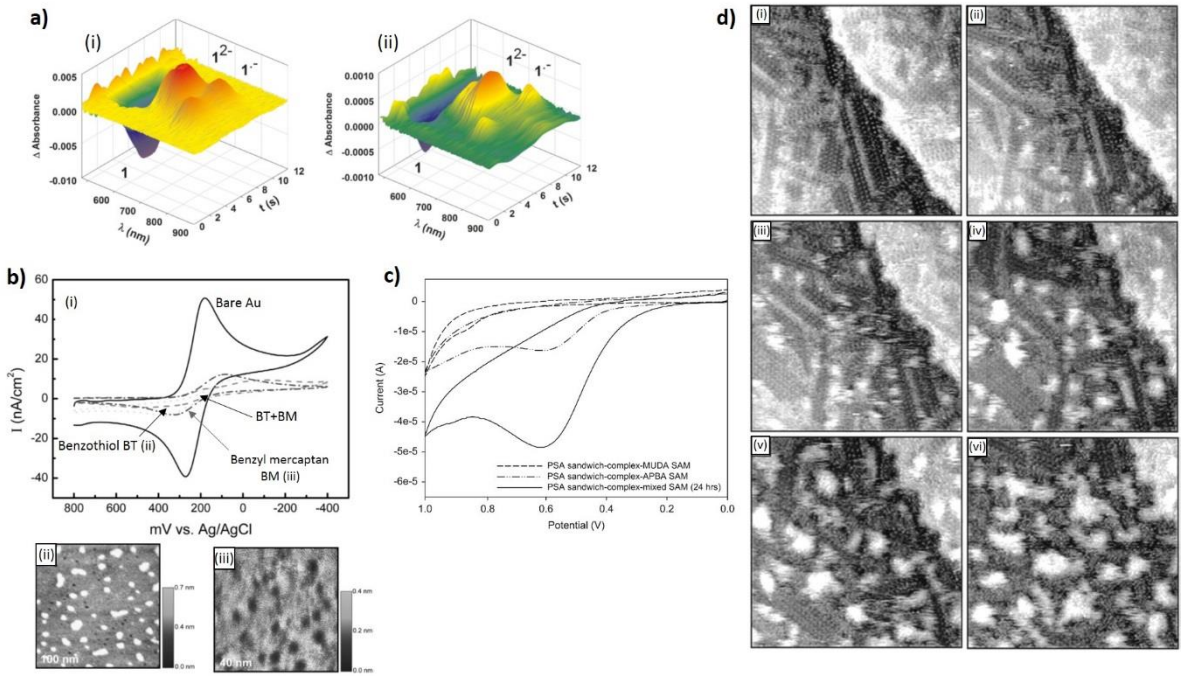

Figure 1.4. Structure-reactivity relationships in thiols SAMs – a) Modification of the optical properties: Absorption spectroelectrochemical experiments on mixed SAMs in 0.1 mol.L^{-1} Bu_4NPF_6/CH_2Cl_2 at 10 mV.s^{-1} and 293 K. On the time axis, 0, 6 and 12 s correspond to the potentials -0.25 (first vertex), -1.05 (potential of reverse scan) and -0.25 V (second vertex) of the CV experiments. From (i) to (ii) the perylenediimide full steady-state coverage rate decreases from 96% to 4%. The overall absorbance decreases too and the absorption maxima shift. Adapted from [32]; **b) Conductive substrate passivation:** (i) shows the voltammograms recorded on both bare and functionalized gold substrates in 1 mmol.L^{-1} $K_4[Fe(CN)_6]$ containing 1 mol.L^{-1} KNO_3. Despite in these latter the ferrocene electrochemical signature decreases considerably, the passivating effect is more consistent in BT layers, whose looser arrangement is shown in the STM map (ii), while the gold surface is not completely insulated by BM layers, with a denser structure shown in (iii). Adapted from [33]; **c) Influence of a mixed-monolayer structure on ET:** Oxidation peaks of naphthol for PSA sandwich-complex-MUDA SAM (single alkylthiol monolayer), PSA sandwich-complex-APBA SAM (single arenethiol monolayer) and PSA sandwich-complex-mixed SAM (24 h incubation). The electron transfer through the layer is more efficient in the mixed SAM (wider peak area). Adapted from [34]. **d) Substrate modification *via* layer electrochemical transformation:** Sequence of STM images (35x35 nm^2) showing the formation of island during the reduction of 4-NTP on Au (111) in 50 mmol.L^{-1} Na_2SO_4. The applied potentials are -230 mV (i) and -240 mV (ii-vi) *vs* SCE. As the polarization time increases, gold islands appear and nucleate. Images are affected by slight thermal drift. Adapted from [35].

However, if the anchored molecular species contain electroactive groups, their reactivity might be damped by the excessive compactness of the layer. For instance, it has been shown that the reduction kinetics of azobenzene groups inside close-packed structures is slowed because the conformational changes that accompany its transformation are sterically hindered [36]. Besides, also the electron transfer processes among the redox moieties and the electrode surface might be altered, as it has been shown for dense ferrocenyl-azobenzene-butanethiol layers, where the ferrocenyl and the azobenzene groups were respectively at the extremity and in the middle of the thiol chain [37]. Upon CV recording, the only electrochemical

response was yielded by the ferrocenyl groups, since the compactness of the anchored chains did not allow the incorporation of charge-compensating cations that could promote the azobenzene reduction. A restoration of the ion-gated electron transfer process with the electrode surface within the film was obtained by introducing smaller electrolyte cations (i.e. H^+) that could penetrate the layer, or else by co-adsorption of a second thiol species, which can improve the "accessibility" of the electrolyte to the azobenzene reactive centres [37]. The co-adsorption of two thiol species at different lengths on the surface can as well improve the electron transfer process across the layer: this is the case, for instance, of mixed APBA/butanethiol layer, where the APBA angle with respect to the surface normal is tilted more perpendicularly by the presence of butanethiol species [34]. This orients vertically the π-conjugated backbone and allows more efficient electron transfers through the SAM, thus improving the detection of external biomolecules (**Figure 1.4**c).

The adsorption of layers can, in some cases, generate modifications on the substrate superficial structure, as it was seen before in the example reported in **Figure 1.3**a, where the deposition of arenethiols on gold (differently from alkanethiols) provoked the "extraction" of Au adatoms from the surface [35]. Besides, additional changes to the substrate structure can be promoted by the layer electrochemical reactions. This has been observed by STM mapping *in situ* (in sodium sulphate solution) of the reduction process of a 4-NTP-functionalized gold substrate: when sweeping the potential negatively, the apparition and nucleation of islands (**Figure 1.4**d) was attributed to gold surface reconstruction induced by the transformation of the original species into the reaction product(s). These islands disappeared at -380 mV *vs* SCE, where the anchored species are expected to electrochemically desorb and the original gold surface is restored.

Additionally, the layer dipole might influence the substrate electronic properties, as it has been evidenced for mixed undecanethiol and 11-ferrocene-1-undecanethiol architectures: while the dipolar moment of the pure ferrocene-derived layer, pointing towards the substrate, increased the gold work function, partial substitution with non-electroactive chains provoked a net change in the overall dipole orientation, accompanied by a negative shift in the work function value [38].

Thiols based SAMs can be advantageous for applications where the layer is not subjected to harsh conditions (e.g. desorbing electric potential or immersion in solvents that can induce the chains re-dissolution) or, on the other hand, where it has to be easily removed

(e.g. when it is used as a template [10,16]). However, in other cases the relatively moderate force of the Au-S interactions might be detrimental for the stability of the layers, which should be rather covalently bonded to the metal surface. The next paragraph will discuss about another kind of surface-functionalizing structures that can fulfil this requirement.

1.2.2 Diazonium salts

Differently than thiols, diazonium salts have the advantage of unambiguously form stronger, covalent bonds [39,40]. Most of the knowledge we have today around the chemistry of aryl diazonium salts is due to the thorough and extensive work of Pinson and collaborators, who studied the grafting of these species under different operating conditions, in terms of nature of the solvent (organic or aqueous), solution pH, methodology and substrate [41–43].

1.2.2.1. Reduction mechanism

Figure 1.5 shows the general mechanism accounted for electrochemically-induced grafting [40]: first, the diazonium salt is activated by the transfer of 1 electron from the substrate, which provokes the homolytic cleavage of the C-N bond between the benzene ring and the diazonium functionality. While the diazonium leaves as N_2, the formed aryl radical is highly instable and tends to react quickly with the surrounding species. If these are solvent molecules or other radicals, it will transform into inactive byproducts. However, if the aryl radical is at close proximity to the substrate, it can covalently graft to it. The covalent nature of the bond between the diazonium derivative and the surface has been shown by resistance of the layer to ultrasonic bath in various solvents (e.g. acetonitrile, dimethylformamide or acetone) [40], but also by the presence of specific spectroscopic bands attributed to the bond [44], which were in some cases observed up to 700 K in ultra-high vacuum [40].

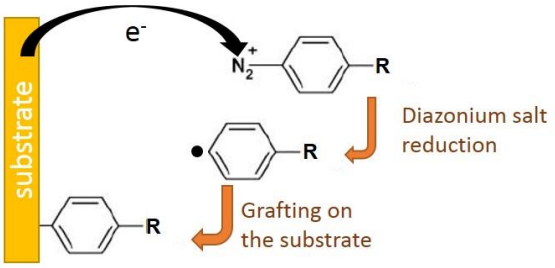

Figure 1.5. General grafting mechanism of an aryl diazonium salts on a reductive substrate.

1.2.2.2. Diazonium-substrate bond

Although the ET from the grafting surface to the diazonium salt is usually promoted by electrochemical polarization of the substrate (*via* cyclic voltammetry (CV) or chronoamperometry [40,45]), the weakly negative (or even slightly positive) reduction potentials of most diazonium salts can induce a spontaneous ET from the substrate surface. It was evidenced that layers grown from 4-NBD solutions in H_2SO_4 onto gold either under electrochemical polarization or at the open-circuit potential (OCP) had comparable surface coverage and thickness values [46], despite layers spontaneously formed were less resistant to sonication. This was attributed either to a higher amount of physisorbed species or to a difference in the binding sites with respect to the electrochemical process [46].

The strength and nature of the diazonium-substrate bond depend as well on the nature of the grafted substrate. Several kinds of surfaces have been successfully modified with diazonium salts, ranging from carbon-based materials [41,47–52], to semiconductors [40,53], to metals [42,44,46,54,55]. Specifically, TOF-SIMS spectrometric analyses showed that diazonium grafting on carbonaceous materials usually proceeds towards the formation of either C-C bonds (with the carbon surface) or C-O bonds (with its superficial oxides) [48]. However, the presence of superficial oxides on carbon surfaces has been suspected to promote the grafting of diazonium salts without dediazonation (**Figure 1.6**), since mass spectrometry investigations revealed the presence of ***C(OH)-C-N=N-C$_6$H$_5$***$^+$ fragments on close-to-monolayer polyphenylene structures [55]. XPS and IR measurements carried out on diazonium-modified metals surfaces concluded that also in this case both C-metal [42,44,56] and C-metal oxide bonds [46] can be formed, although the presence of the latter is minor for some substrates (e.g. copper) [55] or can be minimized under particular working conditions (i.e. substrate polishing before reduction [40] or grafting in deoxygenated solvents [40] or in acid media [56]). In any case, the absence of evidences for direct N=N-metal bonds formation proves that grafting onto these surfaces occurs preferentially *via* dediazonation (rather than through the diazonium functionality), most likely because of the weaker electron-donor nature of metals [55].

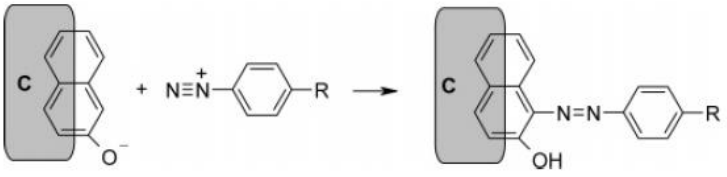

Figure 1.6. Schematic representation of grafting without dediazonation promoted by residual oxides on a carbon surface C. Adapted from [55].

1.2.2.3. Multilayer formation

Previously we used the term "layer" to describe the structure formed by diazonium grafting. In this case, though, this word does not indicate the formation of monolayer structures, as it was intended for thiol-based SAMs, but more generally the assembly of more complex architectures. This can be clearly evinced by the observation of the general trend of a grafting voltammogram: as shown for the electrografting of 4-nitrobenzene diazonium (4-NBD) on glassy carbon [40] or gold [57] surfaces, the first cycle shows the appearance of a huge and broad peak upon scanning the potential towards negative values (**Figure 1.7**a), which was attributed to the 1-electron-induced radicalization of the diazonium species and occurs irreversibly, since no corresponding anodic peaks are registered in the backward potential scan [40]. Analogously, the several peaks recorded on gold (**Figure 1.7**b) were assigned to the same reduction mechanism occurring on different gold crystal facets [57]. The absence of the cathodic peak and of any other feature in the following scans suggests the formation of a passivating structure that inhibits the charge transfer from the electrode surface to the diazonium species left in solution [40].

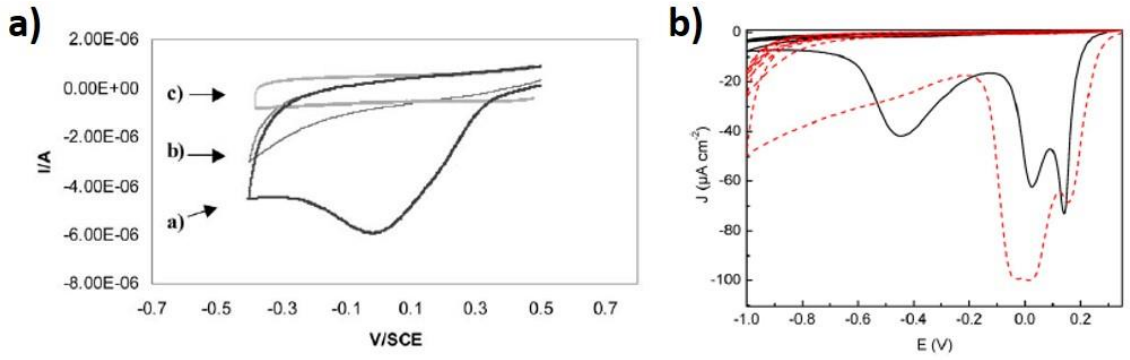

Figure 1.7. Electrografting *via* CV of **a)** 4-NBD salt (2 $mmol^{-1}$ solution in 0.1 $mol.L^{-1}$ NBu_4BF_4 in acetonitrile) onto a glassy carbon disk electrode (Ø = 3 mm). (a) first CV scan, b) second CV scan and c) CV of the same electrode in 0.1 $mol.L^{-1}$ NBu_4BF_4 in acetonitrile (without diazonium salt in solution). Adapted from [40]; **b)** diazonium salts (4-NBD, black solid line, and fluorinated benzene diazonium, red dashed line; 0.005 $mmol.L^{-1}$ solution in 0.05 $mol.L^{-1}$ TEAP in acetonitrile) onto a gold-on-glass electrode. Adapted from [57].

EQCM measurements performed during the electrografting of various diazonium salts on gold in acetonitrile [56] showed that the deposition process follows two steps: during the first one, the increase of mass recorded on the substrate has been assimilated to the formation of a monolayer-like structure. This process terminates concomitantly with the end of the cathodic wave on the CV. The second step is instead characterized by slower increases in mass (as the number of scans increase), thus evidencing the growth of thick multilayers [56]. The same effect

has been observed when the electrografting is performed *via* chronoamperometry: studies performed on 4-NBD grafting on gold showed that the multilayer formation is favoured as the substrate potential is lowered [58], while investigations on carbonaceous materials underlined the influence of the diazonium salts concentration and the electrolysis time on the final film thickness [41].

Doppelt *et al*. explained the formation of multilayer structures considering the electron-rich nature assumed by the species grafted onto the substrate, which can promote the attack of the diazonium-derived radicals in solution [55]. The proposed mechanism, illustrated in **Figure 1.8** (red circles), is supposed to proceed until damping of the electron transfer through the layer, which makes this reaction self-limiting [45]. Moreover, QCM results evidenced the occurrence of layer delamination after a high number of cycles [58]. As it was observed for the substrate grafting mechanism, also the formation of side branches might proceed without dediazonation of the species in solution (green circles in **Figure 1.8**), thus leading to the presence of azo bridges inside the layer [55], as evidenced by XPS, IR and TOF-SIMS analyses [56,59].

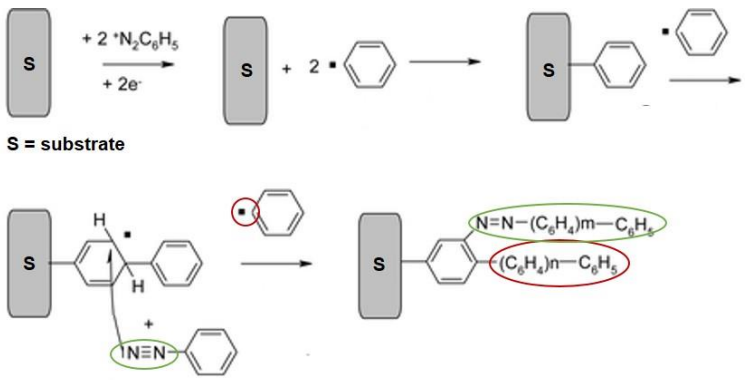

Figure 1.8. General mechanism for the formation of C-C branches *via* radical attack (red circles) and azo bonds *via* diazonium attack (green circles) in a diazonium-derived organic layer (S = substrate). Adapted from [55].

In a similar way as it was discussed for thiols, also in this case the presence of thick and dense structures impacts the overall structure reactivity. This was already demonstrated by the surface passivation effect observed during the multilayer grafting, but can also affect the reactivity of the grafted molecules, if they possess electroactive functionalities. For instance, CV measurements on the reactivity in acid medium of azobenzene moieties inside a nitroazobenzene multilayers, grafted on carbon, showed a negative shift of the azobenzene reduction peak with the increase in the layer thickness, related to variations in the dielectric properties and slower proton diffusion rates inside the film [60].

For some applications, the blocking effect of dense, covalently bonded multilayers can be advantageous. This is the case, for instance, of interference-free glucose amperometric biosensors, obtained by immobilizing glucose oxidase enzymes on fluorophenyl multilayers, grown from the corresponding diazonium salt on platinum [61]. Thanks to the blocking properties of the thick structure, the only electrochemical response derive from the selected ET to the enzymes, while the reaction of interfering substances on the substrate was inhibited. Moreover, thick 3,5-di(trifluoromethyl)benzene layers were grown on copper meshes to obtain super-hydrophobic an super-oleophilic metal structures, which can be efficiently used e.g. for oil/water separation or self-cleaning surfaces [8]. However, in most of the case the unpredictable three-dimensional arrangement of the multilayers makes it difficult to implement their use for more specific and precise application. The next section will review some of the proposed approaches for modulating the diazonium grafting deposition.

1.2.2.4. Thickness control

In order to gather control over the grafting procedure, and therefore tuning the final structure and reactivity of the structure, several methods have been proposed. The easiest way consists in varying the diazonium solution concentration, as well as the grafting electrolysis charge [53] or time [41]. This approach was employed by Allongue *et al.* for modulating the CV grafting of different aryldiazonium salts on glassy carbon (GC) or highly oriented pyrolized graphite (HOPG) [41]. On the basis of the post-grafting measurements obtained by XPS and PMIRRAS, an empirical formula was elaborated that allowed predicting the final surface coverages depending on the diazonium solution concentration and the scanning speed. Nevertheless, the calculated values were slightly underestimated with respect to the analytical results and a proper monolayer structure could not be formed [41].

Another possible way to control the layer growth consists in employing bulky substituents on the benzene rings, which sterically hinder the formation of branches after the grafting of the first layer on the substrate [52]. A thorough study in this extent was carried out by Combellas *et al.* [62], who showed that only molecules presenting encumbering substituents in positions 3 and 5 of the benzene ring could efficiently gather a monolayer structure. This result was confirmed later on by a study of Greenwood *et al.*, who compared STM images acquired on 3,5-D-*t*-BuBD layers with those obtained on 4-nitrobenzene diazonium (4-NBD) structures (**Figure 1.9**a) [52]: since 4-NBD is not "protected" by bulky groups, it tends promoting branching

already at low concentration (most likely on the *ortho* position with respect to the nitro group), thus yielding rougher and thicker profiles with respect to 3,5-D-*t*-BuBD.

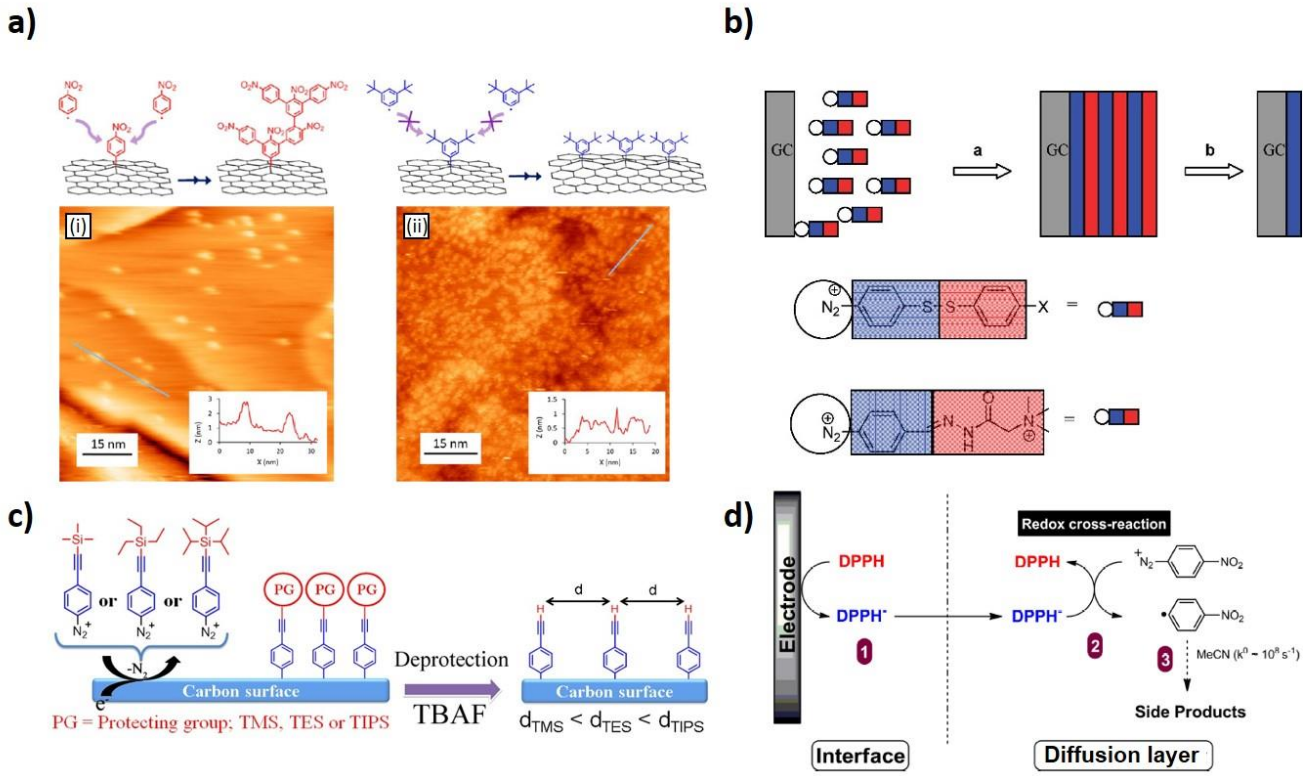

Figure 1.9. Approaches for controlling the grafting of aryldiazonium layer - a) Bulky substituents in positions 3 and 5: On top, the schematized view of the grafting processes with 4-NBD (multilayer formation) and 3,5-D-*t*-BuBD (monolayer formation) is shown. On the bottom, STM height images (BV = -0.7 V, I_T = 80 pA) acquired on layers grafted from 1 mmol.L^{-1} solutions of (i) 4-NBD and (ii) 3,5-D-*t*-BuBD. The insets show the profiles extracted from the sections evidenced in the corresponding maps: in (i) tall and spaced clusters are formed (clustered multilayers), while in (ii) the formed layer is thinner and more homogeneous (dense monolayer). Adapted from [52]; **b) 2-step formation/degradation:** Schematic view of the (a) formation of multilayers from disulfide (top molecule) or aryl alkyl hydrazone (bottom molecule) derivatives and (b) subsequent cleavage by acid electrolysis to obtain a single monolayer. Adapted from [63]; **c) 2-step protection/deprotection:** Schematic view of the grafting of trialkyl silyl-protected ethynyl aryldiazonium salts in ordered monolayers (left) and subsequent protecting group removal in TBAF (right) to yield an ethynyl-functionalized monolayer. The inter-molecular spacing is determined by the size of the protecting group. Adapted from [64]; **d) redox cross-inhibition:** Schematic view of the inhibition mechanism of DPPH, which reduces on the sample surface and then diffuse to re-oxidize at the expenses of 4-NBD. This forms the corresponding aryl radical and is deactivated in the solution bulk, therefore it cannot form branches with the surface-grafted species. Adapted from [49].

In order to extend the possibility of forming controlled structures also on molecules that do not possess already encumbering substituents, Daasbjerg *et al.* adopted a two-step formation/degradation approach (**Figure 1.9**b): this consists in an initial grafting on GC of multilayers, derived from aryldiazonium salts substituted in position 4 with sterically hindering aryl disulfide [65] or alkyl hydrazone groups [63], which limit already the layer thickness (formation

step). Later on, acid hydrolysis can be used to cleave the bond of the surface-grafted molecules with the branches and therefore to obtain a single monolayer (degradation step) [63,65].

A similar strategy was proposed by Leroux *et al.*, who used bulky Si-derivatives (as TIPS [66], TMS or TES [64]) to protect the ethynyl function in position 4 of the aryl diazonium salt (**Figure 1.9**c): in this case, the steric hindrance does not allow the formation of multilayers, hence a monolayer is formed (more or less compact, depending on the dimension of the protective group [64]), which can be subsequently de-protected in 0.1 mol.L^{-1} TBAF in THF to restore the ethynyl group. For both approaches, the post-grafting evaluation of the layers thicknesses and coverages corresponded to those expected for near monolayers [63,64], which can be therefore employed as such or modified upon desire *via* "click chemistry". For instance, TIPS-protected diazonium monolayer grown on carbon could be later on deprotected and "clicked" by cycloaddition with differently terminated azides, in order to create molecular bilayers that can improve the tunneling ET with top carbon electrodes (thanks to the energy level alignments) [67] or work as a (bio)chemical sensors (thanks to the introduction of redox-active probes) [12].

In alternative, a growth control method proposed by Breton's group is based on the use of molecular inhibitors (as DPPH or quinone derivatives). Initially, it was thought that these species were working as radical scavengers, hence removing the exceeding electron from the diazonium-derived radicals in order to inhibit their polymerization on the surface [68–70]. However, more recent studies [49,50,71] showed that inhibitors are rather involved in a redox "cross-reaction" (**Figure 1.9**d), which leads to the deactivation of diazonium-radicals far from the electrode surface and, in turn, to their impossibility of reacting on the substrate-anchored molecules. AFM "scratch" images of layers grafted onto HOPG, in presence of 4-substituted diazonium salts and an excess of DPPH, showed a 3 to 7-fold decrease in the thickness with respect to the same layers grafted without inhibitor [50], which corresponded to the formation of a monolayer structure. With respect to the previous approach, this latter has the advantage of fabricating layers that bear already the desired substituents and in a single reaction step. However, the choice of the best inhibitor for the chosen molecular species and of the proper concentration for obtaining more or less thick layers is not trivial; further details will be provided in Chapter 3. Also in this case post-functionalization of the monolayers can be performed and has shown to be more effective than for multilayer structures. This has been evidenced by attaching a redox and electrocatalytic TEMPO unit on top of a 4-NBD-derived

monolayer on carbon (obtained *via* DPPH inhibition), which resulted in higher surface coverages and improved interfacial reactivity (faster ET) with respect to the what obtained on thick, disordered structures [72].

Ultimately, structures derived from both thiols and diazonium salts can be conveniently prepared for the most different applications, thanks to the vast range of properties they can be designed to possess in terms of reactivity, substrate modification, interactions with the outer environment, and so on. In order to gather a precise knowledge of the characteristics and behaviours of these systems, with the aim of developing more and more specific designs for targeted applications, the techniques employed to investigate them should be able to operate in their working conditions and at very low resolution, hence at the scale of single molecules. The next paragraph will review some of the dynamic investigations technique so-far implemented.

1.2. Dynamic investigations

As it was previously discussed, layer-functionalized surfaces present novel structural properties that influence their response to external stimuli. In order to interpret correctly their behavior and modulate it for the envisaged applications, an investigation technique should ideally be able to correlate the surfaces composition (in terms of arrangement on the substrate, intermolecular orientation and packing) with their reactivity in real working conditions (i.e. *in situ* or *operando*). For this purpose, several methods have been developed throughout the years, aiming more and more to increase the analytical sensitivity from macro to micro and, most recently, even to nano structures. In the following paragraphs we will briefly review a few of the more striking analytical techniques allowing to characterize *in situ* or *operando* the properties of molecular layers, thiol- and diazonium-based layers mostly.

1.2.2 Characterization at the macro/microscale

1.2.2.1. Quartz Crystal Microbalance

The working principle of QCM relies on the use of a disk made of a piezoelectric material, i.e. of crystalline structures with no inversion symmetry, which can deform mechanically under the application of an external electric field across two thin metal electrodes deposited on each side. *Vice versa*, these materials can be electrically polarized when subjected to a mechanical stress [73]. In both cases, the intensity of the deformation and the polarization are proportional to each other. Hence, an alternate voltage (MHz regime) will induce a constant oscillation on the crystal and can excite the crystal to resonance, the frequency of which

depends on the thickness (mass) of the disc. When the piezo-material is modified by the deposition of a molecular layer on its surface, a shift in the resonance frequency is recorded and can be related to the mass of the deposited layer thanks to the Sauerbrey relationship. The sensitivity of the technique, called *microbalance*, can detected mass variations (increase, decrease) ranging from several hundreds of micrograms down to nanograms [73,74].

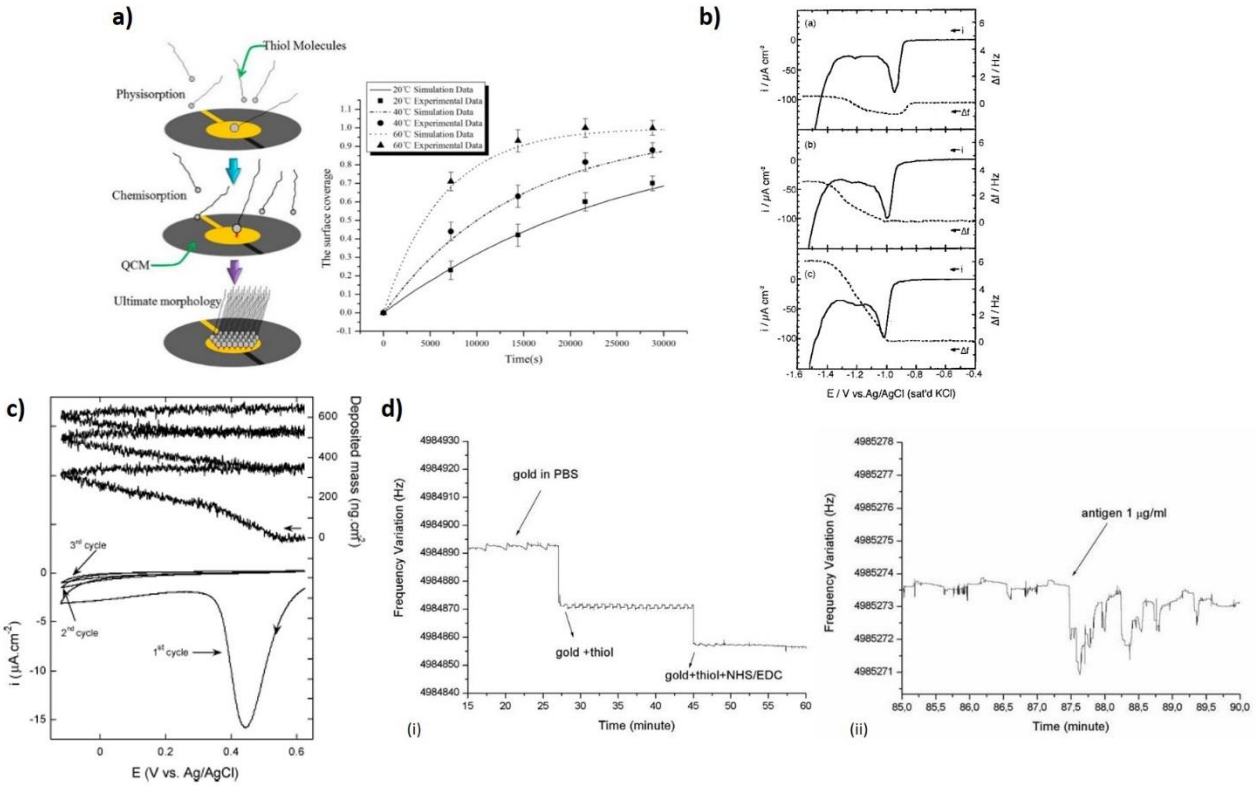

Figure 1.10. (E)QCM application for the study of thiol- and diazonium-based structures on gold – **a)** On the left, schematic view of the adsorption process of alkylthiole species on the gold-coated QCM chip (first physisorption in lying-down arrangement, then structuration in standing-up conformation). In the right, comparison between experimental and simulated data for the thiols coverage rate as a function of time at different working temperature. The close proximity of the values for each set of data confirms the sensitivity of QCM for precise analytical investigations. Adapted from [19]; **b)** EQCM responses for the reductive desorption of (a) C8-SH SAM, (b) C12-SH SAM, and (c) C-16 SH SAM. In all the potential sweep, the appearance of a first cathodic peak and of a weaker one at lower potentials is due to the heterogeneous substrate reactivity and/or to the influence of the molecular coverage on the desorption process. The frequency (i.e. mass) variations recorded for each sample are related to the cation adsorption onto the substrate, which follows the reduction process and is dependent on the chain length (as shorter-chain SAMs will facilitate the penetration of solution cations, which can adsorb even prior to thiol desorption). Adapted from [75]; **c)** Mass-potential curves (top) and CV plot (bottom) of a gold electrode in 0.1 $mol.L^{-1}$ NBu_4BF_4 + $5mmol.L^{-1}$ 4-NBD in acetonitrile (scan rate = $5 mV.s^{-1}$). The highest increase of mass on the gold substrate coincide with the end of the cathodic peak on the first voltammetric cycle (monolayer formation), then the mass increases more slowly with the number of cycles (multilayer formation). Adapted from [56]; **d)** Decrease of the resonance frequency of the quartz (i) from the bare gold substrate, to the adsorption of 11-mercaptoundeanoic acid SAM (20 Hz shift), to the final addition of NHS/EDC cross-linker (15 Hz shift), which can couple specifically with antibodies; (ii) upon reaction of the antibody-modified cross linker with the antigen (injected with a pump at a flux of 1 $\mu g.mL^{-1}$, 3 Hz shift). Adapted from [76].

Among the possible piezoelectric materials, quartz (Quartz Crystal Microbalance QCM) is usually preferred for its good chemical stability, high shear modulus and low resistance to acoustic wave propagation [73]. Since the quartz crystal is sandwiched between gold contacts, functionalization with thiol or diazonium-based structures is possible and interesting for the investigation of their structures and properties.

For instance, the comparison between measurements on QCM chips before and after the deposition of 11-mercapto-1-undecanol SAMs allowed formulating a novel adsorption/desorption kinetic model for thiol deposition, which takes into account the dependency on the temperature and incubation times [19] (**Figure 1.10**a). Note that Quartz Crystal Microbalance with dissipation monitoring (QCM-D) measures an additional parameter, the dissipation ΔD, which gives information about the energy losses in the system and is particularly useful in the study of soft layers and quantification of their properties.

However, for monitoring *in situ* the reaction processes, an important development of this technique is constituted by the electrochemical QCM (EQCM), where one metal contact of the quartz crystal is used as working electrode and the recorded mass variation can be related to a variation in the electrical charges (thanks to the combination of the Sauerbrey relationship with the Faraday law) [73]. For this purpose, specific cells were designed to perform analyses in both aqueous and organic electrolytes [73]. This allowed monitoring in real time the thiols adsorption process and to assess the role of the solvent: for instance, fabrication of stable SAMs of dodecylthiol was shown to occur faster and more straightforwardly in DMF, rather than in ACN [77]. Successive EQCM investigation on SAMs of alkanethiols of different lengths showed that the stability to desorption is also influenced by the heterogeneous reactivity of the substrate and to the molecular layer density, and that electrolyte cations tend to replace the empty spaces left inside the layer after partial chains desorption [75] (**Figure 1.10**b).

The possibility of performing *in situ* electrochemical reactions was exploited also to study the diazonium salts grafting process: as it was previously mentioned in Section 1.2.2.3, EQCM could reveal the occurrence of two distinct steps in the CV-induced electrografting of aryldiazonium salts [56,58] (**Figure 1.10**c). Besides, it provided evidence for direct aryl radical-gold bonding (e.g. in the case of anthraquinone-based diazonium salts [78]) and revealed the influence of the electron-withdrawing nature of 4-substituted diazonium precursor on the efficiency of the attack to the gold surface and on the tendency for multilayer formation [79].

Moreover, modifying EQCM chips with thiol- or diazonium-based layers, decorated with specific functionalities, paved the road to a whole new series of electrogravimetric measurements. These exploit the (enhancing or passivating) ET properties provided by the molecular layers, along with their anchored functional groups, to use EQCM as an extremely sensitive detector for biomolecules (as antigens, antibodies, DNA) [76,80], but also inorganic water pollutants [81,82] (**Figure 1.10**d). Apart from the obvious advantages they can provide, these methods can be also employed to investigate the surface-structure reactivity relationships of post-functionalized molecular layers prior to their application in real devices.

The extreme sensitivity of (E)QCM (whose limit of detection is of few ng per unit of frequency shift in Hz), along with the possibility of working in controlled environment (e.g. under vacuum [73] or in Ar [58]), results advantageous for measuring the size of very thin layers. Besides, its label-free nature makes it ideal as *in situ* sensing technique [83]. However, films can be properly analyzed only if they are homogeneously spread over the quartz, rigidly attached to it and not heavier than the 2% of the crystal weight [73]. Moreover, no information about the nature of the species and/or of the chemical transformations occurring on the sample surfaces can be revealed.

1.2.2.2. Spectro-electrochemistry

Classic optical spectroscopy

Optical spectroscopies employ light sources in the 100-2000 nm wavelength range, spacing from the ultraviolet (UV) to the infrared (IR) radiations, thus stimulating transitions involving the electronic/vibrational/rotational (vibronic) levels of the studied sample. These spectroscopies can be coupled to optical microscopes providing spatial resolution. More specifically, the lateral resolution Δx is limited by the Rayleigh criterion [84]:

$$\Delta x > (0.61\,\lambda)/(n\,\sin\theta) \qquad (1.1)$$

where λ is the wavelength of the incident radiation and $NA = n\,\sin\theta_{coll}$ is the objective lens numerical aperture (depending on the refractive index n of the measuring medium and on the half angle θ_{coll} of the illuminating cone). This means that for visible light (λ = 300-800 nm) the resolution will be limited to around 0.2-0.4 μm [84] and improves to tens of μm in UV; however, shorter wavelengths would need to be used to reach lower resolutions and therefore observing smaller objects. The depth resolution (along the *z* axis) is instead defined by the

Abbe criterion and is significantly lower than the lateral resolution (in the order of 1 to 2 µm, depending on the wavelength of illumination):

$$\Delta z = 2\lambda/NA^2 \tag{1.2}$$

The transitions observed in optical spectroscopy are schematized in the Jablonski diagram (**Figure 1.11**). If the light energy matches exactly the difference between the ground level and an excited level, it will be absorbed and used to promote the electrons to the upper state. According to the Boltzmann distribution principle, this brings instability in the system, which naturally tends to keep an overall low energy. In order to regain stability, it will therefore proceed to the repopulation of the ground state by electron decay. This process is accompanied by an emission that can be radiative or non-radiative (the absorbed photon is converted to heat). In the first case, the molecular spin can stay unchanged (fluorescence) or can have a transition among singlet and triplet, forming a so-called inter-crossing system, before relaxing to the ground state (phosphorescence). These phenomena are exploited in UV-vis and fluorescence spectroscopy.

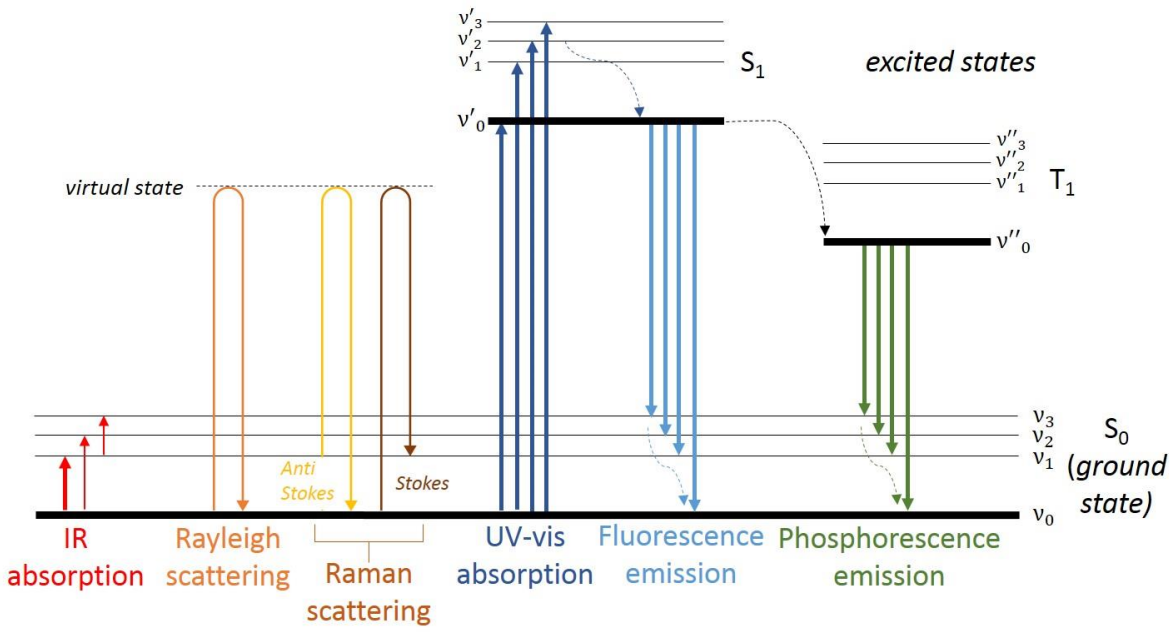

Figure 1.11. Jablonski diagram showing the photon transitions stimulated in the IR to UV light range. S_i stands for singulet state, T_i for triplet state, while ν_i represent the vibrational states. The colored dashed arrows indicate vibrational relaxation, while the black dashed arrow identifies an inter-crossing system.

Absorption also occurs with photons at lower frequency, in the near, mid and far IR regions (4000-400 cm^{-1}), as their energy matches the difference between vibrational levels.

Also in this case the Boltzmann distribution is valid, hence the most numerous and intense transitions are expected to start from the ground vibrational level. Nevertheless, some hot bands may originate from vibrational levels different from the ground one.

Raman effect: an inefficient inelastic scattering process

It is also possible that the photon energy is intermediate between the ground level and the first excited electronic level; in this case, absorption cannot occur and the photon will be scattered. Most commonly, the scattering occurs elastically, hence the scattered photon maintains the same energy as the incoming one (Rayleigh scattering). However, if the photon is scattered inelastically, its final energy will show a negative (Stokes shift) or positive (anti-Stokes shift) variation that matches the energy between two vibrational levels. While the signal originated by the elastic scattering does not gather any chemical information on the sample, the inelastic scattering is at the basis of the Raman technique [85].

Despite the intrinsically different nature of the Raman scattering with respect to the IR absorption, both techniques are in fact employed to probe the transitions among vibrational levels in the studied systems and can sometimes yield complementary information. This is due to their particular "selection rules", i.e. to the conditions a vibrational transition should fulfil to be detected by either of the two spectroscopic techniques. Specifically, absorption in IR will be observed if the transition generates a variation in the molecular *dipolar moment*, while Raman scattering will be produced when a change in the molecular *polarizability* occurs. Because vibrations often modify only one of the two parameters and leave the other unaffected, IR and Raman results are usually considered as complementary [86].

As in this work we mainly employed Raman spectroscopy, we will focus in the following on its description. Raman scattering experiments are generally easy and straightforward to perform, as they do not require any sample preparation and can be performed in normal ambient conditions. In a basic setup, the sample is mounted on the sample stage and illuminated through a confocal microscope (see Chapter 2) with a visible or NIR laser light source. The signal scattered back from the sample is collected again by the objective and directed towards the spectrometer, where it is detected. According to Equation (1.1), the achievable lateral resolution reaches values down to a few microns. Note that the spatial resolution in Raman spectroscopy is nearly constant along the spectrum, as a typical Raman shift (up to 4000 cm^{-1}) is contained within 30 to 200 nm depending on the monochromatic

excitation wavelength. This is not the case for IR spectroscopy, which uses broad band sources like globars. The range of the mid-infrared domain is typically between 4000 cm^{-1} and 400 cm^{-1} (or between 2.5 µm and 25 µm)., thus the spatial resolution varies along the spectrum between ~1 to 10 µm. This aspect, along with the lower sensitivity of Raman spectroscopy to water (whose vibrations are accompanied by small changes in the polarizability, hence by weak scattering), makes it preferable to the IR technique, especially in those applications (such as biological and medical compositional analyses [87–89]) where the samples need to be kept in a wet state.

However, standard Raman analyses on nanostructured materials are not expected to detect precisely the characteristics of single adsorbed molecules, but rather to obtain a collective signal averaged over large (micrometric) areas. Besides, because of the low Raman scattering efficiency, signals are usually very weak and difficult to detect when arising from thin molecular layers. In general, when a molecule scatters an external light source, the total intensity of the radiation is proportional to the square of the induced dipole moment:

$$I = \frac{16\pi^4}{3c^3}\nu^4 \cdot \mu_{i,0}^2 \tag{1.3}$$

where c is the speed of light and $\mu_{i,0}$ is the amplitude of the induced dipole moment. Due to its dependence on the fourth power of the frequency ν, the scattered intensity is much stronger for radiations of short wavelength, i.e. high frequency. The intensities of the scattered lines depend also on the intrinsic properties of the studied system, more specifically on the cross-section σ, which is defined as the ratio between the total scattered power (in W) and the irradiance of the incoming radiation (in $W.m^{-2}$) and has therefore the dimensions of an area. For a single Stokes transition i, the number N_s of light quanta inelastically scattered per atom, per length of material dz per solid angle element $d\Omega$, can be defined as [90]:

$$dN_s = N_a N_o \left(\frac{\partial \sigma_i}{\partial \Omega}\right)_i d\Omega dz \tag{1.4}$$

where N_a is the number of molecule per unit volume in the lower energy state, N_0 is the number of incident light quanta and the ratio $\left(\frac{\partial \sigma_i}{\partial \Omega}\right)_i$ is the differential cross section, described by a complex formula [91]. Respect to the other optical spectroscopies, the Raman effect appears to have the lowest cross section: averagely, for an incident flux of 10^8 photons, only one photon will be inelastically scattered. For comparison, a single fluorescent impurity with a quantum yield of 0.1 can produce ten fluorescence photon for the same incident flux. In summary, not

only the Raman transitions are difficult to observe, but also they can be easily and completely covered by other light-emitting effects (as fluorescence).

Nevertheless, despite the low sensitivity of Raman spectroscopy, McCreery's group proved the possibility of imaging in air diazonium-derived layers (presumably multilayers) grafted on carbon thanks to the use of short-wavelength lasers, powerful CCD detectors and, mostly, a spectrometer configuration optimized to yield the best collection efficiency [92,93]. The same analyses could be performed also upon immersion of the sample in an electrolyte solution [94], paving the way to the spectro-electrochemical analyses presented in the next paragraph.

Raman spectroelectrochemistry (SEC)

As the name itself suggests, Raman-SEC analyses are performed by introducing an electrochemical cell inside a Raman spectrometer setup. This is particularly easy to do, thanks to the open configuration of the Raman microscope (which does not require a particular working environment), and can be developed more conveniently than the corresponding IR-SEC setup, because it is not restricted to the use of transparent electrodes, non-aqueous solvents, nor thin layers of aqueous solvent and transparent samples [86].

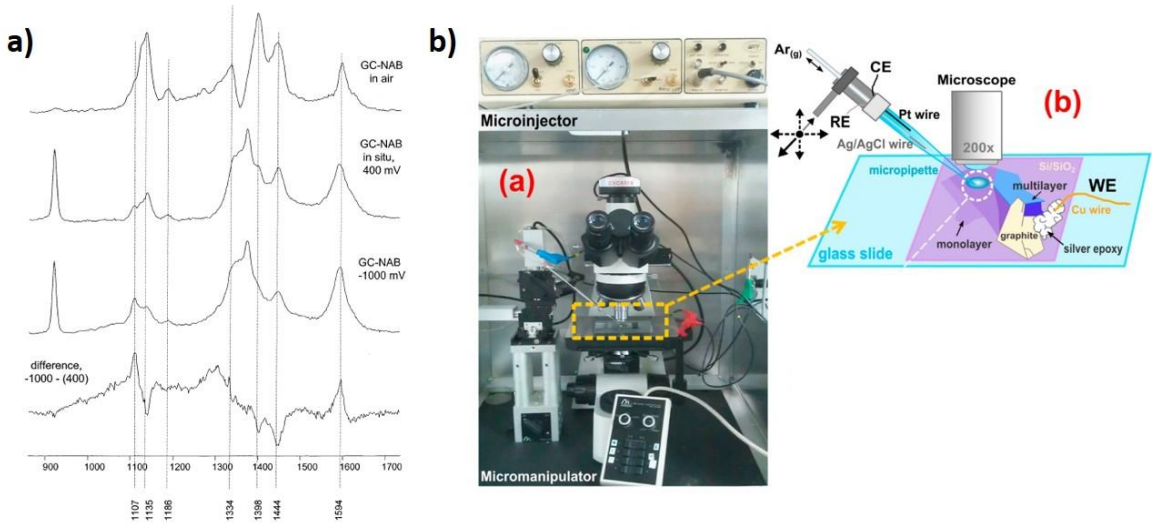

Figure 1.12. Raman-SEC – a) First proof of concept: Raman-SEC spectra acquired on 4-nitroazobenzene layers on GC, from top to bottom: in air; in liquid at 400 mV; in liquid at -1000 mV; subtraction of the -1000 mV spectrum to the 400 mV spectrum, showing the apparition of some bands (1107 and 1594 cm^{-1}) and the disappearance of others (1135, 1398 and 1444 cm^{-1}) due to the reduction process. Laser power: 8.2 mW, acquisition time: 100s, supporting electrolyte: 1.0 $mol.L^{-1}$ $TBABF_4$ in acetonitrile, reference electrode: Ag/Ag^+. Adapted from [94]; **b) Raman-µSEC:** (a) Picture of the experimental setup; (b) Scheme of the sample with the graphene layers (working electrode, WE) contacted via silver epoxy and copper wire, microscope objective and a micropipette, which contains reference (RE) and counter electrodes (CE) and is connected to a micromanipulator and microinjector. Adapted from [95].

In the pioneering work of Itoh and McCreery [94], the laser was focused through a sapphire window on the electrochemical cell (~1 mm thick), filled with acetonitrile and containing the functionalized GC sample, which acted as a working electrode in a three-electrode system (reference Ag/Ag^+). Spectral modifications occurring *in situ* on the grafted 4-nitroazobenzene layer could be detected upon application of reductive potentials on the substrate (**Figure 1.12**a), thus allowing to propose a hypothesis relative to the nature of the chemical transformations. Moreover, the authors signaled that the potential application generated also an electric field at the substrate solution interface, which was considered responsible for a change in the frequency and intensity of the recorded Raman bands and attributed to surface-enhancing effects (see Section 1.2.2.3). Changes in the spectral intensity were in some cases related to electrochemically induced chemical enhancements, due to the different nature of the grafted species after electroreduction [96]. Later on, Raman-SEC experiments have been also carried out on gold-grafted samples, as in the case of thionine diazonium-derived layers, which were subjected to polarization at different pH to monitor the effect of the solution composition on the oligomerization reaction, occurring in real time [97].

However, the total immersion of the sample inside the electrochemical cell only allows the polarization of the whole electrode surface at once [98], thus averaging also the electrochemical response over a large area. Moreover, this classic setup possesses a few technical limitations, as the presence of the window that distorts the optical path, or else the need for a proper sealing of the electric contact to the working electrode. As an alternative, a microdroplet Raman-SEC (Raman-μSEC) system was implemented, which localizes the electrochemical cell within a single droplet (diameter ~10-20 μm), produced at the extremity of a micropipette [98]. This setup was employed to study the ET rate of several redox mediators through a variable number of graphene monolayers (**Figure 1.12**b) and could successfully demonstrate the strong influence of the ET process on the particular local surface conditions [95]. Raman-μSEC spectra recorded on inorganic hole-transport CuSCN layers, deposited on both carbon and carbon-free substrates, were also proved to be very sensitive to changes in C-S bond delocalization (revealed by spectral band shifts) provoked by the local charges of oxygen-bearing groups on the substrate [98].

Despite this implementation improves considerably the performances of Raman-SEC, the issues related to the low scattering intensity and the generally poor spectral resolution are not resolved. In fact, in order to collect enough signal, both high laser powers (up to 10 mW

[96]) and long acquisition times (up to 100 s [94]) needed to be used, which could be detrimental for the sample (beam damages). This aspect can be ameliorated through the signal enhancing effect provided by some substrates, as it will be detailed in the next paragraph.

1.2.2.3. Enhanced Raman spectroscopy

Plasmonics

Enhancement of electromagnetic fields can be achieved on plasmonic surfaces. Plasmon states are observed in those materials (as silver, gold, copper or aluminum) whose superficial conductive-band electrons, at the interface with a dielectric medium (e.g. air), are in a quasi-free state. Under the effect of an external electromagnetic field, these electrons will start oscillating coherently with the field, thus generating a propagating wave named *surface plasmon polariton* (SPP) [99,100] (**Figure 1.13**). This surface plasmon resonance (SPR) phenomenon is responsible for the intensification of the electromagnetic field. In 1908, Mie [99] relied the occurrence of this effect to the particular complex dielectric constant of plasmonic materials, which is characterized by a negative real part and a slightly positive imaginary part within a certain wavelength range [99].

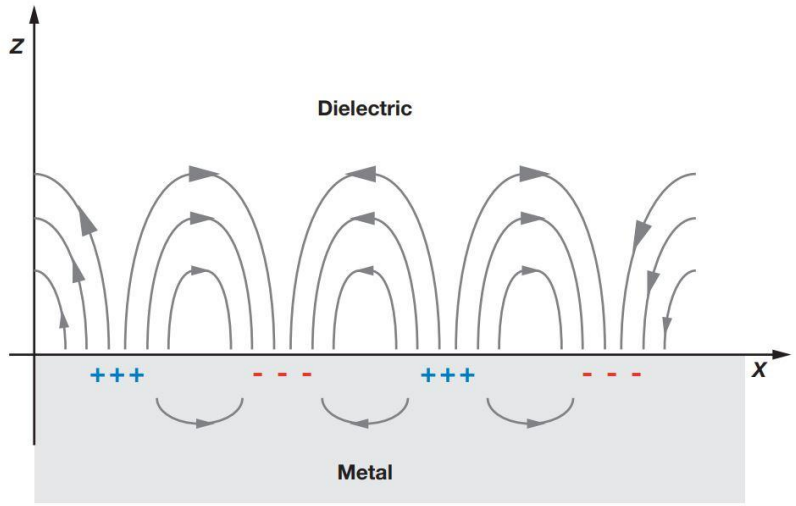

Figure 1.13. Schematic diagram illustrating a surface plasmon polariton (or propagating plasmon). Adapted from [100].

SPPs can propagate over the surface for tens or even hundreds of micrometers, while along the *z* axis their propagation has an evanescent nature and decays quickly within a length 1/*e* (around 200 nm) [100]. However, if the surface does not extend on the plane but it is confined in a nanostructure (as a roughness grain or a nanoparticle), whose dimensions are inferior to the excitation wavelength, then the SPP starts oscillating locally around the nanostructure with

a typical frequency, thus generating a localized surface plasmon resonance (LSPR, illustrated in **Figure 1.14**) [100]. Differently from SPR, for LSPR the resonating frequency does not only depend on the metal nature and on the external medium, but also on the nanostructure size and shape.

When this is approximated to a sphere of radius *a*, much smaller than the excitation wavelength λ, so that the magnitude of the *z*-polarized external electric field E_0 appears static around the particle (quasi-static approximation), then the solution for the electromagnetic field outside the nanoparticle can be found *via* Maxwell's equation:

$$E_{out\ NP}(x,y,z) = E_0\hat{\mathbf{z}} - \left(\frac{\varepsilon-\varepsilon_m}{\varepsilon+2\varepsilon_m}\right)a^3E_0\left(\frac{\hat{\mathbf{z}}}{r^3} - \frac{z}{r^5}(x\hat{\mathbf{x}} + y\hat{\mathbf{y}} + z\hat{\mathbf{z}})\right) \qquad (1.5)$$

where ε and ε_m are the dielectric constants, respectively, of the nanoparticle and of the external medium. The second term of Equation (1.5) dictates the dielectric resonance conditions, which are satisfied when $\varepsilon = -2\varepsilon_m$ and provoke the enhancement of the incident electromagnetic field [100].

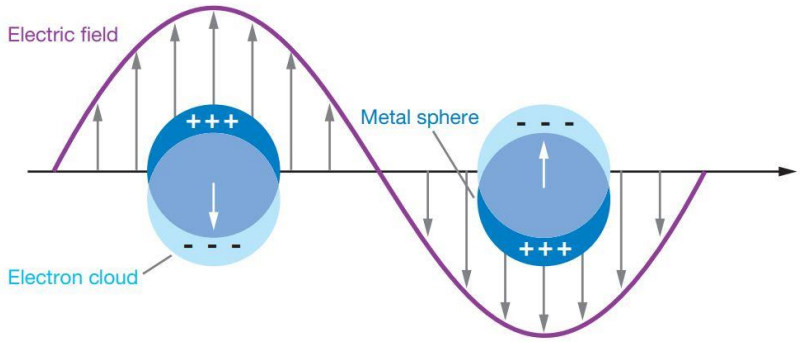

Figure 1.14. Schematic diagram illustrating a localized surface plasmon (LSPR). Adapted from [100].

Surface-enhanced Raman spectroscopy

All the phenomena described so far were fundamental for the development of surface-enhanced Raman spectroscopy (SERS), which relies on the enhancing properties provided by a rough or nano-shaped plasmonic metal substrate for increasing the signal intensity of a surface adsorbate.

The very first observations of the SERS effect were made by chance upon attempt of following by Raman spectroscopy the electrochemical reactivity of molecules adsorbed on metal surfaces: measurements carried out on platinum foils modified with droplets of mercury

salts solutions [101], or else on pyridine adsorbed on roughened silver wires [102] and plates [103], showed indeed an incredible signal enhancements («roughly 5 times as intense» with respect to liquid samples[103]). Later, in 1977, Van Duyne decided to replicate and optimize the control over the experiments on silver-adsorbed pyridine [104], in order to quantify precisely the enhancement effect. He reached the conclusion that the recorded signal was 10^6 times more intense than for liquid samples and that the enhancement depended on both the molecular orientation (with molecule perpendicular to the surface more enhanced than the flat-lying ones) and on the potential applied to the surface [104].

In fact, despite the electromagnetic (EM) enhancement provided by the metal LSPR accounts for the majority of the SERS effect (and therefore depends on the metal nature and the surface structure), also the presence of molecules at close proximity to the metal surface (distance $z \ll \lambda$) plays an important role. As Philpott theorized in 1975, when the external source illuminates the metal substrate at a frequency close to the one of surface plasmons, where the electronic states of the metal are very dense, charge transfer can occur from the metal to the first excited state of the nearby molecules. These will in turn transfer this excitation energy to the adjacent species through either radiative interactions (on long distances) or dipole-dipole interactions (on short ones) [105]. This broadens the width of the excited levels and influences the scattering intensity, so that resonant Raman effect can be observed at a frequency for which isolated molecules would only show normal (non-resonant) Raman scattering [105]. This phenomenon is called chemical or charge-transfer enhancement and, despite it is less pronounced than the EM effect, it still contributes to the overall SERS enhancement [99]. The total enhancing factor for SERS is defined as follow:

$$EF_{SERS} = \frac{I_{SERS}/N_{SERS}}{I_{NRS}/N_{NRS}} \tag{1.6}$$

where N_{SERS} represents the number of molecules probed by SERS (correspondent to the species adsorbed on the metal surface) and N_{NRS} those yielding normal Raman scattering (contained in the sample bulk) [99]. It has been estimated [99] that EM contributes to the EF_{SERS} up to 10^8-10^9 orders of magnitude, while chemical enhancement only up to 10^2-10^3. The two enhancing effects do not act over the same range [100]: this was deduced, for instance, from the decrease of the SERS signal intensity of a pyridine layer adsorbed on metal NPs upon progressive thickening of an alumina layer at the metal/molecule interface. As a consequence, it was concluded that chemical enhancement operates on much shorter ranges than EM and that the SER signal evolution can be described as:

$$I_{SERS} = \left(1 + \frac{z}{a}\right)^{-10} \quad (1.7)$$

where *a* is the radius of the enhancing nanostructure. This result shows that SERS is mostly a "long-range" effect (*z* from 1 to 10 nm) and that close proximity between metal and sample is essential for chemical enhancement [100].

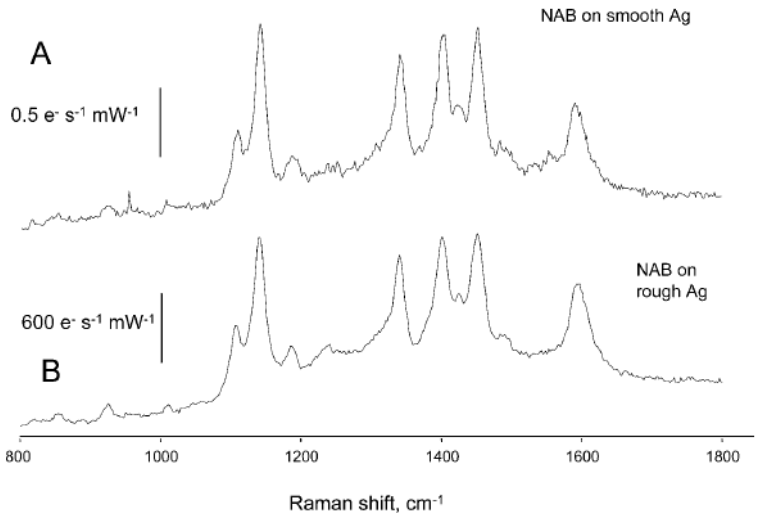

Figure 1.15. SERS effect - Raman spectra of NAB chemisorbed to (A) smooth and (B) rough Ag (2-min incubation of the substrates in 1 mmol.L^{-1} NAB diazonium ion in acetonitrile). (A) is averaged over five 5-second spectra, acquired with 35 mW laser power, while (B) is obtained from a single, 1-second exposure with 0.35 mW of laser power. This aspect, along with the large difference in intensity scale for the two spectra, underline the importance of the plasmonic metal nanostructures for the enhancement effect. Adapted from [106].

As a consequence, Raman characterization of thin films deposited on plasmonic substrates is expected to yield more intense chemical signatures with respect to non-enhanced experiments, and moreover at shorter acquisition times and lower illumination powers. This was proved by McCreery comparing the spectra of 4-nitroazobenzene in liquid and upon grafting on PPF and silver substrates [106]. Although films anchored on PPF and smooth Ag substrates gave already more intense spectra than solution molecules (chemical enhancement), a neat 10^3 fold enhancement could only be obtained when performing SERS measurements on molecular layers grafted on rough Ag surfaces (**Figure 1.15**). This confirmed the prime importance of the nanostructuration of the plasmonic substrate (LSPR effect) for obtaining a proper EM enhancement. However, the authors pointed out that coarsely roughened structures might not always be ideal substrates for the final system use, e.g. for molecular junctions, where shortcuts could occur upon insertion of top contacts on irregular substrates [106]. In alternative,

plasmonic nano-objects can be fabricated and used as local surface enhancers, as it will be discussed in the next paragraph.

SERS effect in nanostructures

In order to gather a better control over the characteristic of the enhancing structures, it is possible to fabricate and tune the plasmonic properties of different kinds of nanosystems, such as metal nanoparticles (NPs), heterogeneous core-shell nanostructures, or also ordered arrangements of nano-objects.

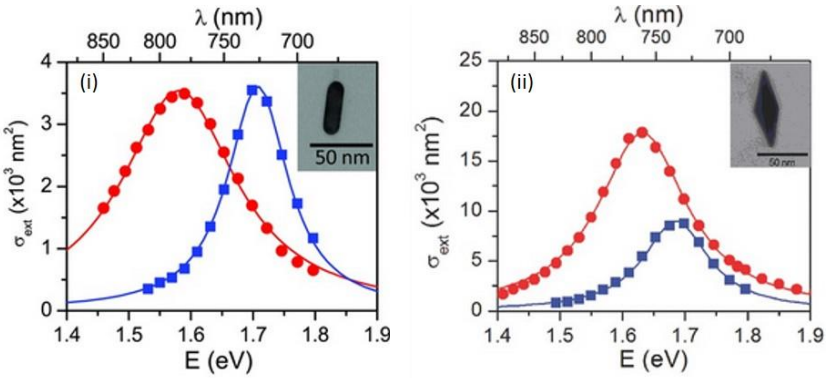

Figure 1.16. Influence of the NP shape and of the substrate on the light scattering enhancement - Longitudinal extinction spectra measured for (i) single gold nanorod (with aspect ratio length/diameter = 3) and (ii) single gold nanobipyramid (aspect ratio = 2.7) on silica (blue squares) and carbon (red circles) substrates, with light polarization parallel to their long axes. Lorentzian fits of these spectra are shown by solid lines. TEM images of the nanoparticles on carbon are shown in inset. Adapted from [107].

As it was previously mentioned, the enhancing conditions can be calculated precisely for spherical NPs of small radius. However, since the light scattering cross-section scales with the sixth power of the sphere diameter, reducing too much the size of the nanoparticle would compromise its scattering efficiency [108]. On the other hand, when the NP radius increases, its resonant frequency red shifts and starts broadening, due to the no longer negligible multipole contributions [109], hence the analytical formulation will no longer be valid. This is why alternative shapes to spheres have been designed for the plasmonic nanostructures [109,110], although their enhancing effects are not directly accessible as for nanospheres and can be influenced by numerous factors.

Optical extinction spectra acquired, for instance, on gold nano-bipyramids and nanorods deposited on silica or carbon surfaces evidenced the dependency of the LSPR, apart from the substrate nature, also on the particle shape and on its particular orientation over the substrate [107] (**Figure 1.16**). Besides, since the LSPR frequency depends also on the dielectric

constant of the surrounding environment, it will be affected (generally red-shifted) by the presence of an adsorbate or an external coating, as it has been shown for Ag nanostructures functionalized with thiol SAMs [111] or coated with TiO_2 (which also influenced the plasmon decay dynamics) [112]. Moreover, because the highest enhancement for a specific Raman vibrational mode of the molecular system is achieved when the LSPR frequency falls half-way between the frequency of this mode and the excitation wavelength [100], tuning the nanoparticle structure depending on the studied system is essential to achieve the highest signal intensification and reach the lowest detection limit.

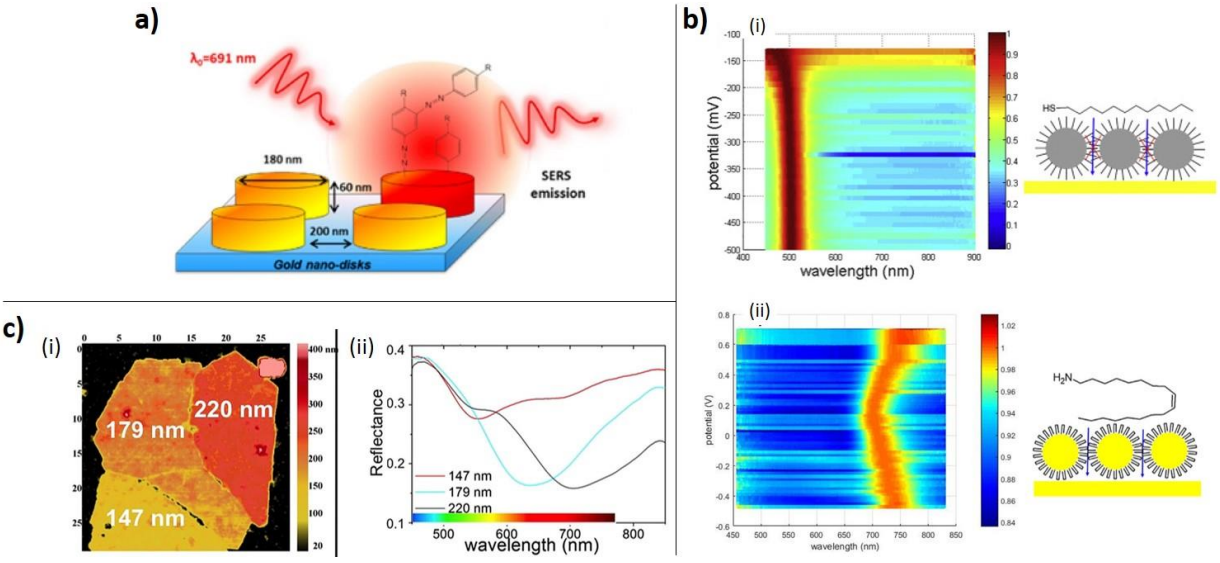

Figure 1.17. Nanoparticle structuration on the sample surface – a) Patterning of metal substrate: Gold nano-cylinders (geometrical details on the figure), fabricated by electron beam lithography on a 60 nm gold layer (evaporated on a 3 nm chromium adhesion layer) and successively grafted in presence of 4-NBD (spontaneously, by incubation in a 1 mmol.L^{-1} solution in 1 mmol.L^{-1} H_2SO_4 for 12 h) for the SERS measurements. Adapted from [113]; **b) Nanocrystals immobilized on the substrate *via* molecular layers:** Intensity maps constructed with reflectance spectra acquired every 10 mV between −500 and –130 mV (i) or +700 mV (ii) *vs* MSE, after normalization by their maximum, on (i) gold wafer modified with 5.2 nm diameter Ag NCs caped with hydrophobic ligands (hindering of electrolyte penetration) and (ii) platinum electrode modified with Au NCs caped with hydrophilic ligands (electrolyte permeation). Both the polarization and the nature of the organic ligand affect the LSPR of the NPs. Adapted from [114]; **c) Ordered arranges of multiple nanoparticles:** (i) AFM image of 3D $C_{12}SAg_{5nm}$ NP SLs of different thicknesses (detailed on the figure) and (ii) associated reflectance spectra. The different trends in the spectra evidence the influence of the 3D superlattice thickness on its optical properties. Adapted from [115].

Also the distribution of the enhancing particles on the sample surface can influence the optical properties. More or less uniform coverages of nanoparticles can be obtained by simple drop casting from solution [116], but more often they are arranged in an ordinate fashion, so that to exploit the additional enhancement effect generated by the proximity of two enhancing

objects (and depending on their reciprocal distance). This can be achieved by simple metal surface nano-patterning *via* electron beam lithography, which guarantees a precise control over the geometrical parameters of the nanostructures [113,117]. For instance, SERS investigations on gold nanocylinders, grafted with different diazonium salts derivatives (**Figure 1.17**a), revealed the preferential enhancement of few vibrational modes, from which the orientation of the molecule on the surface and the preferential sites for side-chains branching could be deduced [113].

In alternative, thiol- or, more recently, diazonium-based layer can also be used to attach SERS-active NPs on substrates [118]. As an example, gold or silver colloidal crystals, composed of nanoparticles branched together with dodecanethiol or oleylamine chains, were first self-assembled on a gold surface, and then used to immobilize redox molecules and probe *in situ* their electrochemical reactivity [114]. The variation of the nanocrystal optical properties with the potential variation was shown to depend on the more or less hydrophobic nature of the connecting molecular layer (**Figure 1.17**b). Another method consists in fabricating structures containing several metal NPs [119–121], which increases the number of enhancing hotspots and therefore guarantees intense enhancement and homogeneous SERS signals. This is the case of 3D superlattices, containing several metal nanoparticles interconnected *via* alkanethiol chains: the modification of the NP nature and of their reciprocal distance allows tuning their optical properties (**Figure 1.17**c) and adapt their SERS response to the studied system, as it was shown for 4-NTP SAM investigations [115].

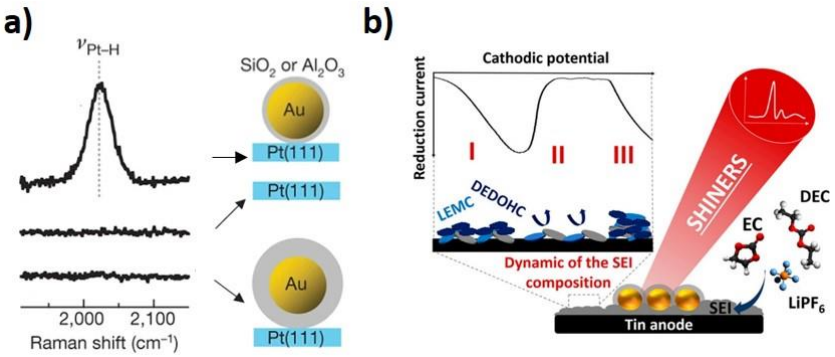

Figure 1.18. SHINERS method – a) Proof-of-concept: The SHINERS signal of H adsorbed on Pt is revealed by the presence of a NPs deposited on the Pt surface and coated with a thin insulating layer (top), while no signatures are recorded when illuminating the bare substrate (middle) or a when the NP coating is too thick (bottom). Adapted from [122]. **b) Application to Li-ion batteries *in situ* investigations:** The SHINERS are deposited on top of the tin anode of the Li-ion battery, where the passivating solid-electrolyte interface (SEI) layer forms upon subjecting the battery to charge/discharge cycles. Thanks to the enhancing effect of the SHINERS, the evolution in the SEI composition with the applied current could be monitored *in situ*. Adapted from [123].

On the other hand, if interactions with the surrounding molecular species (such as adsorption or catalytic reactions) want to be avoided, the NPs can be covered with a thin dielectric coating (e.g. silica or alumina), which provides insulation and (electro)chemical inertia, without affecting their enhancing properties (**Figure 1.18**a) [122]. This shell-isolated nanoparticle-enhanced Raman spectroscopy (or SHINERS) method has been recently exploited in our research group to perform *operando* investigations of interfaces in Li-ion batteries (**Figure 1.18**b): thanks to the deposition of non-reactive NPs onto the anode surface, chemical transformation occurring at the interface with the electrolyte could be monitored during the charge/discharge cycles [123].

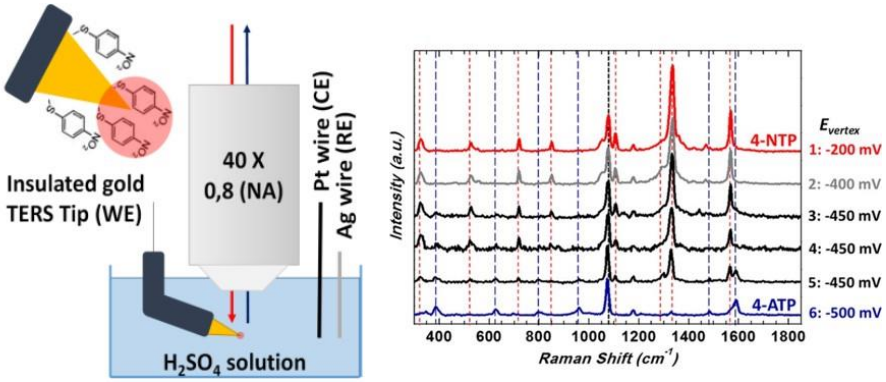

Figure 1.19. Tip-SERS method: On the left, schematic view of the experimental setup for *in situ* measurements and functionalization of the gold tip with a few 4-NTP molecules. On the right, tip-SERS spectra recorded on the same tip in 50 mmol.L^{-1} H_2SO_4. Each spectrum was acquired at $E_{tip} = -200$ mV *vs* Ag with a 100 µW laser power and a 5 s integration time after a CV (scan rate: 100 mV.s^{-1}) covering the range [+250 mV – E_{vertex}]. E_{vertex} was set to −200 mV down to −500 mV *vs* Ag. Red and blue dashed lines highlight the band associated with 4-NTP and 4-ATP respectively. Adapted from [124].

Another method successfully implemented in our team consisted in absorbing electroactive molecules on conical-shaped metal probes (microelectrode) with radii of curvature in the nanometer size, which can provide further enhancement thanks to the combination of antenna effect (due to the charge separation inside the conical structure under the effect of the external field) with lightning rod effect (i.e. the concentration of the surface charge density on the probe apex) [125,126]. This so-called tip SERS technique, which stands as a single hot-spot platform, showed an extraordinary sensitivity, as it was able to detect a neat spectral signature for the 4-NTP molecular species adsorbed on the limited area of the tip apex and allowed monitoring *in situ* their electrochemical reactivity [124] (**Figure 1.19**). However, the real-time tracking of the SERS signal at the tip apex during the potential exploration turned out to be challenging due to a sudden surge of signal intensity (leading to the detector saturation), which is up-to-date not understood.

In conclusion, SERS is a very versatile technique, which can be easily adapted for the detection of a wide range of samples on virtually any substrate and in different working conditions, including *in situ* and *operando* reactivity analyses. Besides, the enhancement of the signal up to 10^{10} with respect to classical Raman spectroscopy (combining both EM and chemical enhancement effect) makes it ideal for the detection of very small molecular quantities. However, it lacks of spatial resolution, which is still limited by classical optical diffraction [127]. The next paragraph will present a technique that can partially circumvent this issue.

1.2.2.4. SECM

The scanning electrochemical microscope (SECM) is a local electrochemical probe technique based on the use of an ultramicroelectrode (UME) that can be used to probe the electrochemical reactivity of numbers of interfaces [128], including the electrochemical behavior of film-modified substrates.

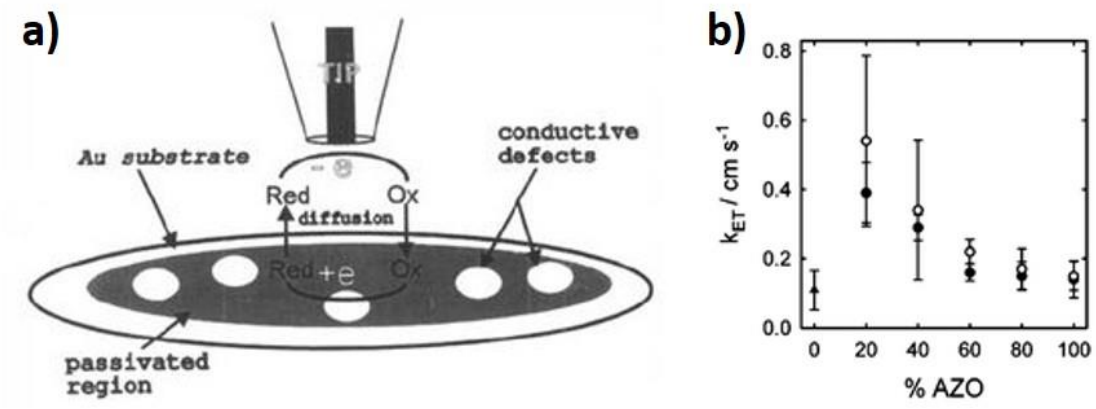

Figure 1.20. SECM investigations on surfaces functionalized with thiol-based SAMs – a) Schematic diagram of a SECM experiment with a gold substrate partially covered with a long-chain, non-electroactive thiol layer. The monolayer defects are assumed to be disc-shaped. The rate of mediator regeneration at the SAM-passivated surface is negligible. The tip current is a function of the surface coverage and of the average defect radius. Adapted from [129]; **b)** Electron transfer rate constants measured on mixed azobenzene (AZO)/2-polyethyl phenyl (PET) monolayers on gold, kept under a 436 nm illumination (*trans* AZO) or a 366 nm illumination (*cis* AZO). Approach curves were recorded through the *trans* AZO SAM (black dots), the *cis* AZO SAM (circles) and the PET SAM (black triangle). The error bars represent the standard deviation of the apparent rate constants. Adapted from [130].

Particularly, SECM in feedback (FB) mode, which uses a redox probe generated at the UME to investigate indirectly the electronic property of the sample, has been widely employed to characterize both insulating and electroactive films deposited on surfaces. This strategy was employed to evaluate quantitatively the electron transfer (ET) process at various organic

monolayers and film-modified surfaces, such as those occurring through SAMs made of alkyl thiols adsorbed on metal surfaces, as schematized in **Figure 1.20**a [129]. The rate constant of the ET through the SAM could be extracted and the presence of pinholes within the film was revealed. This methodology was further employed to probe dynamically the evolution of the pinholes during the adsorption of the SAM on gold surface.[129]

Such SECM investigations allowed demonstrating the possibility to have additional tunneling currents flowing between the redox probe and the surface through the SAMs, which depends on their chain length [131] but also on their spatial arrangement. This second aspect has been investigated [130] for mixed azobenzene/2-phenylethyl (PET) thiol SAMs (with different ratios of the two species), which were imaged by SECM under constant irradiation in order to keep all the azo group in their *cis* (366 nm) or *trans* (436 nm) form. The highest ET rates were recorded for those layers where the azobenzene molecules were kept in *cis* conformation (thinner layer) and dispersed by the presence of consistent amount of PET, while pure *trans* azobenzene monolayer (thicker) or PET monolayer (more packed) showed higher insulating properties (**Figure 1.20**b).

Diazonium-based films immobilized on conductive substrates were also studied by SECM. This was for instance used to evidence the spontaneous grafting of 4-nitrobenzene diazonium salts on both glassy carbon and gold electrodes [132]. Specifically, the formation of the spontaneous layer, upon partial immersion of the substrate in the diazonium salt solution, was revealed by recording SECM images in feedback mode as shown in **Figure 1.21**a. Such an image, recorded by sweeping the UME on the XY plane while keeping a constant Z distance from the surface (typical few µm), represents the contrast of conductivity of the surface recorded due to the presence of the thick layer on half of the scanned area.

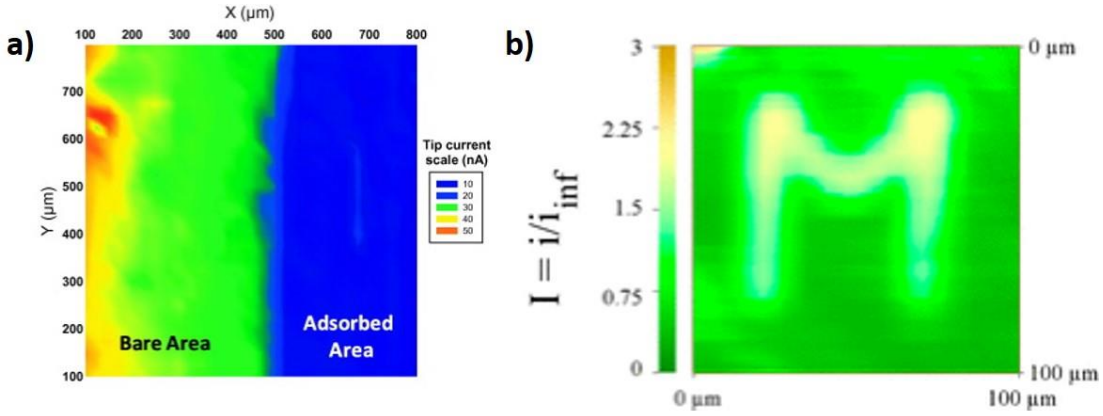

Figure 1.21. SECM imaging on diazonium-modified surfaces – a) Image of a half-modified gold substrate by immersion for 1 h in a 4-nitrobenzene diazonium (4-NBD) solution, obtained with a 12.5 µm radius Pt tip ($I_{T,\infty}$ = 17 nA) in 5 mmol.L^{-1} in 0.1 mol.L^{-1} KCl solution (E_{tip} = 0.5 V/AgCl/Ag). Adapted from [132]; **b)** Image of a "M" motif patterned monolayer (grafted on glassy carbon) recorded with dopamine as redox probe in H_2SO_4 aqueous solution. Adapted from [133].

SECM was also suitably used to image (and modify) diazonium monolayers grown on glassy carbon. These were first grafted thanks to the use of a protecting group, which hindered the uncontrolled branching mechanism and yielded a thin film (~2.5 nm thick), and then patterned with a Pt UME, which removed locally the grafted species to leave the surface uncovered [133]. FB mode imaging performed without surface polarization (minimization of the tunneling current contribution) and with a dopamine redox probe (which, differently from classic ferrocene, reacted specifically on the substrate) allowed retrieving the patterned profile by contrast from the conductive map, as depicted in **Figure 1.21**b.

Quantitative analyses of charge transfer processes can be carried out *via* SECM also on anchored films that contain redox active species. In such conditions, three kind of transfers occur, depicted in **Figure 1.22**a: (i) bimolecular reactions between anchored and solution redox species, (ii) electron tunneling inside the layer and (iii) pinhole ET to the solution redox probe. The various contributions can be separated and gather information, for instance, about the effect of the anchoring on the electroactivity of the redox species [134], or about the influence of the layer structure on the transfer rate [135,136].

This was shown to be crucial on thiol-based SAMs: studies carried out on layer terminated with ferrocene [134] or porphyrin [135] moieties showed that longer anchoring alkyl chains increased the molecular surface coverage, thus leading on one side to a decrease in the tunneling and pinhole ET rate constant (higher insulating properties), and on the other side to

an increase of the bimolecular ET with the redox probe. Mixed thiol structures and different redox probes can as well have an effect on the reactivity of the anchored redox group [134].

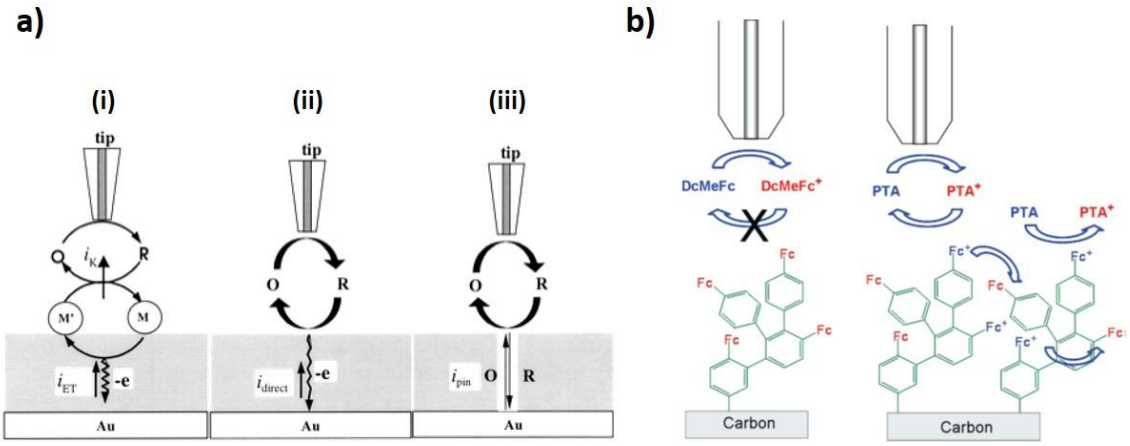

Figure 1.22. SECM on conductive surfaces modified with electroactive layers – a) Schematic view of the processes involved in the SECM measurements of ET across an electroactive SAM: (i) bimolecular reaction between anchored/solution redox species; (b) direct electron tunneling through monolayer; (c) ET through pinholes. Adapted from [134]. **b)** Charge transfer mechanism in the polyaryl multilayers containing the immobilized ferrocenyl moieties. Decamethylferrocene (DcMeFc) and tri-*p*-tolylamine (PTA) work as redox mediators in solution. Adapted from [137].

On diazonium-derived layers, such SECM investigation also revealed the occurrence of electron hopping phenomena among adjacent redox moieties, facilitated by their dense packing inside the multilayer structures. On ferrocene-functionalized structures, FB mode studies on unbiased surfaces with weakly reductive or oxidizing redox mediators only showed the insulating properties of the film, while strongly oxidizing probe (as PTA^+) yielded consistent positive feedbacks. This was attributed to ET among ferrocene centers inside the layers, which leads to the re-oxidation of the solution redox mediator in order to maintain the charge balance within the layer in steady-state conditions (**Figure 1.22**b) [137].

Ultimately, SECM shows a great potential for *in situ* and even *operando* investigations of structure-reactivity relationships. Thanks to this information, the (electro)activity of the final system can be precisely tuned depending on the sample fabrication procedure, or *vice versa* it can be predicted from the observation of its structural characteristics. However, the use of a UME affects consistently the spatial resolution and, as it is for every electrochemical tools, this technique alone is not able to yield any information about the chemical composition of the samples. This means that the compounds involved in the electrochemical reactions need to be known *a priori*, as their nature cannot be revealed just by their electrochemical signature.

All the techniques presented so far showed very interesting performances for *in situ* and *operando* characterization of the composition and reactivity of functional molecular structures. However, they all lack of a resolving power that could allow distinguishing spatially two adjacent nano-objects. Recently, further technical developments allowed achieving such low resolution; a few state-of-art implementations will be presented in the next paragraphs.

1.2.3 Characterization at the nanoscale

1.2.3.1. Scanning electrochemical cell microscopy

Scanning electrochemical cell microscopy (SECCM) can be considered as an evolution of SECM, implemented with the aim of reaching single-entity sensitivities. Instead of an UME, in SECCM the probe is constituted by a single or double barrel (theta) nano- or micropipette, filled with the electrolyte solution and integrating a quasi-reference electrode (QRE). Similarly to what was observed for Raman-μSEC, also in this case the interactions between the probe and the substrate are limited by a meniscus of few micro- or nano-liters, which localizes the origin of the signal from a restricted sample area. The pipette can therefore be scanned over the surface and collect an array of measurements, which will yield a surface reactivity mapping.

For instance, SECCM was shown to reach better resolution than conventional SECM in the detection of pinholes in a 4-NBD-derived layers grown onto glassy carbon: thanks to the coupling with numerical simulations, details down to 20 nm, much smaller than the pipette size itself, could be successfully resolved [138] (**Figure 1.23**).

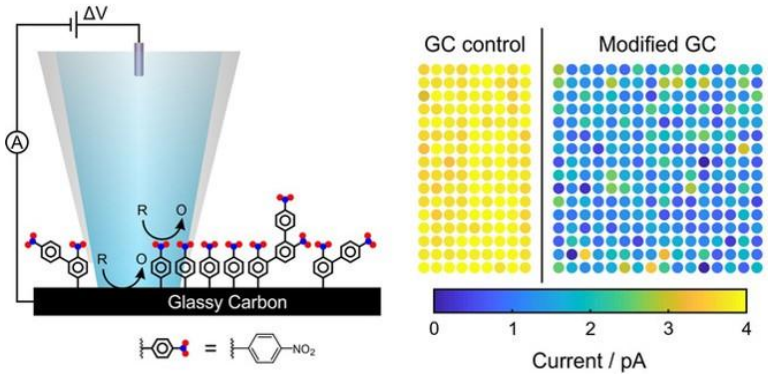

Figure 1.23. SECCM measurements – On the left, schematic view of the pinhole detection in 4-NBD-dervived disordered layers, grafted on GC. The single-barrel nanopipette is electrochemically connected to the substrate (which is not completely insulated) and filled with a solution of ferrocene methanol, which acts as redox probe. On the right, currents measured on bare GC (left) and grafted GC (right) at large overpotential (0.4 V). The yellow and green spots, which reports higher surface current, corresponds to the presence of pinholes inside the aryl layer. Adapted from [138].

Besides, SECCM can be used to perform fast voltammetric measurements on single, localized spots and simultaneously probe the sample response by recording the resulting superficial current. This allows collecting broad sets of data on large samples and monitoring, for instance, the influence of the substrate superficial structure on the reactivity of molecular species at its interface. Step-edges (≤ 1 nm thick) in HOPG electrodes were therefore proved to be more efficient than terraces in promoting the electrolyte reduction and, hence, the formation of SEI upon Li-ion battery cycling [139], while different activities for hydrazine reduction, especially in the presence of atmospheric oxygen, where observed for (111) and (100) nanocrystal domains on Pt surfaces [140].

SECCM can also work as a precise tool for designing molecular patterns over both conductive and non-conductive surfaces. This was shown by growing spatially resolved polyaniline motifs (**Figure 1.24**) on mixed substrates with the use of a dual pipette to promote the electropolymerization [141]. While the pattern width was limited by the pipette size to ~1 µm, the thickness could be modified by modulating the applied current and reduced to less than 1 nm. Another nanolithographic approach with SECCM consisted in using a single-barrel nanopipette to fabricate *in situ* H_2 micro-bubbles, produced by water electrolysis, which were then deposited onto the desired substrate and worked as templates for the polymerization of pyrrole in the shape of micro-containers [142].

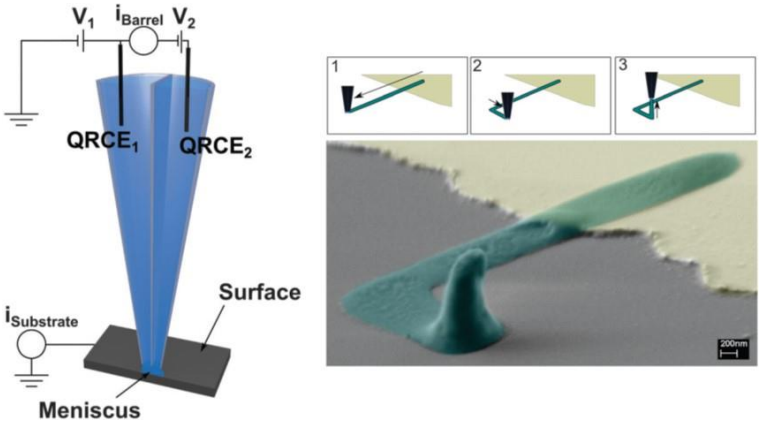

Figure 1.24. SECCM for patterning - On the left, schematic view of a dual micropipette (which can work on both conductive and insulating surfaces). On the right, SEM image of the three-dimensional polyaniline pattern (green), formed both on a conductive (beige) and on an insulating (grey) surface. The drawings 1-3 show the displacement effectuated from the pipette to yield this particular structure. Adapted from [141].

In conclusion, SECCM is a very powerful and versatile tool for the characterization and manipulation of small molecular assemblies, down to single entities. It can as well be

implemented on both conductive and insulating substrate and is very sensitive to the influence of their structure on the electrochemical reactivity of the adsorbed molecules. However, the resolution of dual pipettes is strongly limited by the larger aperture required to fit the channel for the two barrels. Moreover, as for SECM, it cannot give any compositional information regarding the studied sample. Finally, to the best of our knowledge, only few studies report so far the use of SECCM on organic samples. This might be due to the most difficult realization of a stable meniscus in organic solvents, although developments in this direction were recently made [143].

1.2.3.2. AFM-SECM

Another improvement to the resolution and the versatility of the SECM consists in its combination with AFM (**Figure 1.25**a), which enables the access to the nanometer scale and to a more precise control of the tip-sample separation. Besides, a direct correlation between the surface electrochemical activity and its morphological changes can be achieved [144].

Demaille's group, for instance, demonstrated the possibility of probing individual nanoparticles (diameter ~20 nm) [145] or single gold nanodots (diameter ~15 nm) ranged in dense arrays [146] thanks to their functionalization with ferrocene(Fc)-terminated polyethylene glycol (PEG) chains, where Fc moieties act as redox labels. These are then oxidized by direct contact with the SECM-AFM probe (mediator-tethered Mt mode), which can quantify them from the oxidation current response and correlate this information with the nanostructures positions and sizes, obtained by the topographic image. The correlation of the two information guarantees the achievement of high lateral resolution (down to few tens of nm) in short investigation times [146] (**Figure 1.25**b).

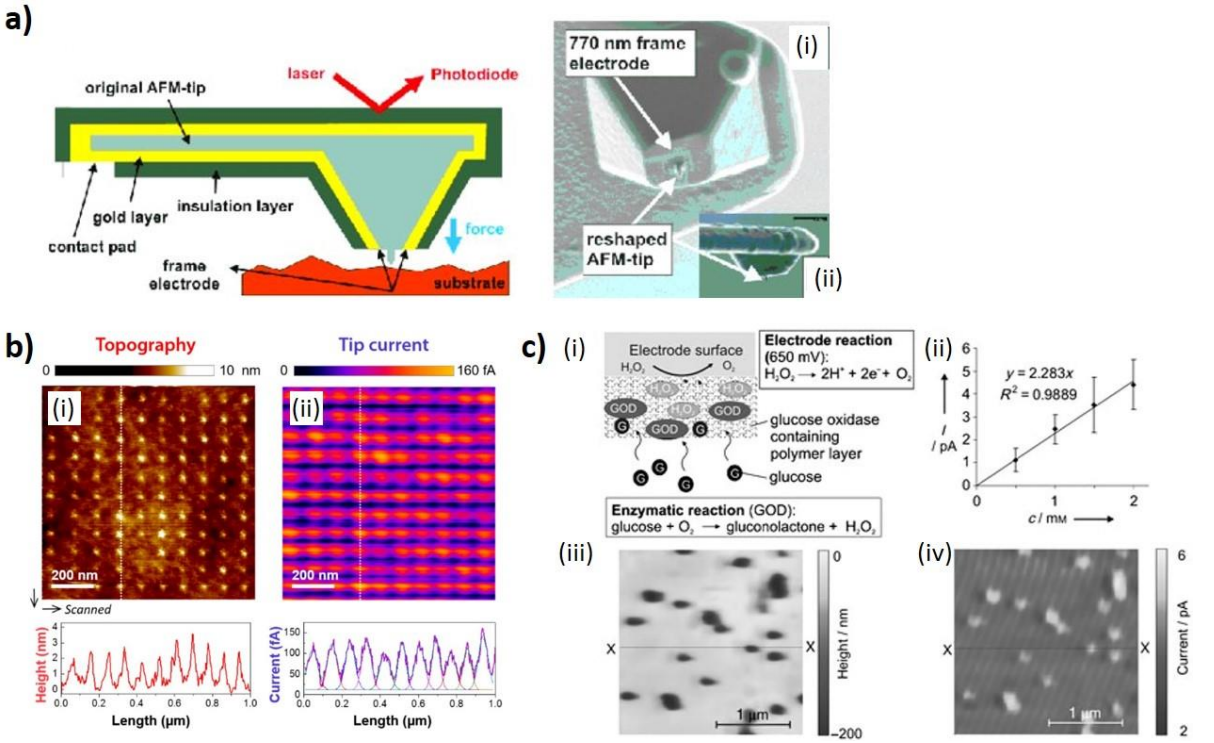

Figure 1.25. SECM-AFM imaging –a) Experimental setup: On the left, schematic view (in cross section) of an integrated AFM-SECM tip fabricated by using FIB technology. On the right, (i) shows a FIB image of an integrated frame submicroelectrode (gold) with Parylene C insulation (electrode edge length: 770 nm), while (ii) illustrates a reshaped AFM-tip and tilt correction for a cantilever mounting angle of 10° in a tapping-mode liquid cell. Adapted from [147]. **b) Use of a redox label:** Mt/AFM-SECM *in situ* imaging of Fc-PEG-functionalized nanodots ranged in an array: (i) topographic AFM image and (ii) tip current SECM image. Cross sections of the images taken along the column of nanodots, indicated by a vertical white dotted line, are shown below. Adapted from [146]; **c) Probing catalytic reactions:** (i) Mechanism of glucose detection: as glucose molecules crosses the polycarbonate membrane, they are intercepted and oxidized by glucose oxidase enzymes, tethered to the AFM-SECM probe; (ii) Calibration curve for AFM-tip-integrated biosensor; (iii) Topographic AFM image and (iv) tip current SECM image revealing the transport of glucose through the polycarbonate membrane. Adapted from [148].

The use of a redox label in Mt-SECM-AFM mode was proved to be extremely useful for characterizing the properties of several kinds of species immobilized on a surface [149]: these can be simple molecular layers (e.g. PEG chains), for which the thickness and the end-to-end diffusion coefficient can be easily extracted by both the topographic and the current information [150], but also more complex biological structures. For instance, high-resolution images (~100 nm) of proteins could be obtained thanks to their labeling with Fc-PEG-antibody redox probes [151]. Alternatively, the SECM-AFM probe can be functionalized to detect a specific analyte: for instance, functionalizing the tip with glucose oxidase allowed detecting the diffusion of glucose through a polycarbonate membrane [148] (**Figure 1.25**c). As it is shown by these examples, SECM-AFM can be conveniently applied to image a wide range of

biological samples [152] with exceptional sensitivity and lateral resolution, although the need for labeling and/or probe specific functionalization prior to the analyses might be a limitation.

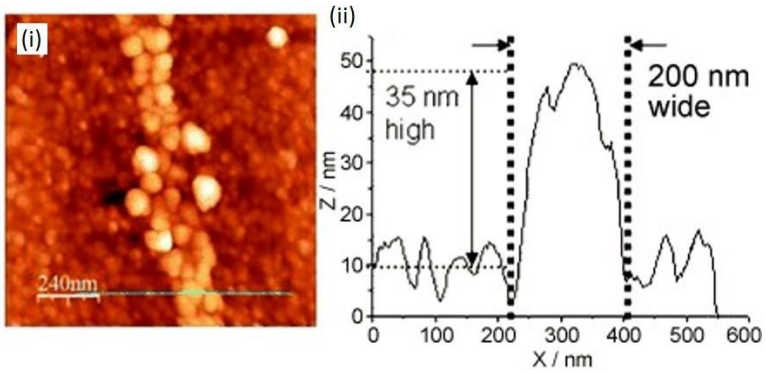

Figure 1.26. SECM-AFM for electro-induced patterning – (i) AFM image recorded after electroinduced patterning *via* SECM-AFM on a gold substrate immerged in a mixture of 4-NBD and vinyl monomers. The section in the bottom identifies the height profile reported in (ii). Adapted from [153].

Also label-free SECM-AFM analyses were implemented, aiming at studying, for instance, the spatial variations in the catalytic activity of heterogeneous surfaces for the oxygen reduction reaction [154], or else the ET phenomena occurring at the electrode/electrolyte interfaces in redox flow batteries (which are known to impact the batteries kinetics and operational reversibility) [155]. Besides, as it was previously observed for SECCM, also SECM-AFM probes could be used as electrochemical lithographic tools: for example, they were used to pattern a homogeneous gold substrate immerged in a mixture of 4-NBD and vinylic monomers [153]. In the experimental setup, the substrate was polarized negatively while the probe, acting as counter electrode, scanned the surface following a precise pattern to trigger locally the 4-NBD electroreduction and subsequent radical grafting. Because the vinylic monomers are not electroactive, they branches as side chains to the diazonium-derived anchored structures *via* radical activation. The final pattern (**Figure 1.26**) showed a thickness of around 35 nm and had a width comparable to the tip size [153].

These were only a few examples among the recently developed nano-investigation methods, each one presenting very good imaging skills at the molecular or atomic scale and very high sensitivity for little amount of samples. However, the lack of a straightforward way to characterize also the system chemical composition remain a major drawback in their use. In fact, it must be pointed out that, differently from SECCM, the use of a metal tip in SECM-AFM might theoretically open the road to possible implementations of nanospectroscopy, where the tip could act as a SERS enhancer. However, to the best of our knowledge, no

successful results have been reported so far because of the technical challenges related to system stability, or else to the Raman activity of the polymeric coating used to partially insulate the tip.

This issue can be overcome by the TERS technique, which has been employed in this thesis work and whose characteristics will be presented in detail in the next paragraph.

1.3. Electrochemical tip-enhanced Raman spectroscopy

In the panorama of nanoscale dynamic investigation techniques, electrochemical tip-enhanced Raman spectroscopy (EC-TERS) can be considered as a very successful hyphenation of powerful and complementary techniques. Indeed, EC-TERS gathers together the atomic/molecular-size spatial resolution provided by scanning probe microscopy (as STM or AFM), the extraordinary chemical sensitivity and wealth of information of SERS (chemical signal enhancement) and even the characteristics of an electrochemical probe, which can be conveniently employed for the investigation and/or promotion of electrochemical reaction under *in situ* and *operando* conditions.

In the next paragraphs we will first introduce the original developments of the TERS technique and its implementation within different SPM setups. Later on, we will focus on the most recent state-of-art configurations that allows its use in liquid and under electrochemical conditions. Finally, we will present the issues and challenges that are currently impeding the large and fast development of this technique.

1.3.1 First TERS developments

A first precursor of the TERS technique can be considered the scanning near-field microscope (SNOM). The principle of this technique was first proposed theoretically by Synge in 1928 as a solution to overcome the problem of diffraction-limited spatial resolution in optical microscopes [156]. Synge's idea consisted in illuminating the sample through a minute aperture, whose diameter is smaller than the wavelength λ of the beam that crosses it, and that is placed at a distance z ($\ll \lambda$) from the measured surface, i.e. at near-field distance [84,156]. Thanks to this expedient, the lateral resolution was expected to be no longer limited by diffraction (i.e. by the use of optic lenses), and to depend only on the size of the aperture (which determines also the sampled volume) [84]. Almost 60 years passed before Synge's idea could be put in practice: the breakthrough consisted in the invention of STM and, successively, of the other SPM techniques that allow placing a probe at very close proximity to the sample surface [84].

In order to improve the resolution and, at the same time, intensify the signal in SNOM, it was proposed to substitute open optical fibers with apertureless probes, whose tapered apexes can enhance the electromagnetic field of the far-field illuminating source [157] and behave like a light scatterer. This had first been theorized when it was observed that the light travelling inside an open probe had a maximum enhancement in the lobes near the aperture rims. This means that field confinement was limited by the size of the aperture diameter, which should have been reduced to a single point to provide the strongest field localization (and corresponding enhancement) [157], as it was also observed for the tip-SERS technique. Moreover, because of the lateral resolution dependency on the tip diameter, reducing this parameter was also expected to improve the imaging quality.

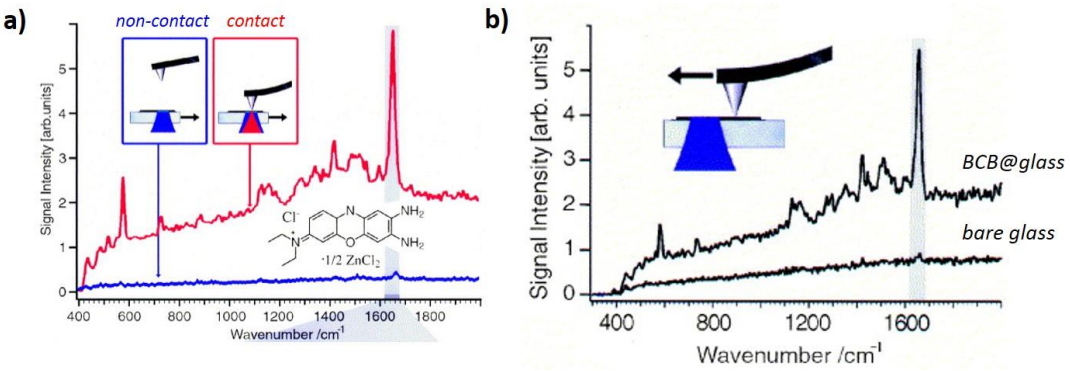

Figure 1.27. First TERS proof of concept – a) Evidence of tip enhancing ability: TERS spectra of brilliant cresyl blue (BCB) dispersed on a glass support, measured with a silver-coated AFM probe with the tip retracted (blue) and in contact (red) with the sample. Estimated EF > 2000; **b) Spatial resolution:** TERS spectra recorded on two different positions of the sample surface (on the BCB layer or on the bare glass substrate) in tip-scan mode, while the same sample spot remains in the laser focus. In both (a) and (b) the evidenced spectral range (1630-1680 cm^{-1}) corresponds to the main BCB Raman band. Each spectrum was acquires for 60 s. Adapted from [158].

These considerations suggested that sharp apertureless probes, thanks to their enhancing abilities, could be used as nanoscopic light sources for the illumination of sample surfaces [84,157]. A first attempt in this direction was reported in 2000 by Deckert and Zenobi [158] and consisted in the use of either AFM probes coated with silver (diameter ≤ 50 nm) or etched gold wires (diameter ≤ 20 nm, shear-force microscopy ShFM), illuminated by a laser source and raster scanning the sample surface. The illuminating objective was placed below the sample (inverted Raman microscope) and focused the laser beam on semi-transparent samples (thin films of BCB or C_{60} fullerene deposited on glass), which were either translated while keeping the tip in place (sample scanner) or, *vice versa*, maintained still on the laser focus while scanning the tip (tip scanner). This prototypical implementation of tip-enhanced Raman

spectroscopy (TERS) measurements in an AFM-Raman coupled configuration presented already very high enhancing factors and moreover, differently from the SERS technique, it could resolve spatially the spectral information [158]. Indeed, recognizable spectral features on the sample could only be detected when the tip was brought in close contact to the sample surface (**Figure 1.27**a), i.e. when coupling the EM effect of the illuminated tip with the chemical enhancement provided by the proximity of the molecular layers with the plasmonic nanoamplifier. The estimated enhancement factors ranged from 10^3 up to 10^4, thus allowing a neat distinction between the near-field signal at the tip-sample junction and the far-field background. Besides, different signatures could be recorded depending on the tip position on the surface, e.g. over the bare glass or the molecular layer (**Figure 1.27**b). Therefore, differently from SERS, TERS could gather spatially resolved chemical information, with a lateral resolution of around 50 nm. Besides, because the enhancement derives always from the same hotspot (and not from multiple, possibly heterogeneous enhancing sites, as in SERS) and is therefore supposed to be uniform, the authors proposed the possibility of performing quantitative measurements [158].

During the same year, other research groups published pioneering studies based on TERS [159–161]. More specifically, Kawata and Inouye (who had already successfully implemented the scattering SNOM technique a few year before [162]) performed studies on Rhodamine 6G molecules adsorbed on a silver substrates with a similar configuration as the first one proposed [160]. Although their enhancement factor was estimated to 40, lower than the previous experiment, they could still record sharp spectra at shorter acquisition times and lower laser power. Besides, as it was pointed out later [163], their far-field spectra presented already evident molecular spectroscopic signature, more likely due to the SERS activity of the substrate, but still the signal recorded with the tip in contact on the surface resulted more intense: this would suggest that a single hotspot in TERS can be as efficient as a series of SERS-active hotspots. Even better performances were achieved from the implementation of TERS in a STM setup, proposed by Pettinger [161], which allowed decreasing to 1 nm the distance between the tip (an electrochemically etched gold wire) and the sample (BCB deposited onto a thin, smooth gold layer, transparent to the bottom illumination source) during the measurements. This had the effect to increase the enhancing factor up to 10^4 at very low laser powers (50 μW), which avoided the occurrence of photobleaching or fluorescence phenomena.

1.3.1.1. Enhancing factor and influencing parameters

More specifically, the aforementioned TERS enhancement factor, originated by the tip EM enhancing effect, can be expressed as [163]

$$EF_{TERS} = \left(\frac{I_{nf}+I_{ff}}{I_{ff}} - 1\right)\frac{V_{ff}}{V_{nf}} \quad (1.8)$$

I_{ff} represents the far-field intensity, recorded when the tip is retracted from the sample, which arises from the focal volume V_{ff}. This is approximated to a cylinder with diameter coincident to the laser beam size (R_{focus}) and height equal to the effective focus depth. Upon tip landing on the sample surface, the sampled volume decreases to the so-called TERS volume V_{nf}, approximated to a cone with radius equal to the tip radius of curvature (R_{tip}) and height coincident to the near-field separation [163]. In this case, the near-field intensity term I_{nf} adds up to I_{ff} in the expression for the total recorded intensity. The first term of the Equation (1.8) represents the TERS *contrast* and is usually employed to express the enhancement quality. As for the second term, it expresses the dependency of the enhancement factor on the reciprocal tip-sample distance and on the tip geometrical shape. Indeed, for thin samples, the focus depth can be considered as coincident to the near-field separation height [163], hence Equation (1.8) can be rewritten as

$$EF_{TERS} = 4\left(\frac{I_{nf}+I_{ff}}{I_{ff}} - 1\right)\left(\frac{R_{focus}}{R_{tip}}\right)^2 \cos(\alpha) \quad (1.9)$$

where the term $\cos(\alpha)$ corrects the elliptical shape of the illuminating beam by the angle to the normal surface.

Equation (1.9) expresses clearly the dependence of the enhancing factor on the tip dimensions. In fact, although only a single nanoparticle at the apex of the tip is responsible for the enhancement of the incoming field, the plasmon resonance arises from the coupling of all the adjacent illuminated nanoparticles [108]. These will support together the propagating SPP and transform the tip apex into a "plasmonic antenna" (**Figure 1.28**a), i.e. an oscillating nano-dipole, upon induced electric charge alternation across its structure [108]. In addition to the antenna effect, if the tip presents an extremity with a small radius of curvature, both the SPP and the induced dipole will concentrate on the sharp apex surface and be furtherly intensified (lightning rod effect) [157]. All these enhancing effects lead to localized second-harmonic

generation on the tip apex, which is responsible for the creation of a confined photon source [164].

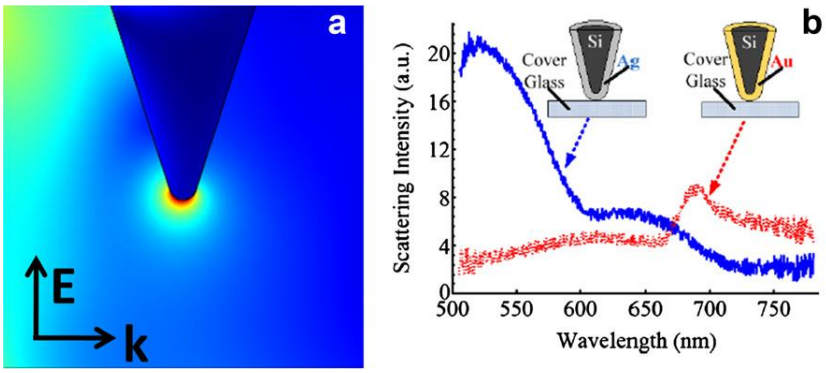

Figure 1.28. Antenna effect and plasmon characteristics of TERS probes - a) Calculated image (COMSOL Multiphysics® software) of the effect of an incident p-polarised laser (of wave vector k) with an electric field (E) parallel to the tip-axis at a metal or metal-coated tip (radius: 15 nm). The red color around the tip apex attests of the confined enhancement of the EM field; **b)** Light scattering spectra from silver- and gold-coated silicon AFM tips, showing the different plasmonic properties of the two metals. Adapted from [126].

Of course, as it was mentioned for SERS, the nature of the plasmonic metal used for the tip has still an essential role on the optical properties of the final structure (**Figure 1.28**b), but in this case it can also affect the tip mechanical stability and its resistance to contamination. Therefore, fabricating sharp and stable TERS probes in a reproducible way constitutes one of the most important factors to consider when performing TERS measurements. As it was mentioned in the previous examples, tips are usually obtained by vacuum deposition of metal on a dielectric tip or by electrochemical etching of metal wires. The first method is often employed for functionalizing commercially available AFM probes (usually made of insulating silicon nitride). The deposition procedure generally forms a metallic film made of small nanoparticles aggregates and confers to the tip a rough morphology. Depending on the dimension of the grains and on their reciprocal distance, a variation in the tip LSPR frequency and in its enhancing properties is observed [108] . As **Figure 1.29** shows, rougher structures are expected to provide higher EF, although they are also most sensitive to carbon contamination, especially if employed in normal atmospheric conditions [165].

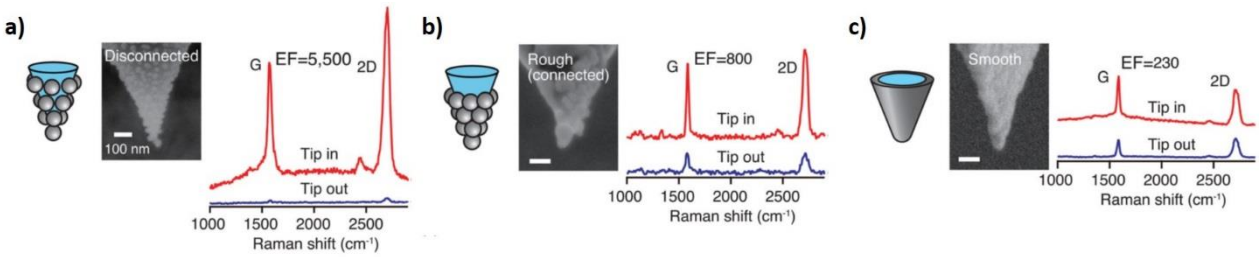

Figure 1.29. Effect of the metal coating over an insulating probe on the enhancing properties of the TERS tip - Enhancement provided by **(a)** a tip with discretely arranged grains, **(b)** a rough corrugated granular tip, **(c)** a smooth tip. The EF is evaluated by approaching (tip in) and retracting (tip out) the probe from a graphene sample (excitation wavelength: 488 nm). Adapted from [108].

For STM applications, instead, it is usually preferred to produce probes *via* electrochemical etching of bulk wires, which insures a better mechanical stability on the final structure and a more homogeneous current flow. Both requirements are essential for establishing good tunneling conditions at the tip-sample gap and performing reliable STM measurements. Further details about STM tips fabrications will be provided in Chapter 2.

Regarding the choice of the feedback technique for controlling the tip-sample distance, the previous examples showed that the TERS setups are mostly implemented in AFM and STM setups. AFM bases its working principle on the local forces experienced by the tip, placed at the extremity of a flexible cantilever, when it approaches the sample surface. A laser beam focused on the end of the cantilever and reflected toward a quadrant photodiode detector, allows to precisely track the vertical (deflection) and lateral (torsion) motions of the probe. The deflection of the cantilever, when the tip encounters a protruding or depleted structure on the sample, induces a change of the beam position on the photodiode and triggers the response of a feedback loop acting on the displacement of the piezo-stage acting as tip- or sample-scanner. A variant of the AFM, called shear-force microscopy, uses a tuning fork carrying the probe on one of its prong (instead of a cantilever) to position and scan the tip on the surface: in this case, the feedback loop is based on the change of resonance frequency of the fork upon the shear forces experienced by the tip [126]. In STM, an atomic-scale gap is established between the scanning probe and the sample allowing some electrons to pass across the planar tunnel barrier (or work function). A bias voltage BV applied between the two generates the flow of a net tunnelling current I_T [166,167]. In this case, the feedback loop acts on the piezo-stage to keep a constant I_T value so that to keep the tip at a fixed distance from the surface during the scanning. The exponential dependence of I_T with the tip-sample distance explains the extreme sensitivity of the technique.

The choice among these different setups can be based on the degree of sensitivity and resolution required by the analyses: overall, STM establishes the closest and most stable tip-sample interaction and is therefore preferred for highly resolved measurements [168,169]. On the other hand, working in particular operating conditions and/or using delicate samples (e.g. biological tissues), which are not compatible with polarization, limits the choice of the feedback only to AFM [170] or tuning fork [171] setups. Besides, it must be considered that the classical Raman selection rules can be altered by chemical processes (especially in AFM) or by electric field gradients in the tip-sample gap (as in the case of STM), and hence that using a particular setup might provoke the appearance in TERS of normally prohibited vibration modes and associated energy transitions.

All these aspects have been investigated in the past few years to optimize the TERS technique and have gathered a whole new series of information on the sample structure, composition and reactivity at the nanoscale. The next paragraphs will review some of the most striking results achieved so far.

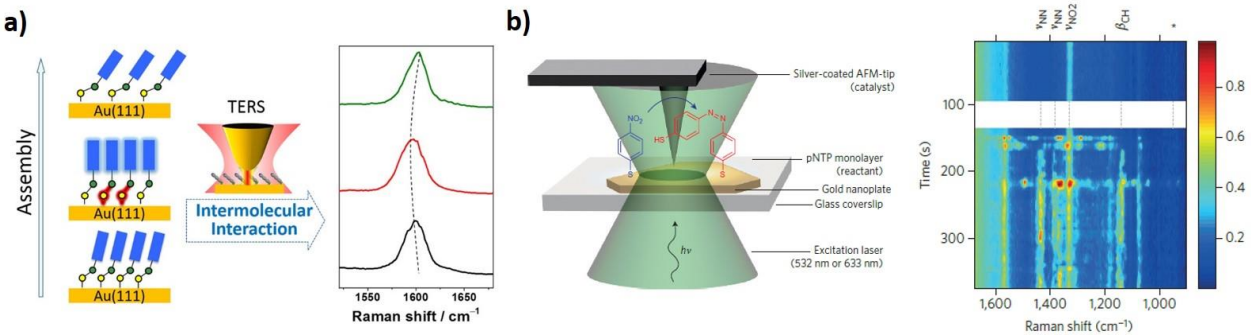

Figure 1.30. TERS as both probing and manipulating technique at the nanoscale – a) Revealing the packing dynamics of SAMs: On the left, schematic view of the variation in the inter-molecular arrangement of a pyridine-terminated SAM at different stages of the assembling process, monitored by the TERS probe (depicted in the center). On the right, spectra acquired at different assembling times, revealing the modification of the SAM packing by the shift in the aromatic C=C stretching band. Adapted from [172]; **b) Inducing and detecting photocatalysed reactions:** On the left, schematic view of the photocatalytic effect of the Ag-coated AFM tip on the 4-NTP coupling into DMAB, adsorbed on gold, under a 532 nm excitation. On the right, TERS time maps acquired at 633 nm (no photocatalytic effects) to probe the variation in the sample spectral signature before and after the photocatalytic illumination step (individuated by the white band). Adapted from [20].

1.3.2 TERS developments in air

On the wave of success of the first pioneering approaches, successive developments in the TERS field were made to improve the signal enhancement, the collection efficiency and the spatial and temporal resolution, with the aim of characterizing at the local scale functional

materials under their operating conditions (e.g. gas atmosphere other than air) and performing localized modifications (e.g. photocatalytic reaction).

For instance, TERS was used to probe the variations in the molecular orientations of pyridine-terminated arenethiol SAMs at several stage of the assembly process [172] (**Figure 1.30**a). These could be revealed by the shift of the Raman ring stretching band, which is sensitive to the π-stacking between adjacent molecules and evidenced an initial strengthening of the intermolecular interactions, which fades at longer incubation times. Such analyses are particularly interesting to investigate the ET efficiency through a SAM, which, as it was mentioned in Section 1.2.1.3, is strongly dependent on the structure of its layer.

Another interesting application consists in exploiting the TERS tip both to induce (photo)chemical reactions and to probe straight after the effects on the sample surface. For instance, Deckert's group [20] acted on single 4-NTP molecules deposited on gold to promote *in situ* their photocatalytic dimerization into DMAB by illumination with a green laser source (**Figure 1.30**b). The successful outcome of the reaction was revealed by comparison of TERS time maps, acquired with a non-photocatalytic red laser source before and after the green laser illumination. Later on, a similar TERS experiments carried out by Bin Ren *et al.* revealed that the efficiency of the photocatalytic-induced dimerization of 4-NTP (and 4-ATP) molecules depended in fact on the particular molecular arrangement over the surface and on the nature of the metal substrate [173].

These examples showed the great analytic interest in using the TERS technique to probe structure-reactivity relationships of functional materials. Further developments in other working environments than air will be presented in the next paragraphs.

1.3.3 TERS in liquid and under electrochemical conditions

A much ambitious task endeavored this last decade in the TERS community has consisted in implementing the TERS setups under liquid conditions. Liquid-TERS indeed allows to perform *in situ* imaging of either more sensitive samples, as biological tissues, which need to be kept in wet state in order not to collapse [3], or of functional devices under their conditions of operations (*operando* analyses). A first success was achieved in 2009 by Zenobi's group, which carried out measurements over a thiophenolate (PhS) SAM on gold in liquid environment thanks to an Ag-coated tip, protected with an ethanethiolate (EtS) layer and mounted on an inverted AFM setup [3]. As **Figure 1.31**a shows, the measurements were performed in the solution meniscus between the tip scanner and the sample. Besides, the tip

movements could be precisely followed thanks to presence of a window just above the cantilever head that allowed focusing the tracing laser beam; this did not interfere with the laser beam used for TERS measurements, since the system worked in bottom-illumination mode and back scattering [3]. The presence of the EtS protective layer was shown to be essential to avoid the contamination of the tip apex with the thiol sample, which could partially re-dissolute and adsorb on the silver surface. Although the presence of this coating affects the EF (which decreases from 10^4 to 10^3), the obtained signal was still very sharp and resolved (**Figure 1.31**b).

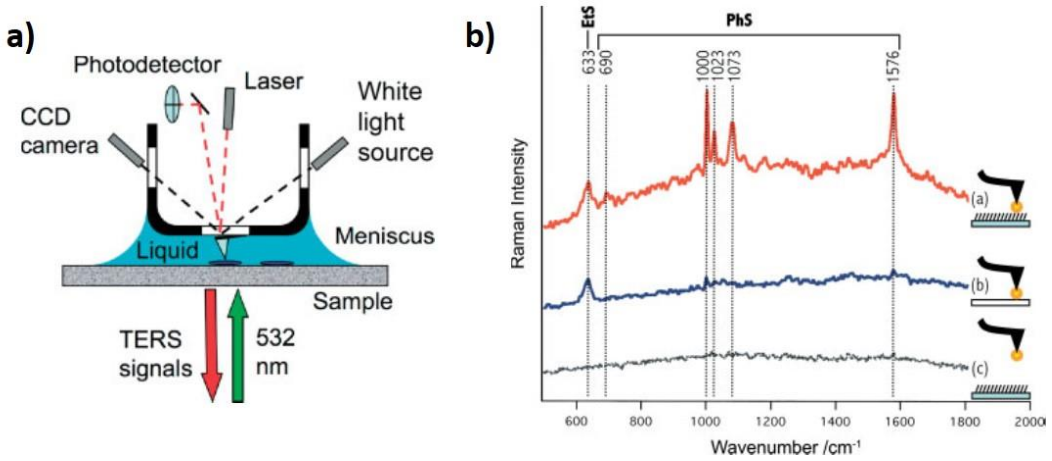

Figure 1.31. First TERS experiment in liquid conditions – a) Schematic diagram of the TERS setup in aqueous environment (AFM system, bottom illumination); **b)** Proof of principle of the feasibility of TERS in liquid and importance of the tip coating: (a) TERS spectrum of a PhS SAM recorded in liquid with an EtS-coated tip, (b) spectrum recorded after (a) on a clean gold surface (the absence of the PhS signature attests of the non-contamination of the tip); (c) far-field spectrum corresponding to measurement (a) (the comparison between the two demonstrates the enhancing effect provided by the TERS-active probe even in liquid and upon coating). Each spectrum was collected for 10 s. Adapted from [3].

This first important implementation of TERS measurements in liquid was shortly after followed by a series of development aiming at transforming the sample holder in an electrochemical cell, which could access *in situ* or *operando* characterization of electrochemical processes occurring on a surface with exceptional sensitivity and spatial resolution.

The first prototype of an EC-TERS setup was proposed in 2015 by Bin Ren's group [4], who designed an electrochemical cell; adapted to the sample holder of a homemade STM-TERS setup, using a side-illumination configuration (**Figure 1.32**a). Both the tip and the sample constituted the working electrodes (WEs) and their polarization was controlled against a common reference electrode (RE) by a bi-potentiostat. This allowed applying a defined potential on the two WEs at the same time and recording the evolution in time of a 4-PBT SAM

sample adsorbed on gold under a fixed -500 mV potential [4]. Besides, small spectral changes in the molecular response of 4-PBT could be detected by TERS measurements at different potentials, which were not observed by SERS analyses performed in the same conditions. This evidenced the higher accuracy of TERS-active probes with respect to SERS-active substrates, where the presence of multiple hotspots can affect both the spatial and spectral resolution [4].

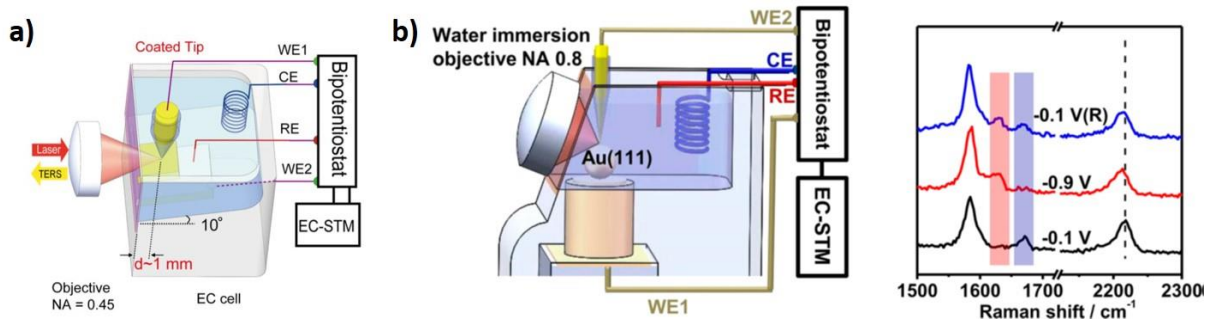

Figure 1.32. EC-TERS in side illumination - a) First implementation of an EC-TERS setup: Schematic view of the first EC-STM-TERS setup, where the bottom of the sample holder/electrochemical cell is tilted of 10° towards the glass wall of the cell. The long-distance objective can therefore be placed horizontally and illuminate the tip with a 90° angle. Adapted from [4]; **b) State-of-art improvement of the side-illumination configuration for EC-TERS:** On the left, a schematic view of the new side-illumination setup, where the glass window is tilted towards the water immersion objective, to which it is optically coupled through a thin layer of water. On the right, examples of TERS spectra acquired on anthraquinone-based SAMs adsorbed on gold and subjected *in situ* to irreversible reduction, as it can be evinced from the modification of the spectral signatures. Adapted from [174].

However, the particular geometry chosen for the tip illumination was not ideal for the collection efficiency, since it employed a long-distance air objective at low numerical aperture. As a consequence, both the incoming and the scattered light were heavily refracted in their optical path, due to the presence of multiple interfaces at different refractive indexes, and could not be effectively captured in back scattering, thus the overall detected intensity was quite weak. An improved configuration, recently reported, [174] substituted the vertical glass wall with a 55°-tilted glass window on the side of the EC cell (later employed also by Domke's [168] and Van Duyne's [175,176] groups), so that to avoid tilting the sample, and, more importantly, introduced the use of a short-length immersion objective (**Figure 1.32**b). This has the advantage of reducing the diffraction at the objective/window interface and, thanks to the higher numerical aperture of the objective, of increasing the light collection efficiency. As a consequence, a 5-fold increase in the sensitivity with respect to previous setup was recorded and well-resolved redox signatures arising from the irreversible reduction of anthraquinone-based SAMs on Au could be acquired [174]. Although, a main drawback of this configuration consists in the immobility of the sample position, which means that the nanometric

displacements of the tip and the objective need to be precisely synchronized in order not to lose the best optical alignment.

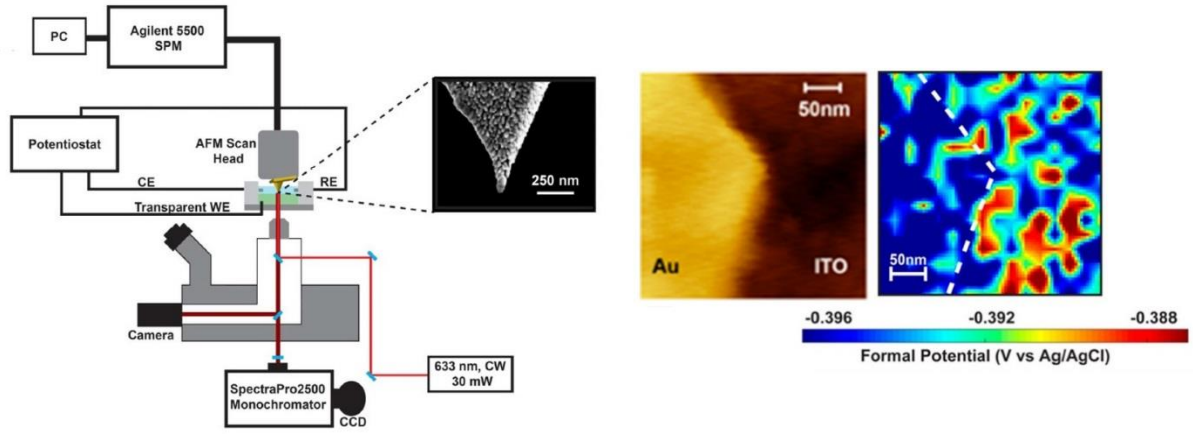

Figure 1.33. EC-TERS in: a) bottom-illumination configuration: On the left, schematic view of the AFM/inverted optical Raman microscope coupling for bottom-illumination on the AFM tip and on the sample cell. Adapted from [177]. On the right, AFM image (left) and formal reduction potential map (right) acquired on the edge between a gold nanotriangles and the underlying ITO, both covered by a sub-monolayer of NB, in a neutral buffer. The formal reduction potential on the maps were extracted (through the Nernst equation) from the corresponding intensity of the spatial TERS map. Areas of different color evidence the heterogeneities of the NB reduction process on the two substrates. Adapted from [178].

In alternative, Van Duyne's group resumed the use of an inverted configuration, which was implemented for EC-TERS measurements in an AFM setup [177,178] (**Figure 1.33**). Indeed, the vertical laser/tip alignment provided by the bottom-illumination mode, along with the imposition of a radial polarization to the laser (more than 4-fold EM enhancement with respect to linear polarization [126]), guarantees the best possible enhancing conditions in TERS, yielding up to 10 time higher sensitivities with respect to side-illumination configurations [174]. Besides, the light refraction at the objective/glass interface is also in this case minimized by using an oil-immersion objective. This configuration allowed monitoring the spatially dependent redox behavior of sparse Nile Blue (NB) molecules, deposited partially on semi-transparent Au nanotriangles (3.5 % coverage rate) and partially on the underlying indium tin oxide (ITO) substrate (0.5 % coverage rate): upon polarization towards progressively negative potentials, a bimodal distribution of NB formal reduction potentials could be recognized on ITO, due to the higher heterogeneity of its surface with respect to the gold plates [178] (**Figure 1.33**). However, this configuration is limited to the use of transparent samples and, besides, it cannot be easily implemented in STM setups, because the mechanical coupling generated by the vertical alignment of the components might perturb the flowing of the tunneling current and thus lead to tip crashing over the surface.

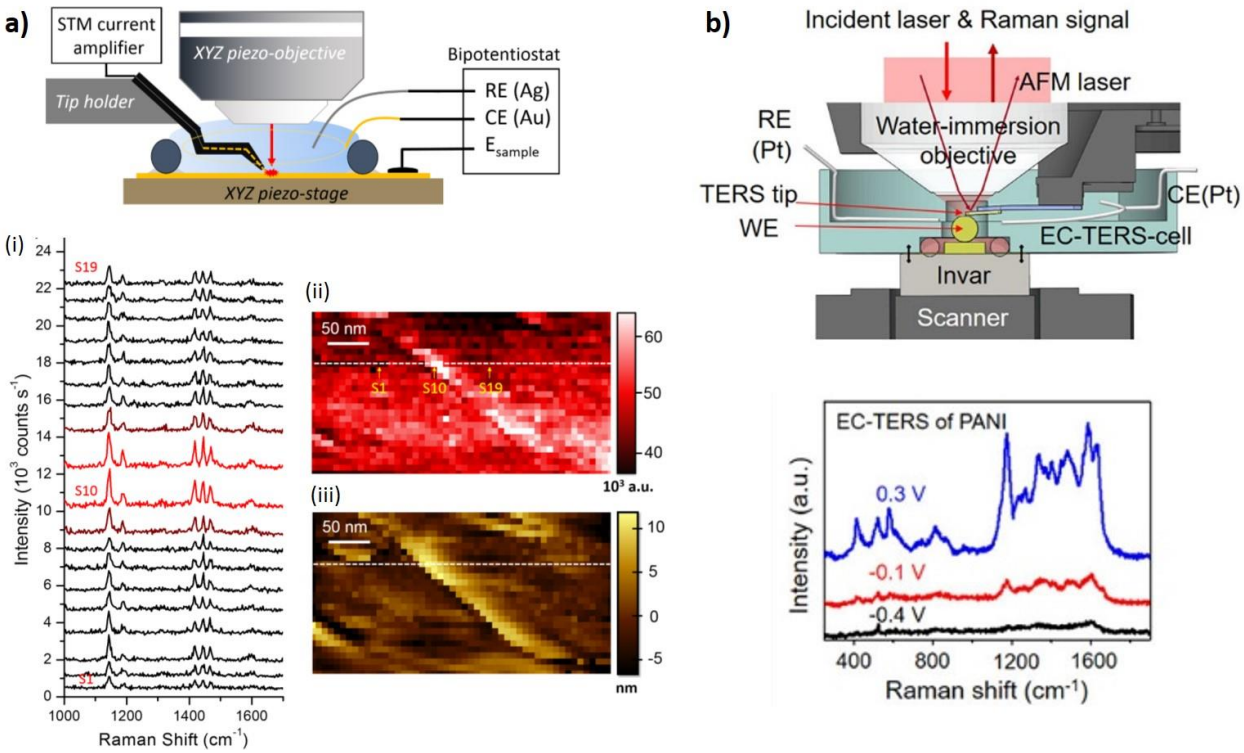

Figure 1.34. EC-TERS in top-illumination configuration – a) EC-STM-TERS: On top, schematic view of the setup with a water-immersion objective illuminating from the top the sample surface and the bent STM tip approaching from the side. On the bottom, the TERS spectra (i) extracted from the pixel indicated by the white dotted line on the spatial TERS map (ii), recorded simultaneously to the corresponding STM map (iii) on azobenzene-derived alkanethiol SAMs adsorbed onto gold and immerged in 50 mmol.L^{-1} Na_2SO_4, under fixed polarization of 0 V. The lateral resolution of the maps was of 8 nm. Adapted from [169]; **b) EC-AFM-TERS:** On top, schematic view of the setup with a water-immersion objective illuminating both the AFM cantilever (for detecting its deflection) and the TERS-active tip. A sample scanner is used, so that the objective and the tip stay in place and do not lose their alignment. On the bottom, potential-dependent TERS spectra of 2.2 nm PANI on Au film in 0.1 mol.L^{-1} HCl solution, showing the change in the spectral signature at different stages of the PANI redox reaction. Adapted from [179].

The third alternative consists in a top-illumination configuration, where the tip approaches from the side and is tilted to fit below the focus of the overlying objective. This configuration was successfully implemented in our group [169] (**Figure 1.34**a) and possess the main advantage of using a short-distance water-immersion objective that can plunge inside the electrochemical cell, hence minimizing the light refraction effect. Thanks to this expedient, STM-TERS maps could be recorded on gold, functionalized with a non-electroactive SAM, with a lateral resolution of 8 nm and under constant polarization [169] (**Figure 1.34**a).

Recently, also by Bin Ren [179] developed a top-illumination configuration in an AFM setup (**Figure 1.34**b), which has the advantage of using the same objective to focus both the laser recording the AFM cantilever displacement and the light source for illuminating the tip. Besides, the presence of a sample scanner avoids the displacement of the tip and the objective,

which therefore do not lose their optimal alignment: this allowed observing the reversible transformations of a polyaniline layer deposited on gold when subjected to oxidative potentials (**Figure 1.34**b).

1.3.3.1. Issues associated to electrochemical STM-TERS

The extreme sensitivities and resolving powers obtained for the top-illumination EC-STM-TERS setup encouraged us to pursue the optimization of this configuration to reach even higher quality results and, most importantly, to follow the occurrence of electrochemical reactions in their real working conditions. Nonetheless, this achievement is fundamentally complicated by the influence of the STM parameters on the TERS enhancement qualities.

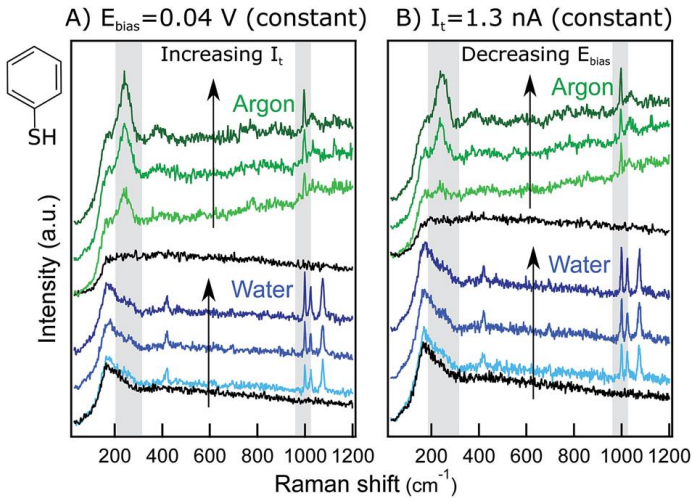

Figure 1.35. Effect of the STM measurement parameters on the TERS enhancement - Raw spectra recorded on SAMs of thiophenol (inset molecular structure), adsorbed onto gold, in Ar (green) and in water (blue) at **a)** constant BV = 0.04 V and variable I_T (from 0.3 to 0.8 to 1.3 nA) and **b)** constant I_T =1.3 nA and variable BV (from 0.1 to 0.04 to 0.02 V). For each series, 20 nm retraction spectra (far-field) are included in black. Gray rectangles indicate the characteristic thiophenol bands, whose intensities variate more drastically in Ar and under the effect of BV decreasing at a constant I_T value. Adapted from [180].

Domke's group thoroughly investigated this matter by evaluating the dependency of the bias voltage (BV) and tunneling current (I_T), imposed to the STM tip, on the TERS intensity recorded on thiophenol monolayers, adsorbed onto gold, both in deoxygenated Ar environment and in liquid [180] (**Figure 1.35**). As it will be further detailed in Chapter 3, increasing the I_T set-point and/or decreasing the BV imposed between the tip and the sample is expected to reduce the dimension of the tip-sample gap and, therefore, to improve the signal enhancement. However, the experimental measurements evidenced that the two parameters do not follow the same trends: while decreasing the BV from 0.5 to 0.02 V provoked an exponential increase in the thiophenol intensity signal, increasing I_T from 0.1 to 1.7 nA provoked a linear intensity

variation. This was proved, though, to have a more dramatic effects on the signal intensities in Ar than in liquid environment [180]. Additionally, the authors pointed out that variating the BV between the tip and the sample, as it occurs when the latter is polarized for *in situ* EC-TERS experiments, provoked a variation in the Au-S bond strength, as it was evidenced by a shift in the Raman band at 245 cm^{-1}, attributed to the correspondent stretching mode.

As a consequence, the values of I_T and BV need to be carefully controlled in order to achieve at any time the best enhancement for the sample signal, and their potential influence on the bands position should be taken into account. Additionally, it must be reminded that the electrochemical processes occurring on the surface can sometime interfere with the spectroscopic acquisition and alter the light-matter interaction. For instance, when polarizing the sample substrate in immerged in the liquid cell, both the Fermi level of the metal and the dielectric constant of the interfacial electrolyte will be modified, thus influencing the chemical enhancing effect of the sample [181]. Besides, an electrochemical double-layer forms at the sample surface/electrolyte interface that generates a static EC field , which influences the interactions between metal and adsorbates, the orientation of the adsorbates and the double-layer structure itself [181]. All these matters have to be considered when performing an EC-TERS measurement, in order to discern between the observations related to the real sample behaviour and the artefacts due to the interactions between spectroscopic and electrochemical processes, and to interpret correctly the experimental data.

Our current challenge, which is at the center of this thesis work, consists in exploiting the skills of EC-STM-TERS to probe *in situ* the electrochemical reactivity of functionalized nanomaterials. In order to do that, our efforts were partially profused in the amelioration and optimization of the above-mentioned measuring setup, as it will be detailed in Chapter 2. First proof-of-concept analyses, performed on thiol-based model samples, will be the object of Chapter 3. Therefore, Chapter 4 will present the results obtained on more complex systems, whose controlled structuration on the substrate constituted another essential part of the work. Finally, we will summarize the main achieved results and propose some perspectives for future investigations.

Chapter 2 STM-TERS under electrochemical conditions - Experimental developments & implementation

2.1. Introduction

TERS stands as a great alternative to ultrahigh vacuum techniques to characterize low cross section materials with minimal beam damages. Although introduced in the early 2000's, the fast TERS development has been hampered by the lack of TERS effective optical probes and robust optical coupling and its use has been therefore limited until recently to only a few laboratories worldwide. The development and use of TERS (nanoRaman) is currently booming after years of "immobilization" thanks to reliable commercial AFM/Raman coupling systems (AIST/Horiba, NT-MDT, Park Scientific) and the demonstration of TERS in liquid in 2009 by the Zenobi group [3] that paved the road to the in situ/operando characterization of functional material. Note that NanoIR is getting also extremely popular (Anasys – NeaSpec) in material and life science, but the strong IR absorption of water (and many organic solvents) has left so far the leadership to TERS for in situ measurements. Only a few groups worldwide have emerged so far as precursors and leaders for TERS[*] and as by 2021, only a handful of these groups have successfully implemented TERS in liquid or under electrochemical conditions by developing their own technical solutions.

Our group in Sorbonne University joined the TERS community in 2015 after acquiring a TERS-ready SPM/Raman coupling system and has since published a few relevant works. The group [125] proposed the first demonstration of TERS mapping of a non-Raman resonant molecular compound in an organic solvent [182] and then introduced EC-Tip-SERS measurements [124], which benefit from the sensitivity of TERS and give access to time-resolved measurements, though without spatial information. The technical developments required for EC-Tip-SERS however laid the foundation for the implementation of TERS under electrochemical conditions and the mapping with an unprecedented 8 nm lateral resolution [169]. The groups' research focus in these last three years has consisted in securing the reproducibility and the ease of TERS implementation under electrochemical conditions, in STM (this work)

[*] In Europe, B. Pettinger, A. Meixner, V. Deckert, M.R Lacroix, **K. Domke** (Germany), R. Zenobi, **N. Kumar**, L. Novotny (Switzerland) and specifically in France R. Ossikovski (LPICM), M. Lamy de la Chapelle (Paris 13 University), **S. Bonhommeau, D. Talaga** (GSM, Bordeaux), B. Humbert (IMN, Nantes). On the international level, TERS is developed by Kawata (Japan), **P. El Khoury** (USA), **B. Ren** (China) and **R. Van Duyne, D. Kurouski** (USA). In bold, groups working on TERS in liquid or EC-TERS.

but also in AFM mode (PhD work of A. Pavlič), and to explore new orientations like SECM-TERS (preliminary data obtained in this work are not presented in this manuscript), enabling local modification (molecular patterning) and immediate characterization. The experience accumulated by the group these last few years has led to the development of a commercial set-up enabling EC-STM-TERS in collaboration with Horiba and the French manufacturer of electrochemical instrumentation Origalys.

In the continuity of Chapter 1, which covered the theoretical principles of TERS and the progress achieved so far in the characterization of electroactive systems with this technique, this new chapter will present the practical aspects of its implementation and the issues encountered in this work when pushing further the development of EC-STM-TERS analyses. First, we will recall the procedure for the elaboration of performant TERS-active probes for measurements in STM mode in liquid medium. Afterwards, we will present the instrumentations and protocols enabling STM-TERS analyses and finally depict the required technical developments for *in situ* measurements, including a design of TERS-compatible spectro-electrochemical cells.

2.2. Elaboration of TERS-active bulk metal probes

The microfabrication of sharp and mechanically stable probes for EC-STM-TERS experiments is essential to ensure an accurate tracking of the sample topography and to access nanospectroscopic analyses. Home-preparation of TERS-active SPM probes is often preferred by academic groups to acquisition of commercial probes, as it allows a fine tuning of their properties according to studied systems (e.g. characterization of hard catalytic surfaces or of soft biological objects, triggering and study of photo-chemical processes using specific metal/excitation combinations, measurement in the air or in liquid, etc.).

2.2.1 Design of plasmonic amplifiers

More specifically, for STM-TERS applications the most employed fabrication procedure consists in etching bulk metal wires [175,183,184] to obtain a tapered profile terminated with a sharp tip apex. The nature of the metal, as well as the opening angle (half cone angle) of the tip and its radius of curvature, are critical parameters to achieve a strong TERS activity at a specific excitation and a mechanical stability suitable for raster-scan nano-imaging.

Tapered gold and silver wires with diameter in the 100-200µm range and small radii of curvature (in the order of tens of nm) can provide high-quality topography images in STM mode. The mechanical properties (rigidity and wear resistance) of these probes is determined by the ductility of the metal (gold is more ductile than silver). Moreover, the sharply curved surface at the probe apex acts as a nano-antenna, as it concentrates and strongly localizes the electric field resulting in a strong amplification of both the incoming light and the scattered signal intensity from the sample in close proximity [108,185]. Hence, they can act also as TERS efficient probes using visible excitations. Plasmon resonance and signal enhancement are indeed usually achieved using red and green excitations for gold and silver, respectively (UV irradiation being suitable for aluminum TERS probes). Note that the roughness of the tip, the nature of the sample and of the environment (dielectric properties) can also determine the plasmonic properties of the tip-sample junction and the amplitude of the signal enhancement. The so-called *gap-mode* configuration, reached when not only the tip, but also the sample substrate is made of a plasmonic metal, and therefore form a plasmonic junction [186], provides additional signal enhancement, in a similar way to what observed for nanoparticle dimers [163]. It has been noted that on dielectric substrates (where no gap-mode occurs) TERS activity can be recovered/enhanced using highly corrugated (AFM) tips. Any alteration of the surrounding medium (air, liquid) or coating of the probe with plasmonic or dielectric materials (for protection against wear or oxidation) shift or damp the plasmon resonance.

2.2.2 TERS probe from etched gold wires

The main advantage of fabricating probes by etching of bulk wires consists in the relatively fast and easy operation procedure, which does not require any specific nor expensive instrumentation. For the targeted applications in this study (alkaline media), gold was preferred to silver due to its better resistance against chemical and atmospheric oxidation, its stability over a large electrochemical potential range (although mostly reductive polarizations were used here) and because the etching sequence for silver has not yet been fully optimized (and yields larger radii of curvature). **Figure 2.1**a schematizes the employed etching station, developed as soon as 2015 in our group (internship of A. Dauphin), and its working principle. A three-electrode configuration was adopted, where a ~1 cm-long segment of gold wire (250 µm-thick, MaTeck, Germany) acts as anode and working electrode (WE), a platinum ring as cathode and counter-electrode (CE) and a silver wire covered in solid silver chloride as an Ag/AgCl reference electrode (RE). Although the presence of a RE in the etching electrochemical setup

had already been introduced from 2015 in our group, only recently its use and the consequent asset have been reported in the literature [187]. Classical electrochemical etching stations consisting in a simple two-electrode setups [188,189] were developed historically by physicists working on STM. The precise control over the tip potential provided by the association of a RE and a potentiostatic regulation of the polarization (not galvanostatic) allows to control the dissolution regime (nature and rate, as explained below) and to minimize the solvent oxidation, prerequisite to the reproducibility of the etching process.

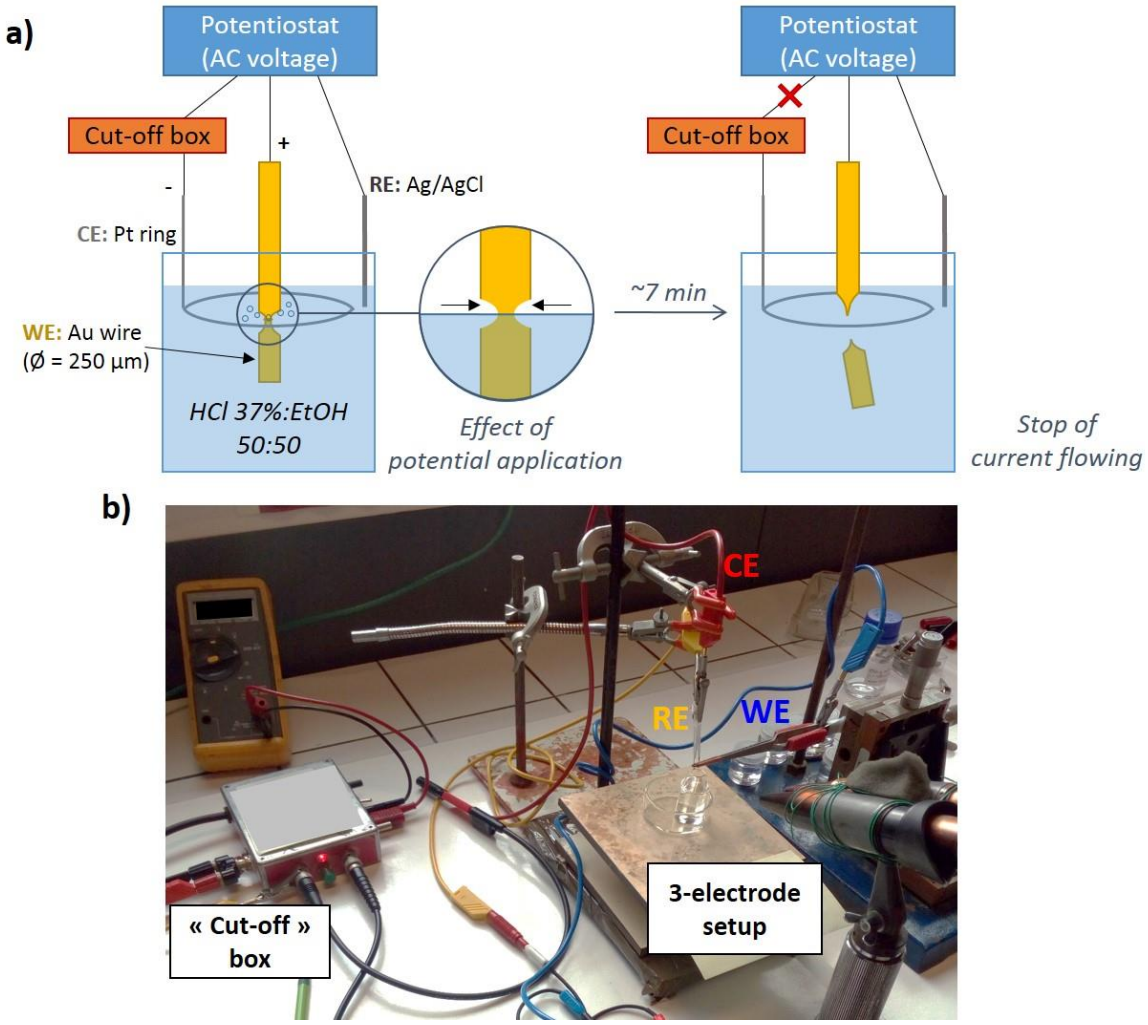

Figure 2.1. Gold wire etching station - a) Schematic view of the etching working principle: on the left, the ongoing process of progressive dissolution of gold at the air/liquid is magnified in the inset circle. On the right, when the lower extremity of the tip drops off and a sudden decrease in the flowing current is registered, the cut-off voltage box disconnects the Pt ring counter-electrode and interrupts the polarization; **b)** Picture of the real etching setup.

In our setup (**Figure 2.1**b), a micrometric positioning stage allows adjusting the wire position inside the platinum ring, so that it is exactly centered and protruding a few millimeters below it, while the RE is kept just outside the ring and in its close proximity. Since all points

on the lateral surface of the wire are equidistant from the ring contour, the current density during the etching process will flow homogeneously. All the electrodes are plunged inside a 5 mL beaker, containing the etching solution, in order for the platinum ring to be just below the liquid surface. This means that the etching process occurs at the solid/liquid/air interface, where the solvent forms a meniscus on the wire. As the process goes on, the immerged part of the wire starts detaching from the upper one (see inset in **Figure 2.1**a) until it falls inside the bulk of the solution, leaving a sharp extremity behind. Boyle's group [189] stressed the importance of leaving a reasonable length of wire immerged in solution (~3-4 mm), as longer or shorter segments might not have the proper weight to trigger a neat detachment and yield a blunt tip.

2.2.2.1. Gold etching mechanism

As for the choice of the etching solution, chlorinated media are most likely used, as they etch gold at relatively low potentials [190]:

$$AuCl_2^- + e^- \rightleftarrows Au + 2Cl^- \qquad (E^0 = 1.154\ V\ vs\ SHE) \qquad (2.1)$$

$$AuCl_4^- + 3e^- \rightleftarrows Au + 4Cl^- \qquad (E^0 = 1.002\ V\ vs\ SHE) \qquad (2.2)$$

$$AuCl_4^- + 2e^- \rightleftarrows AuCl_2^- + 2Cl^- \qquad (E^0 = 0.926\ V\ vs\ SHE) \qquad (2.3)$$

CN^- solutions would actually be ideal to get very smooth tip surfaces, but they are very toxic and require the application of potentials superior to 10 V [165]. Normally, good-quality results can be obtained with mixtures containing concentrated HCl (≥ 37%). However, a too high HCl concentration provokes an intense gas evolution (Cl_2 and O_2) on the wire surface, which may cause strong convection movements compromising the smoothness of the produced tip [188] and also the sharpness (early detachment of the hanging wire in solution). On the other hand, an excessive dilution of the solution leads to a dramatic increase in the etching times [188]. To compromise between the two extremes, it was chosen to employ a 1:1 (v:v) mixture of 37% HCl and absolute ethanol, often reported in the literature [165]. As it is renown in the silicon industry, the presence of absolute ethanol limits the formation of gas bubbles [165], thus preserving the smoothness of the tip and avoiding the risk of current oscillation (see below). However, it is essential for the solution to be freshly prepared just before starting the etching, as an excessive absorption of atmospheric water could compromise the etchant quality. A pre-treatment of the wire with nail varnish has also been reported to prevent the detrimental effect of the bubbling on its surface [189]; as this issue was not encountered, no pre-treatments were performed on our experimental wires.

2.2.2.2. Taming of the etching process

Once the electrochemical cell is set, the etching process can take place. Several dissolution regimes can be observed depending on the polarization, as summarized in **Figure 2.2**a. When gold etching proceeds, the immediate surroundings of the wire become rich in gold-chlorine complexes and poor in Cl^-. Gold cations start therefore reacting with oxygen, forming insulating gold oxides that temporarily passivate the gold wire [165]. Dissolution can resume temporally when chlorine complexes diffuse away (relaxation), giving rise to current spikes. At higher potential, spikes of dissolution overlay with the oxidation of the solvent (gas evolution). A shift in potential of the gold electrochemical response, along with a strong oscillation regime, observed in a two-electrode configuration, as compared to a three-electrode setup, is illustrated in **Figure 2.2**a. Moreover, when using a DC polarization (2.2 V) without reference electrode, the potential of the gold wire keeps oscillating and shifting toward higher values, as illustrated on **Figure 2.2**b.

The use of AC potential pulses, instead of DC polarization, allows a fine control of the etching process. By selecting a proper AC bias, dissolution at higher potential and relaxation at lower potential can alternate in a controlled manner. This procedure allows shortening considerably the etching process, especially when thick wires are used, and its success has been the basis for the developments of highly performant and reproducible potential pulses etching routines[191,192].

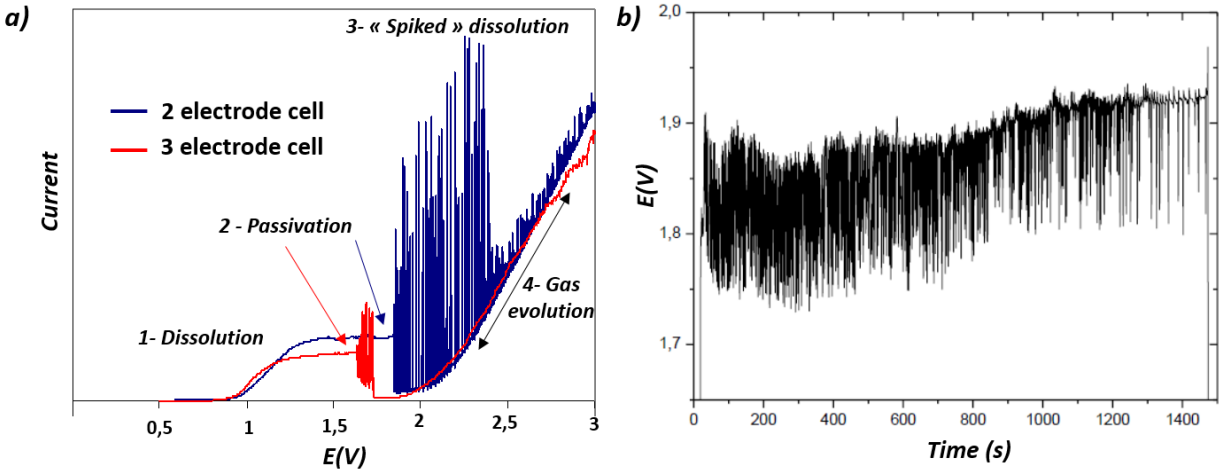

Figure 2.2. Importance of the potential control during electrochemical etching of gold – a) Electrochemical response of a 200µm-diameter gold wire in HCl/EtOH (V:V, 50:50) in a 2-electrode cell (blue; CE : platinum ring) and in a 3-electrode cell (red; Ag/AgCl pseudo reference electrode, CE : platinum ring), linear potential sweep: 0-3V; **b)** Evolution during a DC polarization at 2.2 V in a 2-electrode configuration (CE: Pt) of the gold wire potential measured *vs* Ag/AgCl using a high impedance voltmeter. Adapted from Alice Dauphin bachelor report (LISE laboratory, 2015).

2.2.2.3. Etching termination

As it was emphasized by Billot *et al.* [188] in a "DC voltage" approach, the etching of the gold wire proceeds along two main stages observable on the chronoamperometric response. During the first etching stage, the wire is sharpened horizontally, i.e. axially, and starts assuming a typical cone shape as the position of the solution meniscus progressively lowers. At this stage, the current decreases almost linearly as the etching time increases, until it drops abruptly and then starts decreasing slowly again. This marks the passage to the second etching stage, which proceeds vertically along the wire, thus making the tip blunter and blunter and useless for STM-TERS purposes. The curve of the current evolution against the etching time is shown in **Figure 2.3**, along with its first derivative that clearly shows an inflexion point separating the two etching regimes. This point corresponds to the I_{stop} value, i.e. the current value for which the etching process should be manually stopped, in order to produce sharp probe with a tapered profile.

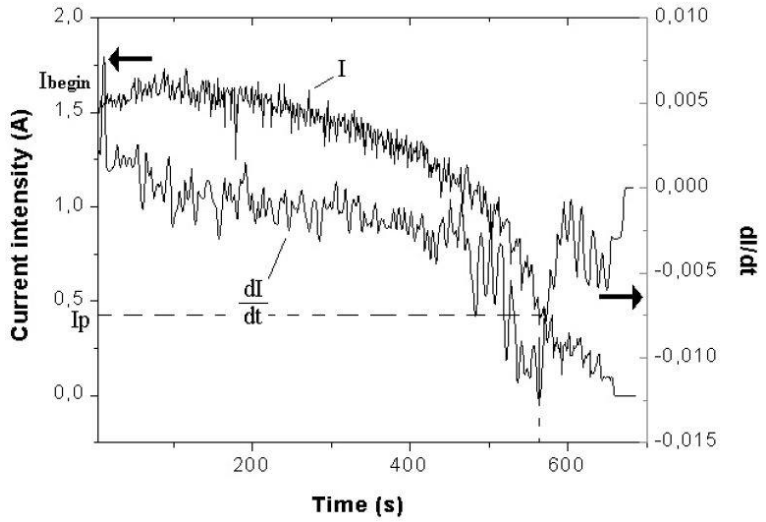

Figure 2.3. Current variation versus time during the etching process and first derivative curve obtained for an applied voltage of 12 V Adapted from [188].

An additional "cut-off" voltage box connected between the counter-electrode and the potentiostat has been developed in LISE to automatize and precisely control the termination of the etching process and avoid over-etching of the gold wire. The "cut-off" box is configured to physically disconnect the CE when the current flowing in the system falls below a set threshold value, which is adjusted to be in proximity to the I_{stop} value previously mentioned. As the CE is disconnected, the etching process is interrupted and the etching sequence on the potentiostat, which is apparently still running, reads zero current. Note that as the "cut-off" box uses a

current/voltage converter, the voltage associated to the desired current threshold depends strongly on the current range set in the potentiostat.

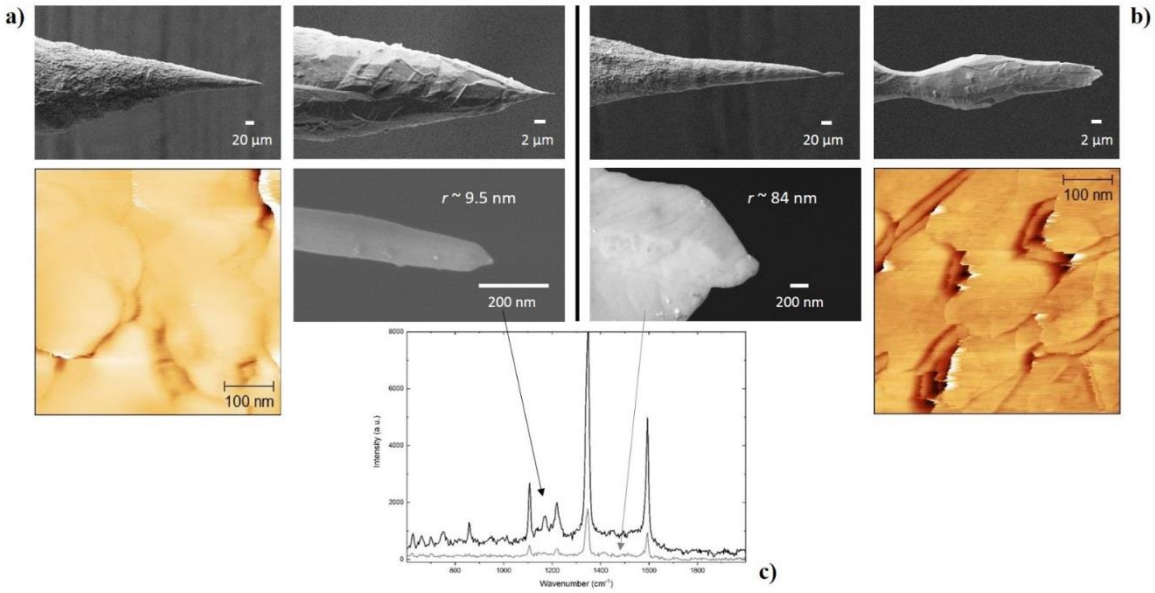

Figure 2.4. Aspect and performances of tips fabricated by electrochemically etching of gold wires in a 1:1 (v/v) mixture of 37% HCl and absolute ethanol, using potential pulses. SEM images at three different magnifications and STM maps, acquired on a bare gold plate (500x500 nm^2, 256x256 pixels, I_T=1000 pA), are shown for two tips, with radius 9.5 nm (a) and 84 nm (b) respectively. A comparison of the TER spectra recorded with the two tips on the same sample is shown in (c). Each spectra has been recorded by accumulating 3 spectra, acquired for 3 s each, with 160 µW power of the 632.8 nm laser line.

2.2.2.4. Tip taper profile and performances

The influence of the "cut-off" current value on the performance of the tip is illustrated in the following paragraph. However, neither the "cut-off" values nor the parameters of the electrochemical sequence will be disclosed here, as a *Soleau* envelop protecting this know-how has been filed in 2015. For each combination of pulses and "cut-off" values, the set of etched tips was first analyzed *via* SEM to closely observe their morphology and shape. Their STM imaging performance and TERS activity were eventually tested in the air on a bare gold electrode and on a model 4-nitrobenzyl mercaptan (4-NBM) SAM deposited on gold. Depending on the cut-off value, the radii of curvature can strongly vary, ranging from ~10 to 90 nm as shown in **Figure 2.4**a-b. Note that the opening angle (half cone of the tip apex) is quite different as well. Albeit, the produced tips looked sturdy and smooth and surprisingly gave decent topographies, which showed in detail terraces steps on flamed-annealed gold surfaces.

As for the Raman signal enhancement, **Figure 2.4**c confirms (as affirmed before) that the spectral intensity depends on the tip apex dimension. In the shown example, decreasing the radius of curvature by a factor of ~8 induces a 4-fold increase in the number of counts for the same spectral signature. Nonetheless, even the tip with a larger apex showed quite good performances: the overall signature was quite neat and sharp, and the most intense peak almost reached 2000 counts, far above the background. Similar STM and TERS performances were observed also for the other tips obtained following the same etching procedure, with intermediate radii of curvature. We can therefore conclude that, in spite of the variation in the tip profiles, the probes fabricated following this protocol can be reliably used for STM-TERS investigation. Note the resulting quality of the tip is strongly user-dependent, as many parameters (non-fresh solutions, water contamination, CE passivation and "polluted" RE, contact resistance due to corrosion with acid vapors, etc.) influence the correct outgoing of the procedure. The specific probe preparation for liquid application (insulation, bending) will be detailed later on, when presenting the implementation of the EC-STM-TERS setup.

2.3. Raman and STM coupling: technical implementation

As it was previously mentioned, in a STM-TERS setup the same probe is employed simultaneously to map the sample morphology and to enhance its Raman signature by acting as a plasmonic resonator. This can only be possible, though, if a robust optical coupling is implemented. Therefore, the focus of the laser Raman probe on the tip, which occurs through the piezo-controlled objective lens, must be perfectly adjusted on the hotspot position at the tip apex and remain stable over time, while the signal scattered from the sample and enhanced by the tip must be efficiently collected. Several instrument manufacturers have ventured and successfully achieved the realization of hybrid STM/AFM-nanoRaman setups that can be conveniently used for TERS purposes: notable examples are the alpha300 RA (WITec, Germany), the NTEGRA Spectra II (NT-MDT, Russia), or also the hyphenation between the inVia™ confocal Raman microscope and the Dimension Icon® AFM, obtained from the collaboration of two different enterprises (Renishaw, UK, and Bruker, US, respectively).

The TERS-ready platform in LISE lab, shown in **Figure 2.5**, couples two different setups: a *LabRAM HR Evolution* Raman spectrometer (HORIBA Scientific, Japan-France) and an *OmegaScope 1000* scanning probe microscope (AIST-NT, US). The characteristics and specifics of the two different instruments will be discussed separately in the next paragraphs.

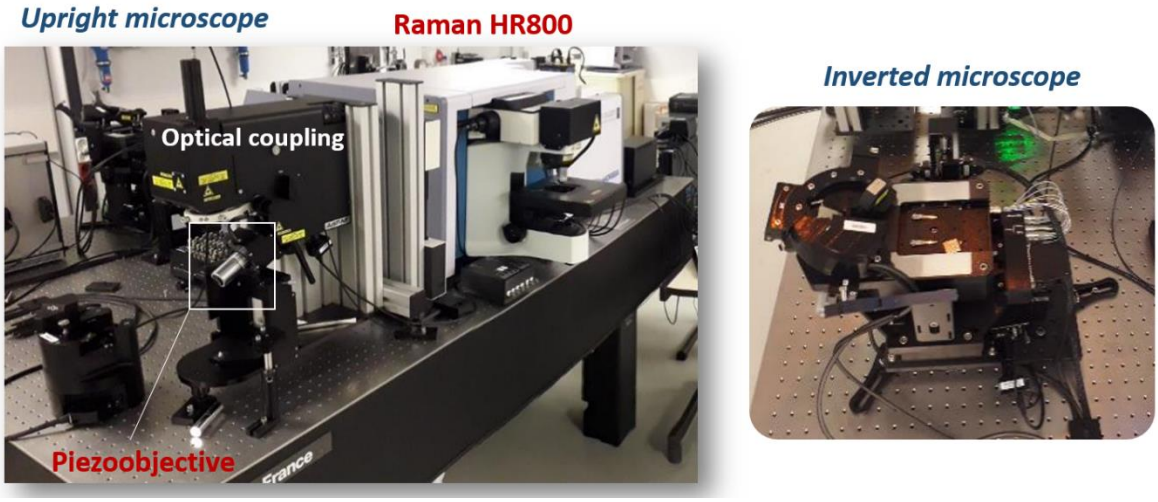

Figure 2.5. NanoRaman platform in LISE, consisting in the hyphenation of an *OmegaScope 1000* optical platform carrying a piezo-controlled objective and coupling the upright SPM microscope *SmartSPM* (on the left) to a *LabRAM HR Evolution* Raman spectrometer (on the right). An inverted SPM microscope (Combiscope) positioned behind the *OmegaScope* can be also coupled optically to the Raman spectrometer.

2.3.1 Optical construction of the Raman microscope

The *LabRam Evolution* spectrometer is equipped with 5 different laser lines (from the near-UV 473 nm to the near-NIR 785 nm) and also of two detectors, an EM-CCD[†] detector with back illumination (*Newton 971*, Andor, Oxford Instruments), for fast Raman acquisition (in time or spatial mapping), and a CCD detector (*Syncerity*, Horiba), with a higher sensitivity (quantum efficiency of 55% at 800 nm, only 27% at 250 nm) in the near-infrared. The spectrometer is coupled to a true confocal microscope enabling to spatially filter the analysis volume of the sample, both in *xy* (lateral resolution) and in *z* (depth resolution), through the adjustment of a pinhole aperture positioned at the entrance of the spectrometer. This guarantees a high resolution, both spatially (at the diffraction limit ~ half of the illumination wavelength) and spectrally (thanks to the 800 nm focal length of the single stage spectrometer).

In order to perform ultra-fast confocal imaging, two recent implementations were introduced: the *SWIFT*^{TM} mode, where an optimized detector-stage coordination enables a fast (sub-second) spectral acquisition and also the *DuoScan*^{TM} technology, which provides ultra-fast movements of two piezo-controlled optical mirrors to create specific laser raster scans over the sample surface (line, square, disc). This latter mode, also used on sensitive sample to

[†] The acronym EM stands for Electron Multiplier, since the charge stored in each pixel is multiplied before readout, thus lowering in theory the limit of detection to a single photon.

distribute the energy over the surface and minimize sample damages during the Raman recording cannot be used in TERS because of the strong divergence of the beam induced over the distance.

As illustrated in **Figure 2.6**, the optical path of the spectrometer can be modified depending on the desired use, and configured toward the optical microscope attached to the facade of the spectrometer or toward the *OmegaScope* setup positioned on the left side (see **Figure 2.5**). The *OmegaScope* is an optical coupling system hosting both an optical microscope (equipped with two vertical and side piezo-mounted objectives) and the scanning probe microscope (*Smart SPM,* AIST).

Laser and signal filtering. The Raman spectrometer construction is depicted in **Figure 2.6**. Before entering into the Raman spectrometer, the laser passes through narrow bandpass "cleaning" filters that suppress non-lasing lines (i.e. background plasma and secondary emissions). Afterwards, the pre-filtered laser enters through the input E2 and is directed to the main path by the mirrors M3 and M4. It therefore passes through the polarizer P1 to reach the laser intensity attenuation filter F3. This consists in a software-driven wheel hosting 9 different neutral density (ND) filters, each with a different optical density (100%, 50%, 25%, 10%, 5%, 1%, 0.1% and 0.01%), to tune the laser power depending on the sample sensitivity and/or the measurement requirements. An additional ND filter wheel, which can be manually operated, has been added to furtherly modulate the laser power, allowing to transmit 100%, 79%, 63%, 50%, 32% and 25% of the already filtered source power. The outgoing beam passes through the beam expander lens L1, which focuses it on the pinhole H1, and reaches F4. F4 is a laser rejection filter (consisting in a stop-band notch filter for the laser lines at 632.8nm, or in pass-band Edge filters for lines at 473, 532, 591 and 785 nm) which acts here as a mirror reflecting the laser toward the microscope objective lens‡. Afterwards, the reflected beam passes through lens L2 and a retractable mirror directs it towards either the microRaman microscope head, holding several objective lenses, or the *OmegaScope* optical microscope. In the latter, another retractable mirror reflects the beam either to the top or to the side objective. The *OmegaScope* is placed on the same optical table as the spectrometer (as shown in **Figure 2.5**) in order to

‡ Notch filters can selectively block a small wavelength portion (with over 99% of efficiency)[193], and are preferred when both Stokes and anti-Stokes Raman acquisitions are needed. Edge filters instead can only reject all the light passing above or below a certain wavelength, and they usually have less sharp transitions amongst the high-diffraction and high-transmission zone [193].

insure a proper optical coupling amongst the two. The optical signal, back-scattered from the sample, is collected through the same objective and directed toward the spectrometer, where again the filter F4 (rejection filter) suppresses the elastic scattering (i.e. Rayleigh) contributions. The beam can also pass through an optional element F5, consisting usually in a polarizer or in an ultra-low frequency filters (ULF). This latter allows observing spectral signatures down to 10 cm^{-1} off of the laser line.

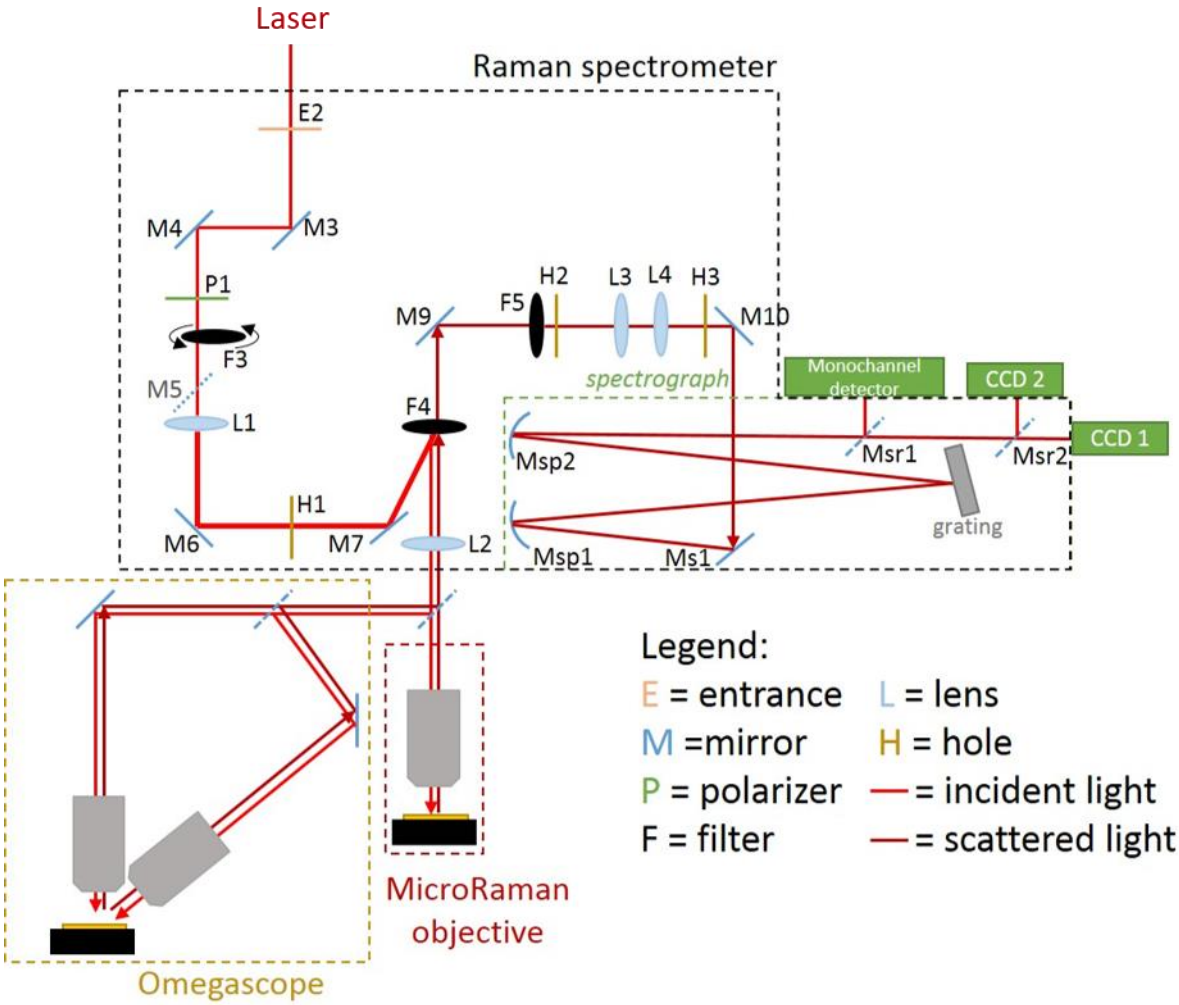

Figure 2.6. Schematic view of the *LabRAM* HR Evolution optical path and spectrograph and of its optical coupling with the microRaman optical microscope and the *OmegaScope* SPM.

***Confocality*.** The signal reaches therefore an adjustable pinhole aperture, constituted by two holes H2 and H3, spaced by the lenses L3 and L4. This system enables to control the confocality of the microscope: the smaller the hole, the smaller the volume of the analysis, hence the better the depth and lateral resolutions of the analysis [87]. In TERS, the confocality guarantees a better focus of the Raman probe on the tip, hence a stronger intensification of the near-field signal at the expenses of the far-field background contributions.

Signal detection/resolution. The beam then reaches a shutter positioned after H3 at the entrance of the spectrometer (the shutter operates during normal spectral acquisition, but not in *SWIFT* mode), and is then reflected by the mirror M10. Here the beam enters a symmetric Czerny-Turner monochromator: after reflection in mirror Ms1, the beam is collimated by the spherical mirror Msp1 and hits the diffraction grating. Two different diffraction gratings (with 300 or 1200 grooves per mm, $gr.mm^{-1}$) can be selected depending on the resolution desired for the acquired spectra. As the number of grooves per mm increases, the optical signal is more spread out on the photodetector, thus improving the spectral resolution as the expense of the spectral range accessible. For our experiment, we privileged the possibility to measure a larger spectral window at once, hence the 300 $gr.mm^{-1}$ grating was the most employed. The *Newton* (Andor) EM-CCD photo detector consists of a 1600 x 400 array of 16µm-wide pixels, giving for the 633 nm Raman probe (and for a 300 $gr.mm^{-1}$ grating) a resolution of 1.4 cm^{-1} and a 165-2360 cm^{-1} spectral range. A "binning" parameter (number of camera pixels employed to yield a single spectrum pixel) can be used to artificially record more intense spectra at the expense of the spectral resolution. Note that, as a result of the proximity of the *OmegaScope* platform with the spectrometer, STM performances can be impacted by mechanical noise originated from the CCD or laser cooling system, or else from the movement of optical parts in the spectrometer (pinhole adjustment, mechanical shutter). To reduce the environmental noise during STM-TERS operation, the fan-cooled built-in 633 nm laser, initially positioned within the *LabRam* enclosure, was transferred to an optical bench at the rear of the spectrometer together with the other lasers. This allows turning off the fan cooling system during STM operation and hence decreasing the noise. Additionally, a water-cooling system was installed on the EM-CCD camera to minimize mechanical noise and improve the detector sensitivity (reduction of the "dark" current of the detector at lower cooling temperature accessible to the thermoelectric Peltier device).

2.3.2 SPM/ Raman coupling platform and choice of the illumination geometry

The *OmegaScope* 1000 used in this work and presented earlier on **Figure 2.5** was specifically designed to optically couple Raman spectroscopy with the *SmartSPM* microscope. The latter is provided with different measuring heads depending on the imaging mode implemented, i.e. AFM, shear-force microscopy (ShFM, using tuning forks) and STM. Only this latter was used in this work, in order to carry out *ex* or *in situ* STM-TERS experiments.

The STM head consists in a simple platform holding in place both the tip holder and a conductive unit connected to the tip and the sample (**Figure 2.7**a.). The conductive unit establishes a bias voltage between the tip and the sample (typically 0.1 V) and also measures the net tunneling current flowing between them. Several amplifications gains are available, allowing currents from pA to µA to be measured. The current feedback loop should have a bandwidth large enough to allow fast adjustment of the tip-sample distance. However, since the noise level increases with the bandwidth, this should also not be too large. In this work, low-pas cutting frequency was set to 25 kHz.

The open design of the microscope head (clearly visible in **Figure 2.7**b) allows a high flexibility over the experimental conditions, easing, for instance, the introduction of more elaborated tip and/or sample holder designs or the coupling to external instrumentations (see EC-STM-TERS setup, presented later). Note that on the *SmartSPM* microscope, a sample piezo-scanner ensures the raster scanning for topography/composition imaging of the sample without compromising the optical coupling, i.e. the precise focusing of the laser beam on the tip apex using a piezo-controlled objective lens (carried by the *OmegaScope* coupling platform). This represents an advantage respect to Ren's STM-TERS configuration, described in Section 1.3.3. The accessible *x*, *y*, *z* scanning range of the sample scanner is 100x100x15 µm, 30x30x10 µm for the objective scanner.

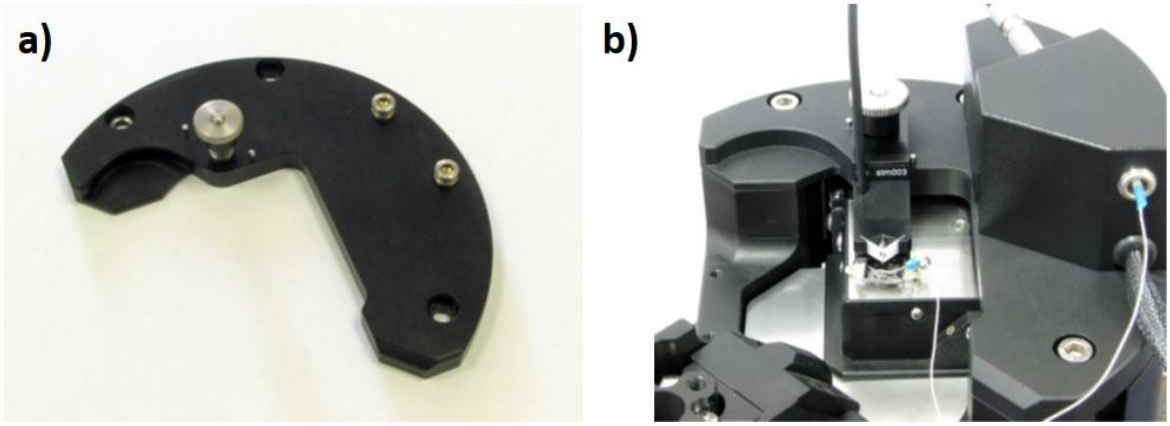

Figure 2.7. STM mode on the *SmartSPM* microscope - a) STM head design, **b)** STM head carrying both the tip holder and the conductive unit (connected to both the tip and substrate) and mounted on the microscope. Images taken from the *SmartSPM* 1000 Instruction Manual (Horiba, AIST).

Choice of the illumination geometry - Since the relative position/orientation of the tip shaft, of the objective lens and of the substrate influences the efficiency of the TERS signal excitation and collection (see Section 1.3.3), it is not trivial to select an ideal configuration, and especially in liquid where the multiple interfaces brings up issues of optical path distortion.

Different configurations can be distinguished, bottom, side and top illumination, which are schematized in **Figure 2.8**.

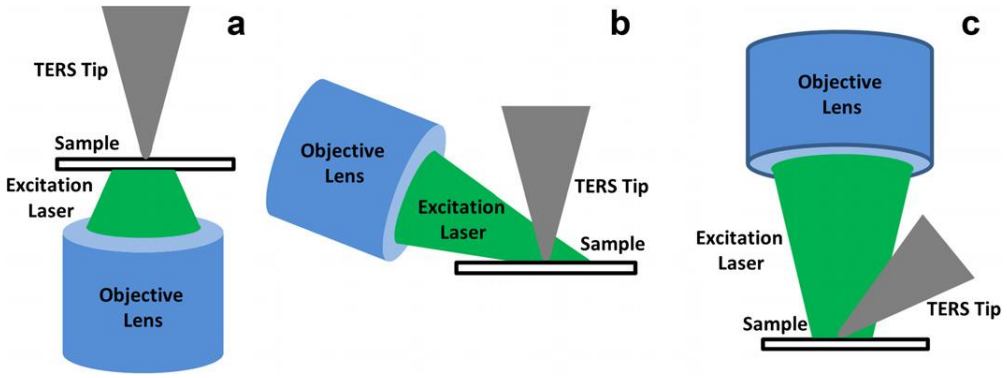

Figure 2.8. TERS illumination configurations - Schematic illustrations of laser/probe optical coupling: **a)** bottom-illumination (inverted SPM microscope, transparent sample; **b**) side-illumination and **c)** top-illumination and upright SPM microscopes. Adapted from [126].

***Bottom illumination*.** As it was said in Section 1.3.3, the inverted configuration using bottom illumination (**Figure 2.8**a) has been the very first one employed to carry out AFM-TERS measurements in liquid, by Zenobi's group [3]. In their setup, the tip was illuminated through the sample (functionalized glass cover slip) using a high-NA oil immersion objective. Bottom illumination combined with radially polarized laser and high NA objectives provide an optimal TERS signal enhancement [108] while minimizing the far-field background contributions from both the liquid and the sample [108]. Van Duyne's group [177], further developed this configuration for *in situ* EC-AFM-TERS experiments. Such configuration, though accessible in LISE using the inverted microscope (*CombiScope*^{TM}), was not developed for STM-TERS purposes because of the microscope mechanical instability and the mechanical coupling between the sample and the oil-immersion objective through the thin oil layer, which leads to repeated crashes of the tip over the sample surface.

Side- and top-illumination setups are preferred when working with non-transparent substrates, despite the difficult signal excitation/ collection through the air/liquid interface.

***Side illumination*.** For side-illumination (**Figure 2.8**b), long-working objectives, oriented with a 45-70° angle with respect to the tip shaft, are combined with p-polarized laser, so that the largest component of light electric field is set parallel to its axis, for maximum TERS signal enhancement [194]. In side illumination, the beam spot assumes a large elliptical shape when reaching the sample, hence higher laser powers will be required for the excitation to be more effective [108,194]. An original solution, introduced by Ren's group [4], employs a vertical STM tip and a 10° angle tilted sample immobilized in a transparent liquid cell, which allows

the illumination of the tip from the side using a long-distance objective positioned horizontally. The light can therefore reach the probe from a 90° angle without being blocked by the sample; however, its optical path is distorted by the presence of the glass window on the cell wall. This effect can be minimized by employing an immersion objective, separated from the cell window by a water or an oil droplet [174] (depending on the objective specifics). Another improvement proposed by Domke *et al.* [195] consists in using a liquid crystal display that, thanks to the electrical and optical anisotropy of the crystals, allows the modulation of light polarization until the best enhancement conditions are reached.

Top illumination. Top illumination (**Figure 2.8**c) is also used for TERS, but combined with slightly bent probes (AFM or STM) for the laser to be focused on the apex of the tip. Measurements in this configuration have been successfully performed both by Ren's [179] and our own group [169,182]. They could be carried out either using a 100x air objective (Mitutoyo MY100X-806 - Plan Apochromat Objective, NA: 0.7, working distance WD: 6mm) focused on thin layers of non-volatile liquids, with limited distortion of the optical path, or else using a water-dipping objective (Olympus, LUM PlanFLN – 40x, NA: 0.8, WD: 3mm - 60x, NA: 1, WD: 2mm) directly in contact with the electrolyte solution. In this configuration, the signal excitation/collection efficiency is higher than with the 100x air objective thanks to the suppression of the air/liquid interface, to the higher angle of collection and to the smaller working distances of such objective lens.

More specifically, the angle of collection is related to the numerical aperture NA according to the expression

$$\mathrm{NA} = n \sin\theta_{coll} \tag{2.4}$$

where n is the refractive index of the immersion medium (equal to 1 for air and to 1.33 for water and aqueous solvents) and θ_{coll} is the half-angle of the lens collection cone [196]. This parameter influences also the fraction f_{NA} of photons emitted by an isotropic source, which can be expressed as

$$f_{\mathrm{NA}} = \frac{1-\cos\theta_{coll}}{2} = \frac{1-\sqrt{1-(\frac{\mathrm{NA}}{n})^2}}{2} \tag{2.5}$$

This means that an objective possessing a high NA, i.e. working in water (high n) and/or at short distance from the illuminated source (high θ_{coll}), will be able to gather a very intense signal [196].

Given the short working distance of water-dipping objective, the STM probe design has to be optimized so that the tip apex can reach the focal point of the objective at a final angle of 30-50°. This allows a beam/tip alignment suitable for TERS signal enhancement [125,169,197], while ensuring a mechanical stability for STM imaging.

Additional improvements in the overall EC-STM-TERS setup were introduced in this work and will be presented in the next section.

2.4. EC-STM-TERS analyses: setups and *modus operandi*

Electrochemical STM-TERS measurements have been demonstrated in our group [125] by developing an EC-cell prototype, a tip holder compatible with the use of short working distance water dipping objectives and a specific electrochemical instrumentation. In this work, important efforts have been engaged to secure the reproducibility and the ease of EC-STM-TERS implementation by revisiting the design of the cell, optimizing and introducing new protocols and further developing the electrochemical instrumentation.

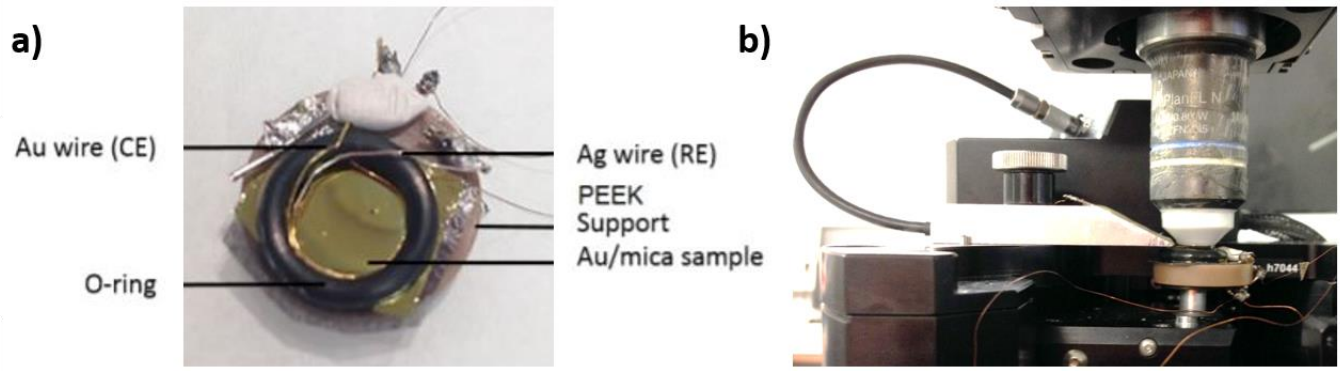

Figure 2.9. First EC-STM-TERS set-up developed in the group: **a)** 4-electrode cell prototype and **b)** set-up showing the cluttered arrangement of the EC-Cell (with electrical connections), the tip-holder (conductive unit behind) and of the water-dipping objective lens. Adapted from [125].

2.4.1 First prototype of the EC-STM-TERS setup

When performing EC-STM-TERS, a 4-electrode system must be used, where the tip and the sample act both as working electrodes (WEs), whose potential is set against a reference electrode (RE), while the counter-electrode (CE) provides the required current flowing through the two WEs. This double potential regulation implies the use of a bi-potentiostat, the major difficulty here being to integrate to it the conductive unit of the *SmartSPM*^{TM}. This is necessary to ensure the efficient control over the STM tip-sample distance using the tunneling current as a feedback parameter. A dedicated bi-potentiostat was designed in LISE to provide potential

control and exploration while maintaining a constant bias voltage between the tip and the sample, and to enable the proper amplification of the tunneling current measurement by the conductive unit.

Figure 2.9 shows the cell prototype designed by T. Touzalin [125]. The sample is immobilized on a poly-ether-ether-ketone (PEEK) support, and above it is glued to a rubber O-ring, which defines the actual volume of the electrochemical cell (capacity of ~1 mL of electrolyte) and constitutes its wall. Both the rubber and the PEEK are resistant to aqueous and organic solvents. A gold wire, following the contour of the O-ring inner walls, is used as CE, while a silver wire protruding inside the cell works as RE. Both are fixed to the PEEK support and, along with the gold surface, are connected to external bi-potentiostat by long and thin copper wires. The overall setup is quite bulky and cluttered, but sufficiently light and stable at the same time to ensure proper topography tracking by STM. However, within this design the electrodes are all very close to each other and their position is difficult to adjust, hence shortcuts can occur quite easily. Moreover, sample damage and contamination can easily occur upon gluing of the O-ring. Also, the thin and long wires employed as connectors for the electrodes are not shielded, with the risk of electrical noise and shortcuts.

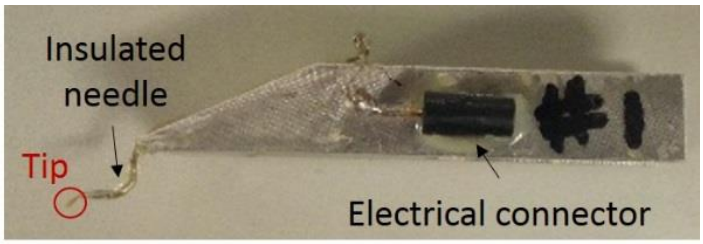

Figure 2.10. Homemade STM-tip holder - This specific design use a bent tube (needle) carrying the slightly bent gold STM-TERS tip to accommodate the profile of the water-dipping objective shown in **Figure 2.9**b, hence allowing the tip apex to reach the focal point of the objective. All metallic parts in contact with the electrolyte are insulated with bi-component epoxy glue and *Zapon* varnish.

As for the tip, it also needed to be mounted on a homemade-designed tip holder, since the commercial one, provided by AIST-NT, is neither adapted for the top-illumination configuration, nor for the cell geometry. **Figure 2.10** shows the tip holder, consisting in a right trapezoidal prism, made of stainless steel, with a tube (~ 300 µm diameter needle) glued along the oblique part. In the top part, the needle extremity is electrically linked to the input of the electric connector, which can be plugged in the STM conductive unit. On the bottom part, the needle is bent so that its shape can fit inside the electrochemical cell below the immersion objective. The etched tip is inserted inside the needle for a few millimeters, and its protruding

part is bent of around 45°. As it was mentioned before, this allows positioning the very apex of the tip at the focal point of the objective lens while ensuring some component of the electric field of the p-polarized incoming laser beam to be aligned with the shaft of the tip.

Finally, both the gold tip and the part of the needle in contact with the electrolyte are covered with *Zapon* varnish (Laverdure) (**Figure 2.11**a-b). *Zapon* shows no Raman signature, differently from the *Apiezon* resin classically used in the SPM community. As *Apiezon*, though, *Zapon* provides great electrical insulation and is not too viscous, thus leaving only the very apex of the tip uncovered upon drying. Moreover, *Zapon* turns out to be chemically stable in aqueous solution under "soft" acidic or alkaline conditions (not in organic solvents, e.g. ethanol or acetonitrile).

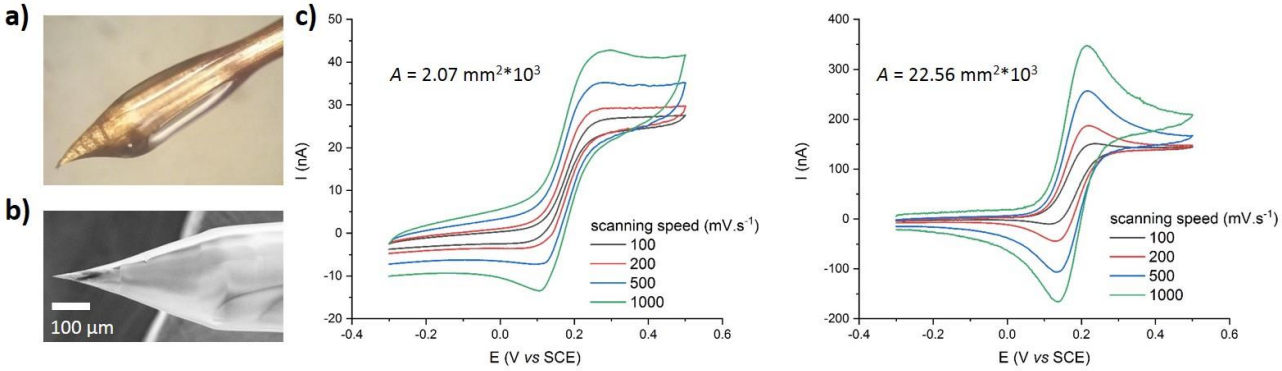

Figure 2.11. Zapon coating on TERS-active probes – a) Optical image (10x objective magnification) and **b)** SEM image of a gold TERS tip coated with Zapon varnish; **c)** Evaluation of Zapon insulation properties by CV in 1.8 mM $K_4Fe(CN)_6$ in 0.1 mol.L^{-1} KCl. On the left, a well-coated tip shows a steady-state current regime and therefore acts as an UME. On the right, a tip with a bad coating shows a transient regime, characteristic of a millimeter-size electrode. The active areas, indicated on the graph, were calculated from the Randles-Sevcik equation.

When performing measurements in liquid, the *Zapon* coating minimizes leakage currents, associated to faradaic reactions of the electrolyte (reduction of dissolved oxygen, reduction or oxidation of the solvent), on the exposed parts of the tip (**Figure 2.11**c). It is indeed important that faradaic currents are much smaller than tunneling currents to guarantee the effectiveness of the STM feedback for the control of the tip-sample distance over time. Usually, two applications of *Zapon*, followed each time by 10-minute drying in the oven (at around 80°C), are sufficient to yield well-insulated tips.

In conclusion, the overall fabrication protocol of the tip/tip-holder system resulted quite robust and convenient for routine application, and was therefore followed in this work.

2.4.2 Optimization of the EC-STM-TERS setup

To circumvent the critical technical points associated to the prototype described above, a new cell design was proposed, whose schematic view is shown in **Figure 2.12**.

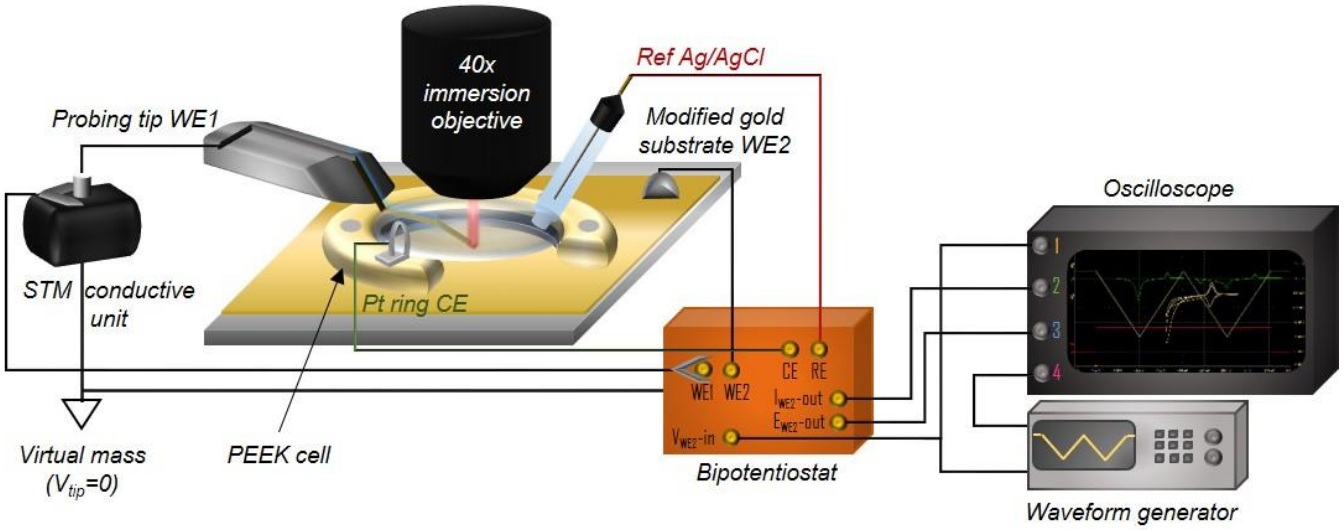

Figure 2.12. Schematic view of the homemade EC-STM-TERS setup associating: a magnetic liquid cell mounted on a thin ferromagnetic sample holder, a bi-potentiostat connected to a platinum counter electrode, a real Ag/AgCl reference electrode, the sample (working electrode WE 2), the STM-TERS tip (WE1) connected to the conductive unit and maintained at the virtual ground of the current amplifier. A waveform generator can be connected to the external voltage input of channel 1 and/or 2 to adjust and sweep the potential of the tip ($E_{WE1} = V_{WE1} - V_{ref}$) and/or of the sample ($E_{WE2} = V_{WE2} - V_{ref}$). The current response of channel 2 (WE_2) can be recorded on an oscilloscope. The tunneling current between the tip and the substrate is measured and amplified by the conductive unit.

EC cell. To avoid possible contamination related to the manipulation and gluing of the O-ring on the sample, a new cell made of PEEK was designed with a flat ring shape hosting 6 small magnets (SuperMagnet) and an O-ring. Thanks to the magnets, this cell can be immobilized on the sample holder, made of a thin ferromagnetic plate (size 30x20x0.3 mm). This latter, inspired from the AIST sample holders, can also be easily mounted/dismounted on the sample scanner. The pressure on the cell/O-ring/sample/metallic plate applied by the six magnets is sufficient to avoid any possible leakage of electrolyte, while still allowing an easy dismantling of the cell after use, leaving the sample intact. To further preserve the sample, its electrical contact is ensured through the use of a conductive magnet placed on its surface outside of the cell.

Additional electrodes. A platinum ring attached to a ferromagnetic holder can be conveniently positioned on the electrochemical cell magnet and act as CE. Additionally, an Ag/AgCl home-made electrode, employed as RE, is approached from the side of the cell and

immersed into the electrolyte in the meniscus formed on the objective lens. The use of a real Ag/AgCl reference electrode, instead of an Ag wire *pseudo* reference, guarantees a better control of the potential, especially in alkaline medium, where the surface composition of the silver wire can evolve with time and induce a potential drift. The total cell weight was kept minimal, similar to the previous prototype and only around 3 g heavier than the commercial AIST sample holder, designed for measurements in the air. This insured similar performances in liquid compared to those realized in the air, particularly for the minimization of the drifts. A close view of the real system (comprising the cell set with all the electrodes in place and the objective) can be seen in **Figure 2.13**a.

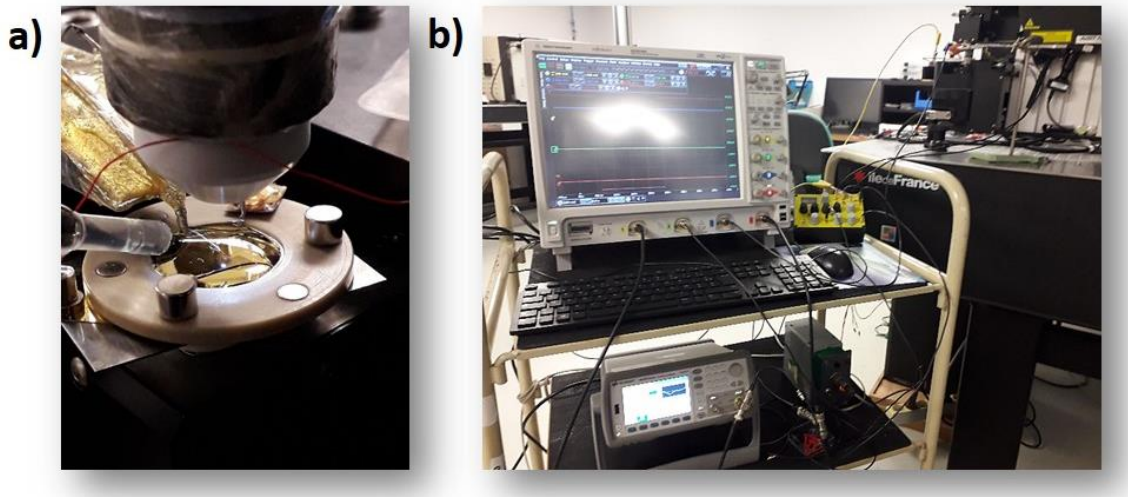

Figure 2.13. New design of the EC-STM-TERS setup: **a)** the electrochemical cell is immobilized via magnets on a ferromagnetic sample holder mounted on the sample stage of the *SmartSPM*^{TM}, the platinum ring CE electrode is mounted on the cell magnets, while the RE is approach to the side (left) the tip is introduced in the middle of the cell and the immersion objective is lowered down) **; b)** and the connected external units (oscilloscope, bi-potentiostat and waveform generator), placed in close proximity.

***Electrical connections and polarization*.** Another amelioration regards the connections employed for the sample (WE2) and the CE: instead of thin, long and bare wires, shorter segments of insulated copper wires were used to link the sample and the CE connections to a socket placed on the side of the *OmegaScope* unit. From the socket, two shielded cables insure the connection to the bi-potentiostat. Also the RE is connected with a shielded cable to the potentiostat. This reduces the risk of capturing electrical noise during the measurements and avoids the accidental detachment or rupture of the wires during the experimental preparation.

In our setup, we choose to keep using the conductive unit from AIST because it provides a low noise current signal to the feedback loop. It was verified that the tip was poised at V = 0

V *vs* ground, as it is the norm when using current-tension converters based on operational amplifiers. Therefore, in order to control the electrochemical potential difference $E_{tip} = V_{tip} - V_{ref} = e_1$ (e.g. in cyclic voltammetry or chronoamperometry), the bi-potentiostat unit applies $-e_1$ to the reference electrode. The sample potential (directly related to the bias voltage control) is applied through a differential stage included in the bi-potentiostat. With this configuration, we observed that the noise level in liquids was kept below 20 pA, provided that the tip insulation is correct.

***Real-time measurements*.** A waveform generator (Trueform 33500B Series, Keysight), is connected to the external voltage input of the bi-potentiostat of channel 1 (WE1) and 2 (WE2) to apply potential ramps (linear sweep, cyclic voltammetry) or potential step (chronoamperometry) to the two electrode simultaneously or independently while still (see **Figure 2.12** and **Figure 2.13**b). A four-channel oscilloscope (DSO9104A, Agilent Technologies), allows the real-time observation and recording of potentials and currents involved in the electrochemical reaction process. In a normal EC-STM-TERS experiment, the first channel is employed to observe the potential sequence designed on the function generator, while the second and the third channels show, respectively, the current and the potential evolutions on the sample surface (WE 2). The fourth channel of the oscilloscope is connected to the external trigger of the waveform generator (which is in turn linked to the output of the Andor EM-CCD camera). Thanks to this configuration, the square pulses generated by the camera at each Raman acquisition can be recorded and used as a trigger of the potential sequence on the waveform generator, thus allowing a perfect synchronization between the spectral acquisition and the electrochemical experiment. This technical development allows the real-time assessment of the effective polarization of the cell (hence of the actual electrochemical potentials, along with the occurrence of side reactions or ohmic drops), and the dynamic observation of the composition changes occurring on the sample upon polarization (time-resolved TERS measurements). A few successful applications of this configuration will be presented in the next paragraphs.

2.4.3 EC-STM-TERS analyses - Step-by-step implementation

2.4.3.1. STM-TERS measurements in the air

Before implementing the delicate STM-TERS measurements *in situ* (in liquid environment), it is preferable to assess first if the quality of the tip and/or the sample in the air is suitable for STM and TERS characterization.

Rough optical alignment. The cell-sample-holder assembly and the STM tip holder are mounted to the *SmartSPM* microscope and connected to the AIST-NT conductive unit. The *SmartSPM* is attached to the *OmegaScope* platform, which carries a 50x air objective lens (Mitutoyo MY50X-805 - Plan Apochromat Objective, NA: 0.55, WD 13mm) set vertically above the tip-holder. The tip apex is brought to the focal point of the objective using three millimeter-precision screws (two for the *xy* displacements and one for *z*) acting on the position of the *SmartSPM* microscope on the *OmegaScope* platform.

Tip-sample approach and landing in the air. The bias voltage BV and the tunneling current I_T are set to 0.1V and 1000 pA, respectively. These values of BV and I_T should correspond to a distance of less than 1 nm between the tip and the sample when the STM feedback control is enabled. Note that the conductive unit grounds the tip (V_{tip} = 0 V) and applies the polarization on the sample (opposite value of the chosen bias voltage BV, e.g. for BV = 0.1 V, V_{sample} = -0.1 V). The sample is therefore approached to the tip first through a rough motorized movement of the sample stage, and then by an automatized mechanism. This latter consists in the progressive approach of the sample piezo-scanners and of the step-motor to the tip by little upward steps of a few microns per second (usually 5 $\mu m.s^{-1}$). Between one step and the other, the instrument checks whether the tunneling conditions are reached; if so, the approach ends, otherwise it keeps going on. The tip, if well prepared and mechanically stable, should reach the sample surface without crashing on it, nor showing major current oscillations (recorded on the oscilloscope of the AIST-NT software).

Hotspot screening. Once the tip has "landed" on the sample surface (**Figure 2.14**a), its position at the focal point of the objective is readjusted. This approximated positioning, though, does not guarantee a good focus of the laser beam on the *hotspot*, i.e. on the point of the tip apex that provides the maximal signal enhancement. A finer adjustment is therefore carried out by displacement along the XY and the XZ plans of the piezo scanners carrying the objective lens, while acquiring the enhanced Raman signal at the tip-sample junction (TERS).

An example of a XY hyperspectral objective map of the tip apex (in liquid conditions) is shown in **Figure 2.14**b: each pixel on the map corresponds to a single spectrum, while the color code is representative of the relative intensity of a certain spectral range (black to white for low to high intensity).

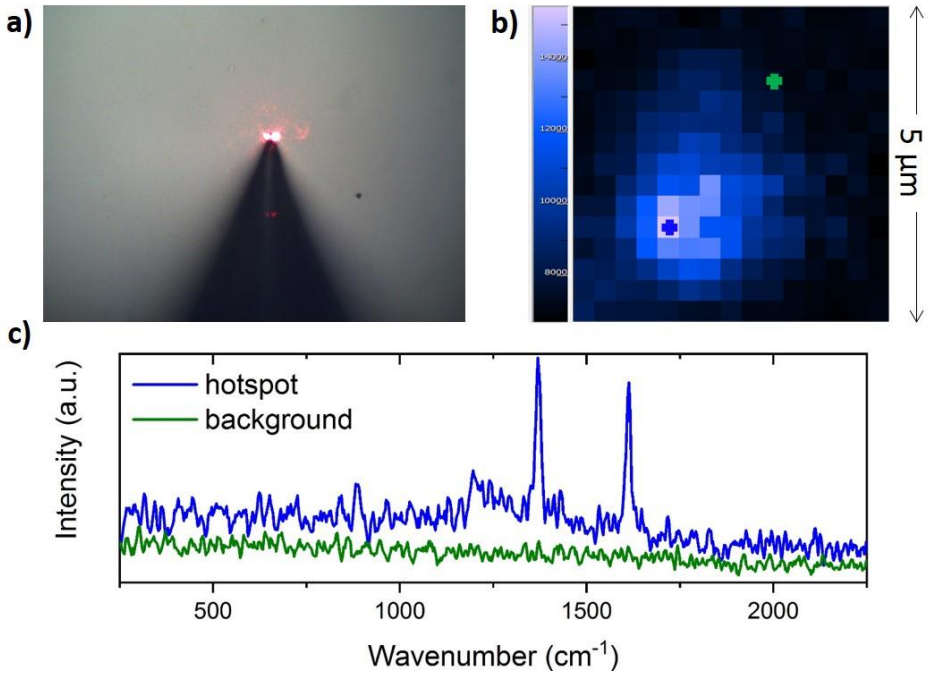

Figure 2.14. a) Tip visual optical micrograph, captured from the 40x immersion objective; **b)** TERS XY map acquired on the tip apex by scanning of the objective piezo-scanner. The map was recorded on a 5x5 µm^2 area with 10x10 pixels, each corresponding to a spectrum acquired in 0.3 s with 160 µW power (1% of the nominal laser power) of the 632.8 nm laser line. The colored bar indicates the intensity scale (arbitrary units); **c)** individual spectra associated to the blue and green crosses on the objective map.

The map shows a few bright pixels surrounded by many others at lower intensities. As it can be observed in **Figure 2.14**c, the brightest pixel corresponds in fact to a sharp spectral signature, while one of the black pixels only shows a background noise spectra. The tip hotspot is therefore expected to be somewhere in proximity of the brightest pixel, since it guarantees the acquisition of the most intense spectra on the sample surface, and the focal point of the objective can be positioned in correspondence to it. The same procedure is replicated several times in both the XY and the XZ planes, until the best objective position (with respect to the tip) is found.

***Assessment of STM performances*.** The stability and ability of the STM probe to track the sample topography are evaluated by performing a STM scan over the sample surface (e.g. on a 1x1 µm^2 area, with 256x256 or 256x128 pixels, at 1 Hz; see **Figure 2.15**a), while acquiring single TER spectra. After the adjustment of the STM feedback parameters (gain, imaging rate),

if the image shows topographic details with reduced noise/drift, and if the TERS signal does not fade during the imaging process, the tip can be conveniently employed as both STM and TERS probe.

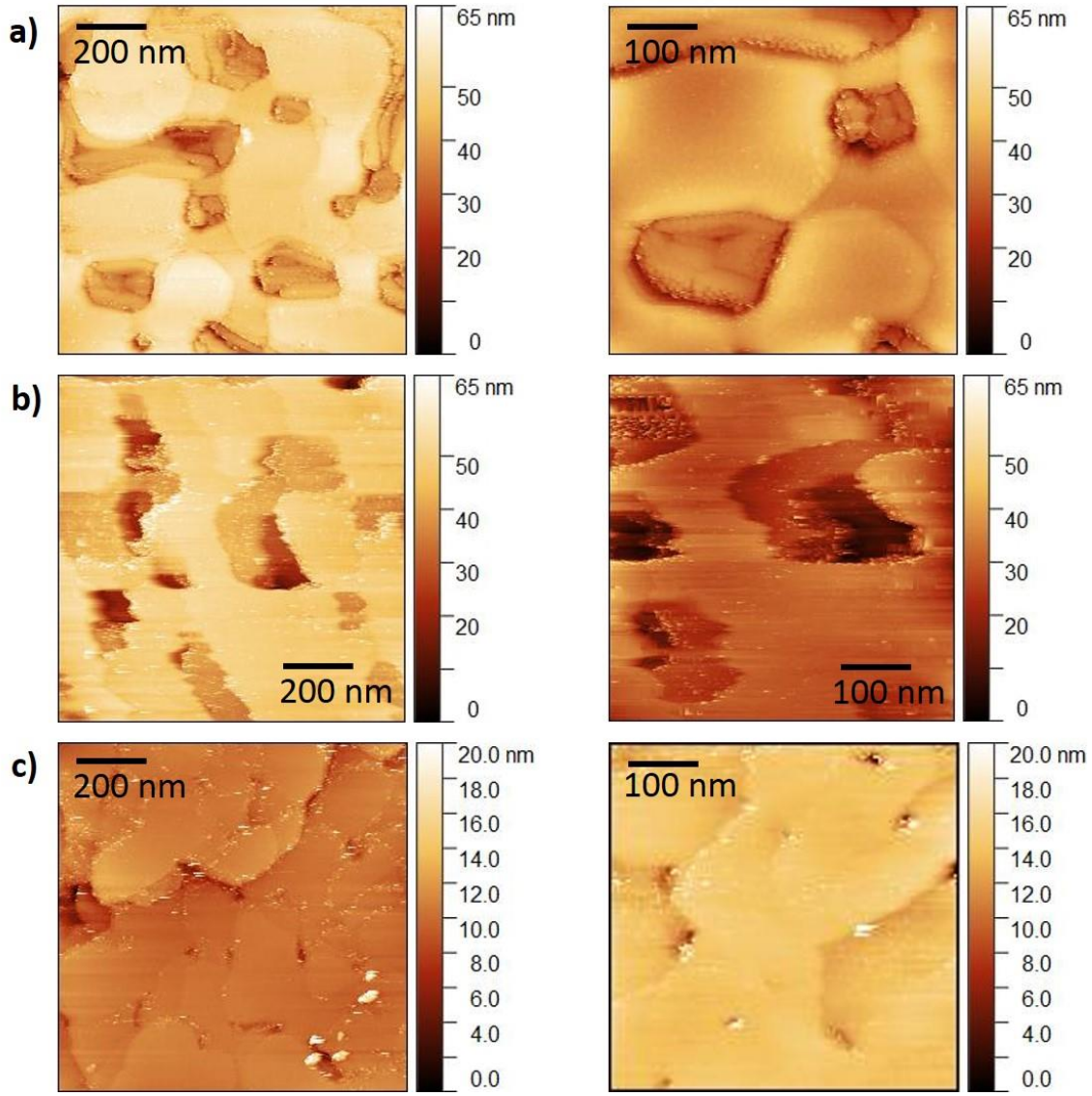

Figure 2.15. STM mapping – Maps acquired **a)** in the air or **b)-c)** in liquid environment on 1x1 μm^2 areas (left) or 500x500 nm^2 areas (right), with 256x256 pixels in both cases (BV = 0.1 V, I_T = 1 nA). Images on a bare gold substrate reported in **b)** were acquired just after **a)** after filling the sample holder cell with KCl 0.1 $mol.L^{-1}$. Due to the still non-optimized configuration of the sample holder, a poor topography is shown due to drift issues. Images in **c)** were acquired on a gold substrate functionalized with 4-NBM in the optimized setup and under the bi-potentiostat control in an alkaline buffer at pH 10.7.

2.4.3.2. *In situ* STM-TERS measurements

Once the probe performances are validated in the air, the cell-sample-holder assembly is retracted from the tip of a few millimeters, so that the system can be modified to be used

under electrochemical conditions. The air objective is substituted with the 40x water-dipping objective described earlier, the sample is disconnected from the AIST-NT conductive unit and reconnected to the bi-potentiostat, along with the CE, while the RE is approached from the side. The ground of the conductive unit and of the bi-potentiostat are connected to ensure the potentiostatic polarization of the STM tip and the application of the STM bias between the tip and the sample.

The cell is then filled with the electrolyte (previously deoxygenated by argon bubbling for at least 15 minutes) and the cell-sample-holder assembly is approached to the STM probe. Only when all the four electrodes and the objective are well immerged in the solution, the bi-potentiostat is switched on after the input potentials associated to channels 1 and 2 are adjusted, so that to avoid possible electrochemical transformation of the functionalized sample, or oxidation/reduction of the solvent on the tip or the sample surfaces. The stability and low value of the tunneling current (< 100 pA) measured and amplified by the conductive unit guarantees the proper insulation of the tip and tip holder with *Zapon* varnish ($I_F << I_T$). If strong current oscillations occur, the tip-holder is coated again with *Zapon* before use.

The BV voltage is set to 0.1 V by adjusting the electrochemical potential of the tip (+100 mV *vs* Ag/AgCl) and of the substrate (0 V *vs* Ag/AgCl) respectively. The tip-sample approach can therefore proceed until the I_T value reaches the STM set-point value (1000 pA). The STM (**Figure 2.15**b-c) and TERS performances are assessed after the tip hotspot positioned is screened according to the aforementioned procedure. The EC-STM-TERS analysis can finally start.

2.4.4 Assessment of the TERS signal stability with the potential

As it will be described in Chapter 3, the real-time STM-TERS study of the reactivity of electroactive 4-NBM SAMs in alkaline medium requires the recording of the TERS signal while scanning the potential of the derivatized gold electrode on large potential ranges (down to -1 V vs SCE). However, it has been shown in Chapter 1 that, in STM mode, the TERS signal of SAMs shows a strong dependency with the bias voltage (BV) and tunneling current (I_T) [180]. This was explained by the alteration of the signal enhancement at the tip-sample junction (particularly in gaseous atmosphere as compared to liquid), due to changes in the tip/sample distance and also, possibly, in the interactions between the metal and the adsorbates (e.g. charge transfer or change in the molecular orientation). In this section, the different strategies to

explore large potential ranges in EC-STM-TERS will be discussed and the stability of TERS signal with the potential will be assessed.

Specificity of STM tip/sample junction under EC conditions. Exploring the spectroscopic transformations on the functionalized sample upon polarization at highly negative potential indeed raised a crucial question: which potential should the STM-tip assume? Should it be kept at a constant BV from the sample or should it be maintained at the higher potential value?

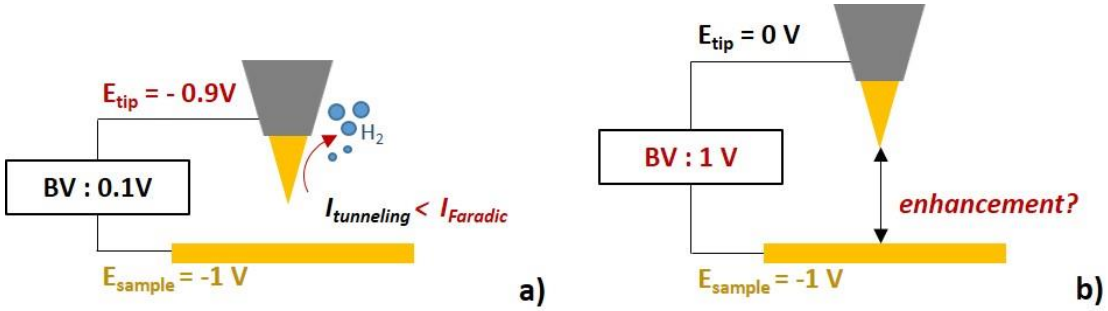

Figure 2.16. Influence of the polarization of the tip-sample junction on STM-TERS - a) Possible detrimental effect to the STM feedback effectiveness when polarizing the tip at too negative potentials, while keeping a low bias voltage (close tip-sample distance): promotion of Faradaic current associated to electrolyte reduction (gas evolution) which can dominate the tunnelling current flowing in the tip-sample gap ; **b)** Possible detrimental effect to the TERS signal amplitude when applying a too high bias voltage while keeping constant the tunnelling current value (increased tip-sample distance): loss of near-field coupling, hence of TER effect.

In fact, the answer is not trivial, as both choices could be detrimental for the good outcome of the measurement. It must be recalled that the tip sample distance using STM feedback regulation depends both on the BV and the tunnelling current I_T:

$$d = \frac{1}{\beta}\ln\left(\frac{\mathrm{BV}}{\mathrm{I_T}\cdot R(z_0)}\right) \tag{2.6}$$

with β the tunneling decay constant (dependent on the barrier height, or working function) and $R(z_0)$ the junction resistance at landing position z_0. This relationship is obtained by considering Simmons' description of the electron transport between electrodes separated by a thin insulating film in the low bias range [180], so it can be easily assimilated to our experimental conditions.

In turn, the TERS intensity I_{TERS} depends on the tip-sample distance d [180]:

$$I_{TERS} \sim \left(1 + \frac{d}{\rho}\right)^{-p} \quad (2.7)$$

where ρ is the dipole (hence, the tip) radius and p is a factor linked to the scattering process (for instance, it is equal to 10 for fully incoherent scattering).

When the BV is kept constant (situation illustrated in **Figure 2.16**a) the tip might reach very low potential values, which could promote the electrolyte reduction (hence the formation of gaseous hydrogen bubbles, in aqueous media) in the close proximity of the probe. If bubbles develop in the interspace between the tip shaft and the *Zapon* coating, this might no longer insulate properly the probe. Also residual molecular oxygen can reduce on the tip apex due to the low polarizations. The Faradaic currents deriving from these reduction processes risk to be of the same order of magnitude or even higher than the imposed tunnelling current value, thus perturbing the effectiveness of the STM feedback control and hence the tip-sample distance. As a consequence, the instability of the plasmonic coupling at the tip-sample junction leads to TERS signal fluctuation. In the worst case, the tip could simply crash repeatedly on the sample surface, promoting its contamination and compromising both its TERS activity and its imaging capability.

Sweeping of the bias-voltage. One alternative consists in keeping the tip at a constant potential while increasing the BV (**Figure 2.16**b). However, this affects the tip-sample distance d according to the previous Equation (2.6) [180] and may provoke a dramatic decay in the TER signal intensity, thus making it impossible to follow the electrochemical modifications occurring in real time on the sample. A systematic study was carried out by Domke's group on thiophenol SAMs to verify the validity of these expression in predicting the TER signal trend when variating BV and I_T [180]. The influence of the imposed BV was proved to be more crucial than I_T on the quality of the signal enhancement, which increased abruptly when decreasing the BV value from 500 to 20 mV. However, choosing such a low BV can also be detrimental for the measurements sake, as the strong and localized electric field in the gap may affect the molecules orientation and therefore alter their signal [180]. It should also not be neglected the role of the reaction medium. Working in liquid rather than in air comports already a loss in the signal intensity, due to beam aberrations and laser distortion. Besides, as the junction resistance decreases in liquid, an additional loss in intensity can be expected, with respect to measurements in the air at equal experimental conditions. On the other hand, it was remarked

that the variations in the signal intensity among different applied BV values was lower in liquid than in the air [180].

TERS signal stability with the potential. To evaluate the TERS-intensity dependence with the potential and the bias voltage, real time EC-STM-TERS measurements were carried out on an aminothiophenol (4-ATP) molecular layer self-assembled on a gold plate while scanning the potential. A composite potential ramp from -100 to -850 mV at 50 $mV.s^{-1}$ was applied by keeping the potential of the tip at 0 V vs Ag/AgCl and varying the bias-voltage (E_{tip} - $E_{substrate}$ from 100 to 850mV). The full description of the experiment and the Raman band assignment can be found in Chapter 3. **Figure 2.17**a-b shows the time dependent voltage and current response of the electrode and the corresponding evolution of the TERS intensity. No electroactivity of 4-ATP is expected in the potential range explored. The slight drop in current (**Figure 2.17**a) is indeed attributed to the slight electrolyte reduction. As can be seen on **Figure 2.17**b, the intensity of the spectral features of 4-ATP remain constant on the full potential range explored, confirming the possibility to follow TERS signature of molecular compounds in real time and on large potential ranges in STM.

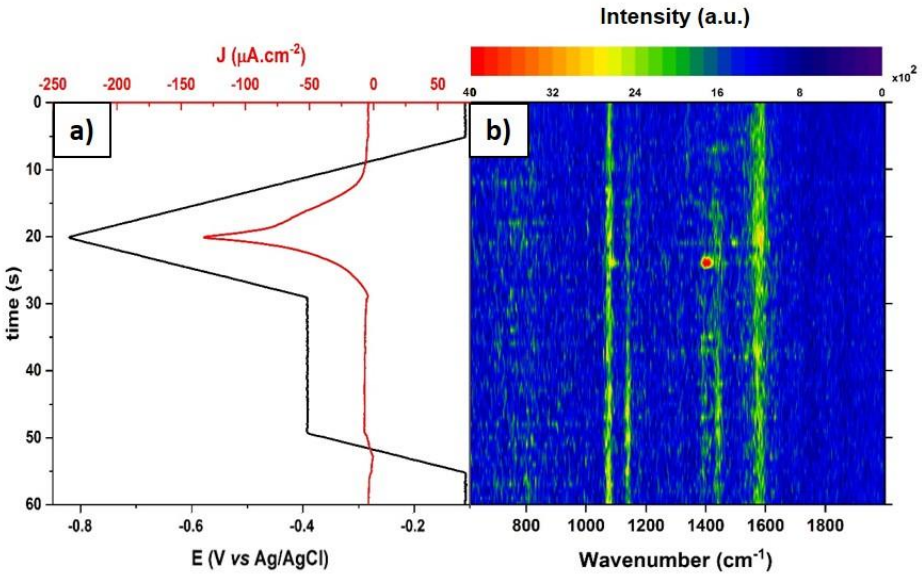

Figure 2.17. EC-STM-TERS measurements on 4-ATP SAM in alkaline medium: a) polarization sequence (a "composite" potential ramp), **b)** spectral signature dependence with the potential. Each line on the map corresponds to a single Raman spectrum (acquired in 1 s with 250 µW power of the 632.8 nm laser line, BV variable, I_T = 1 nA) and to a 50 mV potential shift. The spectra have been subjected to background removal.

This important founding will be exploited in Chapter 3 for the EC-TERS characterization of 4-NBM SAMs. Note that in Chapter 4, dedicated to the study of

electrochemically grafted 4-NB layers, highly negative polarization during STM-TERS mapping will be accessible through a combination of large BV and polarization of the substrate.

2.5. Conclusion

In this work, the developments initiated by the group before 2018 were pushed further to secure the ease and reproducibility of EC-STM-TERS implementation and to access electrochemical techniques (e.g. multisteps chronoamperometry, linear sweep and cyclic voltammetry) and time-resolved EC-TERS measurements.

In this optic, a new 4-electrode EC-cell was designed to ease the cell assembly, minimize sample damages, facilitate the positioning of the electrodes and avoid shortcut/disconnection/noise (thanks to the reliable shielded electrical connections). The open configuration of the cell enables the use of a real reference electrode for an accurate control of the potential applied to the STM tip and to the sample. Also, the electrochemical instrumentation (bi-potentiostat) developed in the lab was hyphenated with a waveform generator and an oscilloscope synchronized with the CCD detector of the Raman spectrometer. This allows the real-time assessment of the effectiveness/adequacy of the polarization applied on the electrochemical system under scrutiny, and above all insures the correlation of the TERS response at the tip-sample junction to the potential perturbation at the interface. Specific polarization sequences can be designed in STM-TERS to access highly negative polarizations of the substrates without compromising the signal enhancement at the tip/sample junction.

Further developments, not presented in this manuscript, aimed at applying ultra-short potential pulses to the STM-TERS tip and specific scanning patterns (lithography tool) to locally modify the composition of the functionalized sample. This yields the generation of molecular nanopatterns that can be characterized immediately *in situ* by EC-STM-TERS. If the use of nanoelectrodes for patterning is not new [198,199], the simultaneous characterization by TERS is unprecedented.

The low-cost fabrication of gold STM probes with strong TERS activity and STM mechanical stability, the design of a probe holder compatible with the use of high-NA dipping objective (for maximum TERS signal excitation/collection efficiency), together with the efficient insulation of STM probes with non-Raman active coatings are additional important developments which have paved the road to routine STM-TERS measurements under electrochemical conditions. Two studies illustrating the power of EC-STM measurements to

analyze electrochemical systems, i.e. electroactive self-assembled monolayers and electro-grafted molecular layers, will be detailed in Chapters 3 and 4.

Chapter 3 Study of a complex reduction mechanism on a model sample

3.1. Introduction

This chapter illustrates the ability of the EC-STM-TERS setup (presented in Chapter 2) in solving complex reaction mechanisms. Following the work of T. Touzalin in our group, who focused on single hot-spot SERS characterization of electrochemical transformation on nitrobenzene derivatives, we have decided to push further the investigation using EC-TERS. *p*-Nitrobenzene derivatives have been widely employed for functionalization: they can, for instance, induce p-type doping in graphene sheets [200], tune the electronic properties of silicon substrates [201], or mediate the immobilization of NPs on metal surfaces (through their NO_2 group [5] or its reduced form NH_2 [13]). Moreover, their affinity for adsorption on metal surfaces has been exploited to selectively retrieve and separate them from superficial water streams, where they can be present as pollutants [202,203]. Once immobilized on a surface, these compounds are subjected to a series of modifications involving the nitro group, which can undergo different kinds of transformations.

In order to investigate these phenomena, the most employed model sample in literature is 4-nitrothiophenol (4-NTP) [204–206], whose SAMs show uniform reactivity, along with sharp and recognizable electrochemical features [35,207]. These have been object of thorough electrochemical studies, as they arise from a complex mechanism that involves several reaction paths and is pH-dependent [204,208]. Besides, 4-NTP has been often employed for enhanced Raman experiments thanks to the easy interpretation and sharpness of its signature [205]. This characteristic makes it an ideal probe to study, for instance, the SERS performances of active substrates, as it allows separating the EM from the chemical enhancement effects (see Section 1.2.2.3) [204,207,209]. Both 4-NTP and its reduced amine form (4-ATP) have also been used in enhanced Raman spectroscopy to study and correlate the efficiency of the photo-induced coupling of nitro groups with the excitation wavelength, the underlying substrate, or also the surrounding environment [204,209,210].

4-NTP has been therefore previously employed [206] in our research group, to introduce the use of single hot-spot SERS platform (i.e. the tip-SERS technique presented in Section 1.2.2.3) for the study of electroactive molecules and molecular architectures. 4-NTP-functionalized SERS-active probes were subjected to *in situ* enhanced Raman measurements,

acquired before and after applying several voltammetric cycles at more and more negative potentials [206]. This led to the progressive disappearance of the 4-NTP spectroscopic signatures and to the appearance of new bands, attributed to 4-ATP, although no reaction intermediates were detected. Besides, upon negative polarization of the tip, a strong surge of signal occurred leading to the saturation of the detector. This phenomenon, whose origin has not yet been identified, made it impossible to follow in real time the evolution of the sample signature during the potential ramp. Another critical point encountered in this work regarded the apparently low stability of the thiol bond with the gold surface: contamination of the sample holder and of the underlying substrate was suspected to derive from an easy desorption of 4-NTP from the tip.

This led to the choice, for our work, of using an analogue of 4-NTP, i.e. the 4-nitrobenzyl mercaptan (4-NBM), as model sample. This species differs from 4-NTP only for an additional methyl group CH_2, which separates the benzene ring from the SH group, and which seems providing 4-NBM with a higher chemical stability [30] , thus limiting contamination issues. Thanks to this model sample, we could work on the development and implementation of EC-STM-TERS measurements in the setup presented in Section 2.4.2.

With respect to the first prototype designed in our group [182], which could be used for TERS measurements in liquid under polarization, this new setup has the main advantage of performing simultaneously spectral and electrochemical measurements on electroactive molecular layers in a dynamic way (potential ramps), thus enabling a real-time deduction of the ongoing reaction process. Different analytical strategies were explored in our work: Raman signatures of 4-NBM SAMs were acquired on single sample spots or averaged over larger areas, either at fixed potentials or under polarization ramps, and in different pH conditions (which, as for 4-NTP [206], are expected to influence the kinetics of the nitro groups electroreduction). The ultimate aim of these investigations consisted in capturing the possible reaction intermediates, in order to get a better understanding of electrochemical reduction mechanism of nitrobenzene derivatives. Additionally, the obtained results can yield information about the surface reactivity (e.g. in terms of homogeneity in the current density distribution) and the influence of the probe on the studied process (i.e. the occurrence of photo- or hot-electron-induced processes).

To summarize, in the following paragraphs we will first investigate the 4-NBM SAM reduction mechanism *ex situ*, at two different solution pH, so that to compare the reactivity of this sample to the results obtained on 4-NTP. Later on, we will discuss about the technical

issues that needed to be overcome in order to perform dynamic electrochemical investigations while recording STM-TERS maps, with the aim of detecting in real time the ongoing chemical transformation on the sample under polarization. Finally, the results obtained by EC-TERS will be presented and, based on them, a hypothesis for the reduction mechanism of 4-NBM SAM in the employed working conditions will be proposed.

3.2. 4-NBM as model system

3.2.1 SAM sample preparation

4-nitrobenzyl mercaptan (4-NBM) powder was obtained from Sigma-Aldrich and used without further purification to prepare a 10^{-4} mol.L^{-1} solution in absolute ethanol, purchased from VWR. This solution was employed to functionalize both the gold disk electrodes (for the preliminary electrochemical analysis) and the gold plates (for EC-STM-TERS measurements). Before use, the gold disk electrode surface (OrigaLys, 3 mm diameter) was first polished on a polishing disk covered in 0.1 µm diamond paste, and then sonicated in acetone and in ethanol (180s each). A final cleaning step consisted in applying three voltammetric cycles from -100 to +1500 mV *vs* SCE at 50mV.s^{-1} in a 0.5 mol.L^{-1} solution of H_2SO_4 [211]. As it can be seen in **Figure 3.1**, this provokes the subsequent formation and dissolution of gold oxides on the surface, thus reconstructing the original Au(111) surface. Moreover, blanks were performed on the electrode before functionalizing it to insure that no residual molecules were left adsorbed on the surface.

The gold plates were prepared by high-vacuum thermal evaporation of a 100-nm gold layer on a mica substrate. The evaporation was preceded by 1-hour heating at 430 °C and followed by 2-hour annealing at the same temperature. In order to insure the homogeneity of the mica surface before depositing the gold layer, the most superficial layer was peeled-off prior to the insertion in the evaporation chamber. The so-obtained gold plates do not show any SERS effect and their root mean square roughness, evaluated *via* AFM, is in the order of hundreds of pm (see **Figure 4.8**a in Chapter 4).

The deposition of 4-NBM was achieved by incubation of the desired gold surface in the 10^{-4} mol.L^{-1} solution and lasted 10-15 minutes for disk electrodes and a few hours (up to overnight) for the plates. Afterwards, the surfaces were incubated again in absolute ethanol for 5 or 30 minutes (in the case of disk electrodes or plates, respectively), in order to remove the physisorbed species, and finally dried under an argon stream.

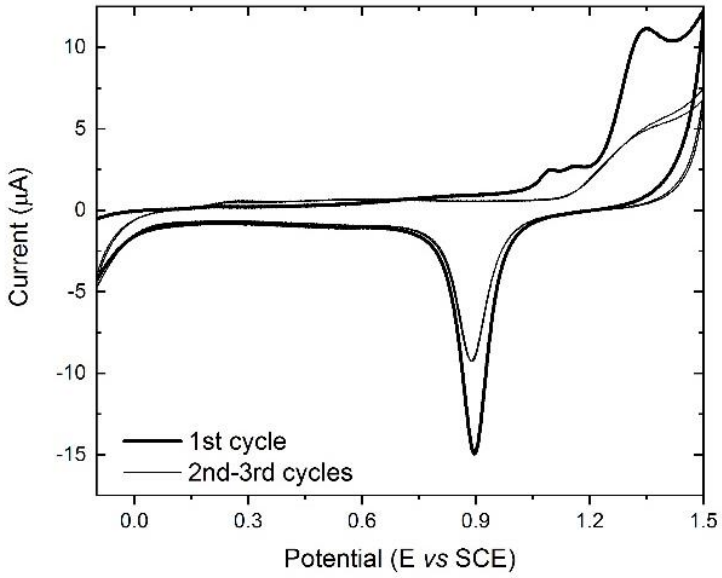

Figure 3.1. Surface reconstruction of a gold disk electrode – Gold electrodes were subjected to repeated potential scans in acidic medium (cyclic voltammetry CVs) from -100 to +1500 mV *vs* SCE (scan rate 50 $mV.s^{-1}$, supporting electrolyte 0.5 $mol.L^{-1}$ H_2SO_4, reference electrode Saturated Calomel Electrode SCE).

The *ex situ* electrochemical measurements were carried out on three different potentiostats: an Autolab PGSTAT100N (Metrohm), a Gamry 600+ (Gamry Instruments) or a CHI 600 E (CH Instruments). Unless where specified, all the potentials reported in the next paragraphs are referred to an Ag/AgCl electrode (with a saturated KCl solution, $E°_{Ag/AgCl}$ = +197 mV *vs* SHE at 293 K)

3.2.2 Electrochemical measurements

Cyclic voltammetry (CV) experiments were performed on 4-NBM SAM adsorbed on gold disk electrodes, in order to study *ex situ* the transformation of the nitro group under polarization. The same experiments had been previously carried out also on 4-NTP [206], which was probed in a 50 $mmol.L^{-1}$ H_2SO_4 solution: as **Figure 3.2** illustrates, during the first voltammetric cycle the current dropped abruptly in the forward scan, then gave rise to an anodic peak in the backward scan. The voltammetric reduction peak at around -250 mV *vs* SCE had been attributed to the total, irreversible reduction of the nitro into the amine function, thus to the formation of 4-aminothiophenol (4-ATP), in a global 6-proton/6-electron step.

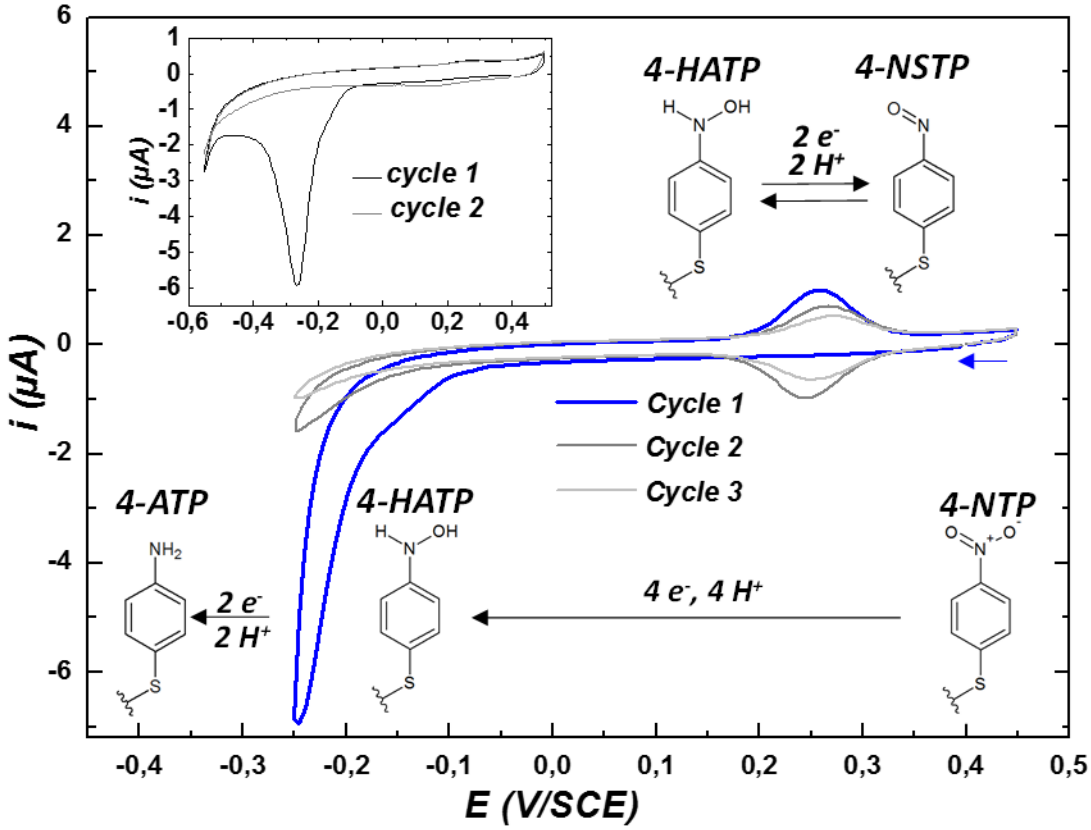

Figure 3.2. Electrochemical reduction of a 4-NTP in acidic medium – A 4-NTP functionalized gold sphere electrode was subjected to cyclic voltammetry (CV) in a 50 mM H_2SO_4 solution (scan rate: 100 mV s^{-1}) with a -250 mV vs SCE vertex potential. 4-NTP is partially reduced to 4-hydroxylamine thiophenol (4-HATP) below -100 mV vs SCE. 4-HATP is reversibly oxidized into 4-nitrosothiophenol (NSTP) at +241 mV vs SCE. **Insert:** full irreversible reduction of 4-NTP into 4-ATP at potential as low as -600 mV vs SCE. Reproduced from [206].

However, if the potential excursion was not negative enough, this reaction did not transform all the 4-NTP molecules adsorbed on the surface: some of them only underwent a partial reduction into 4-hydroxylamino-thiophenol (4-HATP), through an overall 4-proton/4-electron mechanism. In fact, the process should be divided in two successive 2-proton/2-electron steps, involving 4-nitrosothiophenol (4-NSTP) as intermediate species. Nevertheless, because the reduction potential of 4-NSTP is more positive than the one of 4-NTP [204], not only the cathodic wave of the 4-NTP→4-NSTP was not observed, but 4-NSTP transformed also right away into 4-HATP. Since this transformation is reversible, the part of NHOH groups that did not reduce completely could oxidize back to NO, which explains the presence of the anodic peak in the backward scan. When performing several voltammetric cycles, all the 4-HATP molecules eventually converted into 4-ATP: this can be deduced by the progressive lowering in intensity of the anodic peak as the number of scan increased (dark and light grey curves in **Figure 3.2**).

In our experiments, we chose to perform the characterization in the same acid medium, so that to compare the reactivity of 4-NBM with 4-NTP, but also in a basic environment. Since the nitrobenzene reduction mechanism is pH-dependent, it is expected to be less thermodynamically favoured when the medium alkalinity increases, and also its kinetics might be affected [212]. However, 0.1 mol.L^{-1} solutions of electrolytes as NaOH [208] or KOH [213], usually employed for characterizing nitrobenzene reactivity, have a pH of around 13 that is not compatible with the experimental setup for EC-TERS. Such a basic solution could in fact corrode the immersion objective and seriously damage the piezo-sensor stage in case of leakage. As a consequence, it was preferred to perform the analysis in a bicarbonate buffer, obtained by mixing 100 mL of 0.05 mol.L^{-1} $NaHCO_3$ (NORMAPUR®) with 40.4 mL of 0.1 mol.L^{-1} NaOH (Carlo Erba). The pH of the resulting solution was verified by mean of a pH-meter and yielded a value of 10.7, which should guarantee the protection of the opto-mechanical setup. Moreover, thanks to the presence of the conjugated acid/base species, this solution should contain enough ionic species to avoid current flow limitations due to charge migration issues. This could not be the case if the same pH should have been reached by dilution of stronger bases.

Figure 3.3 shows cyclic voltammetry (CV) experiments, carried out in acid and alkaline media, on 4-NBM- functionalized gold disks electrodes. Note that the species illustrated in both **Figure 3.2** and **Figure 3.3** have the same functional groups, while the thiolate part is different: TP stands for thiophenol (Ar-S-) while BM for benzyl mercaptan (Ar-CH_2-S-). During the forward scan of the first cycle, a cathodic peak arises (at -723 mV at pH 11, -299 mV at pH 1), followed by an anodic peak in the backward scan (at -229 mV at pH 11, +297 mV at pH 1). A second, smaller cathodic peak appears then in the forward scan of the second cycle, almost at the same position of the anodic peak (-255 mV at pH 11, +272 mV at pH 1). The backward scan of the second cycle shows again the anodic peak, though weaker in intensity. This result resembles to some extent to what observed for 4-NTP in acid medium [206] (**Figure 3.2**), hence the main cathodic peak (corresponding to the current drop in the 4-NTP CV) should arise from the irreversible reduction of 4-NBM into the reaction intermediates (partial reduction) or into 4-ABM (total reduction).

The presence of the anodic/cathodic couple at higher potentials attests instead of the reversible 4-HABM↔4-NSBM transformation (2-proton/2-electron) [71,206]. As it was observed for 4-NTP [206], also in this case the anodic peak decreases in intensity after the first cycle,

meaning that part of the 4-HABM formed during the first cycle has been irreversibly reduced during the second one. CV analysis on monolayers can also be useful to evaluate the molecular surface coverage on the electrode surface [71], as it will be explained in the next paragraph.

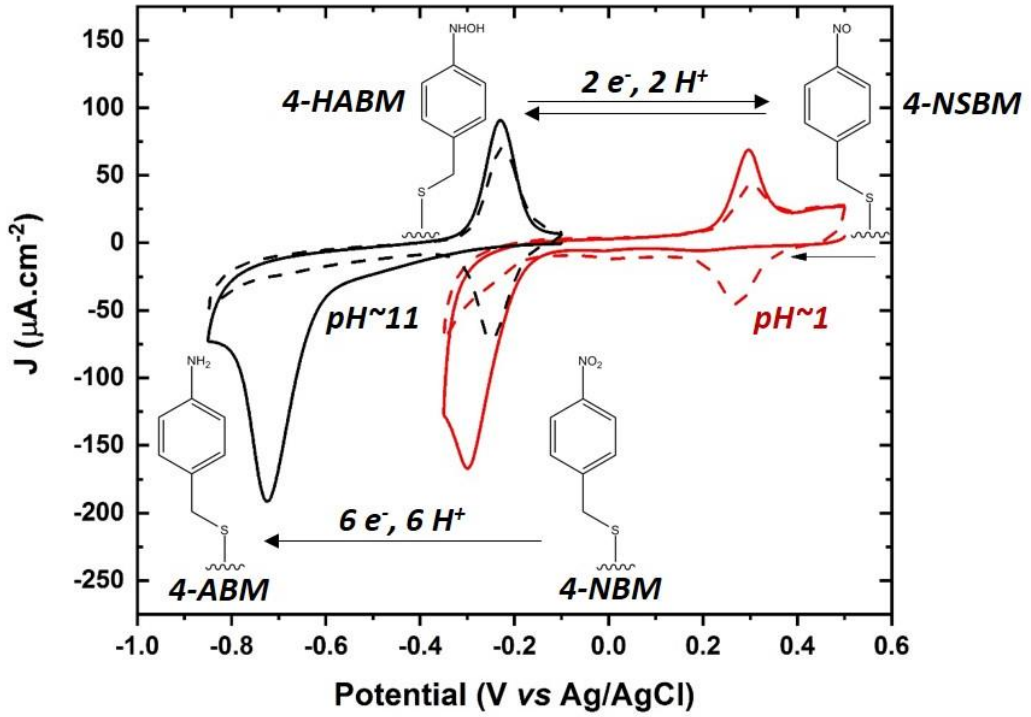

Figure 3.3. Influence of the pH on the electrochemical response of 4-NBM - CV acquired on 4-NBM adsorbed on a gold disk electrode (Ø = 1.5 mm). The supporting electrolyte consisted in a bicarbonate buffer solution (black curve, scan range -100/-850 mV) or in a 50 mmol.L^{-1} H_2SO_4 solution (red curve, scan range +500/-350 mV). The solid and the dotted lines represent the first and the second cycles, respectively. The scanning speed was v = 50 mV.s^{-1}.

Calculation of the surface molecular coverage* via *CV - Due to the high nitrobenzene reduction yields, it is possible to consider that all the NO_2 groups have been reduced (partially or totally) at the end of the first forward scan. This means that the total amount of NO_2 groups present on the surface before the potential ramp can be deduced from the charge Q_{red} integrated from the cathodic peak. This charge can be expressed as the sum of two contributions:

$$Q_{red} = Q_{4-HABM} + Q_{4-ABM} \quad (3.1)$$

where Q_{4-HABM} and Q_{4-ABM} are the charges associated, respectively, to the 4-proton/4-electron reduction into 4-HABM and 6-proton/6-electron reduction into 4-ABM. In order to quantify the relative contributions of the two charges to the total integration of the reduction peak, it is assumed that all the 4-HABM formed at low potentials re-oxidizes completely into 4-NSBM during the backward scan, through a 2-proton/2-electron exchange. Therefore, the charge Q_{ox} integrated from the anodic peak can be expressed as:

$$Q_{ox} = Q_{4-NSBM} = \frac{Q_{4-HABM}}{2} \quad (3.2)$$

where Q_{4-NSBM} is the charge associated to the 4-HABM→4-NSBM oxidation and therefore corresponds to half of the charge needed to reduce 4-NBM into 4-HABM. By substitution of the Equation (3.2) in the Equation (3.1), it is obtained:

$$Q_{red} = Q_{4-ABM} + 2Q_{ox}; Q_{4-ABM} = Q_{red} - 2Q_{ox} \quad (3.3)$$

Now, the surface coverage Γ is expressed as the number of moles of adsorbate per unit of surface. Because the total number of reacting adsorbates can be retrieved from the charge of Q_{red}, it is possible to express Γ as:

$$\Gamma = \frac{Q_{red}}{nFS} \quad (3.4)$$

where n is the number of electrons involved in the reaction, F is the Faraday constant (~96500 C.mol^{-1}) and S is the electrode surface (in cm^{-2}). Equation (3.4) can be rearranged by taking into account Equations (3.1) and (3.3), and by introducing the effective number of electrons involved in the two reduction processes of 4-NBM:

$$\Gamma = \frac{1}{FS}\left(\frac{Q_{4-ABM}}{6} + \frac{Q_{4-HABM}}{4}\right) = \frac{1}{FS}\left(\frac{Q_{4-ABM}}{6} + \frac{2Q_{ox}}{4}\right) = \frac{1}{FS}\left(\frac{Q_{4-ABM}+3Q_{ox}}{6}\right) = \frac{1}{FS}\left(\frac{Q_{red}+Q_{ox}}{6}\right) \quad (3.5)$$

In conclusion, Equation (3.5) allows calculating the nitrobenzene surface coverage from the integrated areas of the first cathodic and anodic peaks.

Since the potential excursion is not negative enough at pH 1, the surface coverage was estimated only from the CV at pH 11 in **Figure 3.3** and yielded a value of $7.06 \cdot 10^{-10}$ mol.cm^{-2}. This result is consistent with the data reported for both 4-NTP [125] and 4-NBD [71] monolayers and confirms, along with the symmetrical bell shape of the peaks in the voltammograms, that the 4-NBM is well anchored on the gold surface in an ordered monolayer. As for the slight slope in the voltammogram background, it is most likely due to the presence of residual oxygen in the electrolyte solution, despite thorough deoxygenation by Ar bubbling before performing the electrochemical characterization.

3.3. EC-STM-TERS: real-time following of the reduction mechanism

3.3.1 EC-TERS experimental conditions

In situ measurements on 4-NBM-functionalized gold plates were performed on the novel EC-STM-TERS setup described in Section 2.4.2. Before starting the analysis, the sample is mounted on the sample stage, fixed with the PEEK electrochemical cell (which also hosted the counter-electrode) and accommodated in the AIST *Omegascope* setup along with the Ag/AgCl reference. The three electrodes are connected to the homemade bi-potentiostat, controlled in turn by the function generator. Then, the electrolyte buffer, previously deoxygenated by Ar bubbling for at least fifteen minutes, is poured in the cell volume. Finally, the tip is introduced inside the cell and its position adjusted at the centre of the 40x immersion optical objective. The sample vertical position is first adjusted manually in order to bring the surface as close as possible to the tip apex. Therefore, the bi-potentiostat is switched on to maintain a 0.1 V BV between the two working electrodes while controlling their respective potential versus the reference electrode. If the tip is properly coated with the *Zapon* varnish, the noise level remains below 100 pA, which is negligible respect to the set-point tunnelling current threshold (i.e. I_T = 1000 pA). This allows the piezo scanner performing precisely the final approach between the tip and the sample, until the tunnelling conditions are reached. EC-TERS measurements have been performed during extended time (for 3-4 hours), scanning the tip potential as high as +470 and as low as -400 mV (see Chapter 4), without noticing any instability in the current value recorded on it. This proves the resistance of the *Zapon* coating under the experimental conditions of electrolyte pH, BV and I_T. It occurred that a few already-used tips could still be employed for other measurement sessions without any current instability issues. However, more often the noise recorded on the tip current had substantially increased from one day to another. In this case, covering the tip with another *Zapon* layer was usually sufficient to re-establish a uniform insulating coating prior to use.

As described earlier in Chapter 2, it was first tested in our experimental setup the possibility of keeping a constant BV value of 0.1 V while decreasing the respective potentials of the tip and the sample. However, important current oscillations were recorded on the tip (retracted from the sample) when it was polarized below -400 mV, thus making the landing on the sample surface impossible. It was then tested the possibility to perform a potential ramp on the tip (down to -600 mV, at 50 $mV.s^{-1}$) while it was already in the landing position; also in

this case, though, when reaching a potential of around -400 mV the tip automatically retracted from the sample and the current dropped to 0. It was therefore chosen to keep the tip at 0 V and modifying only the sample potential, in a variable range from -0.1 to -1 V (see example in **Figure 4.15**), either by chronoamperometric steps or by cyclic ramps. By doing so, no dramatic changes were observed on the noise level of the tip current, neither when it was retracted nor when it landed on the sample. Moreover, with tips for which the hot spot could be clearly identified at the beginning of the experiment, the TER signal was always observed, even at low potentials.

3.3.2 Mapping at fixed potential

Before proceeding to the reduction of the 4-NBM SAM, its distribution on the sample surface was mapped by STM-TERS while keeping a fixed polarization of 0 V on the tip and -100 mV on the sample (BV = 0.1 V). No transformations are expected to occur on 4-NBM at -100 mV, since this value is close to the system open circuit potential (OCP). After performing a first map, the sample was subjected to a reductive potential ramp from -100 to -850 mV and back (BV ranging from 0.10 to 0.85 V), at the end of which another STM-TERS mapping at the OCP was recorded. Finally, the sample was brought at -400 mV (BV = 0.4 V) and imaged again; as it is shown in **Figure 3.3**, at this potential value 4-NSBM is expected to have reconverted into 4-HABM. The spectra averaged over all the pixels of the TERS maps are shown in **Figure 3.4**a (corresponding maps in **Figure 3.5**); besides, in order to help the spectral features attribution, μRaman spectra were acquired on the powders of 4-NBM and of a few compounds bearing the same functional groups as the expected intermediates, i.e. nitrosobenzene (TCI), N-phenylhydroxylamine, 4-ATP and azobenzene (Sigma-Aldrich) and reported in **Figure 3.4**b. Raman signatures of adsorbed species and of reference samples (powders), are reported in Table 3**.1** at the end of this section, together with the mean spectral feature assignment (vibration modes) found in the literature.

Before reduction (**Figure 3.4**a, top), the average spectrum recorded on the whole imaged area matches with the one observed for the 4-NBM powder (**Figure 3.4**b, top): the characteristic signature is represented by the symmetric NO_2 stretching, which falls at 1346 cm^{-1} (1352 cm^{-1} in the powder). Other remarkable features are the CH bending at 1107 cm^{-1} (1110 cm^{-1} in the powder) and the ring stretching at 1594 cm^{-1} (1600 cm^{-1}); however, as all the compounds involved in the reaction possess a benzene ring, these bands are present in all the

spectra, even though more or less shifted in frequency, so they are less useful for the unequivocal compound characterization.

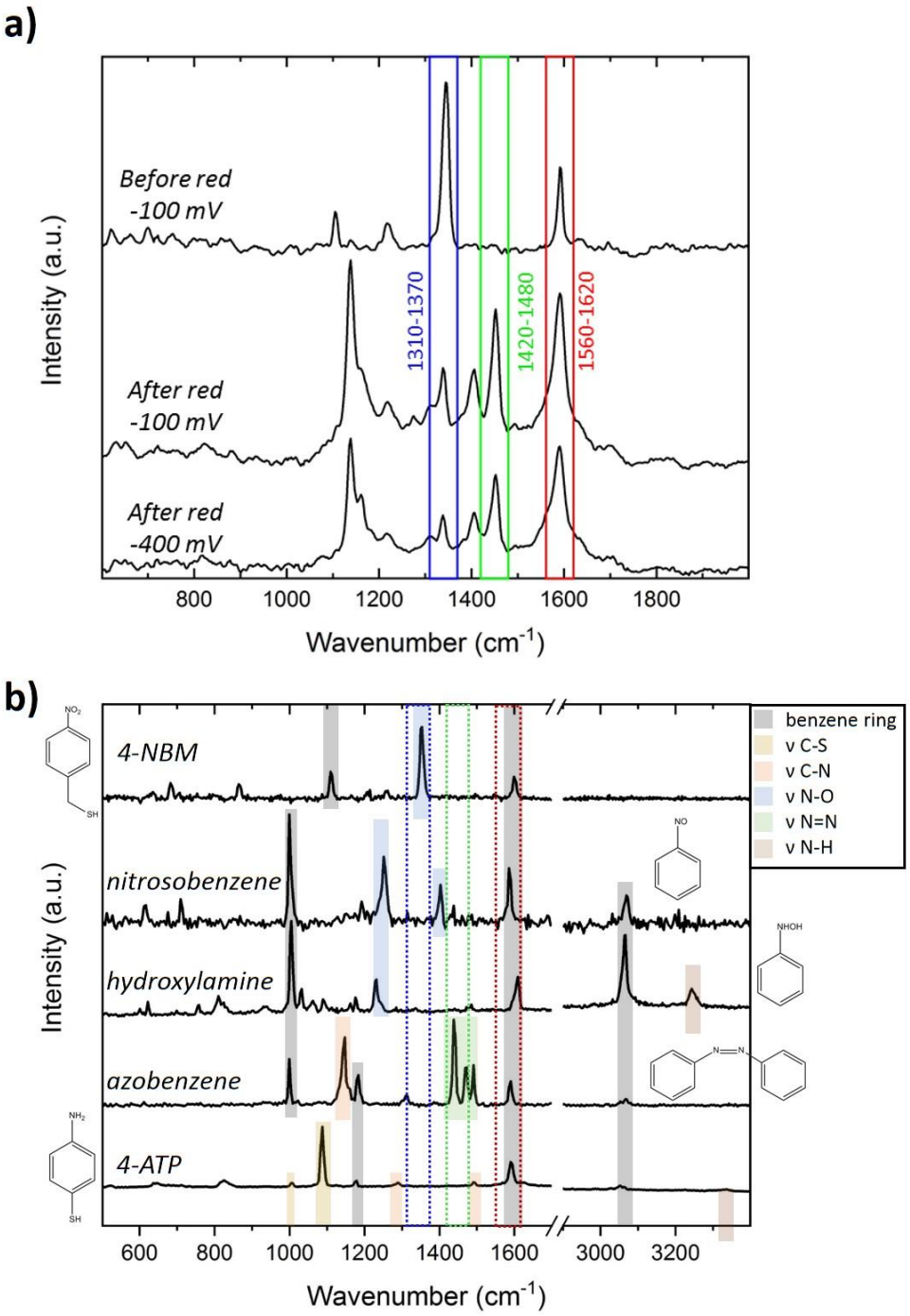

Figure 3.4. TERS signatures upon reduction of 4-NBM in alkaline medium and comparison to the Raman signature of benzene derivative analogues - a) TERS spectra obtained by integration of all the pixels for each TERS map recorded *in situ* and presented in **Figure 3.5**. **b)** From top to bottom: confocal Raman spectra of powder samples of 4-NBM (λ_{exc} = 785 nm), nitrosobenzene (λ_{exc} = 632.8 nm), hydroxylamine (λ_{exc} = 532 nm), azobenzene (λ_{exc} = 632.8 nm) and 4-aminothiophenol (λ_{exc} = 632.8 nm). The legend indicates the position of the signature bands for each compound.

After reduction, the spectrum recorded at the OCP (**Figure 3.4**a, middle) shows that the ring stretching band keeps being quite intense, while the signal at 1346 cm^{-1} broadens, weakens and shows a new shoulder at 1343 cm^{-1}, suggesting the reduction of 4-NBM into 4-NSBM. This signature should indeed correspond to the band at 1403 cm^{-1} in the powder spectrum of nitrosobenzene in **Figure 3.4**b, which is attributed to the N-O stretching. Moreover, along with it, another weak feature appears at 1309 cm^{-1}, which should arise from the combination of CN stretching and ring modes in the totally reduced 4-ATP species (1288 cm^{-1} in the 4-ATP powder of **Figure 3.4**b). The presence of this product might be proved also by the appearance of a shoulder at 1165 cm^{-1}, corresponding to the CH bending (band at 1177 cm^{-1} in the 4-ATP powder). Overall, despite some local heterogeneities on the substrate might have inhibited the reduction process for few NO_2 groups, as it has already been observed [206], it is possible to consider that the majority of them converted in the reduction products. Additionally, new intense features appear at 1138, 1408 and 1452 cm^{-1}, which could match with the a_g-type bands of azobenzene (attributed to the C-N stretching and to the N=N stretching modes). The reason for the presence of this band will be further discussed in the next paragraphs.

The overall spectral look after reduction does not change significantly when sweeping the potential down to -400 mV (**Figure 3.4**a, bottom). However, the CV of **Figure 3.3** shows that at this potential the 4-NSBM is supposed to have reduced again into 4-HABM (reversible cathodic peak at -255 mV). Hence, since nitrosobenzene and hydroxylamine powder spectra show some dissimilarities (**Figure 3.4**b), it was expected also for the average spectra extracted from the maps at -100 and -400 mV to differ from each other. Recording *in situ* maps at fixed potential might therefore not be the more suitable method to capture intermediates and therefore solve the reaction mechanism of the adsorbed species.

Nonetheless, some information about the layer composition and the substrate reactivity can be retrieved already from static analyses. Let us look first at the TERS maps on the right column of **Figure 3.5**, which are obtained by integration and superposition of the bands intensities in the ranges of NO_2 stretching (blue), N=N stretching (green) and ring stretching (red), as shown in **Figure 3.4**a. The map on top, recorded before reduction, shows a majority of blue pixels, which are sparse over the whole surface, thus attesting of the uniform coverage of the gold substrate with the 4-NBM species. On the other hand, once subjected to reduction, the scanned area assumes an overall green coloration, while only few bright blue pixels remain:

this confirms again that almost all the NO_2 groups were irreversibly reduced and that transformation into reaction products has occurred.

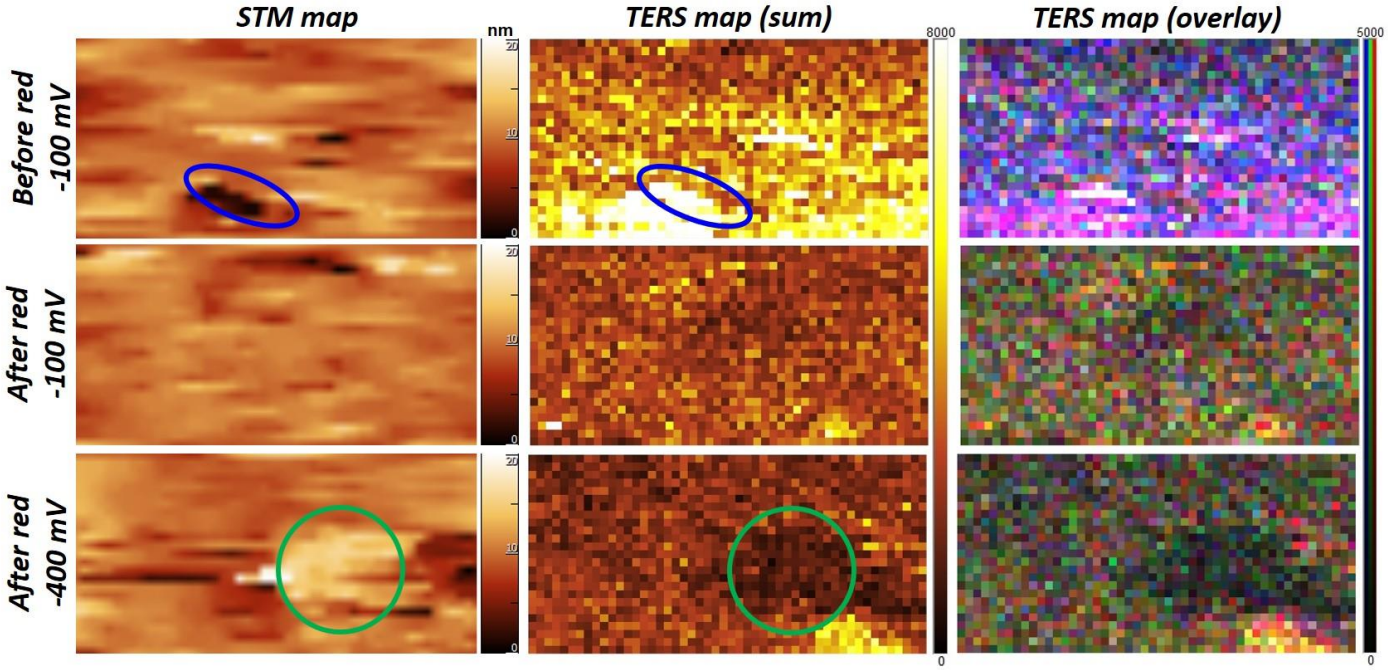

Figure 3.5. In situ TERS mapping in alkaline medium - STM-TERS maps acquired on 4-NBM before and after reduction at -100 mV (top and middle maps) and after reduction at -400 mV (bottom). The STM maps showed in the left column were acquired simultaneously to the TERS maps, presented in the other two columns, which are obtained by integration of the band energy ranges shown in (**Figure 3.4**b): the intensity of the three ranges is summed in the middle column (to show the overall molecular distribution) and superposed in the right column (to show the distribution of the predominant species among the pixels. The colored bars indicate the height (nm) and the intensity (arbitrary units) scales in the STM and TERS maps, respectively. All the maps were acquired on 200x100 nm^2 areas with 50x25 pixels, each one corresponding to a single Raman spectrum, acquired in 0.5 s with 250 µW power(1.56% of the nominal laser power) of the 632.8 nm laser line (BV = 0.1 V, I_T = 1 nA). The STM maps were treated with the AIST software tool. The areas encircled in blue and in green identify, respectively, a terrace edge and a flat protuberance.

The maps on the middle column of **Figure 3.5** result instead from the sum of the intensities recorded in the three above-mentioned ranges, with the aim of observing variations in the total TER signal over the scanned surface. These can be compared also to the correspondent STM maps (on the left column of **Figure 3.5**), which were recorded simultaneously to the TERS maps and report the height profiles over the scanned area. Each pixel in the maps has a dimension of 4 nm, which is quite high respect to the usual resolution achieved by STM. As a consequence, the cartographies only show a blurred image of the substrate, where the gold terraces are just hinted and no clear presence of molecular layers is noticed. In fact, the molecular layers were not observed either when performing STM alone (at better spatial resolution) on functionalized-substrates (see **Figure 2.15**c). Nevertheless, it is possible to remark that the TERS intensity trends seem following the height profiles: the bright

zones correspond to terraces edges in the STM maps (e.g. in the areas encircled in blue in **Figure 3.5**), because these curved surfaces have a higher effective area for adsorption and can therefore host a higher number of molecules, or else enhance more strongly the local electric field [214]. Oppositely, flat protuberances correspond in the TERS map to darker zones (as in the zone identified by the green circle in **Figure 3.5**). Loss of signal on these terraces could be explained by less efficient topography tracking by STM, or partial gold oxidation leading to partial desorption of the mercaptan species [215] or to possible temporary loss of "gap mode" enhancement.

Table 3.1. Attributions of the main bands observed in the TERS (adsorbates) and μRaman (powder) spectra of the compounds involved in the 4-nitrobenzene reduction mechanism. Intensities: *vs* (very strong), *s* (strong), *m* (medium) and *w* (weak).

Attribution	**$\tilde{\nu}$ –TERS (cm^{-1}) – adsorbates**	**$\tilde{\nu}$ – μRaman (cm^{-1}) – powders**	**References**
Nitrobenzene			
δ (C-H)	1107 *w* (1098 *w*)	1110 *m* (1108 *m*)	[204,208]
CH_2 wag. + ring stretching	1220 *w* (1222 *s*)	1220 *w* (1222 *s*)	[216]
ν $(N\text{-}O)_{sym}$	1346 *vs* (1339 *vs*)	1352 *vs* (1346 *vs*)	[204,208]
Ring stretching	1594 *s* (1586 *s*)	1600 *s* (1586 *s*)	[204,208]
Monomers			
δ (C-H)	1165 *m*, 1504 *w* (1170 *w*, 1494 *w* amino)	1001 *vs* (1002 *vs* nitroso) 1005 *s* (996 *m* hydroxylamine) 1177 *w* (1178 *w* amino)	[125,208,216]
ν (C-S) + ring modes	-	1006 *w*, 1087 *vs* (1002 *w*, 1076 *vs* amino)	[216]
ν (C-N) + ring modes	1309 *w* ?	1288 *w*, 1493 *w* (1284 *w*, 1484 *w* amino)	[208,216]
ν (N-O)	1343 *m* ? (1332 *m* nitroso)	1252 *m* + 1403 *m* (1265 *s* + 1407 *m* nitroso) 1230 *m* (1230 hydroxylamine)	[125,208,217]
Ring stretching	1592 *s* (1589 *s* nitroso, 1585 *s* hydroxylamine, 1595 *s* amino)	1587 *s* (1593 *s* nitroso) 1606 *m* (1585 *m* hydroxylamine) 1591 *s* (1588 *s* amino)	[208,216]
ν (C-H)	-	3067 *w* (nitroso) 3020 *s* (hydroxylamine) 3054 *w* (3055 *s*)	[218]
ν (N-H)	-	3244 *w* (hydroxylamine) 3336 *w* (3355 *m* amine)	[218]

Dimers			
δ (C-H)	-	1000 *m*, 1183 *m* (1002 *s*,1182 *m* azobenzene)	[208,219]
ν (C-N) + ring modes	1138 *s* (1144 *s* azoxybenzene, 1146 *s* azobenzene)	1146 *s* (1147 *s* azobenzene)	[208,219]
ν (N=N) + ring modes	1408 *m*, 1452 *s* (1388 *m*, 1424 *s*, 1463 *w* azobenzene)	1439 *vs*, 1471 *m*, 1491 *m* (1440 *vs*, 1472 *m*, 1492 *m* azobenzene)	[208,219]
Ring stretching	1578 *m* (1590 *m* azoxybenzene, 1592 *m* azobenzene)	1589 *m* (1590 *m* azobenzene)	[208,219]

These results manifest the utility of STM-TERS not only as mere spectroscopic technique, but also as highly sensitive tool for structural investigations. However, there are still some questions that could not be properly answered by fixed-potential space maps: why no evident spectral changes occur when polarizing negatively after reduction? And what is the origin of azobenzene bands? Time-resolved EC-TERS investigations are expected to provide answers to these interrogatives, which will be discussed in the next paragraphs.

3.3.3 Deciphering of the reaction mechanism by real-time TERS

3.3.3.1. Hypotheses for the reaction mechanism

First and second hypotheses: mono* vs *bimolecular paths. In Section 3.2.2 we proposed a reduction mechanism for nitrobenzene derivatives that is summarized by the black path shown in **Figure 3.6**. Since all the reaction steps involve the presence of protons, it is expected that performing the reduction in acid or even neutral media leads quite fast and directly towards the final amino product, following a first-order reaction path, as it has been previously observed [206].

However, **Figure 3.6** shows also a bimolecular path, in blue, that involves the condensation of adjacent NHOH and NO groups into a dimeric species, the 4,4'-dimercapto-azoxybenzene (DMAOB), which reduces irreversibly into 4,4'-dimercaptoazobenzene (DMAB). This, in turn, can convert reversibly into 4,4'-dimercaptohydrazobenzene (DMHAB), its "open" form, which finally splits into two amino monomers. All these processes follow a 2-proton/2-electron reaction scheme. It was observed that this bimolecular mechanism mostly occurs in alkaline media, where the nitrosyl group becomes strongly electrophilic [204]

and therefore promotes the coupling with hydroxylamine and the formation of DMAOB. An *in situ* study on the two different reaction mechanisms was carried out already in 1988 by Gao *et al.* [208]. In this work, the electrochemical and spectral signatures of nitrobenzene (initially in solution) were observed upon its adsorption (irreversible or not) onto a roughened gold rotating disk electrodes, either in acid or in basic media. In both conditions, the application of negative potential values led to a progressive disappearance of the NO_2 band and the appearance of NO spectral features. However, only in alkaline environment the backward scan showed the appearance of additional bands, attributed to the azoxybenzene and/or the azobenzene groups. Nonetheless, these were observed only for solution-phase experiments, whereas they were very weak or invisible in case of irreversibly adsorbed nitrobenzene. No characteristic electrochemical peaks were observed in the voltammograms either for adsorbed nitrobenzene, except for the cathodic wave of the total reduction of nitro into amine.

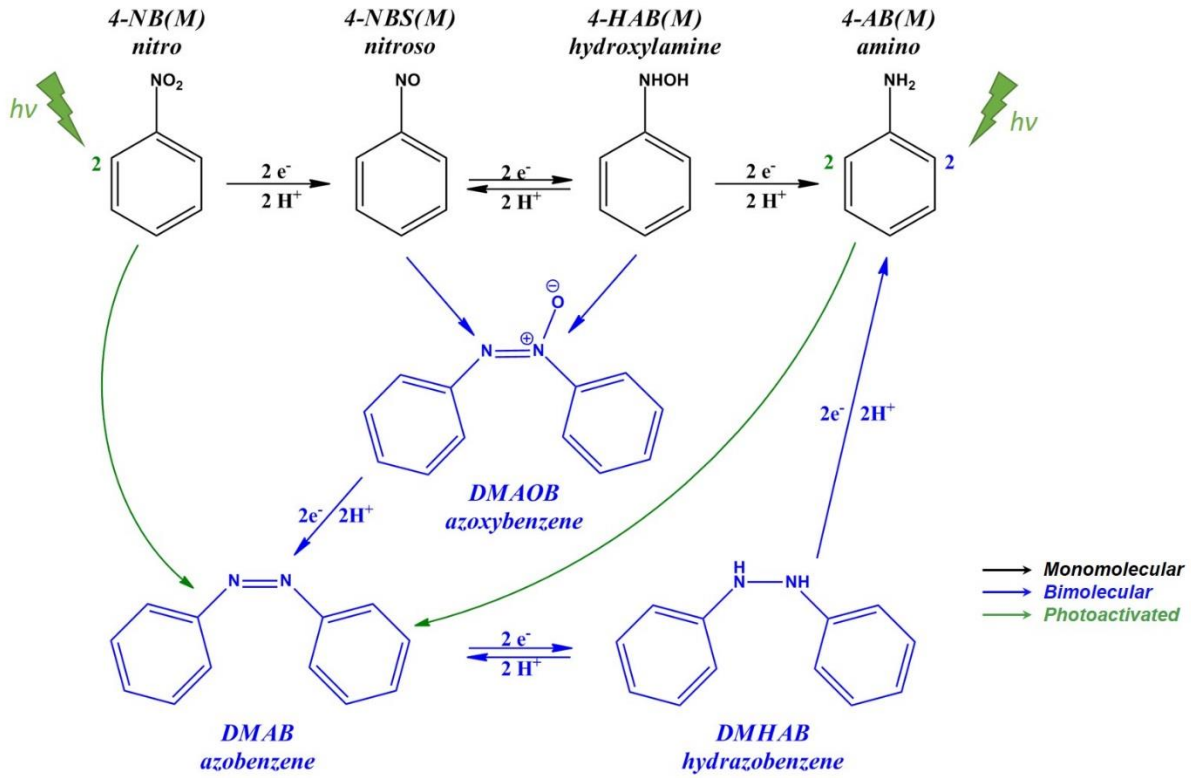

Figure 3.6. Possible reaction mechanisms involving nitrobenzene derivatives: first-order/monomolecular (black), second-order/bimolecular (blue) and photoactivated (green).

Third hypothesis: photochemical effect. The analogies among Gao's observations and our own results would suggest that our experimental conditions favour the occurrence of the second-order mechanism. However, a third hypothetic reaction path (shown in green in **Figure 3.6**) has been recently proposed by Zhao *et al.* [204]. In their work, they developed a metallic cluster model for DFT calculations that allowed investigating the thermodynamics and kinetics

of 4-NTP reduction on gold and silver, and comparing the SERS with the SEIRA (surface-enhanced infrared adsorption) spectra simulated on the reduction products. According to their results, while the electro-reduction of 4-NTP proceeds fully towards 4-ATP under IR irradiation, illumination *via* visible light (employed in Raman analyses) seems to play an important role in the formation of dimeric products. On silver, this can occur by direct photo-reduction (or photoxidation) of adjacent 4-NTP (or 4-ATP) molecules, since the illumination of the surface promotes the metal-to-molecule (or molecule-to-metal) charge transfer. However, gold surfaces have been reported to promote less efficiently these reactions [210,220]. Only gold sols, which have higher surface areas respect to flat substrates and limit the plasmons propagation decay (thanks to the presence of several hot sites for LSPR) showed some important catalytic effects upon irradiation with a 632.8 nm source [210].

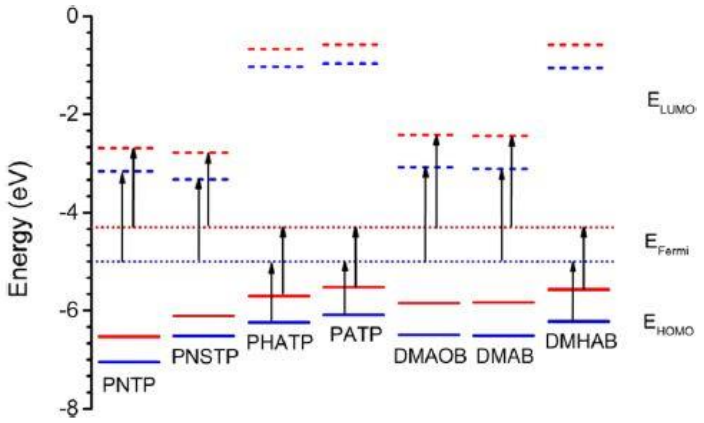

Figure 3.7. Energy diagram of photo-induced CT transitions of 4-NTP on gold and silver within visible light irradiation. Blue and red lines represent the electronic state on gold and silver, respectively. Solid and dashed lines are the HOMOs and LUMOs of the surface complexes. Dotted lines are the metal Fermi levels. Reproduced from [204].

Nonetheless, Zhao's calculations of the metal-to-molecule charge-transfer transition energies (summarized in **Figure 3.7**) predict that photo-induced reduction of 4-NTP adsorbates (into 4-NSTP and, later on, into 4-HATP) should actually be thermodynamically favoured on gold surfaces illuminated by visible light. Therefore, since the LUMO of 4-HATP is too high in energy and would require excitation wavelengths in the ultraviolet range in order to reduce to 4-ATP, 4-HATP might tend to accumulate on the surface and react with 4-NSTP to yield DMAOB [204]. Also DMAOB and DMAB can be photo-chemically reduced, while the LUMO of DMHAB is too high for it to convert into 4-ATP under light irradiation. This means that these specific reaction intermediates could form even without any electrochemical trigger. In our case dimerization may also be favoured by a larger flexibility provided by the addition CH_2 unit in 4-NBM compared to 4-NTP.

Azo or amino? Ambiguous bands attribution. The three presented mechanisms are susceptible to occur under specific conditions, i.e. using silver (possibly gold) SERS platforms, green (possibly red) irradiations and electrochemical polarisation; they might thus compete with each other and generate confusion over the real processes occurring in the studied system. This is the case especially for the bands arising from the C-N and N=N stretching modes, whose real origin of has been object of debates. Although for many years these bands have been unanimously attributed to the dimeric intermediates [208], a SERS study carried out by Kim *et al.* [221] on 4-ATP and DMAB adsorbed on gold (λ_{exc} = 633 nm) showed that the two compounds, when observed in alkaline media, have coincident spectral features that make them undistinguishable from one another. However, in acid media the situation is different: while DMAB shows still its characteristic features, in 4-ATP they progressively disappear as the pH decreases. This observation was explained considering the different nature of the vibrational modes from which such bands originate in the two compounds. In DMAB, they arise from total-symmetric a_g-type modes and correspond indeed to the C-N and to the N=N stretching vibrations of dimers. In 4-ATP, instead, they consists in b_2-type symmetry bands, arising from the $\pi \rightarrow \pi^*$ molecular transition ($^1A_1 \rightarrow {}^1B_1$) at 300 nm. This transition violates standard Raman selection rules, hence the b_2-mode cannot be detected by μRaman analyses on powder or liquid samples. However, upon adsorption on SERS-active substrates, a lift of the selection rules occur due to the different electron density distribution, and symmetry-forbidden transitions can be observed [221]. This ultimately allows the detection of the b_2-type mode bands, the intensity of which though will strictly depend on the sample polarization, on the excitation wavelength and especially on the medium pH. When the acidity increases too much (pH ≤ 4), the amino functionality is protonated, hence the gap between the highest and the lowest occupied molecular orbitals (HOMO and LUMO) becomes too wide for the transitions to be excited in the visible range [221] and the bands disappear.

Ultimately, in order to discern among the different reaction mechanisms and to recognize the origin of the recorded signals, static and dynamic analyses were performed on both 4-NBM and 4-ATP SAMs under different experimental conditions. Conclusions drawn from the comparison of the results allowed us elaborating a hypothesis for the overall reaction mechanism involving 4-NBM SAM.

3.3.3.2. Specific experimental conditions for time-resolved measurements

As it was for the acquisition of space maps at fixed potentials, also time-resolved spectral analyses were performed on the newly developed EC-STM-TERS setup. The only difference respect to previous experiments stands in the configuration of the function generator, delivering the potential sweep command to the bipotentiostat, which is triggered externally by the CCD camera. Thanks to this expedient, it is possible to synchronize the spectral acquisition time with the potential ramp, hence to observe the evolution in the spectral signature at each potential interval. For our measurements, a specific sequence was designed that consisted in: (i) a first chronoamperometric step at the highest voltage potential (= OCP); (ii) a cathodic ramp down to the lowest voltage potential; (iii) a first anodic ramp up to an intermediate potential (chosen in order to be placed just before the 4-HABM reconversion into 4-NSBM, see **Figure 3.2** and **Figure 3.3**); (iv) a second chronoamperometric step at the same intermediate potential; (v) a second anodic ramp back to the OCP; (vi) a final chronoamperometric step at the OCP. For the steps (ii), (iii) and (v), the total time of the ramp was adjusted in order for the potential to be scanned at a speed of 50 $mV.s^{-1}$. Since the spectrometer was set to record a spectrum per second, each spectrum recorded during those steps corresponded to a 50 mV potential variation.

The potentials values were adapted depending on the electrolyte chosen (see **Figure 3.3**) to perform the reduction, i.e. either the bicarbonate buffer (pH 10.7) or a 1 $mmol.L^{-1}$ solution of 96 % H_2SO_4 (Carlo Erba, final pH 2.7); in this case, using a less acidic electrolyte is necessary to avoid dramatic tunnelling current noises (due to gas evolution and large Faradaic currents) observed at lower pH values. Thanks to the open configuration of the cell, it was possible, when required, to change the electrolyte between measurements without losing the tip/laser optical alignment and, as a consequence, to redefine the tip hot-spot position that provides the highest TERS signal level using only slight displacements of the objective scanner. For these experiments, the cell was first emptied from the first electrolyte with a syringe, then it was filled/emptied twice with distilled water and gently dried, in order to remove the residues of the first electrolyte, and finally it was filled again with the second electrolyte.

3.3.3.3. Real-time spectral acquisition during potential ramp

In order to get closer insights into the reaction mechanism of the 4-NBM SAM, it was first chosen to acquire TERS time maps *during* the reductive ramp (from -100 to -850 mV, with the intermediate step at -400 mV), while scanning the sample surface under STM control. Thanks to the CCD camera/function generator synchronization, set as previously explained, each evolution in the spectral time map could be related to the corresponding applied potential, as shown in **Figure 3.8**a-b. The overall CV is illustrated in **Figure 3.8**c, while **Figure 3.8**d reports a few salient spectra and the values of polarization at the time of their acquisition.

Before starting the ramp (spectrum 1 of **Figure 3.8**e), the classic 4-NBM signature is observed, clearly recognizable from the NO_2 and ring stretching bands. This signature stays unaltered until around -550 mV, when the ring stretching broadens and a few bands start appearing in few zones below 1400 cm^{-1}. Then, at -700 mV, the NO_2 mode disappears completely, in correspondence with the peak of the cathodic wave on the CV. Going even lower in potential, at -800 mV, a sudden arise of intense signatures occurs in the energy range belonging to the bands of CH bending and CN stretching (1110-1200 cm^{-1} range), NO stretching (1300-1400 cm^{-1} range) and N=N stretching (1400-1500 cm^{-1}). The overall spectral intensity drops when ramping the potential towards the higher voltage, however the signal never disappears completely and the ring stretching band keeps staying sharp.

This indicates that the new bands arise from species that are well anchored to the gold substrate and that the studied system is unaffected by desorption phenomena. This also demonstrates that the tip-sample feedback current control is operative even for the high BV values reached during the negative scan (0.85 V at the lowest limit), as a TERS signal can still be observed. Moreover, the stronger TERS intensity recorded at highly negative polarisation could originate, as mentioned earlier, from the densification of the electrons at the tip-sample junction, resulting in an extra signal enhancement.

The new signatures, only hinted at low potentials, become sharper and more recognizable during the chronoamperometric step at -400 mV (spectrum 2 of **Figure 3.8**e). The overall spectral profile is then maintained almost unaltered during the final backward ramp and at the OCP (spectrum 3 of **Figure 3.8**e), albeit the CV shows a clear anodic current peak attributed earlier to the reconversion of 4-HABM into 4-NSBM. The appearance of a small intensity signature at 1277 cm^{-1}, which might arise from the NO stretching of either nitroso or azoxybenzene, could be the consequence of this oxidation reaction.

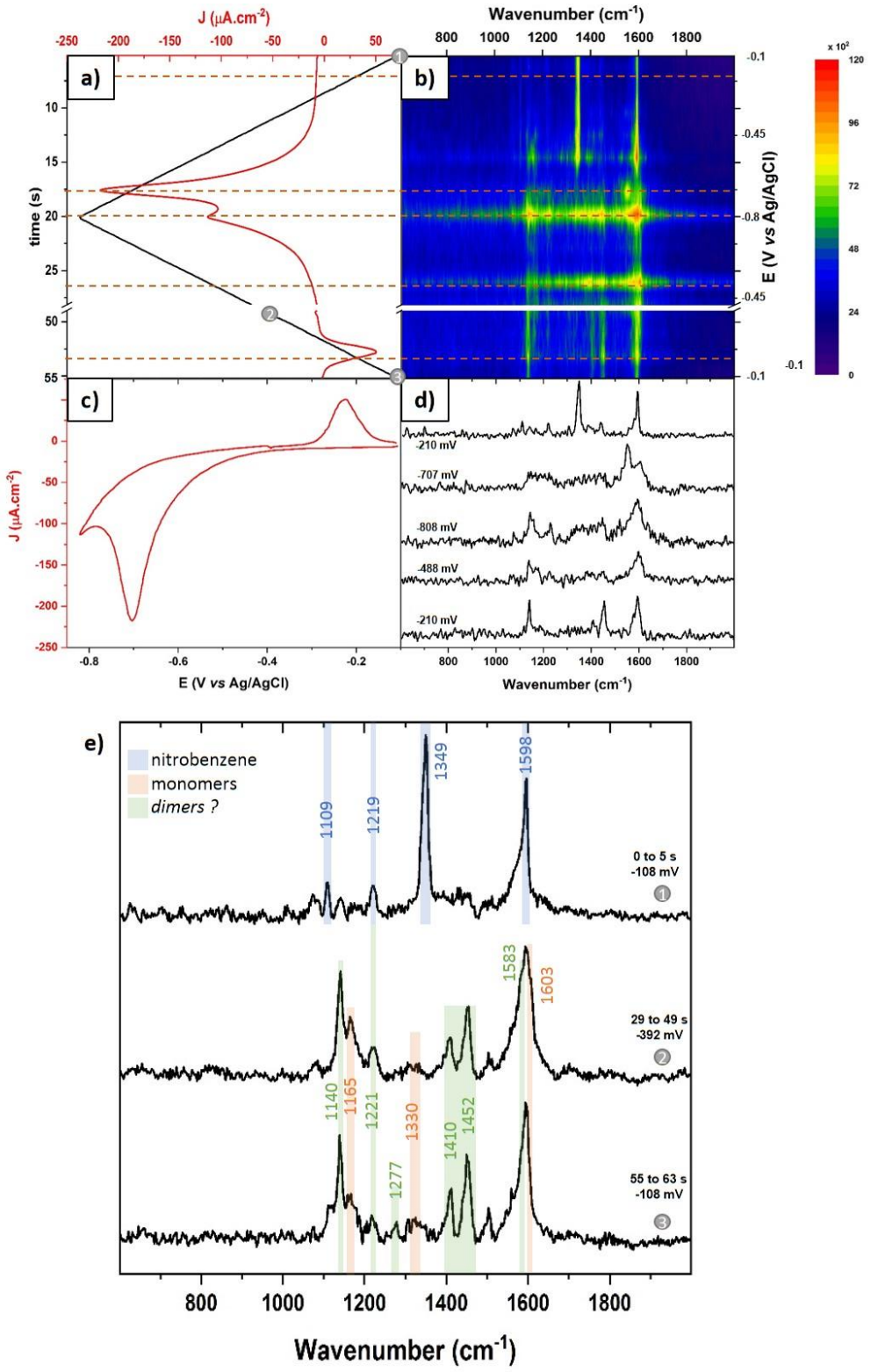

Figure 3.8. EC-STM-TERS measurement on 4-NBM SAM in alkaline medium: a) polarization sequence (three potential ramps), **b)** spectral signature dependence with the potential, **c)** resulting I-E curve (cyclic voltammogram), **d)** most significant spectra extracted from (b) at potential values marked by the red dotted lines in (b), **e)** averaged spectra from the chronoamperometric steps signalled in (a) by the grey dots. Each line on the map corresponds to a single Raman spectrum (acquired in 1 s with 160 μW power (1% of the nominal laser power) of the 632.8 nm laser line, BV variable, I_T = 1 nA) and to a 50 mV potential shift. The spectra have been subjected to background removal.

3.3.3.4. Origin of dimer bands

Although in the previous paragraph we associated some of the novel bands, evidenced in green in **Figure 3.8**e, to the CH stretching and the N=N modes of the azobenzene moiety, their definitive origin and unequivocal identification cannot yet be claimed. First, if these bands were to actually belong to azobenzene, this latter could be formed either through the "bimolecular" electrochemical path or through the photoactivated path (light-induced dimerization). Besides, these bands could originate in alkaline medium from surface-induced promotion of b_2-forbidden modes in the amino product as observed by Kim [221].

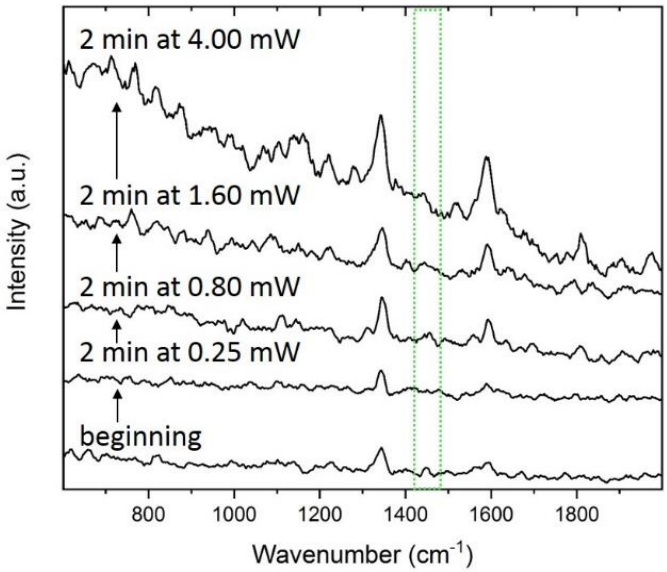

Figure 3.9. Influence of the Raman probe - STM-TER spectra acquired in the alkaline buffer after a 2-min irradiation of the sample using a red laser (632.8 nm) at increasing illuminating power (original source power increasing from 250 µW to 4 mW (1.56% to 25% of the nominal laser power), BV = 0.1 V, I_T = 1 nA). Each spectrum was acquired for 1 s and the tip was let scanning during the whole experiment. The spectra have been lightly smoothed, while the background was not removed. The green dotted lines identify the range where the "dimer" bands should be observed.

Assessment of photo-induced NO_2 dimerization. As it was previously mentioned, the occurrence of photochemical effects can be induced by the generation of "hot electrons" on the gold tip apex maintained in close vicinity to the molecular layer. In our experimental work, this phenomenon was minimized by carrying out the measurements at the minimum possible laser power (i.e. 160-250 µW max, 1-1.5% of the nominal laser power) and by constant raster scanning of the tip across the surface during the TERS acquisition (temporal mapping) synchronized to the potential ramp. Besides, the influence of the irradiation on the TERS response of the 4-NBM SAM at the tip-sample junction was evaluated. For that the Raman response of the functionalized substrate in the alkaline buffer was recorded at the OCP using

the 632.8 nm laser line at increasing laser power. As shown in **Figure 3.9**, even at the highest power (i.e. 4 mW) no dimeric bands can be detected, only an increase in the background noise can be observed. This suggests that the influence of photo-induced effects on the formation of the "dimers" signature observed by EC-TERS is minimal and, therefore, can be, if not neglected, considered secondarily in the interpretation of the reaction mechanism.

Exclusion of photo-induced NH_2 dimerization. Once ruled out the contribution of the photo-activated processes on the nitro groups' transformation, it was necessary to understand if the new intense bands that appeared upon reduction belong rather to the azobenzene dimer or to the amino product. In order to do that, EC-STM-TERS measurements were performed on an aminothiophenol (4-ATP) molecular layer self-assembled on a gold plate (according to the same procedure described for 4-NBM) and mounted in the EC-TERS cell filled with the bicarbonate buffer. Therefore, the composite ramp between -100 and -850 mV described previously was launched, while the TERS probe kept scanning the sample surface, in order to monitor the uniformity of the transformations over the whole scanned area, while minimizing photo-activated reactions. All the results are summarized in **Figure 3.10**.

As expected, no characteristic electrochemical features are observed in the voltammogram, as 4-ATP is the end reduction product of the irreversible nitrobenzene reduction path, therefore is not supposed to be furtherly reduced or re-oxidized in the potential range explored. The slight drop in current (**Figure 3.10**a) and the hysteresis in the backward scan at lower potentials (**Figure 3.10**c) is indeed attributed the slight electrolyte reduction only. This is confirmed by the TERS time map (**Figure 3.10**b) and by the comparison of the spectra recorded before and after the ramps (**Figure 3.10**d), which do not show any change in the vibrational signature of 4-ATP. Interestingly, all the spectra present the same bands at 1140, 1392 and 1440 cm^{-1}, which match with those indicated in Kim's paper as the b_2-type bands [221].

Nonetheless, this result alone is not sufficient to rule out the hypothesis of attribution of these signatures to dimeric species. In fact, a tendency for dimerization has been observed [220] on 4-ATP samples adsorbed on silver and gold nanoparticles, depending on the wavelength and on the power of the irradiating source. Oxidation of aniline to azobenzene under laser irradiation is indeed reported to occur *via* the combined effects of SPR and adsorbed triplet oxygen molecule $^3O_2$ on 4-ATP-capped Ag or Au NPs. The process on gold occurs more efficiently upon red laser (632.8 nm) illumination, whereas green light (514.5 nm) is more effective on silver. However, while conversion of 4-ATP into DMAB on silver is observed

already at low laser power (250 nW), gold surfaces, which are more inert because of the formation of superficial oxides, generally require more intense illumination (up to 650 µW to detect a 1:1 intensity ratio between 4-ATP and DMAB bands) [220].

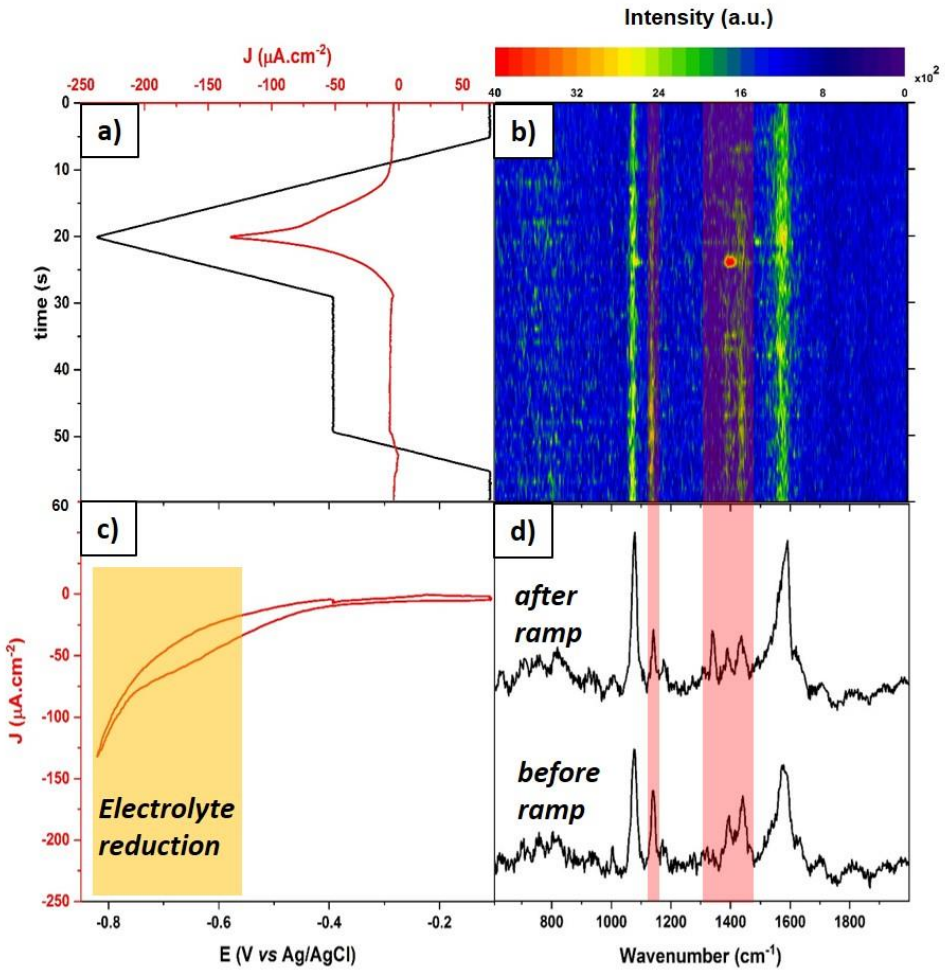

Figure 3.10. EC-STM-TERS measurements on 4-ATP SAM in alkaline medium: a) polarization sequence (two "composite" potential ramps), **b)** spectral signature dependence with the potential, **c)** resulting I-E curve (cyclic voltammogram) and **d)** spectra recorded before and after the ramp (a). Each line on the map corresponds to a single Raman spectrum (acquired in 1 s with 250 µW power (1.56% of the nominal laser power) of the 632.8 nm laser line, BV variable, I_T = 1 nA) and to a 50 mV potential shift. The spectra have been subjected to background removal. The red rectangles highlight the band initially attributed to the "dimer" products but which could stand for forbidden mode of ATP in alkaline medium.

In our working conditions the oxidizing effects due to atmospheric O_2 are supposed to be minimized, first because the experiences are carried out on a liquid electrolyte, which in addition damps partially the power of the illuminating source. Moreover, because the solution was degassed prior to the measurements, it is expected to have a very low content of molecular oxygen. Finally, as for the EC-TERS study of 4-NBM, possible photo-induced effect promoted

at the tip-sample junction were prevented by using illumination powers never higher than 250 µW and keeping the tip scanning the surface.

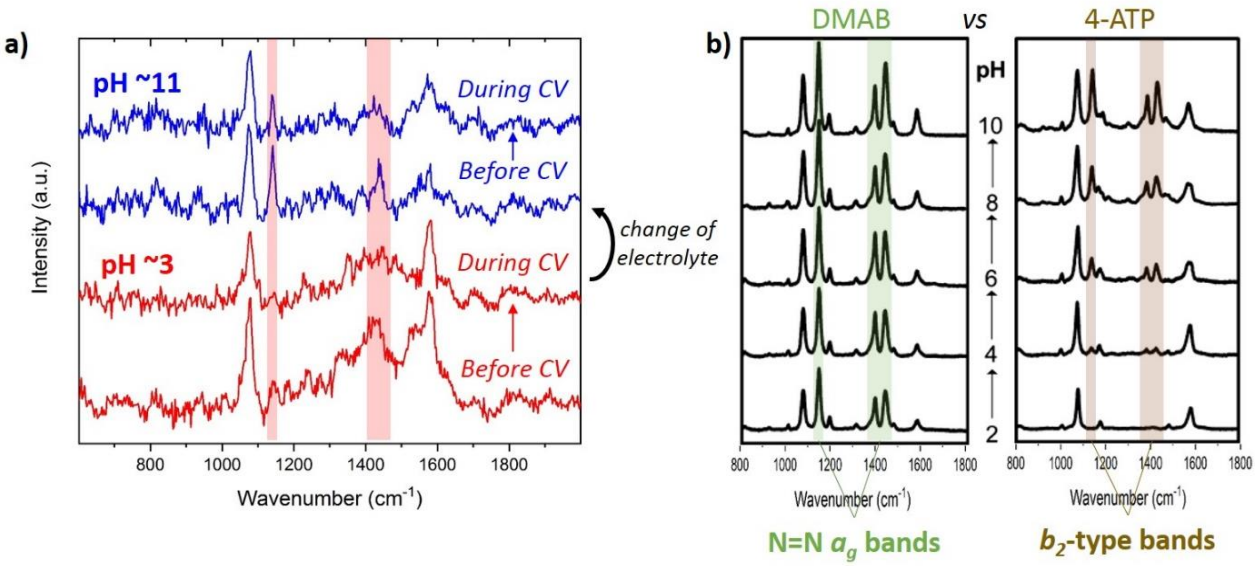

Figure 3.11. TERS/SERS signature dependence with the media for 4-ATP: a) TER spectra in different media recorded on a 4-ATP-functionalized gold plate subjected to a polarisation sequence similar to the one used for 4-NBM (exploration of reductive potential ranges). The plate was subjected to a first potential ramp (370 to -380 mV, scan rate: 50 mV.s^{-1}) in 1 mmol.L^{-1} H_2SO_4 (pH ~3) and then to a second one (-100 to -850 mV) after swapping the electrolyte to bicarbonate buffer (pH ~11). The red rectangles highlight the band expected for a "dimer" reaction products. Each spectrum was averaged from a TERS time map, before and during the potential sweep (30 x 1s spectra, recorded during the 30s time map, power of the 632.8 nm laser line: 160 µW (1% of the nominal laser power), BV variable, I_T = 1 nA). **b)** SER spectra acquired on gold surface functionalized with DMAB thiol (left) and 4-ATP (right) at different pH values using 632.8 nm radiation as the excitation source. Adapted from [221].

To push further the investigation of the possible contribution of photo-dimerization processes, we assessed the influence of the pH of the medium on the TERS response of 4-ATP under similar polarization conditions as the one used for the study of 4-NBM (exploration of reductive potential range). We proceeded as follow: first, the 4-ATP sample was imaged and then subjected to a potential ramp at pH 2.7. The polarisation was temporally stopped, the TERS probe slightly retracted and the electrolyte changed for the buffer at pH 10.7, the hot-spot position checked after the tip was brought back in contact with the sample and a second ramp was acquired. The two ramps were built as described for the experiment in **Figure 3.10**, but in acidic environment the scan range was readjusted to +370 and -380 mV as higher and lower voltage values, respectively (see pH dependence of the potential range on **Figure 3.3**), while the tip was kept at +470 mV. **Figure 3.11**a-b compare the results obtained on 4-ATP in this study with those reported by Kim [221] for both DMAB and 4-ATP at different pH values. In fact, differently from the spectra reported in the literature for 4-ATP, we observed spectral

features in the 1400-1500 cm^{-1} energy range in alkaline but also in acidic medium, which could indicate the formation of the dimer DMAB. These features though do not stand out sharply since the spectra are quite noisy, even after averaging 30 x 1s-acquisition spectra. On the other hand, in our study the band at 1140 cm^{-1} appears neat in basic environment but turns out to be absent in acid medium. This results, along with Kim's observation for 4-ATP [221], suggests that this latter does not dimerize into DMAB under the studied conditions.

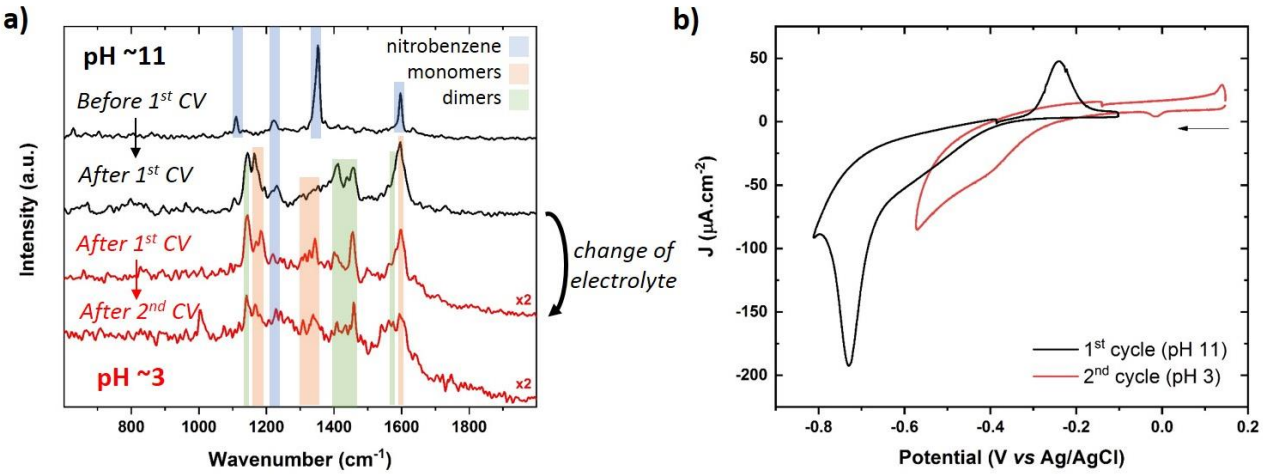

Figure 3.12. TERS signature dependence with the media and polarization for 4-NBM: a) TER spectra taken on a 4-NBM-functionalized gold plate. The plate was subjected to a first potential ramp (-100 to -850 mV at a speed of 50 $mV.s^{-1}$) in bicarbonate buffer (pH 10.7) and, right after, to a second one (+150 to -600 mV at the same speed) in 1 $mmol.L^{-1}$ H_2SO_4 (pH 2.7). Each spectrum is the average of the first or the last chronoamperometric step in the complex potential ramp (5x1s-spectrum, acquired with 160 µW power (1% of the nominal laser power) of the 632.8 nm laser line). The intensities of the spectra taken in acid medium were multiplied by a factor 2 in order to better observe their features; **b)** Superposition of the two CVs recorded during the EC-TERS experiment in the alkaline buffer (black) and in the acidic medium (red).

Confirmation of the electrochemical formation of dimers. Finally, a similar experiment as the last one described was performed on 4-NBM, aiming to recognize whether the 1140 and 1400-1500 cm^{-1} signatures belonged to the amino product or to the dimeric intermediates generated upon negative polarization of the electrode. In this case, the sample was first cycled in the buffer (from -100 to -850 mV), then transferred into the acid electrolyte and cycled again (from +150 to -600 mV). Note that by polarising the electrode in acidic medium, one can expect to promote the reduction of the dimer into the amino analogue as illustrated on **Figure 3.6**. As **Figure 3.12**a shows, on the reduced 4-NBM the characteristic bands of the dimers (in the green ranges), and especially the signature at 1140 cm^{-1}, which in the 4-ATP example disappeared completely at low pH, are still strong after changing the electrolyte from the buffer to the acidic medium. This suggests that the observed signatures

truly belong to the dimeric species and not to the amino product, and that the reaction proceeded along the second-order reaction path when working in basic electrolyte.

Besides, the presence of azobenzene bands even after the second reductive cycle in acidic medium suggests that the dimeric compound is stable enough not to convert totally to the amino product. The amino product (4-ABM) though, might still form to some extent, along with the other monomeric intermediates (4-HABM, 4-NSBM), as it can be seen from the signatures in the orange ranges of **Figure 3.12**a. At the end of the second cycle, however, these bands are expected to belong to the sole 4-ABM, as the correspondent voltammogram (**Figure 3.12**b) does not show any longer the anodic peak of reconversion from 4-HABM to 4-NSBM, meaning that all the intermediate monomers disappeared (either by total reduction to amino or by coupling into dimers).

3.4. Discussions and conclusions

Through important technical developments (4-electrode cell optimization, synchronization of the TERS signal collection with the polarization steps), we have demonstrated in this work that TERS mapping with high lateral resolution (4-nm pixel size) and time-resolved (1s) TERS measurements could be implemented *in situ* to get a deeper understanding of the electrochemical transformation of non-Raman resonant electroactive molecular layers (4-nitrobenzene mercaptan 4-NBM).

This analogue of 4-nitrothiophenol (4-NTP), largely studied by SERS in air and under electrochemical conditions, shows a very similar electrochemical reactivity, although it turns out to be less prone to desorption as contaminations of the TERS during *in situ* experiments or cross contaminations of samples between successive experiments using the TERS electrochemical cell were not observed (as with 4-NTP).

A previous work of our group (T. Touzalin) was dedicated to the study of 4-NTP electrochemical transformation in acidic medium *via* single hot-spot EC-SERS experiments ("tip-SERS": SERS-active gold microelectrode functionalized with 4-NTP). However, only a partial understanding of the system transformation was achieved, because of the fast conversion of 4-NTP to 4-ATP in acidic medium (high proton concentration). Also, real-time SERS signal tracking during the potential exploration was complicated by the sudden surge of signal intensity (leading to the detector saturation), the cause of which is still not understood. In the study presented herein, alkaline medium was favoured to acidic medium as the low

concentration of protons may stabilize reaction intermediates (extended lifetime) and their possible detection by time-resolved TERS.

However, when working in alkaline medium, the extended potential range which has to be explored to fully reduce the 4-NBM compounds constitutes a major bottleneck to EC-TERS implementation using STM feedback for the control of the tip-sample distance. We showed in this work that by holding the gold STM tip at potentials where no electrolyte reduction takes place (Faradaic current lower than tunnelling current), the STM bias between the tip and the sample could be adjusted (increased and decreased) to mimic potential scans (CVs) while allowing strong TERS signals to be registered in real time over large potential windows. No signal surge, as for tip-SERS on 4-NTP, was observed either for 4-NBM or 4-ATP. More importantly, the STM feedback for the tip-sample distance control was not impacted in the alkaline medium by the large bias values that were used. This is, to our knowledge, the first demonstration of EC-TERS experiments at such negative polarisation (down to -1 V).

The information gathered by TERS on the dynamics of the sample composition evolution upon polarisation, along with all the considerations drawn from the additional implemented tests (TERS study of the amino compound 4-ATP, influence of the pH), allows us formulating a hypothesis regarding the reduction mechanism of 4-NBM under the employed conditions. In alkaline medium, 4-NBM should first reduce partially into hydroxy-amino 4-HABM at around -550 mV: this would explain the apparition of weak CH bending and NO stretching bands at this stage. The irreversible reduction of all the nitro groups would then occur around -700 mV, but the main reduction products (i.e. the amino analogue 4-ABM and the dimers, mostly the azobenzene DMAB analogue of 4-NBM) form concomitantly only at lower potentials (-800 mV). We showed that dimers do not originate from 4-ABM photo-oxidation, upon irradiation of the gold tip-sample junction in solution with a red laser, but rather from condensation of 4-HABM with residual nitroso derivative 4-NSBM (or even 4-HABM self-condensation). The conversion of 4-HABM, though, does not seem to be complete, as its re-oxidation into NSBM is manifested in the CV by the anodic peak and hinted in the TER spectrum from the new weak bands appearing above -400 mV.

Several species are therefore present at the end of a single reduction cycle. However, when performing more explorations of the negative potential range, the monomeric intermediates (NSBM,4-HABM) vanish, as evinced by the disappearance of their bands, thus leaving 4-ABM and DMAB analogue as the most abundant and stable reduction products (as

shown in **Figure 3.12**). This means that the reaction does not get to completion, i.e. DMAB azo bond cannot be "opened" to form DMHAB (and eventually split into two 4-ABM monomers) as suggested by Gao's mechanism (see **Figure 3.6**). On one hand, the competitive reaction path leading to 4-ABM and to the DMAB analogue could be explained by the particular working conditions employed (mild alkaline environment, reductive polarizations limited to -0.85V) to study the reaction; acidic conditions and repeated polarizations at more negative potentials might help pushing further the reduction process, towards the formation of the sole 4-ABM product. On the other hand, the simultaneous presence of different products might also be a consequence of the heterogeneity on the gold surface structure [206], revealed by the STM-TERS mapping. Such inhomogeneity may promote a non-uniform charge distribution over the whole active area during the surface polarization and therefore a distribution of reactivity.

These first results obtained on a model 4-nitrobenzene sample show the potential of the EC-STM-TERS experiments to unveil complex reduction mechanisms. Further studies on 4-NBM could aim at investigating other experimental conditions (in terms of pH, potential range, laser excitation power, wavelength, etc.) and at assessing further the possible impact/ contribution of photo-induced processes. The influence of the distance between the NO_2 electroactive group and the anchoring SH group on the kinetics of the electron transfer (between the gold electrode and the nitrobenzene derivative) and on the resulting reduction mechanism would be of great interest. As for the reduction mechanism of anchored 4-nitrobenzene derivatives, the knowledge acquired from the study of the model thiolated sample can be applied for the investigation of more complex molecular structures, as it will be the case for the subject of the following Chapter 4.

Chapter 4 Diazonium-based structures: influence of the thickness on the electrochemical reactivity

4.1. Introduction

Controlling the modulation of the growth of the molecular assemblies, along with understanding its impact on the overall reactivity of the functionalized electrode system, is essential to design robust and device-oriented fabrication procedures. This chapter will focus at establishing the relationship between the structure of electroactive molecular layers and their electrochemical reactivity by implementing EC-TERS measurements. More specifically, it will be dedicated to the study of layers obtained by electro-reduction of aryldiazonium precursors. As already described in Chapter 1, the electrochemical reduction process generates a highly reactive radical intermediate, leading to the spontaneous formation of multilayers in a non-organized fashion. The grafting process can be however controlled using the so-called redox "cross-inhibitor" method, allowing in the best scenario the production of monolayers.

For diazonium precursors carrying redox-active entities, the reactivity of the resulting grafted layers will strongly depends on the distribution of the redox group within the produced 3D structure [222], which impacts both the electron transfer (distance of the redox group to the electrode) and the transport phenomena (e.g. accessibility of the redox groups to water molecules and protons from the electrolyte). The first phenomenon has been observed, for instance, on Si(100) grafted with ferrocene-containing triazene derivatives [223], where the electron transfer rate between the substrate and the ferrocene center decreased dramatically (down to 164 s^{-1}) when thick multilayers were formed, while the second accounts for the reduced bromine reactivity (only 60 %) inside bromoethylphenyl layers [59]. Menanteau *et al.* showed the impact of both factors in a study carried out on 4-nitrobenzene layers: these were first subjected to reduction to transform the nitro groups into amine, and then the amine function was used to attach a TEMPO unit, which has both redox and electrocatalytic properties [72]. When the 4-nitrobenzene species were arranged in multilayers, not only the rate of conversion into amine was lower than for the monolayer structures (slower ET rate), but also the TEMPO units, which could be partially inserted inside the thick architectures and therefore less accessible to the electrolyte, showed a dramatic decreases in their electrochemical reactivity. In conclusion, gathering control over the growth of diazonium-derived layers is essential for fabricating device-oriented structures.

While the previous Chapter 3 focused on the reactivity of well-organized structures, self-assembled in homogeneous monolayers, this new section will evaluate the reactivity of more complex architectures, covalently bounded to the substrate (characteristic of the aryldiazonium salt chemistry, as described in Chapter 1). 4-nitrobenzene diazonium (4-NBD) was selected in this work as a grafting precursor to produce electroactive molecular layers carrying nitro redox entities [51,56,222]. Since important insights in the reduction mechanism of nitro-functionalized molecular compounds have been gained through the EC-TERS study of 4-NBM (described in Chapter 3), these will be used as a base for establishing the impact of the layer structure on its reactivity (preferential intermediate formations, extent of reaction, etc.).

The strategy developed in this work consists first in controlling the reactivity of 4-NBD in the presence of redox "cross-inhibitors" (see Chapter 1) to produce layers of 4-nitrobenzene of different thicknesses on various substrates (gold mostly, although attempts have been made on glassy carbon). Optimization of the grafting conditions (concentration of inhibitor, electro-grafting setup, polarization sequence) was achieved through the assessment of the electrochemical performances and *ex situ* characterization of the grafted electrodes using various analytical techniques (AFM, ellipsometry, XPS). Based on the progress achieved on the instrumentation side (Chapter 2) and on the understanding of the electrochemical reactivity of nitro-based molecular layers (Chapter 3), EC-STM-TERS measurements will be carried out on 4-NB functionalized electrodes. The investigations will be performed in alkaline medium (where, due to the slower reduction kinetics, it is expected to detect more easily the reaction intermediates) and will aim at evaluating the impact of the layers structure on their electrochemical reactivity.

4.2. Elaboration of functionalized surfaces by controlling diazonium chemistry

The first part of the work consisted in studying how to control the growth of 4-NB-derived layers on gold surfaces. In this section we will first illustrate the methods employed to perform electrochemical grafting of 4-nitrobenzene layers from the reduction of the corresponding diazonium salts, then present the inhibition approach experimentally applied to control the layer thickness. Finally, the post-grafting characterization analyses performed *in situ* on the produced layer will be discussed.

4.2.1 Electrochemical grafting of 4-NB radicals on gold

Grafting solutions for gold electrode functionalization were prepared by solubilisation of 4-nitrobenzene diazonium tetrafluoroborate (4-NBD, Sigma Aldrich) and *n*-tetrabutyl ammonium tetrafluoroborate (NBu_4BF_4, Sigma Aldrich) in dry acetonitrile, taken either from a solvent dispenser, or from a septum-sealed bottle (DriSolv®, purity ≥95%, VWR). The final concentrations were 1 or 0.1 $mmol.L^{-1}$ for 4-NBD and 0.1 $mol.L^{-1}$ for NBu_4BF_4, used as the supporting electrolyte. Before use, the grafting solution was deoxygenated by argon bubbling for at least 5 minutes. The modification was performed either on home-made gold sphere electrodes (prepared according to the procedure in ref. [224]) or on a commercial gold disk electrode (as in Chapter 3); in both cases, the same gold reconstruction procedure was carried out. In the electrochemical setup, gold electrodes always constituted the WEs and the platinum wire the CE. As for the reference electrode, initially it was chosen to employ a SCE for the characterization and a simple Ag wire (*pseudo* Ag/Ag^+ reference) for the grafting, so that to avoid dipping the SCE in the non-aqueous grafting solutions [225]. However, it was later noticed that the potential of the *pseudo* Ag electrode tended to shift between experiments and it was therefore not as reliable as a real reference. As a consequence, after this observation we chose to employ also for the grafting a commercial SCE or a home-made Ag/AgCl reference electrode ($E°_{Ag/AgCl}$ ~ -40 mV *vs* SCE in acetonitrile [225]) of smaller dimensions, which could be more conveniently introduced inside the electrochemical cell.

In Section 1.2.2.1 it was explained that diazonium salts produce radicals through a 1-electron reduction process, promoted by a reductive electrode surface, to which the aryl radicals graft. If acid aqueous media were used for the grafting solution, there might be the risk that also the nitro groups of 4-NBD reduce during the process (following the same mechanisms presented for 4-NBM in Chapter 3) when in close proximity to the surface, while it has been observed that diazonium salts are usually instable at pH higher than 2-3 [40]. Instead, using an organic solvent as acetonitrile should prevents this issue, since the potential needed to perform the reduction will be shifted toward more negative values.

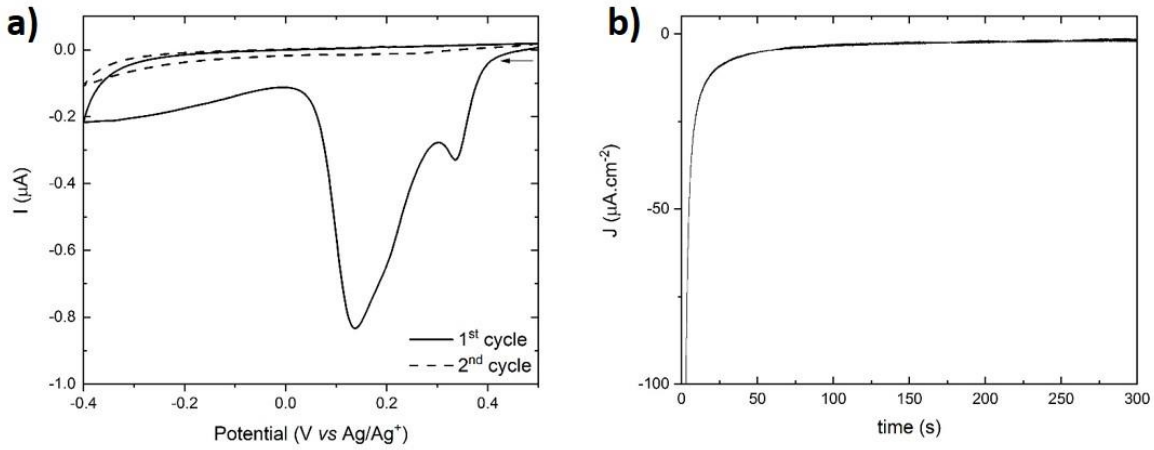

Figure 4.1. a) Electrochemical reduction of 4-NBD *via* cyclic voltammetry on a gold sphere electrode: 2 cycles from +0.5 to -0.4 V *vs* Ag/Ag^+, scan speed 100 $mV.s^{-1}$, in a 0.1 $mmol.L^{-1}$ 4-NBD solution. **b)** Second out of three steps of a 4-NB grafting chronoamperometry on a gold plate: -0.6 V *vs* SCE potential hold for 300 s in a 1 $mmol.L^{-1}$ 4-NBD solution. The first and third steps (not shown) consisted in holding the potential at +0.8 *vs* SCE for 10 and 30 s, respectively. In both (a) and (b), the supporting electrolyte consists in a 0.1 $mol.L^{-1}$ NBu_4BF_4 solution in dry acetonitrile, deoxygenated for at least 5 minutes prior to use.

Experimentally, grafting *via* electroreduction of diazonium salts can be performed either by sweeping the electrode potential (i.e. by CV) or by applying potential steps (chronoamperometry), after immerging the surface in the diazonium salt solution. **Figure 4.1**a shows the first approach: starting from a +0.5 V polarization, where no reaction occurs (I = 0), the potential is lowered down to -0.4 V (forward scan), thus giving rise to two cathodic peaks at around +0.32 and +0.14 V, respectively. The two cathodic peaks observed in the first cycle belong therefore to the 4-NBD specie and represents its 1-electron reduction into radical. In fact, on carbon-based electrodes it is more common to observe a single, broad cathodic peak [40], while on gold the reaction can take place on different crystallographic facets and therefore show two or more peaks [45]. During the backward scan, the current goes back to zero and does not evolve anymore during the second cycle, nor in the following ones. This trend has been typically observed for diazonium salts [40,45] and attests of their blocking properties on the sample surface due to the formation of a thick layer of molecules on the whole electrode surface that provokes its passivation. Similarly, as shown in **Figure 4.1**b, the electroreduction of the diazonium can be performed by chronoamperometry by maintaining a fixed potential allowing its reduction (herein -0.6 V *vs* SCE). As it is characteristic for the reduction of aryldiazonium salts [45], the current density drops already few seconds after the application of the potential and

returns slowly to 0, as it can be expected for a diffusion-limited process that, in addition, involves surface passivation.

In conclusion, the uncontrolled electrografting of 4-NB radicals on gold surfaces leads to the fast formation of thick surface layers, with passivating properties. As explained in Chapter 1, this can occur for many diazonium-derived species, which is why several methods have been developed to gather control over the layer growth. In the next paragraph we will present the specific procedure we adopted to limit this multilayer formation, with the aim of reaching a single layer of molecules.

4.2.2 Control of 4-NBD layer growth with a redox cross-inhibitor

Among all the proposed approaches for tuning the thickness of the layers, we decided to follow the one elaborated by the researchers of Moltech, Angers (France), who optimized the use of the so-called redox "cross-inhibitors" for grafting of diazonium salts on carbon-based surface (as pyrolized photoresistive films PPF or glassy carbon GC) [50,70,71,213].

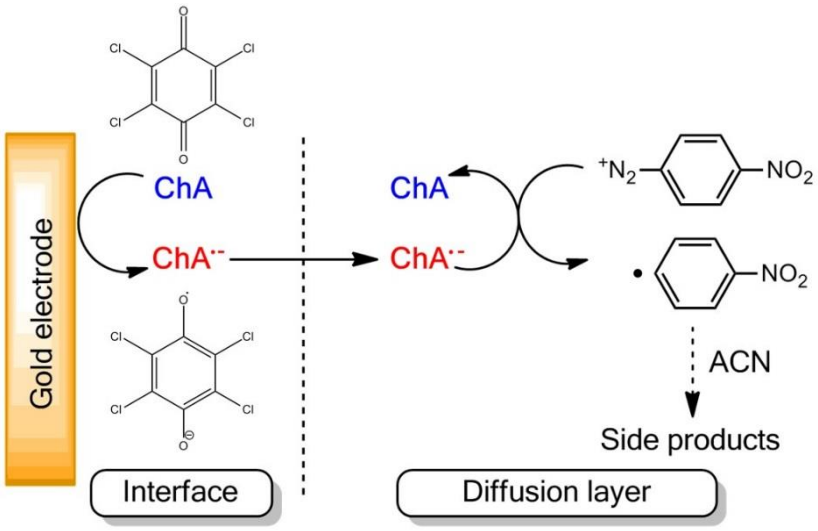

Figure 4.2. Schematic view of the cross-redox mechanism of chloranil (ChA) for the inhibition of the 4-NBD layers growth. Adapted from [213].

A schematic view of the inhibition process, exemplified with 4-NBD as diazonium salt and tetrachloro-1,4-benzoquinone (Chloranil, ChA) as inhibiting agent, is illustrated in **Figure 4.2**. The two molecular species are introduced simultaneously in solution, therefore they can both be reduced at the electrode surface. 4-NBD reduction leads to the formation of a radical, which grafts right away onto the nearby surface. On the contrary, ChA molecules reduce reversibly to their radical anion form (semiquinone), which is more stable than 4-NB radicals and can diffuse far from the electrode interface [213]. If in their way they encounter a diazonium

molecule, the ChA radical anions can therefore oxidize again and provoke 4-NBD reduction far from the electrode surface. Since 4-NB radicals are very reactive, they should not have the time to diffuse towards the electrode and graft on it: instead, they would react faster with the solvent or with each other, thus forming deactivated side products [213]. Eventually, only the 4-NBD species that were already close to the electrode surface when its polarization started, or those who managed to diffuse from the solution bulk to the electrode interface, will be electro-reduced and grafted.

The thickness of the grafted layer is expected to decrease proportionally to the increase in inhibitor concentration and, in the best scenario, hinder the formation of multilayer structures. Although DPPH is more often used to control the grafting of 4-NB layers from the corresponding diazonium salt [70,213], herein we preferred employing ChA [213], which is less toxic and easier to manipulate (ChA solutions are less opaque).

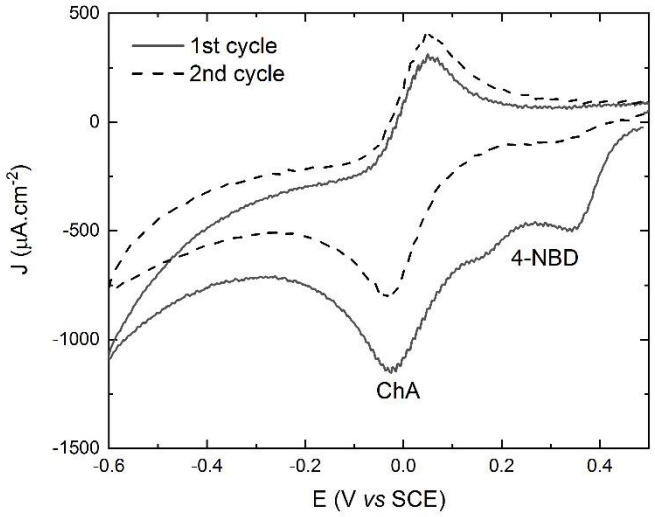

Figure 4.3. 1st and 2nd CV cycles recorded at 500 $mV.s^{-1}$ on a gold disk electrode (Ø = 3 mm) in presence of 4-NBD (1 $mmol.L^{-1}$) and ChA (1 $mmol.L^{-1}$). Electrolyte: 0.1 $mol.L^{-1}$ NBu_4BF_4 in dry acetonitrile.

Figure 4.3 shows a typical voltammogram recorded on a solution containing both 4-NBD and ChA. The electrochemical signature of ChA appears as a reversible peak, falling around -0.02 V in the forward scan and around 0.05 V in the backward scan, respectively. Note that the observation of these signatures is only possible using a relatively fast potential sweep (500 $mV.s^{-1}$), which prevents the immediate electrode passivation of the electrode though the 4-NBD electroreduction (irreversible peak at E < 0.4V). Since the reduction potential of ChA is more negative than the one of 4-NBD, a grafting procedure using CV would promote the 4-

NBD reduction before the activation of ChA, therefore a chronoamperometry at a potential more negative than both the 4-NBD and the ChA cathodic peaks was preferred to enhance the inhibitive effect of ChA [71].

Furtherly, to avoid the issue of spontaneous grafting, the working electrode to functionalize was always immerged in the grafting solution immediately before starting the polarization and pulled out at the end of the electrochemical sequence. Nevertheless, the occurrence of this process, even to a limited extent, cannot be completely excluded, since it is expected that, at the open circuit potential (OCP) of the cell (~ +0.40 V [213]), 4-NBD might already reduce to its radical form, while ChA does not transform and cannot therefore inhibit the grafting process. This issue was partially solved by Breton's group [213] by elaborating an adapted ChA-controlled grafting protocol consisting in the application of two subsequent potential pulses [213]: (1) a 10-s chronoamperometry at +0.80 V, potential higher than the OCP at which no reduction of either of the two species can occur, so that to minimize spontaneous grafting; (2) a 5-min grafting chronoamperometry at -0.60 V, which is lower than the reduction potentials of both 4-NBD and ChA and therefore allows exploiting the inhibitive effect. In our experimental work, a third and last step was added to this protocol, adapted from what reported elsewhere for DPPH [50]: (3) a 30-s polarization at +0.80 V, which prevents the uncontrolled immobilization of diazonium salt, caused by the slow system relaxation toward an arbitrary potential after the negative step (2) [50]. In Breton's group work, all the potentials were referred against an $Ag/AgNO_3$ *quasi* reference, whereas, in our case, a bare Ag wire or sintered SCE and Ag/AgCl electrodes were used. Note that the potential of $Ag/AgNO_3$ is around +300 mV against Ag/AgCl [6], which means that the potentials applied in our experiments are actually more positive than those used in literature. Nonetheless, the lower potential (-0.60 V) was still negative enough to trigger the simultaneous reduction of both species, while no side effects (e.g. oxidation or desorption phenomena) were remarked upon application of the higher potential (+0.80 V).

As it will be illustrated in the following paragraphs, the three-step chronoamperometric grafting protocol was eventually successful in controlling the layer growth thanks to the inhibiting action of ChA. Moreover, when applying the same electrochemical sequence for grafting in presence of DPPH, higher quantities of this inhibitor were required to equal the performances observed for lower concentrations of ChA (see Annexes). This confirms the

potentiality and reliability of such protocol for controlling the growth of 4-NBD layers on gold surfaces.

4.2.3 Characterization of the grafted layers

In order to evaluate the inhibiting effect of ChA, our strategy consisted first in performing electrografting from mixtures of fixed 4-NBD concentration and variable inhibitor content, and therefore in characterizing the grafted electrodes, so that to evaluate the effect of the inhibitor concentration on the layer structure and thickness.

Following the aforementioned protocol, different gold substrates (plates or disks, depending on the post-grafting characterization method) were functionalized in solutions of 4-NBD 1 mmol.L^{-1} only or mixed with ChA (TCI Chemicals) 0.1, 0.25 and 0.30 mmol.L^{-1}, in dry acetonitrile with NBu_4BF_4 0.1 mol.L^{-1}. In all the experiments, the CE was a platinum wire, while the RE was a saturated calomel electrode (SCE). The solutions were always deoxygenated for at least 5 minutes before use. After the functionalization, the surfaces were thoroughly rinsed with acetone, whose excess was dried with an argon stream and/or wiped out. The following paragraphs will illustrate the different kinds of analysis performed on the grafted surfaces and discuss the results.

4.2.3.1. Electrochemical evaluation of the electrode surface coverage

The electrochemical characterization of 4-NBD was carried out in a similar way as for 4-NBM in Chapter 3, i.e. on gold disk electrodes (Origalys), which were polished and reconstructed before use, and in alkaline medium. Both before and after the chrono-amperometric grafting, in presence of different ChA concentrations, the disk electrodes were subjected to cyclic voltammetry experiments in bicarbonate buffer at pH 10.7. The results of the CVs on the grafted electrodes are reported in **Figure 4.4**, while the ones performed before grafting acted as blanks and attested that no residual species were still grafted on the electrode between two different experiments.

Similarly to what has already been observed by Menanteau *et al.* [69], upon structuration of nitrobenzene layers of different thickness from reduction of the corresponding diazonium (under DPPH control), the peak intensities arising from NO_2 reduction tend to decrease with the increase in inhibitor content, while the main cathodic peak shifts towards less negative potential (of around 15 mV [69]). Similar results were obtained by Brooksby and Downard [226] upon functionalization of PPF substrates in the presence of 4'-nitrobenzene-4-azobenzene

diazonium at different electrografting times and were related to a decrease in the molecular layer thickness. These observations evidence the inhibition properties of ChA: as its concentration increases, the layer growth is inhibited, therefore less nitro groups are anchored on the surface and can be reduced during the forward scan of the voltammogram. This explains the decrease in the peaks intensities, but can also explain the shift of the cathodic peak potential: when the layer is thinner, it presumably also contains less hydrophobic "branches" of aryl groups, which means that the electrolyte molecules can solvate better the nitro groups and ease their reduction [45].

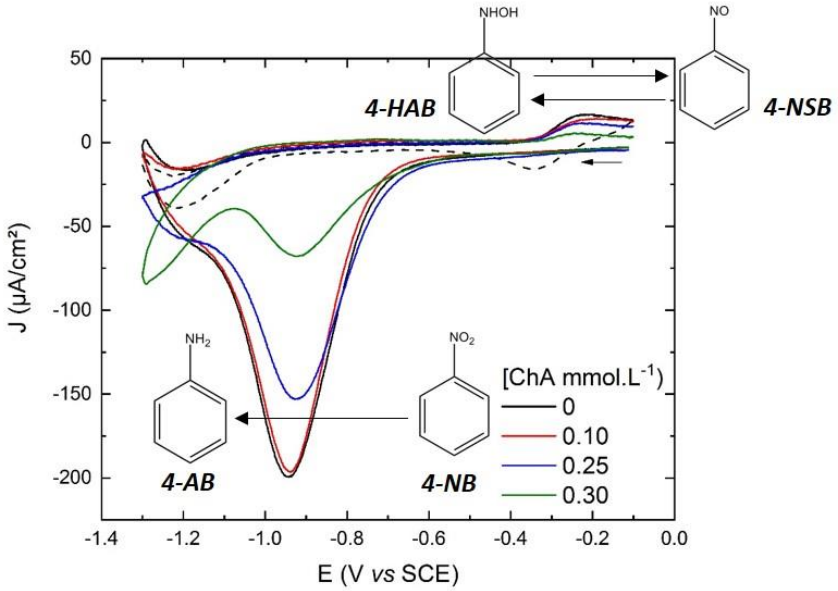

Figure 4.4. CVs recorded in bicarbonate buffer on grafted gold plates (from -0.1 to -1.3 V *vs* SCE, at 50 mV/s). Grafting was previously achieved in the presence of 1 mmol.L^{-1} 4-NBD and different ChA concentrations (indicated in the legend on the graph). The dashed black curve represents the second cycle performed on the disk grafted without ChA.

Also in this case the surface coverage can be evaluated by integration of the cathodic and anodic peaks areas, according to the Equation (3.5) presented in Chapter 3. **Figure 4.6** illustrates the results of these calculations in comparison with the thickness estimation, obtained by ellipsometry analyses on grafted plates, hence they will be discussed more extensively in the following paragraph.

4.2.3.2. Thickness evaluation by ellipsometry

After growing layers in presence of different ChA concentrations, their thickness was measured with a mono wavelength (λ = 633 nm) SE 400 adv ellipsometer (Sentech), interfaced with the homonymous software (version 2.20) that allowed building a layered model

(exemplified in **Figure 4.5**) to represent the samples. The lower layer was identified with the gold substrate, from which the characteristic refractive index *n* and adsorption coefficient *k* were extracted by preliminary ellipsometric measurements (before grafting). The middle layer corresponded to the grafted 4-NB architecture, to which it was attributed a refractive index value of 1.46, plausible for organic compounds [227]. Since no changes in color were observed on the gold substrate before and after the grafting procedure, it was assumed that the layer did not adsorb in the visible range, hence *k* was set equal to 0. Finally, the upper layer was constituted by the medium that surrounds the substrate during the measurements, i.e. air, in our experimental conditions.

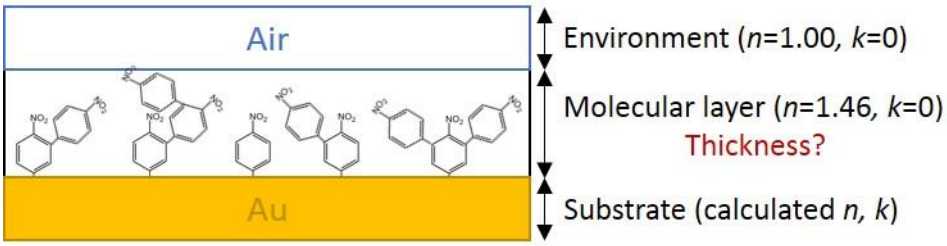

Figure 4.5. Empirical model designed on the SE 400 adv ellipsometry software to retrieve the molecular layer thickness.

Measurements were carried out on commercial gold-coated-silicon plates (Aldrich), which were preliminary sonicated in absolute ethanol and measured by ellipsometry on 10 different spots to retrieve the average *n* and *k* values of the gold surface. Afterwards, they were subjected to the aforementioned grafting procedure in the presence of variable concentrations of ChA and finally measured again on 10 different spots to yield an average thickness for each sample. The results, compared to the surface coverage values obtained by CV, are shown in **Figure 4.6**.

As it was expected from the evolution in the voltammograms intensity observed in **Figure 4.4**, an increase of the ChA content in the grafting mixture corresponds to a decrease in both the thickness and the surface coverage values for the 4-NB layer. More specifically, a 0.25 mmol.L^{-1} ChA concentration yields a surface coverage of around 9*10^{-10} mol.cm^{-2}, which is consistent with what has been reported for a monolayer on gold [56]. In fact, the surface coverage is strictly dependent on the substrate roughness: while values down to 2.5*10^{-10} mol.cm^{-2} have been reported for smooth PPF surfaces [45], higher rates were recorded on rougher carbon [70,71] and gold [56] electrodes. The layer thickness correspondent to the same ChA concentration showed a value of 1.41 nm, slightly higher but still consistent with what has been

reported for 4-NB monolayers (between 0.6 and 0.9 nm) [39,56,71]. However, increasing the inhibitor quantity up to 0.30 mmol.L^{-1} provokes a consistent drop in the surface coverage value, while using an intermediate concentration of 0.27 mmol.L^{-1} does not seem to have a relevant impact on the layer thickness. As a consequence, a ChA concentration of 0.25 mmol.L^{-1} was estimated as the most suitable for the formation of a "monolayer-like" 4-NB structure. Below this limit, thick multilayers are obtained, whereas increasing the quantity of ChA leads to the formation of incomplete sub-monolayers.

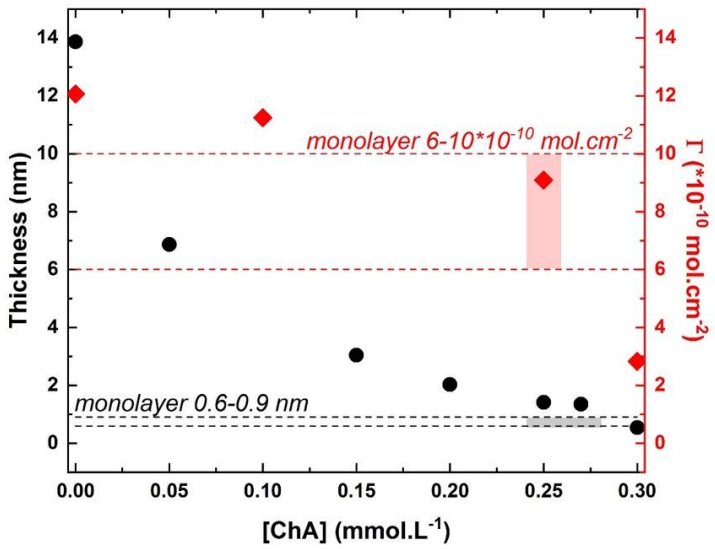

Figure 4.6. Evolution of the thickness (black dots) and the surface coverage (red diamonds, determined in bicarbonate buffer) of 4-NBD layers on gold as a function of the ChA concentration in the grafting mixture. The dotted lines mark the ranges of values reported in the literature for 4-NB monolayers thickness [39,56,71] and electrode surface coverage [56,70,71], while the shadowed areas evidence the experimental values for which it would be expected to obtain a monolayer.

It must be pointed out, though, that the two parameters compared in **Figure 4.6** do not follow the same decreasing trend: the thickness drops much faster already at very low ChA concentrations, then it declines slowly starting from 0.15 mmol.L^{-1} of ChA. On the opposite, the surface coverage decreases just slowly at the beginning and drops at higher values. In fact, the method used for the calculation of the surface coverage relies on the reactivity of the nitro functions, which should all react and reduce during the CV scan in order for this method to be completely reliable. However, as it was mentioned before, the density of the multilayers, accentuated by the presence of forked branches, complicates the proton diffusion inside the molecular structure and therefore affects the reduction process [226]. Indeed, many NO_2 groups will not react and remain "silent" during the CV, thus leading to an underestimation of the surface coverage value. This is why at low ChA concentrations (0.05 mmol.L^{-1}) the formed

layer, which is still so dense that its electroactive groups cannot react, shows almost the same surface coverage value as the layer grown without inhibitor control. In fact, the evaluation of surface coverage *via* integration of CV areas can only be actually reliable for monolayers, or at least to very thin layers [45].

4.2.3.3. Comparison between 4-NBM and 4-NB monolayers

Following the results obtained by ellipsometry, the CV corresponding to the 4-NB "monolayer-like" structure (blue curve of **Figure 4.4**) is compared to the one obtained with the 4-NBM (**Figure 3.3** in Chapter 3) as shown in **Figure 4.7**. Due to the similarity between the 4-NBD and 4-NBM layers, both bearing an electroactive nitrobenzene functionality, we expected to observe similar electrochemical signatures in their CVs: a huge cathodic peak (falling around -920 mV *vs* SCE for 4-NBD), corresponding to the total 4-nitrobenzene (4-NB) reduction into 4-aminobenzene (4-AB), and the couple of redox peaks (whose anodic signature rises around -240 mV *vs* SCE) indicating the reversible transformation of 4-hydroxylamine benzene (4-HAB) into 4-nitrosobenzene (4-NSB).

However, significant differences are observed among the two of them. First, a marked shift of the cathodic peak towards less negative potential is observed for 4-NBM. On one hand, this observation might indicate that the ordered arrangement of the thiol molecules in the SAM structure eases the solvation of the nitro functionalities, which can therefore be reduced more easily (as it was mentioned before). On the other hand, though, it may also attest that the "monolayer-like" 4-NB contains in fact some branches and therefore has a partial multilayer structure. This is suggested also by the difference in broadness of the cathodic peak, which is wider for 4-NB since it should collect the electrochemical contributions of several NO_2 population, more or less solvated inside the structure, hence with different reactivity for the reduction process. Nonetheless, the dissimilar nature of the two grafted species might also play a role on the electronic transfers between the substrate and the electroactive centre.

Another difference observed between the two molecular species is the intensity of the peaks corresponding to the reversible HAB(M)↔NSB(M) formation (~ -240 mV and -330 mV, respectively, for the anodic and cathodic peak). In fact, because in the diazonium-derived layers the main cathodic peak appears at more negative potentials, it might be possible that the total, irreversible reduction of nitro groups into amino (final reduction product) will occur at higher

yield for these systems, therefore less hydroxylamine might be able to reconvert into nitrosobenzene in the backward scan.

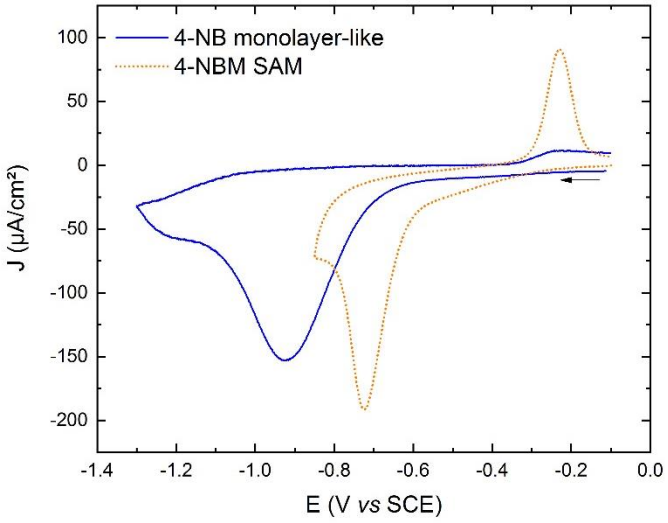

Figure 4.7. Comparison between CVs recorded in bicarbonate buffer at 50 mV/s on 4-NB "monolayer-like" structure (blue curve in **Figure 4.4**) and 4-NBM SAM (**Figure 3.3** in Chapter 3), both deposited on gold electrodes. For further experimental details, please look at the captions of the original figures.

In conclusion, the dissimilarities between the two CVs strongly suggest a difference in the organization of the layer structures for the two compounds. In fact, despite the ellipsometric results reveal the presence of a monolayer on the 4-NB sample, those measurements are averaged over a micrometric area and therefore are not sensitive to local heterogeneities at the nano scale. Additionally, an evaluation of the molecular species distribution over the grafted surface was carried out thanks to AFM imaging, which will be presented in the next paragraph.

4.2.3.4. Structure characterization by AFM imaging

Gold plates were analysed *via* AFM before and after electrografting in order to visualize the overall substrate morphology upon molecular functionalization. The choice of AFM over STM is motivated by its higher performances in imaging soft molecular layers, particularly when working in semi-contact mode (tapping mode), as it was done experimentally. In this AFM mode, the tip periodically touches or taps the surface of the sample and can follow the layers profile without affecting their structure. On the contrary, the STM probe operates at very close distance with the probed surface for the I_T to flow. Since this so-called tunnelling gap is usually lower than 1 nm, the tip is susceptible to penetrate inside the molecular structures (which might have a low electrical conductivity) and therefore will not be able to measure its profile [228].

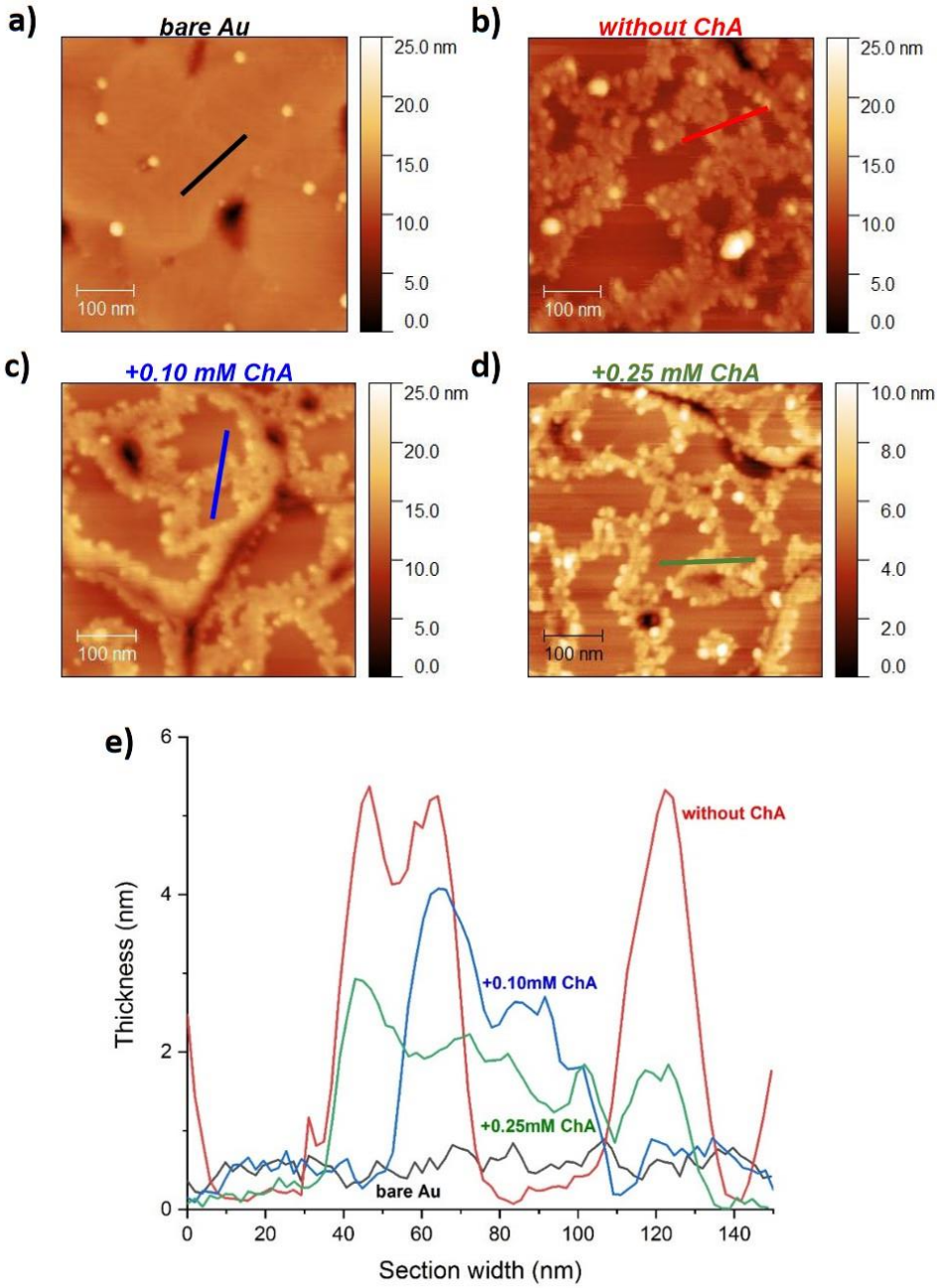

Figure 4.8. AFM maps acquired on gold plates, either (**a**) bare or grafted with 4-NBD (1 mmol.L^{-1}) in presence of (**b**) 0, (**c**) 0.10 or (**d**) 0.25 mmol.L^{-1} ChA. All the maps were acquired in 500x500nm^2 areas with 256x256 pixels in AFM tapping mode. From the colored section shown in the maps, the corresponding morphology profiles (**e**) were extracted.

Since the commercial gold plates previously used for ellipsometric characterizations were not smooth enough to distinguish the molecular structures from the gold electrode surface features, it was decided to use the homemade plates of gold on mica (produced as explained in Chapter 3). As it is observed in **Figure 4.8**a, a bare Au substrate is constituted by relatively large terraces, whose roughness, evaluates from the morphology profile (black section), is averagely 0.5 nm (with maximal peaks of ~1 nm). After electrografting of 4-NBD in presence

of different ChA concentrations, the overall aspect of the surface changes considerably: grainy structures seem nucleating in proximity of the terraces edges and spreading over them (**Figure 4.8**b-d). Without ChA control, these structures are more abundant and thicker: in the section evidenced in **Figure 4.8**e, they reach a 5-nm thickness, corresponding to ~7 layers. As the ChA concentration increases, the structures become less abundant and also their thickness diminishes: the maximum height is around 4 nm (~5 layers) for a 0.1 $mmol.L^{-1}$ ChA concentration and 3 nm (~4 layers) for 0.25 $mmol.L^{-1}$ ChA.

On one hand, these observations confirm the inhibiting role of ChA, but on the other hand they show that molecules rather tend to aggregate in clustered structures, which follow the shape of the terraces edges, instead of yielding uniform layers, as it was expected from the results of ellipsometry (and as reported previously on PPF substrates [222]). It might be possible that the molecules arrangement in clusters derives from a heterogeneous current distribution on the gold surface, caused by its fragmentation in terraces, and from the surface roughness, which is still comparable to the size of a monolayer.

In order to limit the influence of the substrate morphology on the arrangement of the grafted molecules, it was chosen to produce ultra-flat gold plates through a cryogenic cleavage method [229], which is illustrated in **Figure 4.9**. The first step (**Figure 4.9**a) consists in evaporating gold on mica substrates, following the same protocol used to produce the aforementioned plates (1-h heating of mica at 430 °C before evaporation, then growth of a 100-nm Au layer, followed by a 2-h annealing at the same temperature). Afterwards, a p-doped Si plate (previously cleaned by 3-minute sonicating baths in acetone, ethanol and distilled water, successively) was immobilized on top of the gold surface with a biphasic epoxy glue (**Figure 4.9**b). After a minimum resting time of 24 hours, the mica/Au/glue/Si sandwich was immerged in a Dewar flask filled with liquid nitrogen, until a cracking noise signaled the cleavage of the mica substrate [229] (**Figure 4.9**c).

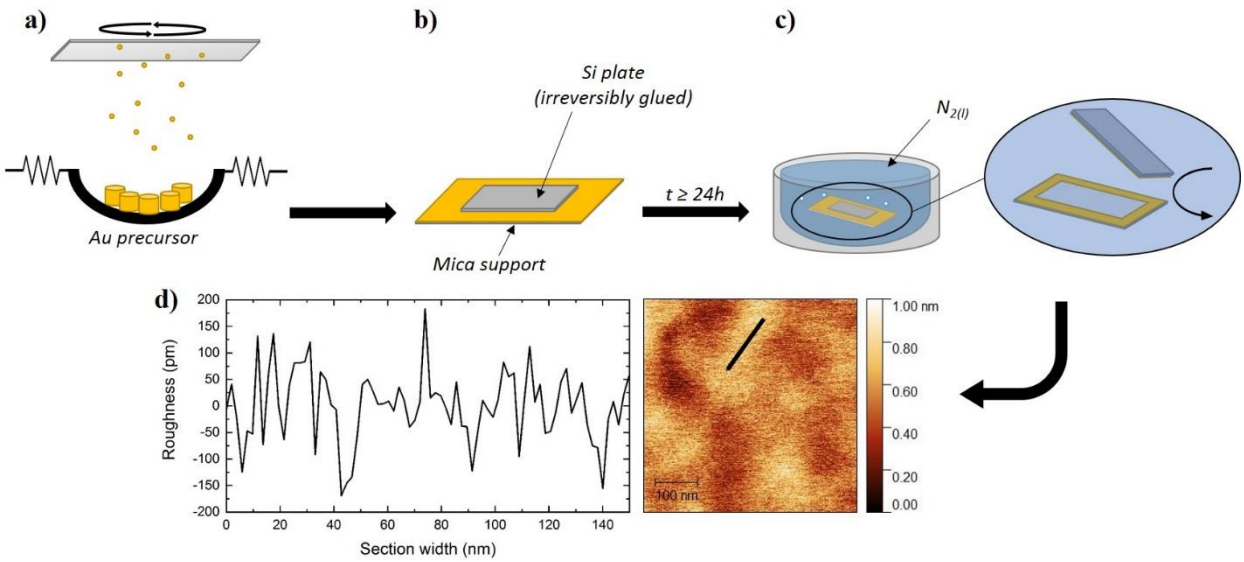

Figure 4.9. Fabrication of ultra-flat gold substrates by cryogenic method: (**a**) gold evaporation on mica, (**b**) gluing of Si plate on Au-on-mica substrate, (**c**) immersion in liquid nitrogen and detachment of the Au-on-Si plate. **d)** AFM maps of the Au-on-Si substrate morphology and roughness profiles on the marked section. The root-mean-square roughness in the evidenced section is ~68 pm.

AFM images taken on the so-produced gold plates (**Figure 4.9**d) show a much smoother surface than the one obtained by simple evaporation of gold on mica (**Figure 4.8**a): not only the edges of the terraces are no longer distinguishable, but also the roughness profile shows a maximum peak-to-peak distance of around 400 pm.

These ultra-flat gold substrates were electrografted as well with 4-NBD in the presence of different ChA concentration, then subjected to AFM imaging. The resulting maps, illustrated in **Figure 4.10**a-c, evidence still the formation of molecular clusters, rather than compact layers, which are though more spread and uniformly distributed on the surface (with respect to the rougher substrate). Similarly to the previous situation, when no ChA control is applied (**Figure 4.10**a) the clusters are densely packed, while they become more loose and disperse as ChA is added (**Figure 4.10**b) and even show the underlying gold terraces at higher concentrations (**Figure 4.10**c). Also the height profiles (**Figure 4.10**d) follow a similar trend to the one previously observed: while the layers grown without inhibitor can reach thicknesses of 9 nm (~12 layers), these values decrease progressively to 6 nm (~8 layers) with 0.1 mmol.L^{-1} of ChA and 4 nm (~5 layers) with 0.25 mmol.L^{-1} of ChA.

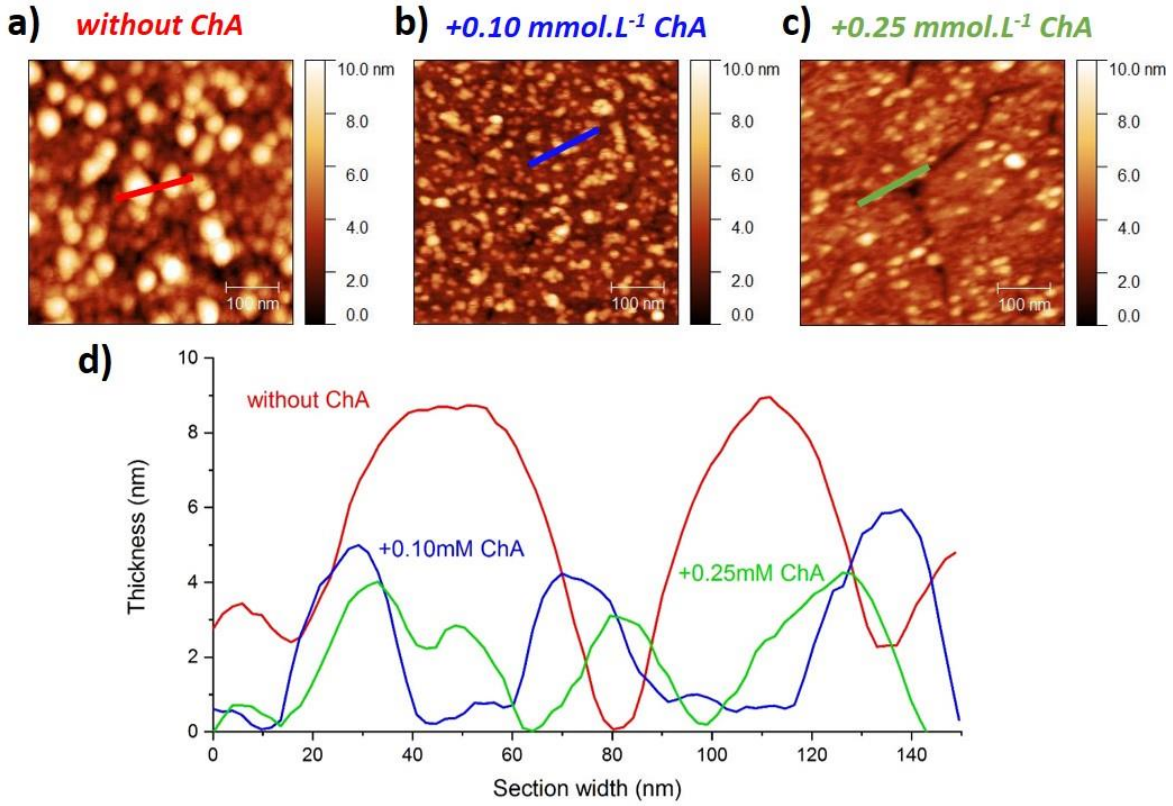

Figure 4.10. AFM maps acquired on ultra-flat gold plates, grafted with 4-NBD (1 mmol.L^{-1}) in presence of (**a**) 0, (**b**) 0.10 or (**c**) 0.25 mmol.L^{-1} ChA concentrations. All the maps were acquired in 500x500nm^2 areas with 256x256 pixels in AFM tapping mode. From the colored section shown in the maps, the corresponding morphology profiles (**d**) were extracted.

In conclusion, even when using smoother and more uniform gold grafting substrates, clustered architectures are always observed, rather than compact layers, especially when the thickness decreases. In fact, despite having the characteristic surface coverage of a monolayer (as it was evinced from the electrochemical analysis), even the structure grafted in presence of 0.25 mmol.L^{-1} ChA is actually composed by isolated chains of molecules, where up to 5 nitrobenzene units can branch together. This result differs from what was observed on PPF [222], where the morphological profile, extracted from the AFM images on the sample at the layer/scratch border, showed compact structures. However, the presence of irregularities in the morphology of 4-NB layers deposited on gold has already been observed [230] upon control of their growth *via* DPPH inhibition: this was revealed by an increase in the gold surface roughness from 1-2 to 6.5 nm before and after grafting of a 4-NB multilayer [230]. Therefore, it is possible that the formation of clustered structures is due partly to the irregularities of the gold surfaces, which might generate local variations on the electrode charge density and therefore heterogeneities in its reactivity, and partly to the presence of the inhibitor molecules, which compete with the diazonium for the reduction on the gold surface and can therefore

hinder its grafting. In any case, since the average thickness and the surface coverage of the 4-NB layer grafted with 0.25 mmol.L^{-1} ChA were comparable to those obtained for monolayers, we will from now on refer to the architecture obtained in such conditions as a "monolayer-like" structure.

4.2.3.5. Composition analysis: IRRAS and XPS

Additional *ex situ* spectroscopic analyses, presented in the next paragraphs, were carried out on 4-NB-grafted gold plates as additional proofs of concept of the inhibition mechanism and to verify that the layers maintained their chemical nature after grafting. For both IRRAS and XPS, the same samples subjected to ellipsometry were employed, grafted on commercial gold plates.

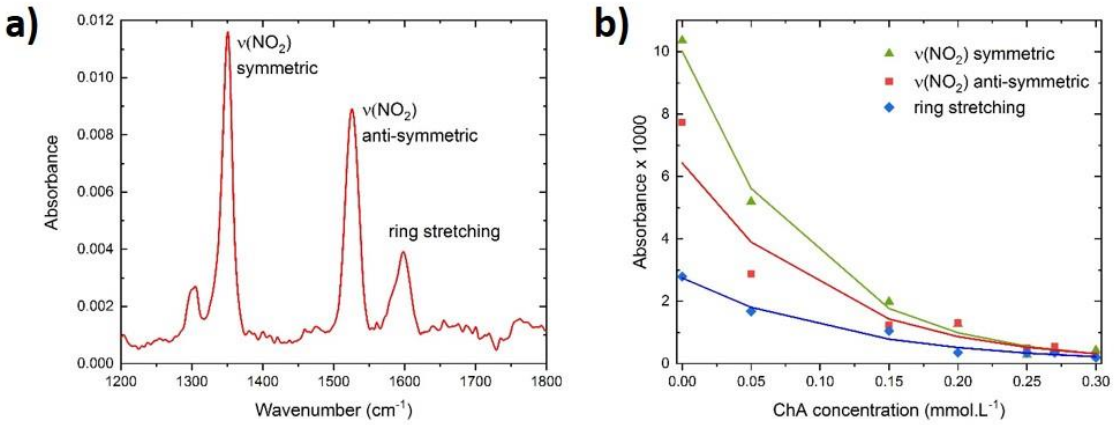

Figure 4.11. a) IRRAS spectrum of a gold surface modified by 4-NBD electrografting (solution without ChA). **b)** IRRAS absorbances as a function of the ChA concentration in the grafting mixture, measured at 1349 cm^{-1} (green, symmetric NO_2 stretching), 1526 cm^{-1} (red, antisymmetric NO_2 stretching) and 1597 cm^{-1} (blue, aromatic ring stretching).

***Layer composition analyses: IRRAS and XPS*.**

The IRRA spectra of modified plates were recorded using a purged (low CO_2, dry air) FT/IR-6100 Fourier transform infrared spectrometer (JASCO), equipped with a mercury–cadmium–telluride detector. For each spectrum, 1000 scans were accumulated with a spectral resolution of 4 cm^{-1}. Before starting the acquisition on functionalized substrates, the background was recorded on a clean, bare gold substrate.

The main IR vibrational features of grafted 4-NB are illustrated in **Figure 4.11**a: the most intense bands arise at 1349 and 1526 cm^{-1}, corresponding, respectively, to the symmetric

and anti-symmetric NO_2 stretching modes, while the ring stretching mode is observed at 1597 cm^{-1} [218].

Figure 4.11b shows the evolution of the band intensities when ChA is added to the grafting solution: as the inhibitor concentration increases, the absorbance first drops abruptly, then declines slightly starting from 0.20 $mmol.L^{-1}$ and reaches almost zero for the submonolayer (0.30 $mmol.L^{-1}$ ChA). The trend resembles mostly to the one observed for the thickness in **Figure 4.6**, thus confirming the higher accuracy of ellipsometry, with respect to the CV-based surface coverage evaluation, in predicting the effect of the increase in inhibitor amount on the layer growth. It also supports the hypothesis that the peculiar trend observed for the surface coverage was related to the limited electrochemical reactivity of NO_2 groups in thick multilayers.

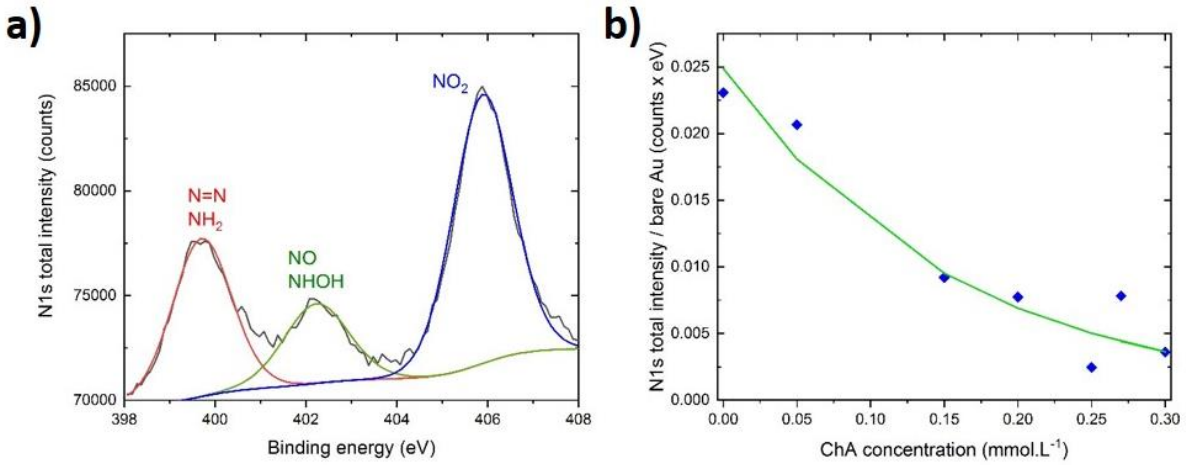

Figure 4.12. a) N1s contributions to the XP spectrum: experimental curve (black) and deconvolutions. **b)** Sum of all N1s peaks for each sample (calculated as the sum of the area of all the N1s peaks in counts per second per eV) as a function of ChA concentration. It was chosen to sum up all the N1s peaks, and not only the NO_2 peak at 406 eV, because of the consistent reduction of nitro groups under the X-ray beam.

XPS measurements were performed using a K Alpha system (Thermo Fisher Scientific, East-Grinstead, UK) fitted with a microfocused and monochromatic Al Kα X-ray source (1486.6 eV, spot size: 400 μm). The pass energy was set to 150 and 40 eV for the survey and the high-resolution spectra, respectively. The spectra were calibrated against the C−C/C−H C 1s component set at 285 eV. The chemical composition was determined with the Avantage software (version 5.9902) by using the manufacturer sensitivity factors.

Figure 4.12a illustrates a detail of the XP spectrum recorded on a 4-NB-grafted sample (without ChA inhibition), showing the energy range where the nitrogen atom bands are found.

The most intense band belongs again to the NO_2 groups and falls at ~406 eV [70,231], while the one slightly above 402 eV is generally attributed to the partially reduced nitrosyl (NO) and hydroxylamine (NHOH) functionalities [70]. As for the peak just before 400 eV, it could either belong to the NO_2 total reduction into amine (NH_2) [232], or else it could signal the formation of N=N bonds inside the multilayer [70]. In fact, despite it would be expected to find azote only in the 4-NBD nitro function, it is likely that the layer partially reduces during the XPS measurement (due to the reducing conditions of the environment during the measurements), thus originating bands belonging also to the nitro monomolecular reduction products. However, if the peak at 400 eV arises from the N=N functionality, this might attest of the formation of branches *via* azo bridges inside the layer [70]. As it was explained in Section 1.2.2.3, this might occur if the molecules grafted directly on the surface are particularly electron-rich and promote the branching of the species in solution through the diazonium functionality, rather than through the radical.

The sum of the intensities of all the peaks belonging to N atoms were calculated for each substrates and plotted against the ChA concentration employed for their grafting: the resulting graph, shown in **Figure 4.12**b, has a less neat decrease, but still shows a similar trend to those previously observed for ellipsometry and IRRAS analysis.

4.2.4 STM-TERS mapping in air

Before following *in situ* the chemical modifications occurring under polarization, the layers were analysed in the ambient *via* STM-TERS. For both these and EC-STM-TERS measurements it was chosen to use the samples grafted onto gold-on-mica substrates. In fact, in spite of the smoother gold surface obtained with the cryogenic cleavage method, the thickness of the silicon support (3 mm) compromises the sample holder stability, because the magnets on the PEEK cell are less efficient in holding it still to the underlying stainless steel plate. The modified substrates were loaded on the homemade sample holder (presented in Chapter 2) and polarized against the tip with a BV of 0.1 V, under the AIST control; the tunnelling current was set at 1000 pA. After mapping the probe surface to find the hotspot, STM-TERS maps were recorded. With respect to the maps acquired on 4-NBM, in this case imaging was performed on smaller areas and with a higher pixel resolution.

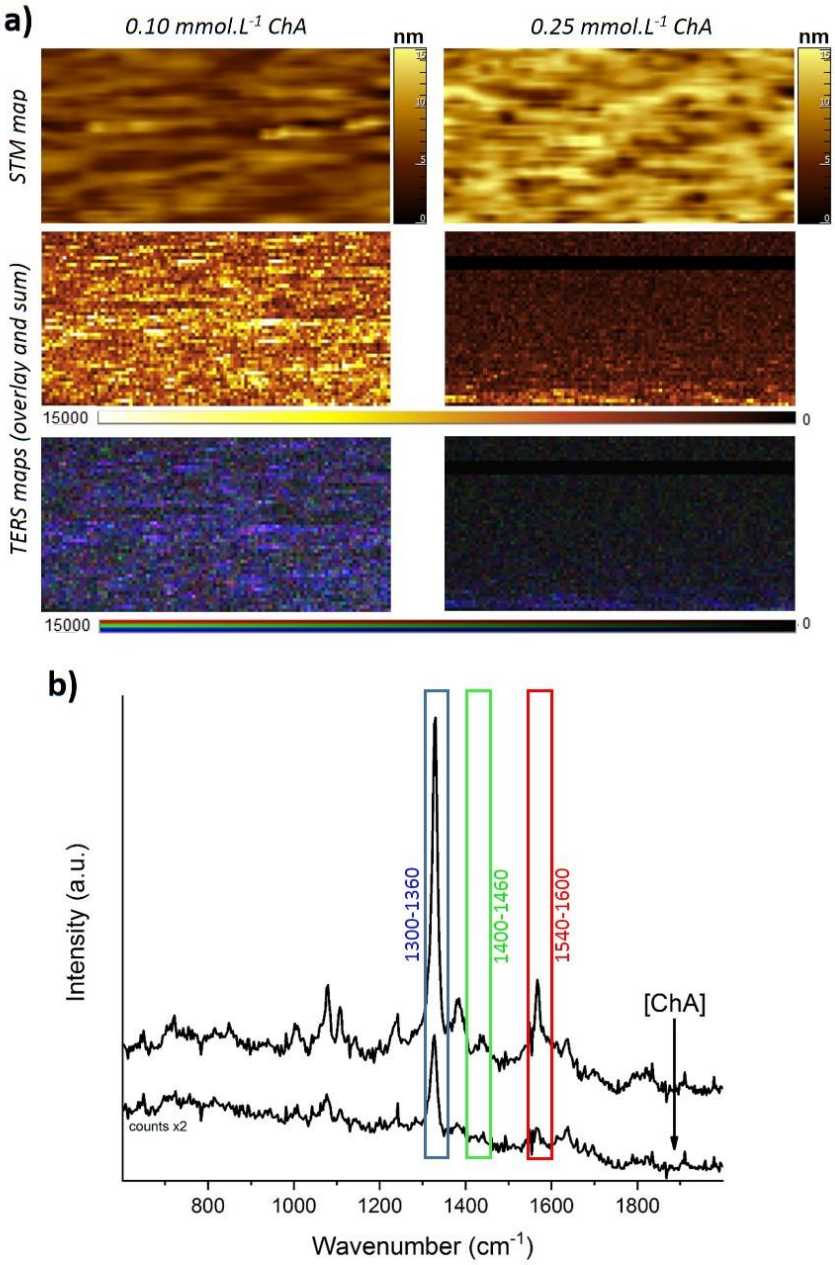

Figure 4.13. a) STM-TERS maps acquired in air on 4-NB grafted in presence of ChA 0.10 (left) and 0.25 mmol.L^{-1} (right). The STM maps showed in the top line were acquired simultaneously to the TERS maps, presented in the other two lines, which are obtained by integration of the band ranges shown in (**b**): the intensity of the three ranges is summed in the middle line (to show the overall molecular distribution) and superposed in the bottom line (to show the distribution of the predominant species among the pixels. The colored bars indicate the height (nm) and the intensity (arbitrary units) scales in the STM and TERS maps, respectively. All the maps were acquired on 300x150 nm^2 areas with 100x50 pixels, each one corresponding to a single Raman spectrum, acquired in 0.5 s with 160 µW power (1% of the nominal laser power) of the 632.8 nm laser line. For STM, it was set BV = 0.1 V and I_T = 1000pA. **b)** Spectra obtained by integration of all the pixels for each map presented in (**a**).

Results for the samples grafted with 0.1 and 0.25 mmol.L^{-1} ChA are shown in **Figure 4.13**a. The overall spectral profiles, averaged from the TERS maps (**Figure 4.13**b), resemble the one observed for grafted 4-NBM (**Figure 3.4** in Chapter 3), although the band positions are

slightly red-shifted for the diazonium-derived layers. This is due to the stronger, covalent bond they form with the gold surface, differently from the mercaptans, which are expected to be less tightly bonded to the gold substrate than diazonium salts [39]. More specifically, the main band at 1327 cm^{-1} belongs to the symmetric NO_2 stretching, while the weaker signatures at 1080 and 1568 cm^{-1} are attributed, respectively, to the O-N-O scissoring (coupled with ring modes) and to the ring stretching modes [44]. A summary of all the signatures encountered in these and the following spectra are reported in Table 4.1.

However, when comparing to each other the two spectra of the diazonium samples, some differences can be noticed. First, the intensity of the spectrum decreases abruptly with the increase in ChA concentration: if on one hand this proves the effectiveness of the inhibition effect, on the other hand it complicates the detection of the 4-NB "monolayer-like" structure. This is evidenced also in the TERS maps (**Figure 4.13**a): while in the sample grafted with less ChA the pixels are brighter and uniformly distributed, an increase in inhibitor content provokes an overall decrease in the pixel intensity and the aggregation of the brightest spots in few, limited areas. This is consistent with what observed by AFM, where the molecular clusters seemed more uniformly distributed over the gold surface on thicker sample, while they become sparser and smaller upon increase in ChA content. Additionally, in the thicker layer it can be noticed the presence of some bands in the N=N stretching range, which do not appear in the "monolayer-like" structure. As it was also observed for the XPS results (**Figure 4.12**a), these bands most likely arise from the branching of 4-NBD species in solution to the pre-grafted layers through the diazo moiety [55,59]: when this occurs, an azo bridge is formed between the grafted and the incoming molecule. For PPF substrates, Menanteau *et al* showed that the number of N=N bonds (evaluated by XPS) increases with the inhibitor concentration, and related this result to the decrease in surface coverage and to the modification in the grafting mechanism *onto* the substrate provoked by the presence of the inhibitor [69]. This might seem in contrast with our results; however, Doppelt *et al* observed that carbon surfaces can already promote the grafting of the first layer of molecules through the diazo function if they present residual oxygens, while this has not been reported for metal surfaces [55]. As a consequence, it is assumed that the N=N bonds will be formed only in the middle of the branched chains and not at the branching point on the gold substrate, therefore it is less likely to find them if the chains length decreases.

A consideration must be done regarding the STM maps. In spite of the impossibility of imaging the molecular species, because of the tip penetration inside the layers, we expected that a higher spatial resolution could be achieved, with respect to the maps previously acquired on 4-NBM samples, by decreasing the scanning size and increasing the number of pixels. However, not only no improvements in the topography could be remarked, but also consistent drifts issues were noticed, most likely due to the longer total acquisition time. This is particularly evident in the TERS maps on the right side of **Figure 4.13**a, which show a black horizontal band on their upper part, most likely corresponding to a temporal loss of the hotspot due to a random tip/objective misalignment. Hence, in order to avoid instabilities in the system during the measurements, lateral resolution should rather be sacrificed in favour of speed.

In conclusion, the results obtained from the different analytical techniques confirm the efficiency of ChA, already at low concentrations, in controlling the 4-NB electrografting process on gold by reducing the excessive layer growth. Without inhibitor (or in presence of very small quantities), the layers tend to arrange in disordered multilayers, where each new unity can branch forming a C-C bond (grafting *via* 4-NB radical formation) or through an azo bridge (grafting *via* diazo function). These tendency is less and less pronounced as the inhibitor amount increases, even though the molecules rather aggregate in shorter and sparse clusters, instead of forming compact and uniform layers. In a "monolayer-like" structure, which is expected to be obtained for a 0.25 $mmol.L^{-1}$ concentration of ChA, the presence of azo bonds is not detected, meaning that branching occurs only to limited extent and, if so, mostly *via* the formation of radical intermediates.

4.3. Surface reactivity screening by EC-TERS mapping

Through *ex situ* characterizations of the 4-NB layers produced by reduction of diazonium salts, important insights on their structure and composition could be gathered. In the following paragraph, the impact of layer properties on the electrochemical reactivity of the derivatized electrodes will be assessed, by extracting the (electro)chemical signatures of the nitro entities distributed within 2D or 3D network of aryl groups interconnected via C-C or azo bonds. The level of complexity of the 4-NBD-derived layer architecture is expected to impact the homogeneity of the nitro reduction reaction and/or to affect its kinetics. To address this question, EC-STM-TERS measurements were carried out on 4-NB-functionalized electrode, prepared *via* the controlled 4-NBD electroreduction in the presence of ChA.

As the kinetics of the nitro electrochemical reduction is not expected to be homogeneous across the electrode surface, the dynamics of composition at the nanoscale accessible through time-resolved TERS measurements, as demonstrated in Chapter 3, would provide an incomplete/inaccurate depiction of the reactivity of 4-NB layers. Instead, spatially-resolved composition mappings (hyperspectral TERS maps) were performed *in situ* at specific polarizations of the derivatized electrodes, in contact with the same alkaline buffer electrolyte used in Chapter 3.

4.3.1 Measurement setup

The EC-TERS setup is similar to the one presented in Chapter 3. Briefly, the open spectro-electrochemical cell specifically designed for EC-STM-TERS uses a partially insulated and bended TERS-active gold STM probe as WE1, a flat 4-NB-derivatized gold electrode as WE2, a platinum ring as CE and a silver wire as *pseudo* RE (instead of Ag/AgCl), both attached to the cell wall, and a 40X water-dipping objective lens. The cell was filled with the bicarbonate buffer, previously deoxygenated, and connected to the homemade bi-potentiostat. This latter controls the electrochemical polarization of both WEs while maintaining a potential difference (STM bias voltage, BV) to ensure a net tunneling current flow upon contact of the STM tip with the sample surface. The tunneling current is measured and amplified by the conductive unit connected to the STM-tip (maintained at the virtual ground). Chronoamperometric potential steps can be applied to both electrodes using a waveform generator connected to the voltage inputs of channels 1 and 2 of the bi-potentiostat.

The issue of the instability of the tip position on the sample surface and/or of the TER signal under large polarization in alkaline medium (already raised in Section 2.4.4) applies here as well. The choice between large polarization of both WEs at constant bias voltage, or large bias voltage at constant tip WE1 potential (polarization of substrate WE2 only) depends mainly on the sequence envisaged for the potential exploration (fast or slow potential scan, lower and higher potential limits), on the electrode nature and on the electrolyte. In the previous study with 4-NBM presented in Chapter 3, where the potential was swept at relatively high scan rate, increasing the BV while maintaining the tip potential at 0 V did not affect the TERS signal intensity. However, as **Figure 4.7** showed, the reduction of the nitro moieties in the diazonium-derived layers occurs at lower potential than in 4-NBM SAMs, therefore larger BV (typically E_{tip}-$E_{substrate}$ > 0.6 V) should be applied during TER mapping to explore their electroactivity. This aspect, along with the particular working conditions employed for the following analyses,

where each potential step lasts a few minutes, might induce the weakening or disappearance of spectral features (even after averaging the signal over all the pixels). The following paragraph will present the experimental conditions adopted to overcome this issue and the results obtained on the 4-NB layers subjected to potential-step reduction.

4.3.2 TERS mapping under polarization

Three gold samples functionalized with 4-NB layers of various thickness and structure were subjected to *in situ* TERS measurements: a first one functionalized without inhibition control, a second one with a moderate ChA quantity (0.10 mmol.L^{-1}) and a third one with a "monolayer-like" structure, obtained with larger ChA quantity (0.25 mmol.L^{-1}).

4.3.2.1. Polarization sequence

Initial conditions for the EC-TERS analyses consisted in the application of E_{tip} = +100 mV and E_{sample} = 0 V vs Ag/Ag^+ (thus BV = 0.1 V) and of a set-point value of the tunneling current I_T = 1 nA. Then, during the exploration of the [0; -500mV] potential range, the potential of both the tip and the sample were decreased by negative steps of 100 mV while keeping the BV at 0.1 V, therefore until E_{tip} = -400 mV and $E_{substrate}$ = -500 mV (**Figure 4.14**a). For more negative potential explorations, the tip potential was not further lowered to limit the occurrence of side reactions (electrolyte and/or oxygen reduction) and the recording of high associated faradaic currents, which could compromise the efficiency of the STM regulation for the control of the tip-sample distance. By maintaining E_{tip} = -400 mV and applying negative potential steps down to – 1 V only to the sample (effective BV increase up to 0.6 V, **Figure 4.14**b), clear TERS spectral signatures could be recorded even when reaching very negative polarizations. Finally, the sample potential was brought back directly to -600 mV and then gradually increased (always in steps of 100 mV) up to 0 V. The tip potential and/or the BV were changed accordingly.

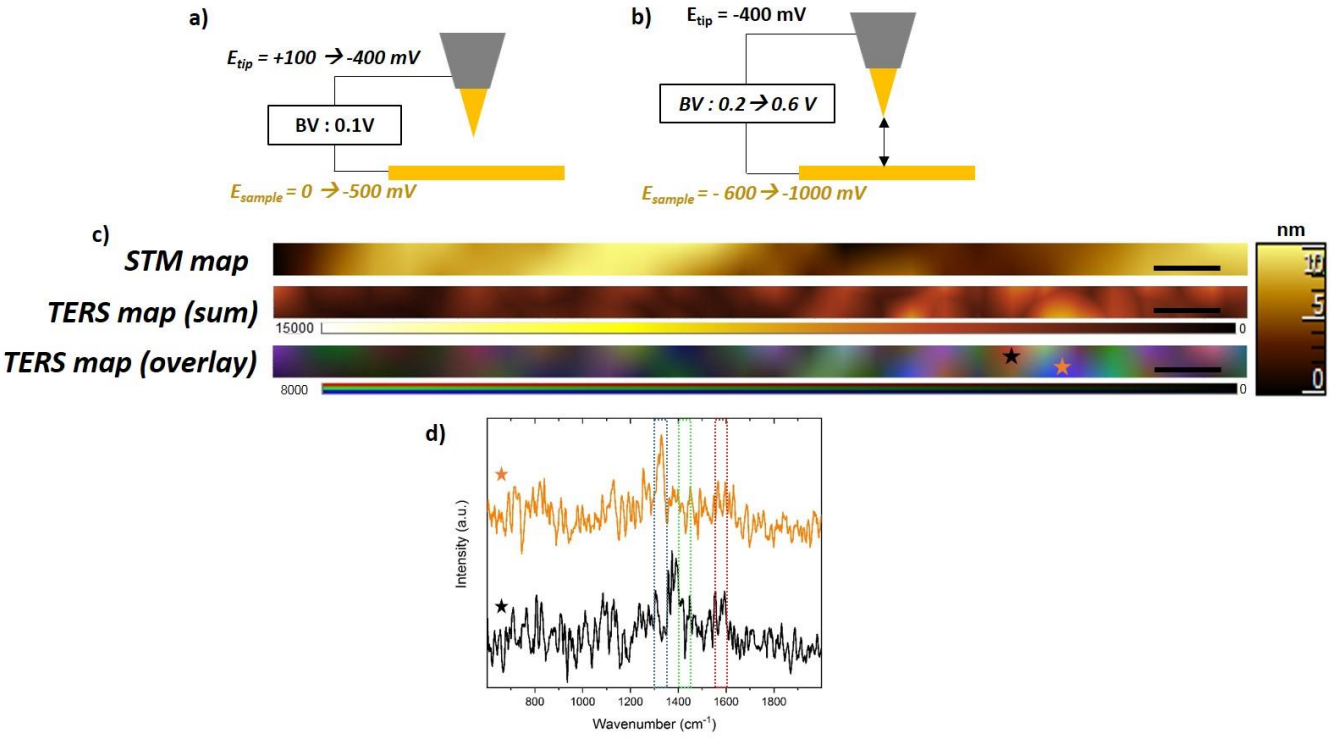

Figure 4.14. Chronoamperometric EC-TERS measurements on the "monolayer-like" sample: **a)** scheme of tip/sample polarizations and BVs for $E_{sample} \leq$ - 500 mV vs Ag and **b)** for E_{sample} > - 500 mV vs Ag; **c)** example of STM-TERS mappings recorded at E_{sample} = -400 mV on the 4-NBD + 0.25 mmol.L^{-1} ChA sample (the scale bars represent 10 nm, while the lateral color scale identifies the height trends in the STM map); **d)** two individual TERS spectra extracted from the TERS map (**c**) (star symbols).The top STM map in (**c**) was acquired simultaneously to the TERS maps below, which are obtained by integration of the band intensity on the 3 energy ranges blue, green, and red in (**d**) (same as the ones shown in **Figure 4.13**b). The intensity of the three ranges is summed in the middle map (to highlight the overall molecular distribution) and superposed on the bottom map (to show the distribution of the predominant species among the pixels. The colored bars indicate the height (nm) and the intensity (arbitrary units) scales in the STM and TERS maps, respectively. All the maps were acquired on the same 300x10 nm^2 area with a resolution of 30x2 pixels (with an acquisition time of 0.5 s/pixel, 160 µW power (1% of the nominal laser power) of the 632.8 nm laser line, BV variable, I_T = 1 nA). Background removal and smoothing were performed on all the spectra.

4.3.2.2. EC-STM-TERS mapping

For each potential step, the position of the tip hotspot was readjusted by slight displacement of the objective piezo-scanner and control of the recorded TERS intensity, then a STM-TERS map was acquired on a 300x10 nm^2 area with a 30x2 pixels resolution (0.5 s acquisition per pixel). **Figure 4.14**c reports, as an example, the maps acquired on the "monolayer-like" structure polarized at -400 mV. Analogously to what observed for 4-NBM, it was possible to correlate the gold sample surface morphology with the molecular distribution. More specifically, the highest molecular density (identified by the brightest spots in the TERS map obtained by the sum of the pixel intensities) seems to be located in the dark zone of the

STM map. This is likely to correspond to an area (most likely an edge) between two adjacent gold terraces, hence it supports the hypothesis (formulated on the basis of the AFM mapping results) that the molecular clusters tend to form preferentially in these zones.

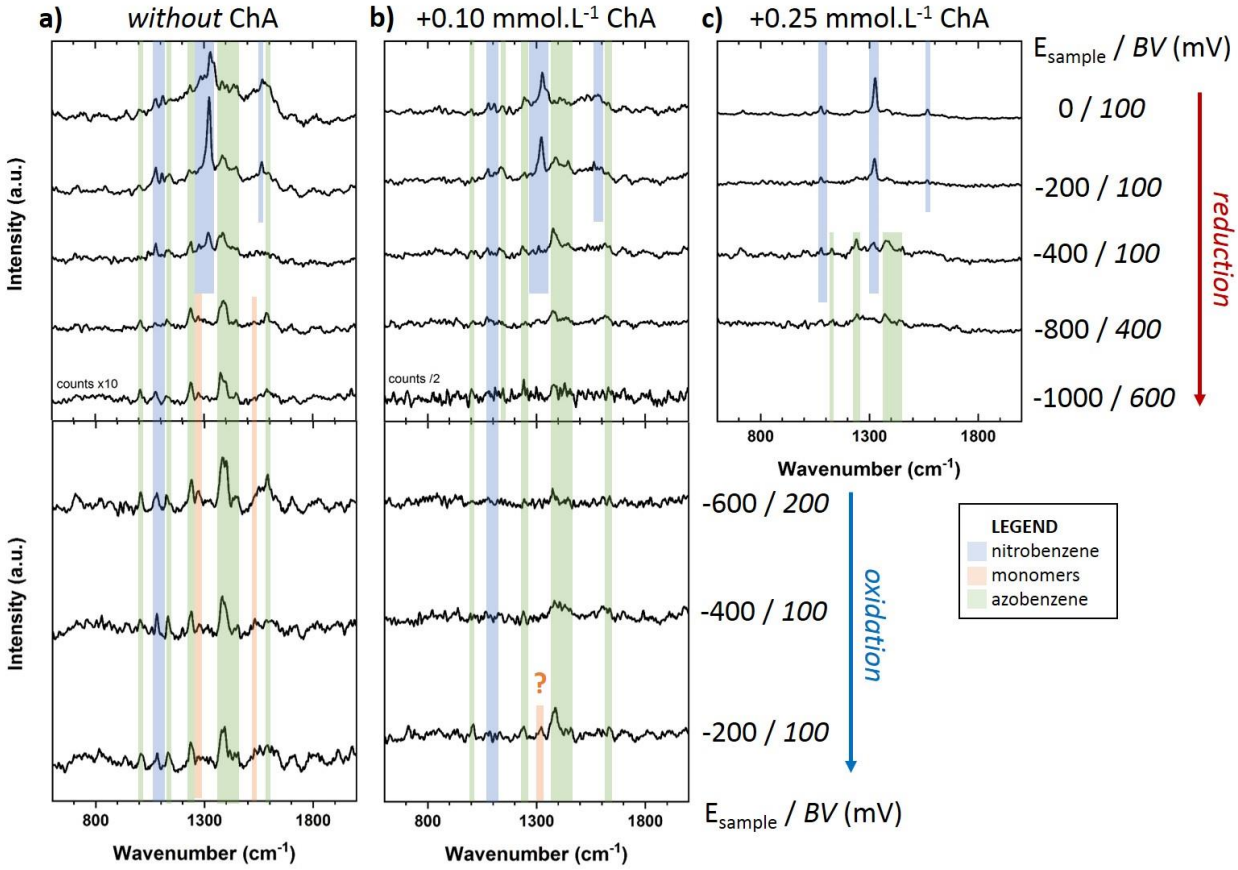

Figure 4.15. TERS signature dependence with the potential - TER spectra averaged from the 60-pixel 300x10 nm^2 maps (acquisition 0.5 s/pixel, 160 µW power (1% of the nominal laser power) of the 632.8 nm laser line), recorded *in situ* onto derivatized gold electrodes in bicarbonate buffer at some of the applied potential steps. The samples were gold plates modified by electroreduction of 4-NBD in presence of 0, 0.10 and 0.25 mmol.L^{-1} of ChA (from left to right). BV indicates the tip-sample bias voltage applied during each polarization step. From one map to the other, the scanned area was shifted respect to the previous one to minimize the production and detection of photo-induced reaction products. Background removal and smoothing were performed on all the spectra.

Moreover, thanks to the TERS map reporting the overlaid intensities for three different spectral ranges, it is possible to assess the spatial distribution of composition (and therefore the reactivity heterogeneity) on the sample surface with a resolution of few nanometers. This aspect is evidenced in **Figure 4.14**d, which reports the different spectral signatures acquired on two adjacent pixels: while in the blue pixel (marked by the orange star) the nitrobenzene signature is still recognizable, in the red/green pixel (black star) it has already disappeared and the azobenzene bands can be identified, while the sample polarization is only -400 mV. Note that the constant raster scanning of the tip, although on a limited scan area (300x10 nm^2),

reduces the risk of photo-induced transformations (formation of dimers); it also increases the probability to extract the composition of the molecular clusters, which are rather sparse on the surface of the "monolayer-like" sample (as highlighted earlier by *ex situ* AFM measurements).

After each acquisition and before the application of the following potential step, the STM-TERS tip was temporarily retracted from the sample surface to minimize possible tip crashing induced by possible transient electrochemical currents impacting the STM regulation of the tip-sample distance control. TERS data at different potential step could be recorded every 5 to 6 minutes. Ultimately, to better assess the difference of reactivity of the three samples, their respective composition at a given potential step was evaluated from the spectral signatures averages on each 30x2 pixels TERS map. All the results, for different samples and potentials, are illustrated in **Figure 4.15**, while all the Raman band assignment can be found in Table 4.1.

4.3.2.3. TERS analysis of the thickest 4-NB layer

In the thickest sample (grafted *without* ChA, **Figure 4.15**a) the average spectrum acquired at 0 V (before starting the reduction) shows quite a noisy background and is characterized by a higher number of characteristic bands than the standard nitrobenzene spectrum. This suggests the presence of disordered and intricate structures on the gold surface, in which molecules with different orientations and different environment may be associated to vibrational bands at various shifted energy positions [44]. For instance, the main NO_2 band at 1327 cm^{-1} is accompanied by a blue-shifted component at 1345 cm^{-1}, while the O-N-O scissoring, usually observed above 1110 cm^{-1} in monolayers, red-shifts at 1080 cm^{-1} in the multilayer structures [44]. Additionally, as it was already observed in XPS and further supported by *ex situ* STM-TERS measurements, the presence of bands around 1400 cm^{-1} may suggest the presence of azo bonds inside the grafted layer that do not derive by electrochemical or photocatalytic reactions, but rather from the diazo-mediated branching of the species in solution [55]. The overall spectral profile does not change at -200 mV, even though an increase in intensity is observed, especially for the main band at 1327 cm^{-1}. This effect might originate from a possible intensification of the local plasmon enhancement while exploring negative polarizations, although not observed with 4-ATP. At -400 mV the nitro group starts reducing, as it can be seen from the drop in its band intensity, and from its total disappearance at -800 mV. Concomitantly, a weak signature at 1271 cm^{-1} arises, maintains its intensity at negative potential and then disappears when scanning the potential backwards to more positive values. This behavior of the band at 1271 cm^{-1} could be associated to the N-O stretching mode of the

intermediate 4-HAB, which is expected to form upon partial reduction of 4-NB but has not been clearly identified for 4-NBM. Meanwhile, the N=N bands grow in intensity and become the dominating features, both at the lowest potential and after re-oxidation of the sample. This is in agreement with what previously observed for 4-NBM. It was then concluded that the bimolecular reaction path may be favored in alkaline medium and may lead to the preferential formation of azo species, which do not (easily) reduce irreversibly to amine.

Table 4.1. Assignment of the main bands observed in the TERS spectra of the compounds involved in the 4-nitrobenzene reduction mechanism. Intensities: *vs* (very strong), *s* (strong), *m* (medium) and *w* (weak). Denominations: SL (single layer), ML (multilayer). The reference values for ML were obtained by calculations in ref. [44].

Attribution	**$\tilde{\nu}$ – EC-STM-TERS (cm^{-1}) – adsorbates**	**References**
Nitrobenzene		
O-N-O scissoring + ring modes	1080 *w*, 1107 *w* (1110 SL; 1091 ML)	[44]
Ring breathing	1296 *w* (1250, 1282 SL;1248, 1289 ML)	[44]
ν $(N\text{-}O)_{sym}$	1327 *vs*, 1345 *m* (1344 SL; 1325, 1365 ML)	[44]
Ring stretching	1568 *m* (1589 SL; 1510, 1598 ML)	[44]
Monomers		
ν (N-O)	1271 *w* (1230 hydroxylamine) 1322 *w* (1320 *m* nitroso)?	[125,208]
Ring stretching	1557 *m* (1585 *s* hydroxylamine)	[208]
Azobenzene		
δ (C-H)	1009 *m* (996 *m*)	[208,219]
ν (C-N) + ring modes	1140 *m* (1143 *vs*)	[219]
ν (N=N) + ring modes	~1380 *s*, 1440 *m* (1388 *m*, 1424 *s*, 1463 *w*)	[204,219]
Ring stretching	1585 *m* (1583 *m*)	[204,219]

4.3.2.4. Intermediate 4-NB thickness

When measuring the response of a slightly thinner layer (grafting with 0.10 $mmol.L^{-1}$ ChA, **Figure 4.15**b), the results are overall similar: the NO_2 and the N=N signals are present from the OCP and the azo bands become the most intense after reduction of the nitro function. However, the average spectral intensity is lower (proportionally to the lower surface coverage

expected for a partially controlled grafting of the layer) and also the background observed for multilayer structures is less intense. The bands previously assigned to 4-HAB (at 1271 and 1577 cm^{-1}) are not detected on this sample, although a weak signature appearing at 1322 cm^{-1} in the -200mV backward step could belong to the N=O stretching of the 4-NSB product, deriving from the re-oxidation of 4-HAB.

4.3.2.5. TERS analysis of the "monolayer-like" sample

Finally, in the "monolayer-like" structure (**Figure 4.15**c), the spectral profile at the OCP decreases even more in intensity but, at the same time, becomes also neater and sharper, thus showing only the standard Raman bands of nitrobenzene, reported for monolayer structures. Moreover, as it was observed for measurements in air, no N=N bands are noticed prior to negative polarizations; they only start arising at -400 mV, concomitantly with the NO_2 band disappearance. However, differently from the other sample, the "monolayer-like" assembly did not show any spectral signature neither upon polarization at -1 V, nor during the backward steps towards less negative potentials. This would suggest that the reaction did not "stop" at the formation of dimers but instead continue towards the 4-AB final product. This compound is known to have less intense signatures with respect to 4-NB when adsorbed on a surface [208]. Nevertheless, similarly to what was shown for 4-ATP by TERS in Chapter 3 (and to what reported by SERS investigations [221]), we would have expected also for 4-AB to observe the b_2-type modes signatures (similar to those of the dimers) in alkaline solution. The absence of these bands, though, might be explained by a difference in the nature of the two kinds of molecules, which differ by a sulfur atom: this is supposed to influence the 4-ATP interaction with the gold substrate (in terms of metal-molecule charge transfers and reciprocal orientation) and therefore to have an effect on the optical properties and/or the CT enhancement of the tethered molecule under TERS investigation. In conclusion, it could be plausible that 4-AB is actually formed, but that its signature cannot be (easily) revealed. A confirmation of this hypothesis could be yielded by performing TERS measurements on a sample grafted with 4-AB by electroreduction of its diazonium salt derivative.

Nonetheless, it cannot be excluded that also detection issues could have occurred, either because of the excessive sparseness of the molecular structures on the surface, or because of the inefficient tip enhancement over little quantities of molecules.

4.3.3 Structure-reactivity relationships

The comparison of the averaged spectra evolution among the different samples shows that stable N=N dimers form in the thickest architectures, while the "monolayer-like" structure should reduce completely to 4-AB. This seems suggesting that thicker layers have slower 4-NB reduction kinetics, most likely due to their disordered molecular architectures and long branched chains, which are expected to hinder the charge transfer through the aryl layer between the metal and the redox groups disseminated within the 3-D structure. Besides, the compactness of the chains inside the layer might promote the coupling of reaction intermediates, given their proximity in the structure, thus explaining the detection of bands belonging to azobenzene groups at potential as high as -400 mV. These add up to the other azo bridges that had formed during the grafting procedure because of the diazo-mediated branching mechanism. Ultimately, the appearance of N=N spectral features already at the beginning of the reduction process, which stay sharp even at low potentials and on the backward potential scan, attests of their high stability and might suggest a densification of the molecular architecture due to the formation of novel inter-molecular bonds. This explains why, even when polarizing the substrate at more negative potential with respect to the cathodic peak in the CV experiment (**Figure 4.4**), the formation of amino moieties is expected to occur only to a limited extent and is therefore not detected.

On the contrary, "monolayer-like" structures seem containing less (or no) azo bridges inside their chains before the application of negative polarizations on the sample. Beside, their arrangement in sparse clusters, where the short molecular chains are supposed to be more rigid and farther from each other than in the multilayer samples, might be a deterrent for the formation of dimeric species during the 4-NB reduction. Dimers are shown to appear only around -400 mV and seem proceeding quickly towards total reduction into 4-AB, as suggested by the disappearance of any signature upon polarization at -1 V and the absence of signals also when bringing the potential back towards more positive values. These results seems in disagreement with what observed in the CV experiment (**Figure 4.4**), which showed the anodic peak belonging to the 4-HAB → 4-NSB transformation in the backward scan and therefore proves that not all the 4-NB groups converted irreversibly to 4-AB. However, it must be reminded that in EC-STM-TERS analyses the samples are subjected to reducing potentials for longer times than the in the CV measurement, hence their transformations can actually get to completion.

Contrary to expectations, 4-NBM SAM show a more similar reactivity to 4-NBD multilayers, rather than to the "monolayer-like" structure: also in the thiol-functionalized surfaces azobenzene appears in short times, becomes the most abundant species and reduces slowly to 4-ABM. This might be due to a difference in the efficiency of the metal-to-molecule charge transfer, which in 4-NB "monolayer-like" samples is supposed to occur faster, since molecules are either grafted directly on the substrate or, if branched, separated by few (~2-3) units from it. On the other hand, in 4-NBM the transfer might be damped by the presence of the methyl group, which separates the aromatic ring from the sulfur atom linked to the surface, while in 4-NB multilayer the damping effect is most likely due to the longer extension of the branched chains. Besides, the high flexibility of the 4-NBM molecules on the surface, due to the presence of the methyl group, should ease the dimerization process among adjacent species and lead to a stabilization of the N=N bond, as it is expected to occur in multilayers. However, these considerations are merely speculative: a proper comparison among the two different systems might be done only after subjecting both to either dynamic or step-by-step EC-TERS analyses.

4.4. Conclusions

To summarize, this experimental work satisfied two important requests. On one side, it allowed elaborating an optimized procedure for controlling the growth of 4-NBD layers on gold under electrochemical conditions. This was possible thanks to the use of the ChA species, which works as redox cross-inhibitor and prevents the excessive formation of 4-NBD-derived radicals close to the sample surface. All the characterization analyses performed on the grafted layers attest of a sharp decrease in the layer thickness with the increase in inhibitor content. More precisely, according to thickness evaluation by ellipsometry, a "monolayer-like" structure is expected to be obtained with a 0.25 $mmol.L^{-1}$ ChA concentration. Only the surface coverage seems decreasing more slowly with the increase in the amount of ChA in the grafting mixture. However, this apparent effect is due to the unsuitability of the electrochemical approach for surface coverage evaluation in thick multilayers. Since their disordered and compact architectures hinder the reduction of the electroactive NO_2 groups inside the layer bulk, these remain silent and lead to an underestimation of the surface coverage value. Albeit, images acquired on the functionalized surfaces show that, rather than spreading uniformly on the sample surface, molecular species tend always to assemble in clusters. These nucleate first on the gold terraces edges, then propagate towards their center, and are observed to be less

thick and sparser as the ChA content in the grafting medium increases. The superficial roughness of the substrate plays as well a role in the clusters distribution, as smoother and more uniform surfaces will favor the densification of the clusters and yield more homogeneous structures.

Once gathered the control over the fabrication of the diazonium-derived layers and the knowledge over their chemical composition and structure, our work focused on the correlation of this information with the layer electrochemical reactivity in *in situ* conditions. This was possible thanks to the EC-STM-TERS setup, which was employed to image the evolution in the chemical composition of the samples surfaces while subjecting them to chronoamperometric steps. Spatially resolved STM-TERS maps allowed at the same time distinguishing among zones of heterogeneous reactivity on the same surface, and also relating the molecular distribution with the surface morphology. Besides, very low potential values (down to – 1 V) could be applied on the sample without affecting the detection efficiency. This was possible by finding a compromise for the tip/sample distance, which had to guarantee a good probe stability and, at the same time, a strong TER effect. Finally, average spectra extracted from all the maps at different potentials were conveniently used to evaluate the electrochemical behavior evolution of the layers under polarization. While thick, compact layers seem to privilege the formation of stable azo bridges, rather than the total reduction into amine, "monolayer-like" structure are suspected to react quicker and to be more prone to reduce totally and irreversibly. Further EC-TERS dynamic studies and TERS investigation on 4-AB grafted layers would be needed to confirm this hypothesis.

In conclusion, the versatility of the employed EC-STM-TERS setup, in terms of limit of detection, spatial resolution and adaptability to work in real operating conditions (i.e. in liquid and under polarization) makes it an ideal analytical tool for relying the reactivity of a functionalized surface with the evolution in its chemical nature and structure.

Conclusions and perspectives

In this thesis work, the level of sophistication reached in the development of the EC-STM-TERS technique has opened the way to dynamical analyses of the electrochemical transformations occurring on electroactive layers, immobilized on conducting surfaces, over a wide range of potential and with a lateral resolution down to 4 nm. The strong analytical potential of this methodology is illustrated by the dynamic or spatially resolved characterization of the chemical transformations involving the nitro functionality, immobilized on gold surfaces through either thiol- or aryldiazonium-derived species.

The wide knowledge of the chemistry of thiols and diazonium salts accumulated over the last decades makes their use strategic for efficient surface functionalization. Nevertheless, the structures elaborated *via* the two approaches show different interactions and organizations (between molecules and with the metal substrate) that impact the electrochemical behavior of the modified surface. Indeed, thiols form well organized but weakly bonded SAMs, whereas the reduction of aryl diazonium produces robust multilayers (covalent bonding) whose growth and organization are difficult to control. To characterize in real time electrochemical processes occurring on such modified surfaces, the most effective *operando/in situ* techniques developed so far show the required sensitivity for small molecular assemblies, but are limited in terms of spatial resolution. Only a few of them, developed lately, give access to the (electro)chemical reactivity at the nanoscale, although rarely in combination with the chemical signature. Among them, EC-TERS has proved to be particularly interesting and already allowed studying electrochemical processes occurring at functionalized surfaces, even if it is still at its infancy for real-time measurements, with respect to its non-spatially resolved SERS analogue.

To this end, we put a particular effort on the technical developments of the EC-STM-TERS, including the fabrication of STM-TERS gold probes adapted for *in situ* measurements (etching to produce tapered profile, shaping to be integrated within the EC-TERS cell and effective insulation), and the conception of a new 4-electrode TERS-compatible spectro-electrochemical cell, which secures the ease and reproducibility of EC-STM-TERS analyses.

The new developed setup has been first employed for assessing the reactivity of a non-Raman resonant electroactive molecular layers (4-nitrobenzene mercaptan 4-NBM) self-assembled on gold. We have demonstrated that TERS mapping with high lateral resolution (4-nm pixel size) and time-resolved (1 s) measurements could be implemented *in situ* and on a large potential range, thus yielding a deeper understanding of the electrochemical

transformation occurring on nitro-functionalized SAMs. Indeed, a reduction mechanism pathway involving intermediates that cannot be detected electrochemically could be proposed. In particular, our results suggest that the formation of dimers do not originate from photo-oxidation, upon irradiation of the gold tip-sample junction in solution with a red laser, but rather from condensation of reaction intermediates.

More importantly, the knowledge acquired from the study of the model thiolated sample with nitro-entities turned essential for understanding the relationship between the layer structure and its reactivity in more complex architectures, as those obtained by electroreduction of aryl diazonium salts (4-NBD). The control over the layer growth was successfully achieved on gold electrodes through the use of a redox "cross-inhibitor" (ChA), already optimized for carbonaceous electrodes, which enabled the deposition of electroactive molecular structures (4-NB) with controlled thicknesses on gold surfaces. Several *ex situ* characterization techniques confirmed the effectiveness of the grafting inhibition; however, they also revealed the tendency of the molecular species to assemble in clusters, which was not observed on carbonaceous materials and could be explained by the heterogeneity of the gold surface. Moreover, spatially resolved composition mappings by EC-TERS at specific, progressive polarizations suggest that thick layers are more subjected to dimer formation, while thin clustered structures are suspected to react quicker and to be more prone to reduce totally and irreversibly. This is, to our knowledge, the first demonstration of EC-TERS experiments at polarizations as negative as -1 V.

The investigations performed in this PhD work underlined the efficiency and reliability of the EC-STM-TERS technique for highly resolved, sensitive and rich characterizations of thin molecular layers. This approach could be then furtherly used for many other applications and more complex systems. Among them, surface-immobilized molecular layers decorated with electroactive species that act as (bio)sensors or catalysts might be of particular interest. The TERS-active probe could indeed scan the sample and detect the spectral features of the reaction products in the course of their formation, thus allowing to map the distribution of the active sites and assess their efficiency. It should also be able to capture the signatures of the reactive intermediates (such as in electrocatalytic processes), to further decipher the mechanism of their formation. Besides, EC-TERS might be used to monitor *in situ* the chemical transformations occurring upon electro-induced molecular motions, as in the case of the "molecular machines" fabricated from giant rotaxanes. Nonetheless, EC-STM-TERS might not

be ideal for the investigation of softer materials or weakly bounded molecular complexes, whose structures might be heavily altered by the close proximity of the tip in tunneling conditions. A valid alternative for these system could be constituted by an EC-TERS configuration implemented in an AFM setup, where the use of a cantilever in non- or semi-contact mode as scanning probe should prevent this risk. Despite some studies in this extent have already been reported, the robustness of AFM-TERS under electrochemical conditions remains still to demonstrate.

An additional implementation of the EC-TERS setup, suggested by some preliminary results obtained in this work (but not presented in this manuscript), would consist in using the tip as both nanolithographic tool for the realization of molecular patterns on a surface, and as TERS-probe for their characterization. Similarly to SECM-based techniques, in this mode the occurrence of electrochemical reactions would be limited to the area under the tapered probe but with a much higher resolution (few tens of nm expected). This aspect would allow, for instance, reducing small quantities (or even single entities) of diazonium salts in solution, thus promoting the formation of few (or single) aryl radicals that graft locally below the tip. As a consequence, a precise motif of strongly bonded molecular species could be obtained. This method could also be extended to those molecular species that radicalize by photoactivation: in this case, the tip would work as a nanosource of illumination and, thanks to the strong enhancement provided by its tapered apex, could promote localized photopolymerization and photoreduction reactions at minimal excitation powers.

Annexes

Comparison of ChA and DPPH performances as inhibitors

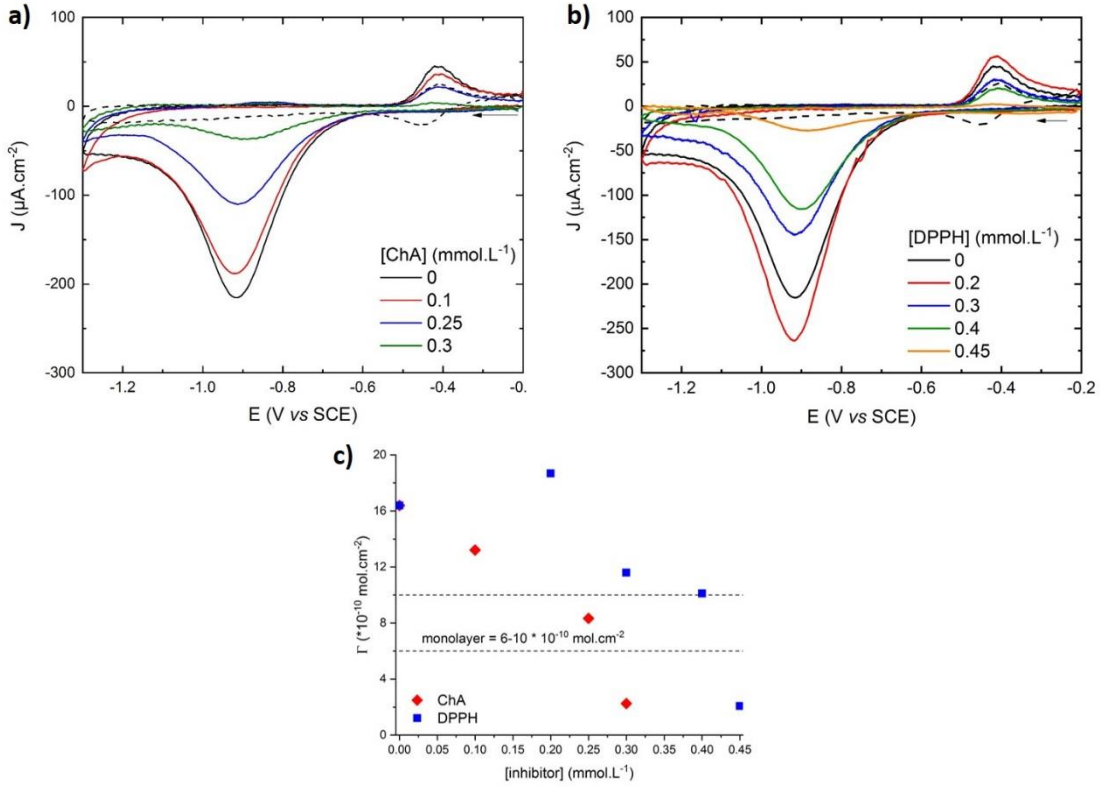

Figure. Comparison ChA *vs* DPPH for the inhibition of 4-NBD-derived layers- CVs recorded in KOH 0.1 mol.L^{-1} on grafted gold plates (from -0.1 to -1.3 V *vs* SCE, at 50 mV.s^{-1}). Grafting was previously achieved in the presence of 1 mmol.L^{-1} 4-NBD and different **a)** ChA and **b)** DPPH concentrations (indicated in the legend on the graph). The dashed black curve represents the second cycle performed on the disk grafted without inhibitor. The values of surface coverage, extracted by the integration of the voltammetric peaks (see Equation (3.5) in Chapter 3), are reported in **c)** for the two inhibitors (ChA, red diamonds, and DPPH, blue squares). The results show that ChA allows obtaining thinner structures at lower concentrations (e.g. for "monolayer-like", 0.25 mmol.L^{-1} for ChA against 0.40 mmol.L^{-1} of DPPH). The overestimation of the surface coverage for 0.20 mmol.L^{-1} of DPPH might be due to the formation of a less dense layer in the presence of small quantities of inhibitor, which ease the solution accessibility to the electroactive groups.

Abbreviations

AC	Alternated Current
AFM	Atomic Force Microscopy
CCD	Charge-Coupled Device
CE	Counter-Electrode
CV	Cyclic Voltammetry
DC	Direct Current
DFT	Density Functional Theory
EC	Electrochemical
EM	Electromagnetic
EQCM	Electrochemical QCM
ET	Electron Transfer
FB	Feedback Mode (in SECM)
FIB	Focused Ion Beam
IR	Infrared
LSPR	Localized SPR
Mt	Mediator-tethered mode (in SECM-AFM)
NC	Nanocrystal
NIR	Near Infrared
NP	Nanoparticle
OCP	Open Circuit Potential
ORR	Oxygen Reduction Reaction
PMIRRAS	Phase-Modulation Infrared Reflection Absorption Spectroscopy
QCM	Quartz Crystal Microbalance

QRE	Quasi-Reference Electrode
RE	Reference Electrode
SAM	Self-Assembled Monolayers
SCE	Saturated Calomel Electrode
SEC	Spectro-Electrochemistry
SECCM	Scanning Electrochemical Cell Micrscopy
SECM	Scanning Electrochemical Microscopy
SEI	Solid Electrolyte Interphase
SERS	Surface-Enhanced Raman Spectroscopy
SHE	Standard Hydrogen Electrode
ShFM	Shear-force Microscopy
SHINERS	Shell-Isolated Nanoparticle-Enhanced Raman Spectroscopy
SNOM	Scanning Near-field Optical Microscopy
SPM	Scanning Probe Microscopy
SPP	Surface Plasmon Polariton
SPR	Surface Plasmon Resonance
STM	Scanning Tunneling Microscopy
TERS	Tip-Enhanced Raman Spectroscopy
TOF-SIMS	Time-of-Flight – Secondary Ion Mass Spectrometry
UME	UltraMicroElectrode
UV	Ultraviolet
WE	Working Electrode
XPS	X-ray Photoelectron Spectroscopy

Acronyms of chemical compounds

3,5-D-*t*-BuBD	3,5-Bis-*tert*-butylbenzene Diazonium
4-ATP	4-Aminothiophenol
4-NBD	4-Nitrobenzene Diazonium (tetrafluoroborate)
4-NTP	4-Nitrothiophenol
4-PBT	(4′-(Pyridin-4-yl)biphenyl-4-yl)methanethiol
ACN	Acetonitrile
APBA	4-(2-(4-Acetylthio)phenyl)ethynyl) Benzoic Acid
BCB	Brilliant Cresyl Blue
BM	Benzyl Mercaptan
BT	Benzothiophene
ChA	Tetrachloro-1,4-Benzoquinone (Chloranil)
DMAB	Dimercapto Azobenzene
DPPH	2,2-Diphenyl-1-Picrylhydrazyl
EDC	1-(3-(Dimethylamino)propyl)-3-ethylcarbodimide Hydrochloride
EtS	Ethanethiolate
Fc	Ferrocene
GC	Glassy Carbon
HOPG	Highly Oriented Pyrolized Graphite
ITO	Indium Tin Oxide
MUDA	11-Mercaptoundecanoic Acid

NB	Nile Blue
NHS	N-Hydroxysuccinimide
PANI	Polyanline
PEEK	Poly Ether-Ether Ketone
PEG	Polyethylene Glycol
PET	2-Phenylethyl
PhS	Thiophenolate
PPF	Pyrolized Photoresistive Film
PSA	Prostate Specific Antigen
PTA	Tri-*p*-tolylamine
$TBABF_4$	Tetrabutylammonium Tetrafluoroborate
TBAF	Tetra-n-butylammonium Fluoride
TEAP	Tetraethylammonium Perchlorate
TEMPO	(2,2,6,6-Tetramethylpiperidin-1-yl)oxyl
TMS	Trimethylsilyl
TES	Triethylsilyl
THF	Tetrahydrofuran
TIPS	Tri(isopropyl)silyl

Symbols and units

a	Radius of a nanostructure	nm
BV	Bias Voltage	V or mV
c	Speed of light	~ 3.10^8 $m.s^{-1}$
EF	Enhancement Factor	-
I_T	Tunneling Current	nA or pA
n	Refractive index	-
NA	Numerical Aperture	-
WD	Working Distance	mm
z	Vertical distance	nm
Δx	Lateral Resolution	µm or nm
Δz	Depth Resolution	µm or nm
ε	Dielectric Constant (of the metal)	-
ε_m	Dielectric Constant (of the medium)	-
λ	Wavelength	nm

Bibliography

(1) Zhang, R.; Zhang, Y.; Dong, Z. C.; Jiang, S.; Zhang, C.; Chen, L. G.; Zhang, L.; Liao, Y.; Aizpurua, J.; Luo, Y.; Yang, J. L.; Hou, J. G. Chemical Mapping of a Single Molecule by Plasmon-Enhanced Raman Scattering. *Nature* **2013**, *498* (7452), 82–86. https://doi.org/10.1038/nature12151.

(2) Chen, C.; Hayazawa, N.; Kawata, S. A 1.7 Nm Resolution Chemical Analysis of Carbon Nanotubes by Tip-Enhanced Raman Imaging in the Ambient. *Nat. Commun.* **2014**, *5* (1). https://doi.org/10.1038/ncomms4312.

(3) Schmid, T.; Yeo, B.-S.; Leong, G.; Stadler, J.; Zenobi, R. Performing Tip-Enhanced Raman Spectroscopy in Liquids: Tip-Enhanced Raman Spectroscopy in Liquids. *J. Raman Spectrosc.* **2009**, *40* (10), 1392–1399. https://doi.org/10.1002/jrs.2387.

(4) Zeng, Z.-C.; Huang, S.-C.; Wu, D.-Y.; Meng, L.-Y.; Li, M.-H.; Huang, T.-X.; Zhong, J.-H.; Wang, X.; Yang, Z.-L.; Ren, B. Electrochemical Tip-Enhanced Raman Spectroscopy. *J. Am. Chem. Soc.* **2015**, *137* (37), 11928–11931. https://doi.org/10.1021/jacs.5b08143.

(5) Hussain, S.; Kongi, N.; Matisen, L.; Kozlova, J.; Sammelselg, V.; Tammeveski, K. Platinum Nanoparticles Supported on Nitrobenzene-Functionalised Graphene Nanosheets as Electrocatalysts for Oxygen Reduction Reaction in Alkaline Media. *Electrochem. Commun.* **2017**, *81*, 79–83. https://doi.org/10.1016/j.elecom.2017.06.009.

(6) Chowdhury, D. R.; Spiccia, L.; Amritphale, S. S.; Paul, A.; Singh, A. A Robust Iron Oxyhydroxide Water Oxidation Catalyst Operating under near Neutral and Alkaline Conditions. *J. Mater. Chem. A* **2016**, *4* (10), 3655–3660. https://doi.org/10.1039/C6TA00313C.

(7) Rao, H.; Bonin, J.; Robert, M. Non-Sensitized Selective Photochemical Reduction of CO_2 to CO under Visible Light with an Iron Molecular Catalyst. *Chem. Commun.* **2017**, *53* (19), 2830–2833. https://doi.org/10.1039/C6CC09967J.

(8) Li, W.; Wang, F.; Li, Z. A Facile Strategy for Fabricating Robust Superhydrophobic and Superoleophilic Metal Mesh via Diazonium Chemistry. *Colloids Surf. Physicochem. Eng. Asp.* **2021**, *630*, 127570. https://doi.org/10.1016/j.colsurfa.2021.127570.

(9) Ielo, I.; Giacobello, F.; Sfameni, S.; Rando, G.; Galletta, M.; Trovato, V.; Rosace, G.; Plutino, M. R. Nanostructured Surface Finishing and Coatings: Functional Properties and Applications. *Materials* **2021**, *14* (11), 2733. https://doi.org/10.3390/ma14112733.

(10) Casalini, S.; Bortolotti, C. A.; Leonardi, F.; Biscarini, F. Self-Assembled Monolayers in Organic Electronics. *Chem. Soc. Rev.* **2017**, *46* (1), 40–71. https://doi.org/10.1039/C6CS00509H.

(11) Skirtach, A. G.; Déjugnat, C.; Braun, D.; Susha, A. S.; Rogach, A. L.; Sukhorukov, G. B. Nanoparticles Distribution Control by Polymers: Aggregates versus Nonaggregates. *J. Phys. Chem. C* **2007**, *111* (2), 555–564. https://doi.org/10.1021/jp065635k.

(12) Mishyn, V.; Rodrigues, T.; Leroux, Y. R.; Aspermair, P.; Happy, H.; Bintinger, J.; Kleber, C.; Boukherroub, R.; Knoll, W.; Szunerits, S. Controlled Covalent Functionalization of a Graphene-Channel of a Field Effect Transistor as an Ideal Platform for (Bio)Sensing Applications. *Nanoscale Horiz.* **2021**, *6* (10), 819–829. https://doi.org/10.1039/D1NH00355K.

(13) Wang, L.; Ye, Y.; Lu, X.; Wu, Y.; Sun, L.; Tan, H.; Xu, F.; Song, Y. Prussian Blue Nanocubes on Nitrobenzene-Functionalized Reduced Graphene Oxide and Its Application for H2O2 Biosensing. *Electrochimica Acta* **2013**, *114*, 223–232. https://doi.org/10.1016/j.electacta.2013.10.073.

(14) Wang, K.; Huang, S.-P.; Wu, Y.; Cai, N.-N.; Li, N.; Xiao, Q.; Sun, Z. Critical Thickness of a Surface-Functionalized Coating for Enhanced Lithium Storage: A Case Study of Nanoscale Polypyrrole-Coated FeS_2 as a Cathode for Li-Ion Batteries. *Nanoscale* **2019**, *11* (35), 16277–16283. https://doi.org/10.1039/C9NR05523A.

(15) Zhao, Y.; Sun, X. Molecular Layer Deposition for Energy Conversion and Storage. *ACS Energy Lett.* **2018**, *3* (4), 899–914. https://doi.org/10.1021/acsenergylett.8b00145.

(16) Love, J. C.; Estroff, L. A.; Kriebel, J. K.; Nuzzo, R. G.; Whitesides, G. M. Self-Assembled Monolayers of Thiolates on Metals as a Form of Nanotechnology. *Chem. Rev.* **2005**, *105* (4), 1103–1170. https://doi.org/10.1021/cr0300789.

(17) Vericat, C.; Vela, M. E.; Corthey, G.; Pensa, E.; Cortés, E.; Fonticelli, M. H.; Ibañez, F.; Benitez, G. E.; Carro, P.; Salvarezza, R. C. Self-Assembled Monolayers of Thiolates on Metals: A Review Article on Sulfur-Metal Chemistry and Surface Structures. *RSC Adv* **2014**, *4* (53), 27730–27754. https://doi.org/10.1039/C4RA04659E.

(18) Capitao, D.; Limoges, B.; Fave, C.; Schöllhorn, B. On the Decisive Role of the Sulfur-Based Anchoring Group in the Electro-Assisted Formation of Self-Assembled Monolayers on Gold. *Electrochimica Acta* **2017**, *257*, 165–171. https://doi.org/10.1016/j.electacta.2017.09.163.

(19) Li, J.; Yuan, Y. J. Physisorption and Chemisorption of a Self-Assembled Monolayer by the Quartz Crystal Microbalance. *Langmuir* **2014**, *30* (32), 9637–9642. https://doi.org/10.1021/la5020187.

(20) van Schrojenstein Lantman, E. M.; Deckert-Gaudig, T.; Mank, A. J. G.; Deckert, V.; Weckhuysen, B. M. Catalytic Processes Monitored at the Nanoscale with Tip-Enhanced Raman Spectroscopy. *Nat. Nanotechnol.* **2012**, *7* (9), 583–586. https://doi.org/10.1038/nnano.2012.131.

(21) Xue, Y.; Li, X.; Li, H.; Zhang, W. Quantifying Thiol–Gold Interactions towards the Efficient Strength Control. *Nat. Commun.* **2014**, *5* (1). https://doi.org/10.1038/ncomms5348.

(22) Vericat, C.; Vela, M. E.; Benitez, G.; Carro, P.; Salvarezza, R. C. Self-Assembled Monolayers of Thiols and Dithiols on Gold: New Challenges for a Well-Known System. *Chem. Soc. Rev.* **2010**, *39* (5), 1805. https://doi.org/10.1039/b907301a.

(23) Xu, S.; Cruchon-Dupeyrat, S. J. N.; Garno, J. C.; Liu, G.-Y.; Kane Jennings, G.; Yong, T.-H.; Laibinis, P. E. *In Situ* Studies of Thiol Self-Assembly on Gold from Solution Using Atomic Force Microscopy. *J. Chem. Phys.* **1998**, *108* (12), 5002–5012. https://doi.org/10.1063/1.475908.

(24) Hu, G.; Jin, R.; Jiang, D. Beyond the Staple Motif: A New Order at the Thiolate–Gold Interface. *Nanoscale* **2016**, *8* (48), 20103–20110. https://doi.org/10.1039/C6NR07709A.

(25) Kang, J. F.; Liao, S.; Jordan, R.; Ulman, A. Mixed Self-Assembled Monolayers of Rigid Biphenyl Thiols: Impact of Solvent and Dipole Moment. *J. Am. Chem. Soc.* **1998**, *120* (37), 9662–9667. https://doi.org/10.1021/ja981187l.

(26) Kang, J. F.; Ulman, A.; Liao, S.; Jordan, R.; Yang, G.; Liu, G. Self-Assembled Rigid Monolayers of 4‘-Substituted-4-Mercaptobiphenyls on Gold and Silver Surfaces. *Langmuir* **2001**, *17* (1), 95–106. https://doi.org/10.1021/la001217+.

(27) Yang, G.; Liu, G. New Insights for Self-Assembled Monolayers of Organothiols on Au(111) Revealed by Scanning Tunneling Microscopy. *J. Phys. Chem. B* **2003**, *107* (34), 8746–8759. https://doi.org/10.1021/jp0219810.

(28) Salvarezza, R. C.; Carro, P. The Electrochemical Stability of Thiols on Gold Surfaces. *J. Electroanal. Chem.* **2018**, *819*, 234–239. https://doi.org/10.1016/j.jelechem.2017.10.046.

(29) Tao, Y.-T.; Wu, C.-C.; Eu, J.-Y.; Lin, W.-L.; Wu, K.-C.; Chen, C. Structure Evolution of Aromatic-Derivatized Thiol Monolayers on Evaporated Gold. *Langmuir* **1997**, *13* (15), 4018–4023. https://doi.org/10.1021/la9700984.

(30) Szafranski, C. A.; Tanner, W.; Laibinis, P. E.; Garrell, R. L. Surface-Enhanced Raman Spectroscopy of Aromatic Thiols and Disulfides on Gold Electrodes. *Langmuir* **1998**, *14* (13), 3570–3579. https://doi.org/10.1021/la9702502.

(31) Inkpen, M. S.; Liu, Z.; Li, H.; Campos, L. M.; Neaton, J. B.; Venkataraman, L. Non-Chemisorbed Gold–Sulfur Binding Prevails in Self-Assembled Monolayers. *Nat. Chem.* **2019**, *11* (4), 351–358. https://doi.org/10.1038/s41557-019-0216-y.

(32) Bkhach, S.; Alévêque, O.; Morille, Y.; Breton, T.; Hudhomme, P.; Gautier, C.; Levillain, E. Absorption Spectroelectrochemistry on Mixed Perylenediimide-Based Self-Assembled Monolayers: Non-Linear Dependence of Absorbance versus Surface Coverage. *ChemElectroChem* **2017**, *4* (3), 601–606. https://doi.org/10.1002/celc.201600770.

(33) Noh, J.; Park, H.; Jeong, Y.; Kwon, S. Structure and Electrochemical Behavior of Aromatic Thiol Self-Assembled Monolayers on Au(111). *Bull. Korean Chem. Soc.* **2006**, *27* (3), 403–406. https://doi.org/10.5012/bkcs.2006.27.3.403.

(34) Lee, J. B.; Namgung, M.; Lee, S.-B.; Oh, S. Y. Fabrication of an Electrically Conductive Mixed Self-Assembled Monolayer and Its Application in an Electrochemical Immunosensor. *Ultramicroscopy* **2008**, *108* (10), 1352–1355. https://doi.org/10.1016/j.ultramic.2008.04.036.

(35) Nielsen, J. U.; Esplandiu, M. J.; Kolb, D. M. 4-Nitrothiophenol SAM on Au(111) Investigated by in Situ STM, Electrochemistry, and XPS. *Langmuir* **2001**, *17* (11), 3454–3459. https://doi.org/10.1021/la001775o.

(36) Yu, H.-Z.; Wang, Y.-Q.; Cheng, J.-Z.; Zhao, J.-W.; Cai, S.-M.; Inokuchi, H.; Fujishima, A.; Liu, Z.-F. Electrochemical Behavior of Azobenzene Self-Assembled Monolayers on Gold. *Langmuir* **1996**, *12* (11), 2843–2848. https://doi.org/10.1021/la950632c.

(37) Campbell, D. J.; Herr, B. R.; Hulteen, J. C.; Van Duyne, R. P.; Mirkin, C. A. Ion-Gated Electron Transfer in Self-Assembled Monolayer Films. *J. Am. Chem. Soc.* **1996**, *118* (42), 10211–10219. https://doi.org/10.1021/ja961873p.

(38) Watcharinyanon, S.; Moons, E.; Johansson, L. S. O. Mixed Self-Assembled Monolayers of Ferrocene-Terminated and Unsubstituted Alkanethiols on Gold: Surface Structure and Work Function. *J. Phys. Chem. C* **2009**, *113* (5), 1972–1979. https://doi.org/10.1021/jp808938d.

(39) Shewchuk, D. M.; McDermott, M. T. Comparison of Diazonium Salt Derived and Thiol Derived Nitrobenzene Layers on Gold. *Langmuir* **2009**, *25* (8), 4556–4563. https://doi.org/10.1021/la8040083.

(40) Pinson, J.; Podvorica, F. Attachment of Organic Layers to Conductive or Semiconductive Surfaces by Reduction of Diazonium Salts. *Chem. Soc. Rev.* **2005**, *34* (5), 429. https://doi.org/10.1039/b406228k.

(41) Allongue, P.; Delamar, M.; Desbat, B.; Fagebaume, O.; Hitmi, R.; Pinson, J.; Savéant, J.-M. Covalent Modification of Carbon Surfaces by Aryl Radicals Generated from the Electrochemical Reduction of Diazonium Salts. *J. Am. Chem. Soc.* **1997**, *119* (1), 201–207. https://doi.org/10.1021/ja963354s.

(42) Adenier, A.; Bernard, M.-C.; Chehimi, M. M.; Cabet-Deliry, E.; Desbat, B.; Fagebaume, O.; Pinson, J.; Podvorica, F. Covalent Modification of Iron Surfaces by Electrochemical Reduction of Aryldiazonium Salts. *J. Am. Chem. Soc.* **2001**, *123* (19), 4541–4549. https://doi.org/10.1021/ja003276f.

(43) de Villeneuve, C. H.; Pinson, J.; Bernard, M. C.; Allongue, P. Electrochemical Formation of Close-Packed Phenyl Layers on Si(111). *J. Phys. Chem. B* **1997**, *101* (14), 2415–2420. https://doi.org/10.1021/jp962581d.

(44) Laurentius, L.; Stoyanov, S. R.; Gusarov, S.; Kovalenko, A.; Du, R.; Lopinski, G. P.; McDermott, M. T. Diazonium-Derived Aryl Films on Gold Nanoparticles: Evidence for a Carbon–Gold Covalent Bond. *ACS Nano* **2011**, *5* (5), 4219–4227. https://doi.org/10.1021/nn201110r.

(45) Pinson, J. Attachment of Organic Layers to Materials Surfaces by Reduction of Diazonium Salts. In *Aryl Diazonium Salts*; Chehimi, M. M., Ed.; Wiley-VCH Verlag GmbH & Co. KGaA: Weinheim, Germany, 2012; pp 1–35. https://doi.org/10.1002/9783527650446.ch1.

(46) Lehr, J.; Williamson, B. E.; Flavel, B. S.; Downard, A. J. Reaction of Gold Substrates with Diazonium Salts in Acidic Solution at Open-Circuit Potential. *Langmuir* **2009**, *25* (23), 13503–13509. https://doi.org/10.1021/la902002n.

(47) Baranton, S.; Bélanger, D. Electrochemical Derivatization of Carbon Surface by Reduction of in Situ Generated Diazonium Cations. *J. Phys. Chem. B* **2005**, *109* (51), 24401–24410. https://doi.org/10.1021/jp054513+.

(48) Combellas, C.; Kanoufi, F.; Pinson, J.; Podvorica, F. I. Time-of-Flight Secondary Ion Mass Spectroscopy Characterization of the Covalent Bonding between a Carbon Surface and Aryl Groups. *Langmuir* **2005**, *21* (1), 280–286. https://doi.org/10.1021/la048106l.

(49) López, I.; Cesbron, M.; Levillain, E.; Breton, T. Diazonium Grafting Control through a Redox Cross-Reaction: Elucidation of the Mechanism Involved When Using 2,2-Diphenylpicrylhydrazyl as an Inhibitor. *ChemElectroChem* **2018**, *5* (8), 1197–1202. https://doi.org/10.1002/celc.201701331.

(50) López, I.; Dabos-Seignon, S.; Breton, T. Use of Selective Redox Cross-Inhibitors for the Control of Organic Layer Formation Obtained via Diazonium Salt Reduction. *Langmuir* **2019**, *35* (34), 11048–11055. https://doi.org/10.1021/acs.langmuir.9b01397.

(51) Pichereau, L.; López, I.; Cesbron, M.; Dabos-Seignon, S.; Gautier, C.; Breton, T. Controlled Diazonium Electrografting Driven by Overpotential Reduction: A General

Strategy to Prepare Ultrathin Layers. *Chem. Commun.* **2019**, *55* (4), 455–457. https://doi.org/10.1039/C8CC08331B.

(52) Greenwood, J.; Phan, T. H.; Fujita, Y.; Li, Z.; Ivasenko, O.; Vanderlinden, W.; Van Gorp, H.; Frederickx, W.; Lu, G.; Tahara, K.; Tobe, Y.; Uji-i, H.; Mertens, S. F. L.; De Feyter, S. Covalent Modification of Graphene and Graphite Using Diazonium Chemistry: Tunable Grafting and Nanomanipulation. *ACS Nano* **2015**, *9* (5), 5520–5535. https://doi.org/10.1021/acsnano.5b01580.

(53) Allongue, P.; Henry de Villeneuve, C.; Cherouvrier, G.; Cortès, R.; Bernard, M.-C. Phenyl Layers on H–Si(111) by Electrochemical Reduction of Diazonium Salts: Monolayer versus Multilayer Formation. *J. Electroanal. Chem.* **2003**, *550–551*, 161–174. https://doi.org/10.1016/S0022-0728(03)00076-7.

(54) Coates, M.; Cabet, E.; Griveau, S.; Nyokong, T.; Bedioui, F. Microelectrochemical Patterning of Gold Surfaces Using 4-Azidobenzenediazonium and Scanning Electrochemical Microscopy. *Electrochem. Commun.* **2011**, *13* (2), 150–153. https://doi.org/10.1016/j.elecom.2010.11.037.

(55) Doppelt, P.; Hallais, G.; Pinson, J.; Podvorica, F.; Verneyre, S. Surface Modification of Conducting Substrates. Existence of Azo Bonds in the Structure of Organic Layers Obtained from Diazonium Salts. *Chem. Mater.* **2007**, *19* (18), 4570–4575. https://doi.org/10.1021/cm0700551.

(56) Laforgue, A.; Addou, T.; Bélanger, D. Characterization of the Deposition of Organic Molecules at the Surface of Gold by the Electrochemical Reduction of Aryldiazonium Cations. *Langmuir* **2005**, *21* (15), 6855–6865. https://doi.org/10.1021/la047369c.

(57) Benedetto, A.; Balog, M.; Viel, P.; Le Derf, F.; Sallé, M.; Palacin, S. Electro-Reduction of Diazonium Salts on Gold: Why Do We Observe Multi-Peaks? *Electrochimica Acta* **2008**, *53* (24), 7117–7122. https://doi.org/10.1016/j.electacta.2008.05.001.

(58) Haccoun, J.; Vautrin-Ul, C.; Chaussé, A.; Adenier, A. Electrochemical Grafting of Organic Coating onto Gold Surfaces: Influence of the Electrochemical Conditions on the Grafting of Nitrobenzene Diazonium Salt. *Prog. Org. Coat.* **2008**, *63* (1), 18–24. https://doi.org/10.1016/j.porgcoat.2008.04.001.

(59) Bélanger, D.; Pinson, J. Electrografting: A Powerful Method for Surface Modification. *Chem. Soc. Rev.* **2011**, *40* (7), 3995. https://doi.org/10.1039/c0cs00149j.

(60) Brooksby, P. A.; Downard, A. J. Electrochemical and Atomic Force Microscopy Study of Carbon Surface Modification via Diazonium Reduction in Aqueous and Acetonitrile Solutions. *Langmuir* **2004**, *20* (12), 5038–5045. https://doi.org/10.1021/la049616i.

(61) Raicopol, M. D.; Andronescu, C.; Atasiei, R.; Hanganu, A.; Vasile, E.; Brezoiu, A. M.; Pilan, L. Organic Layers via Aryl Diazonium Electrochemistry: Towards Modifying Platinum Electrodes for Interference Free Glucose Biosensors. *Electrochimica Acta* **2016**, *206*, 226–237. https://doi.org/10.1016/j.electacta.2016.04.145.

(62) Combellas, C.; Jiang, D.; Kanoufi, F.; Pinson, J.; Podvorica, F. I. Steric Effects in the Reaction of Aryl Radicals on Surfaces. *Langmuir* **2009**, *25* (1), 286–293. https://doi.org/10.1021/la8025792.

(63) Malmos, K.; Dong, M.; Pillai, S.; Kingshott, P.; Besenbacher, F.; Pedersen, S. U.; Daasbjerg, K. Using a Hydrazone-Protected Benzenediazonium Salt to Introduce a Near-

Monolayer of Benzaldehyde on Glassy Carbon Surfaces. *J. Am. Chem. Soc.* **2009**, *131* (13), 4928–4936. https://doi.org/10.1021/ja809816x.

(64) Leroux, Y. R.; Hapiot, P. Nanostructured Monolayers on Carbon Substrates Prepared by Electrografting of Protected Aryldiazonium Salts. *Chem. Mater.* **2013**, *25* (3), 489–495. https://doi.org/10.1021/cm303844v.

(65) Nielsen, L. T.; Vase, K. H.; Dong, M.; Besenbacher, F.; Pedersen, S. U.; Daasbjerg, K. Electrochemical Approach for Constructing a Monolayer of Thiophenolates from Grafted Multilayers of Diaryl Disulfides. *J. Am. Chem. Soc.* **2007**, *129* (7), 1888–1889. https://doi.org/10.1021/ja0682430.

(66) Leroux, Y. R.; Fei, H.; Noël, J.-M.; Roux, C.; Hapiot, P. Efficient Covalent Modification of a Carbon Surface: Use of a Silyl Protecting Group To Form an Active Monolayer. *J. Am. Chem. Soc.* **2010**, *132* (40), 14039–14041. https://doi.org/10.1021/ja106971x.

(67) Sayed, S. Y.; Bayat, A.; Kondratenko, M.; Leroux, Y.; Hapiot, P.; McCreery, R. L. Bilayer Molecular Electronics: All-Carbon Electronic Junctions Containing Molecular Bilayers Made with "Click" Chemistry. *J. Am. Chem. Soc.* **2013**, *135* (35), 12972–12975. https://doi.org/10.1021/ja4065443.

(68) Menanteau, T.; Levillain, E.; Breton, T. Electrografting via Diazonium Chemistry: From Multilayer to Monolayer Using Radical Scavenger. *Chem. Mater.* **2013**, *25* (14), 2905–2909. https://doi.org/10.1021/cm401512c.

(69) Menanteau, T.; Levillain, E.; Breton, T. Spontaneous Grafting of Nitrophenyl Groups on Carbon: Effect of Radical Scavenger on Organic Layer Formation. *Langmuir* **2014**, *30* (26), 7913–7918. https://doi.org/10.1021/la501437g.

(70) Menanteau, T.; Levillain, E.; Downard, A. J.; Breton, T. Evidence of Monolayer Formation via Diazonium Grafting with a Radical Scavenger: Electrochemical, AFM and XPS Monitoring. *Phys. Chem. Chem. Phys.* **2015**, *17* (19), 13137–13142. https://doi.org/10.1039/C5CP01401H.

(71) Cesbron, M. Vers l'élaboration de Surfaces Modifiées Par Des Monocouches Organiques Mixtes Issues de La Réduction de Précurseurs Diazonium. PhD Thesis, 2019.

(72) Menanteau, T.; Dabos-Seignon, S.; Levillain, E.; Breton, T. Impact of the Diazonium Grafting Control on the Interfacial Reactivity: Monolayer versus Multilayer. *ChemElectroChem* **2017**, *4* (2), 278–282. https://doi.org/10.1002/celc.201600710.

(73) Lemaire, P.; Tarascon, J.-M.; Sel, O. Exploring Interface Mechanisms in Metal-Ion Batteries via Advanced EQCM, Exploration Des Mécanismes Interfaciaux Présents Dans Les Batteries Métal-Ion Par EQCM Avancée, Sorbonne Université, 2020.

(74) Hu, J.; Huang, X. QCM Mass Sensitivity Analysis of Modified Electrode Structures Using Finite Element Method. In *2018 IEEE International Conference on Applied Superconductivity and Electromagnetic Devices (ASEMD)*; IEEE: Tianjin, 2018; pp 1–2. https://doi.org/10.1109/ASEMD.2018.8559025.

(75) Kawaguchi, T.; Yasuda, H.; Shimazu, K.; Porter, M. D. Electrochemical Quartz Crystal Microbalance Investigation of the Reductive Desorption of Self-Assembled Monolayers of Alkanethiols and Mercaptoalkanoic Acids on Au. *Langmuir* **2000**, *16* (25), 9830–9840. https://doi.org/10.1021/la000756b.

(76) Tlili, A.; Abdelghani, A.; Hleli, S.; Maaref, M. A. Electrical Characterization of a Thiol SAM on Gold as a First Step for the Fabrication of Immunosensors Based on a Quartz Crystal Microbalance. *Sensors* **2004**, *4* (6), 105–114.

(77) Schneider, T. W.; Buttry, D. A. Electrochemical Quartz Crystal Microbalance Studies of Adsorption and Desorption of Self-Assembled Monolayers of Alkyl Thiols on Gold. *J. Am. Chem. Soc.* **1993**, *115* (26), 12391–12397. https://doi.org/10.1021/ja00079a021.

(78) Kullapere, M.; Marandi, M.; Sammelselg, V.; Menezes, H. A.; Maia, G.; Tammeveski, K. Surface Modification of Gold Electrodes with Anthraquinone Diazonium Cations. *Electrochem. Commun.* **2009**, *11* (2), 405–408. https://doi.org/10.1016/j.elecom.2008.12.001.

(79) Bouden, S.; Pinson, J.; Vautrin-Ul, C. Electrografting of Diazonium Salts: A Kinetics Study. *Electrochem. Commun.* **2017**, *81*, 120–123. https://doi.org/10.1016/j.elecom.2017.06.007.

(80) Cimpoca, G. V.; Popescu, I. V.; Dulama, I. D.; Radulescu, C.; Bancuta, I.; Cimpoca, M.; Cernica, I.; Schiopu, V.; Danila, M.; Gavrila, R. Self Assembled Monolayer of Ethanthiol on Gold Surfaces by Quartz Crystal Microbalance. In *2009 International Semiconductor Conference*; IEEE: Sinaia, Romania, 2009; pp 135–138. https://doi.org/10.1109/SMICND.2009.5336590.

(81) Etorki, A.; El-Rais, M. Development of an Acoustic Wave Nano Sensor for Hg(II) Using Quartz Crystal. **2020**, 11.

(82) Kandory, A.; Goncalves, A.-M.; Frégnaux, M.; Cattey, H.; Alaoui-Sossé, B.; Aleya, L.; Herlem, G. Gold Modification by Reduction of a Diazonium Salt Prepared from an Aliphatic Diamine: A New Useful Means to Remove Hazardous Substances. *Environ. Sci. Pollut. Res.* **2021**. https://doi.org/10.1007/s11356-021-15696-3.

(83) Cheng, C. I.; Chang, Y.-P.; Chu, Y.-H. Biomolecular Interactions and Tools for Their Recognition: Focus on the Quartz Crystal Microbalance and Its Diverse Surface Chemistries and Applications. *Chem Soc Rev* **2012**, *41* (5), 1947–1971. https://doi.org/10.1039/C1CS15168A.

(84) Heinzelmann, H.; Pohl, D. W. Scanning Near-Field Optical Microscopy. *Appl. Phys. Solids Surf.* **1994**, *59* (2), 89–101. https://doi.org/10.1007/BF00332200.

(85) Raman, C. V. A New Radiation [Reproduced from Indian J. Phys., 1928, 2, 387–398]. *Curr. Sci.* **1998**, *74* (4), 382–386.

(86) Lozeman, J. J. A.; Führer, P.; Olthuis, W.; Odijk, M. Spectroelectrochemistry, the Future of Visualizing Electrode Processes by Hyphenating Electrochemistry with Spectroscopic Techniques. *The Analyst* **2020**, *145* (7), 2482–2509. https://doi.org/10.1039/C9AN02105A.

(87) Lucas, I. T.; Bazin, D.; Daudon, M. Raman Opportunities in the Field of Pathological Calcifications. *Comptes Rendus Chim.* **2021**, *24* (S2), 1–21. https://doi.org/10.5802/crchim.110.

(88) Pilarczyk, M.; Czamara, K.; Baranska, M.; Natorska, J.; Kapusta, P.; Undas, A.; Kaczor, A. Calcification of Aortic Human Valves Studied *in Situ* by Raman Microimaging: Following Mineralization from Small Grains to Big Deposits: Calcification of Aortic

Human Valves. *J. Raman Spectrosc.* **2013**, *44* (9), 1222–1229. https://doi.org/10.1002/jrs.4352.

(89) Czamara, K.; Natorska, J.; Kapusta, P.; Baranska, M.; Kaczor, A. Raman Microspectroscopy of Human Aortic Valves: Investigation of the Local and Global Biochemical Changes Associated with Calcification in Aortic Stenosis. *The Analyst* **2015**, *140* (7), 2164–2170. https://doi.org/10.1039/C4AN01856G.

(90) Bloembergen, N. The Stimulated Raman Effect. *Am. J. Phys.* **1967**, *35* (11), 989–1023. https://doi.org/10.1119/1.1973774.

(91) Eckhardt, G.; Wagner, W. G. On the Calculation of Absolute Raman Scattering Cross Sections from Raman Scattering Coefficients. *J. Mol. Spectrosc.* **1966**, *19* (1–4), 407–411. https://doi.org/10.1016/0022-2852(66)90262-1.

(92) Liu, Y.-C.; McCreery, R. L. Reactions of Organic Monolayers on Carbon Surfaces Observed with Unenhanced Raman Spectroscopy. *J. Am. Chem. Soc.* **1995**, *117* (45), 11254–11259. https://doi.org/10.1021/ja00150a024.

(93) Ramsey, J.; Ranganathan, S.; McCreery, R. L.; Zhao, J. Performance Comparisons of Conventional and Line-Focused Surface Raman Spectrometers. *Appl. Spectrosc.* **2001**, *55* (6), 767–773. https://doi.org/10.1366/0003702011952460.

(94) Itoh, T.; McCreery, R. L. In Situ Raman Spectroelectrochemistry of Electron Transfer between Glassy Carbon and a Chemisorbed Nitroazobenzene Monolayer. *J. Am. Chem. Soc.* **2002**, *124* (36), 10894–10902. https://doi.org/10.1021/ja020398u.

(95) Velický, M.; Bradley, D. F.; Cooper, A. J.; Hill, E. W.; Kinloch, I. A.; Mishchenko, A.; Novoselov, K. S.; Patten, H. V.; Toth, P. S.; Valota, A. T.; Worrall, S. D.; Dryfe, R. A. W. Electron Transfer Kinetics on Mono- and Multilayer Graphene. *ACS Nano* **2014**, *8* (10), 10089–10100. https://doi.org/10.1021/nn504298r.

(96) Itoh, T.; McCreery, R. L. In Situ Raman Spectroelectrochemistry of Azobenzene Monolayers on Glassy Carbon. *Anal. Bioanal. Chem.* **2007**, *388* (1), 131–134. https://doi.org/10.1007/s00216-007-1192-4.

(97) Blacha-Grzechnik, A.; Piwowar, K.; Zassowski, P.; Motyka, R.; Zak, J. In-Situ Raman Spectroelectrochemical Studies on Thionine Layer Electrochemically Grafted to the Gold Surface. *Electrochimica Acta* **2017**, *245*, 902–911. https://doi.org/10.1016/j.electacta.2017.05.132.

(98) Vlčková Živcová, Z.; Bouša, M.; Velický, M.; Frank, O.; Kavan, L. In Situ Raman Microdroplet Spectroelectrochemical Investigation of CuSCN Electrodeposited on Different Substrates. *Nanomaterials* **2021**, *11* (5), 1256. https://doi.org/10.3390/nano11051256.

(99) Ringe, E.; Sharma, B.; Henry, A.-I.; Marks, L. D.; Van Duyne, R. P. Single Nanoparticle Plasmonics. *Phys. Chem. Chem. Phys.* **2013**, *15* (12), 4110. https://doi.org/10.1039/c3cp44574g.

(100) Willets, K. A.; Van Duyne, R. P. Localized Surface Plasmon Resonance Spectroscopy and Sensing. *Annu. Rev. Phys. Chem.* **2007**, *58* (1), 267–297. https://doi.org/10.1146/annurev.physchem.58.032806.104607.

(101) Fleischmann, M.; Hendra, P. J.; McQuillan, A. J. Raman Spectra from Electrode Surfaces. *J. Chem. Soc. Chem. Commun.* **1973**, No. 3, 80. https://doi.org/10.1039/c39730000080.

(102) Fleischmann, M.; Hendra, P. J.; McQuillan, A. J. Raman Spectra of Pyridine Adsorbed at a Silver Electrode. *Chem. Phys. Lett.* **1974**, *26* (2), 163–166. https://doi.org/10.1016/0009-2614(74)85388-1.

(103) Albrecht, M. G.; Creighton, J. A. Anomalously Intense Raman Spectra of Pyridine at a Silver Electrode. *J. Am. Chem. Soc.* **1977**, *99* (15), 5215–5217. https://doi.org/10.1021/ja00457a071.

(104) Van Duyne, R. P. RAMANAPPLICATIONS OF RAMAN SPECTROSCOPY IN ELECTROCHEMISTRY. *J. Phys. Colloq.* **1977**, *38* (C5), C5-239-C5-252. https://doi.org/10.1051/jphyscol:1977531.

(105) Philpott, M. R. Effect of Surface Plasmons on Transitions in Molecules. *J. Chem. Phys.* **1975**, *62* (5), 1812–1817. https://doi.org/10.1063/1.430708.

(106) Liang, H.; Tian, H.; McCreery, R. L. Normal and Surface-Enhanced Raman Spectroscopy of Nitroazobenzene Submonolayers and Multilayers on Carbon and Silver Surfaces. *Appl. Spectrosc.* **2007**, *61* (6), 613–620. https://doi.org/10.1366/000370207781269765.

(107) Pertreux, E.; Lombardi, A.; Florea, I.; Spuch-Calvar, M.; Gómez-Graña, S.; Ihiawakrim, D.; Hirlimann, C.; Ersen, O.; Majimel, J.; Tréguer-Delapierre, M.; Hettich, M.; Maioli, P.; Crut, A.; Vallée, F.; Fatti, N. D. Surface Plasmon Resonance of an Individual Nano-Object on an Absorbing Substrate: Quantitative Effects of Distance and 3D Orientation. *Adv. Opt. Mater.* **2016**, *4* (4), 567–577. https://doi.org/10.1002/adom.201500548.

(108) Deckert-Gaudig, T.; Taguchi, A.; Kawata, S.; Deckert, V. Tip-Enhanced Raman Spectroscopy – from Early Developments to Recent Advances. *Chem. Soc. Rev.* **2017**, *46* (13), 4077–4110. https://doi.org/10.1039/C7CS00209B.

(109) Nehl, C. L.; Hafner, J. H. Shape-Dependent Plasmon Resonances of Gold Nanoparticles. *J. Mater. Chem.* **2008**, *18* (21), 2415. https://doi.org/10.1039/b714950f.

(110) Tréguer-Delapierre, M.; Madeira, A.; Hubert, C.; Ravaine, S. Recent Advances in the Synthesis of Anisotropic Particles. In *Anisotropic Particle Assemblies*; Elsevier, 2018; pp 1–35. https://doi.org/10.1016/B978-0-12-804069-0.00001-0.

(111) McFarland, A. D.; Van Duyne, R. P. Single Silver Nanoparticles as Real-Time Optical Sensors with Zeptomole Sensitivity. *Nano Lett.* **2003**, *3* (8), 1057–1062. https://doi.org/10.1021/nl034372s.

(112) Cheng, J.; Li, Y.; Plissonneau, M.; Li, J.; Li, J.; Chen, R.; Tang, Z.; Pautrot-d'Alençon, L.; He, T.; Tréguer-Delapierre, M.; Delville, M.-H. Plasmon-Induced Hot Electron Transfer in AgNW@TiO2@AuNPs Nanostructures. *Sci. Rep.* **2018**, *8* (1), 14136. https://doi.org/10.1038/s41598-018-32510-2.

(113) Betelu, S.; Tijunelyte, I.; Boubekeur-Lecaque, L.; Ignatiadis, I.; Ibrahim, J.; Gaboreau, S.; Berho, C.; Toury, T.; Guenin, E.; Lidgi-Guigui, N.; Félidj, N.; Rinnert, E.; Chapelle, M. L. de la. Evidence of the Grafting Mechanisms of Diazonium Salts on Gold Nanostructures. *J. Phys. Chem. C* **2016**, *120* (32), 18158–18166. https://doi.org/10.1021/acs.jpcc.6b06486.

(114) Groni, S.; Fave, C.; Schöllhorn, B.; Chapus, L.; Aubertin, P.; Touzalin, T.; Lucas, I. T.; Joiret, S.; Courty, A.; Maisonhaute, E. Long Range Self-Organisations of Small Metallic Nanocrystals for SERS Detection of Electrochemical Reactions. *J. Electroanal. Chem.* **2020**, *872*, 114322. https://doi.org/10.1016/j.jelechem.2020.114322.

(115) Chapus, L.; Aubertin, P.; Joiret, S.; Lucas, I. T.; Maisonhaute, E.; Courty, A. Tunable SERS Platforms from Small Nanoparticle 3D Superlattices: A Comparison between Gold, Silver, and Copper. *ChemPhysChem* **2017**, *18* (21), 3066–3075. https://doi.org/10.1002/cphc.201700601.

(116) Zong, C.; Chen, C.-J.; Zhang, M.; Wu, D.-Y.; Ren, B. Transient Electrochemical Surface-Enhanced Raman Spectroscopy: A Millisecond Time-Resolved Study of an Electrochemical Redox Process. *J. Am. Chem. Soc.* **2015**, *137* (36), 11768–11774. https://doi.org/10.1021/jacs.5b07197.

(117) Félidj, N.; Aubard, J.; Lévi, G.; Krenn, J. R.; Hohenau, A.; Schider, G.; Leitner, A.; Aussenegg, F. R. Optimized Surface-Enhanced Raman Scattering on Gold Nanoparticle Arrays. *Appl. Phys. Lett.* **2003**, *82* (18), 3095–3097. https://doi.org/10.1063/1.1571979.

(118) Luo, Y.; Xiao, Y.; Onidas, D.; Iannazzo, L.; Ethève-Quelquejeu, M.; Lamouri, A.; Félidj, N.; Mahouche-Chergui, S.; Brulé, T.; Gagey-Eilstein, N.; Gazeau, F.; Mangeney, C. Raman Reporters Derived from Aryl Diazonium Salts for SERS Encoded-Nanoparticles. *Chem. Commun.* **2020**, *56* (50), 6822–6825. https://doi.org/10.1039/D0CC02842H.

(119) Le Beulze, A.; Gomez-Graña, S.; Gehan, H.; Mornet, S.; Ravaine, S.; Correa-Duarte, M.; Guerrini, L.; Alvarez-Puebla, R. A.; Duguet, E.; Pertreux, E.; Crut, A.; Maioli, P.; Vallée, F.; Del Fatti, N.; Ersen, O.; Treguer-Delapierre, M. Robust Raspberry-like Metallo-Dielectric Nanoclusters of Critical Sizes as SERS Substrates. *Nanoscale* **2017**, *9* (17), 5725–5736. https://doi.org/10.1039/C7NR00969K.

(120) Courty, A.; Bayle, M.; Carles, R. Plasmon-Enhanced Inelastic Scattering by 2D and 3D Superlattices Made of Silver Nanocrystals. *J. Raman Spectrosc.* **2019**, *50* (1), 74–84. https://doi.org/10.1002/jrs.5502.

(121) Lee, S.; Portalès, H.; Walls, M.; Beaunier, P.; Goubet, N.; Tremblay, B.; Margueritat, J.; Saviot, L.; Courty, A. Versatile and Robust Synthesis Process for the Fine Control of the Chemical Composition and Core-Crystallinity of Spherical Core–Shell Au@Ag Nanoparticles. *Nanotechnology* **2020**, *32* (9), 095604. https://doi.org/10.1088/1361-6528/abc450.

(122) Li, J. F.; Huang, Y. F.; Ding, Y.; Yang, Z. L.; Li, S. B.; Zhou, X. S.; Fan, F. R.; Zhang, W.; Zhou, Z. Y.; Wu, D. Y.; Ren, B.; Wang, Z. L.; Tian, Z. Q. Shell-Isolated Nanoparticle-Enhanced Raman Spectroscopy. *Nature* **2010**, *464* (7287), 392–395. https://doi.org/10.1038/nature08907.

(123) Gajan, A.; Lecourt, C.; Torres Bautista, B. E.; Fillaud, L.; Demeaux, J.; Lucas, I. T. Solid Electrolyte Interphase Instability in Operating Lithium-Ion Batteries Unraveled by Enhanced-Raman Spectroscopy. *ACS Energy Lett.* **2021**, *6* (5), 1757–1763. https://doi.org/10.1021/acsenergylett.1c00436.

(124) Touzalin, T.; Joiret, S.; Maisonhaute, E.; Lucas, I. T. Complex Electron Transfer Pathway at a Microelectrode Captured by in Situ Nanospectroscopy. *Anal. Chem.* **2017**, *89* (17), 8974–8980. https://doi.org/10.1021/acs.analchem.7b01542.

(125) Touzalin, T. Tip-Enhanced Raman Spectroscopy on Electrochemical Systems, Sorbonne Université, 2018.

(126) Kumar, N.; Mignuzzi, S.; Su, W.; Roy, D. Tip-Enhanced Raman Spectroscopy: Principles and Applications. *EPJ Tech. Instrum.* **2015**, *2* (1). https://doi.org/10.1140/epjti/s40485-015-0019-5.

(127) Pérez-Jiménez, A. I.; Lyu, D.; Lu, Z.; Liu, G.; Ren, B. Surface-Enhanced Raman Spectroscopy: Benefits, Trade-Offs and Future Developments. *Chem. Sci.* **2020**, *11* (18), 4563–4577. https://doi.org/10.1039/D0SC00809E.

(128) Bard, A. J.; Faulkner, L. R. Electrochemical Methods: Fundamentals and Applications; 1980.

(129) Forouzan, F.; Bard, A. J.; Mirkin, M. V. Voltammetric and Scanning Electrochemical Microscopic Studies of the Adsorption Kinetics and Self-Assembly of n-Alkanethiol Monolayers on Gold. *Isr. J. Chem.* **1997**, *37* (2–3), 155–163. https://doi.org/10.1002/ijch.199700019.

(130) Ahonen, P.; Laaksonen, T.; Schiffrin, D. J.; Kontturi, K. Photoswitching Electron Transport Properties of an Azobenzene Containing Thiol-SAM. *Phys. Chem. Chem. Phys.* **2007**, *9* (35), 4898–4901. https://doi.org/10.1039/b709025k.

(131) Kiani, A.; Alpuche-Aviles, M. A.; Eggers, P. K.; Jones, M.; Gooding, J. J.; Paddon-Row, M. N.; Bard, A. J. Scanning Electrochemical Microscopy. 59. Effect of Defects and Structure on Electron Transfer through Self-Assembled Monolayers. *Langmuir* **2008**, *24* (6), 2841–2849. https://doi.org/10.1021/la702811t.

(132) Griveau, S.; Aroua, S.; Bediwy, D.; Cornut, R.; Lefrou, C.; Bedioui, F. Spontaneous Adsorbed Layers of 4-Nitrobenzenediazonium Salt on Gold and Glassy Carbon: Local Characterization by SECM and Electron-Transfer Kinetics Evaluation. *J. Electroanal. Chem.* **2010**, *647* (1), 93–96. https://doi.org/10.1016/j.jelechem.2010.05.014.

(133) Lhenry, S.; Leroux, Y. R.; Hapiot, P. Use of Catechol As Selective Redox Mediator in Scanning Electrochemical Microscopy Investigations. *Anal. Chem.* **2012**, *84* (17), 7518–7524. https://doi.org/10.1021/ac301634s.

(134) Liu, B.; Bard, A. J.; Mirkin, M. V; Creager, S. E. Electron Transfer at Self-Assembled Monolayers Measured by Scanning Electrochemical Microscopy. *J. Am. Chem. Soc.* **2004**, *126* (5), 1485–1492. https://doi.org/10.1021/ja038611p.

(135) Wang, W.; Li, X.; Wang, X.; Shang, H.; Liu, X.; Lu, X. Comparative Electrochemical Behaviors of a Series of SH-Terminated- Functionalized Porphyrins Assembled on a Gold Electrode by Scanning Electrochemical Microscopy (SECM). *J. Phys. Chem. B* **2010**, *114* (32), 10436–10441. https://doi.org/10.1021/jp1026064.

(136) Wang, W.; Hu, Y.; Wang, C.; Lu, X. Comparative Electrochemical Investigations on Series of SH-Terminated-Functional Porphyrins. *Electrochimica Acta* **2012**, *65*, 244–250. https://doi.org/10.1016/j.electacta.2012.01.049.

(137) Zigah, D.; Noël, J.-M.; Lagrost, C.; Hapiot, P. Charge Transfer between Electroactive Species Immobilized on Carbon Surfaces by Aryl Diazonium Reduction. SECM Investigations. *J. Phys. Chem. C* **2010**, *114* (7), 3075–3081. https://doi.org/10.1021/jp911550j.

(138) Payne, N. A.; Mauzeroll, J. Identifying Nanoscale Pinhole Defects in Nitroaryl Layers with Scanning Electrochemical Cell Microscopy. *ChemElectroChem* **2019**, *6* (21), 5439–5445. https://doi.org/10.1002/celc.201901394.

(139) Martín-Yerga, D.; Kang, M.; Unwin, P. R. Scanning Electrochemical Cell Microscopy in a Glovebox: Structure-Activity Correlations in the Early Stages of Solid-Electrolyte Interphase Formation on Graphite. *ChemElectroChem* **2021**, *8* (22), 4240–4251. https://doi.org/10.1002/celc.202101161.

(140) Chen, C.-H.; Jacobse, L.; McKelvey, K.; Lai, S. C. S.; Koper, M. T. M.; Unwin, P. R. Voltammetric Scanning Electrochemical Cell Microscopy: Dynamic Imaging of Hydrazine Electro-Oxidation on Platinum Electrodes. *Anal. Chem.* **2015**, *87* (11), 5782–5789. https://doi.org/10.1021/acs.analchem.5b00988.

(141) McKelvey, K.; O'Connell, M. A.; Unwin, P. R. Meniscus Confined Fabrication of Multidimensional Conducting Polymer Nanostructures with Scanning Electrochemical Cell Microscopy (SECCM). *Chem. Commun.* **2013**, *49* (29), 2986. https://doi.org/10.1039/c3cc00104k.

(142) Kim, J. T.; Pyo, J.; Seol, S. K.; Je, J. H. Precise Placement of Microbubble Templates at Single Entity Resolution. *ACS Macro Lett.* **2018**, *7* (10), 1267–1271. https://doi.org/10.1021/acsmacrolett.8b00646.

(143) Bentley, C. L.; Kang, M.; Unwin, P. R. Scanning Electrochemical Cell Microscopy (SECCM) in Aprotic Solvents: Practical Considerations and Applications. *Anal. Chem.* **2020**, *92* (17), 11673–11680. https://doi.org/10.1021/acs.analchem.0c01540.

(144) Gardner, C. E.; Macpherson, J. V. Peer Reviewed: Atomic Force Microscopy Probes Go Electrochemical. *Anal. Chem.* **2002**, *74* (21), 576 A-584 A. https://doi.org/10.1021/ac0221482.

(145) Huang, K.; Anne, A.; Bahri, M. A.; Demaille, C. Probing Individual Redox PEGylated Gold Nanoparticles by Electrochemical–Atomic Force Microscopy. *ACS Nano* **2013**, *7* (5), 4151–4163. https://doi.org/10.1021/nn400527u.

(146) Chennit, K.; Trasobares, J.; Anne, A.; Cambril, E.; Chovin, A.; Clément, N.; Demaille, C. Electrochemical Imaging of Dense Molecular Nanoarrays. *Anal. Chem.* **2017**, *89* (20), 11061–11069. https://doi.org/10.1021/acs.analchem.7b03111.

(147) Kueng, A.; Kranz, C.; Mizaikoff, B. Scanning Probe Microscopy with Integrated Biosensors. *Sens. Lett.* **2003**, *1* (1), 2–15. https://doi.org/10.1166/sl.2003.001.

(148) Kueng, A.; Kranz, C.; Lugstein, A.; Bertagnolli, E.; Mizaikoff, B. AFM-Tip-Integrated Amperometric Microbiosensors: High-Resolution Imaging of Membrane Transport. *Angew. Chem. Int. Ed.* **2005**, *44* (22), 3419–3422. https://doi.org/10.1002/anie.200461556.

(149) Anne, A.; Cambril, E.; Chovin, A.; Demaille, C. Touching Surface-Attached Molecules with a Microelectrode: Mapping the Distribution of Redox-Labeled Macromolecules by Electrochemical-Atomic Force Microscopy. *Anal. Chem.* **2010**, *82* (15), 6353–6362. https://doi.org/10.1021/ac1012464.

(150) Abbou, J.; Anne, A.; Demaille, C. Probing the Structure and Dynamics of End-Grafted Flexible Polymer Chain Layers by Combined Atomic Force−Electrochemical Microscopy. Cyclic Voltammetry within Nanometer-Thick Macromolecular

Poly(Ethylene Glycol) Layers. *J. Am. Chem. Soc.* **2004**, *126* (32), 10095–10108. https://doi.org/10.1021/ja0493502.

(151) Anne, A.; Chovin, A.; Demaille, C.; Lafouresse, M. High-Resolution Mapping of Redox-Immunomarked Proteins Using Electrochemical–Atomic Force Microscopy in Molecule Touching Mode. *Anal. Chem.* **2011**, *83* (20), 7924–7932. https://doi.org/10.1021/ac201907v.

(152) Shi, X.; Qing, W.; Marhaba, T.; Zhang, W. Atomic Force Microscopy - Scanning Electrochemical Microscopy (AFM-SECM) for Nanoscale Topographical and Electrochemical Characterization: Principles, Applications and Perspectives. *Electrochimica Acta* **2020**, *332*, 135472. https://doi.org/10.1016/j.electacta.2019.135472.

(153) Ghorbal, A.; Grisotto, F.; Charlier, J.; Palacin, S.; Goyer, C.; Demaille, C. Localized Electrografting of Vinylic Monomers on a Conducting Substrate by Means of an Integrated Electrochemical AFM Probe. *ChemPhysChem* **2009**, *10* (7), 1053–1057. https://doi.org/10.1002/cphc.200800803.

(154) Fernández, J. L.; Bard, A. J. Scanning Electrochemical Microscopy. 47. Imaging Electrocatalytic Activity for Oxygen Reduction in an Acidic Medium by the Tip Generation−Substrate Collection Mode. *Anal. Chem.* **2003**, *75* (13), 2967–2974. https://doi.org/10.1021/ac0340354.

(155) Watkins, T. S.; Sarbapalli, D.; Counihan, M. J.; Danis, A. S.; Zhang, J.; Zhang, L.; Zavadil, K. R.; Rodríguez-López, J. A Combined SECM and Electrochemical AFM Approach to Probe Interfacial Processes Affecting Molecular Reactivity at Redox Flow Battery Electrodes. *J. Mater. Chem. A* **2020**, *8* (31), 15734–15745. https://doi.org/10.1039/D0TA00836B.

(156) Synge, E. H. XXXVIII. *A Suggested Method for Extending Microscopic Resolution into the Ultra-Microscopic Region*. *Lond. Edinb. Dublin Philos. Mag. J. Sci.* **1928**, *6* (35), 356–362. https://doi.org/10.1080/14786440808564615.

(157) Novotny, L.; Stranick, S. J. NEAR-FIELD OPTICAL MICROSCOPY AND SPECTROSCOPY WITH POINTED PROBES. *Annu. Rev. Phys. Chem.* **2006**, *57* (1), 303–331. https://doi.org/10.1146/annurev.physchem.56.092503.141236.

(158) Stöckle, R. M.; Suh, Y. D.; Deckert, V.; Zenobi, R. Nanoscale Chemical Analysis by Tip-Enhanced Raman Spectroscopy. *Chem. Phys. Lett.* **2000**, *318* (1–3), 131–136. https://doi.org/10.1016/S0009-2614(99)01451-7.

(159) Anderson, M. S. Locally Enhanced Raman Spectroscopy with an Atomic Force Microscope. *Appl. Phys. Lett.* **2000**, *76* (21), 3130–3132. https://doi.org/10.1063/1.126546.

(160) Hayazawa, N.; Inouye, Y.; Sekkat, Z.; Kawata, S. Metallized Tip Amplification of Near-Field Raman Scattering. *Opt. Commun.* **2000**, *183* (1–4), 333–336. https://doi.org/10.1016/S0030-4018(00)00894-4.

(161) Pettinger, B.; Picardi, G.; Schuster, R.; Ertl, G. Surface Enhanced Raman Spectroscopy: Towards Single Molecule Spectroscopy. *Electrochemistry* **2000**, *68* (12), 942–949. https://doi.org/10.5796/electrochemistry.68.942.

(162) Inouye, Y.; Kawata, S. Near-Field Scanning Optical Microscope with a Metallic Probe Tip. *Opt. Lett.* **1994**, *19* (3), 159. https://doi.org/10.1364/OL.19.000159.

(163) Pettinger, B.; Schambach, P.; Villagómez, C. J.; Scott, N. Tip-Enhanced Raman Spectroscopy: Near-Fields Acting on a Few Molecules. *Annu. Rev. Phys. Chem.* **2012**, *63* (1), 379–399. https://doi.org/10.1146/annurev-physchem-032511-143807.

(164) Bouhelier, A.; Beversluis, M.; Hartschuh, A.; Novotny, L. Near-Field Second-Harmonic Generation Induced by Local Field Enhancement. *Phys. Rev. Lett.* **2003**, *90* (1), 013903. https://doi.org/10.1103/PhysRevLett.90.013903.

(165) Ren, B.; Picardi, G.; Pettinger, B. Preparation of Gold Tips Suitable for Tip-Enhanced Raman Spectroscopy and Light Emission by Electrochemical Etching. *Rev. Sci. Instrum.* **2004**, *75* (4), 837–841. https://doi.org/10.1063/1.1688442.

(166) Bian, K.; Gerber, C.; Heinrich, A. J.; Müller, D. J.; Scheuring, S.; Jiang, Y. Scanning Probe Microscopy. *Nat. Rev. Methods Primer* **2021**, *1* (1), 36. https://doi.org/10.1038/s43586-021-00033-2.

(167) Binnig, G.; Rohrer, H.; Gerber, C.; Weibel, E. Surface Studies by Scanning Tunneling Microscopy. *Phys. Rev. Lett.* **1982**, *49* (1), 57–61. https://doi.org/10.1103/PhysRevLett.49.57.

(168) Pfisterer, J. H. K.; Baghernejad, M.; Giuzio, G.; Domke, K. F. Reactivity Mapping of Nanoscale Defect Chemistry under Electrochemical Reaction Conditions. *Nat. Commun.* **2019**, *10* (1). https://doi.org/10.1038/s41467-019-13692-3.

(169) Touzalin, T.; Joiret, S.; Lucas, I. T.; Maisonhaute, E. Electrochemical Tip-Enhanced Raman Spectroscopy Imaging with 8 Nm Lateral Resolution. *Electrochem. Commun.* **2019**, *108*, 106557. https://doi.org/10.1016/j.elecom.2019.106557.

(170) Picas, L.; Milhiet, P.-E.; Hernández-Borrell, J. Atomic Force Microscopy: A Versatile Tool to Probe the Physical and Chemical Properties of Supported Membranes at the Nanoscale. *Chem. Phys. Lipids* **2012**, *165* (8), 845–860. https://doi.org/10.1016/j.chemphyslip.2012.10.005.

(171) Brahami, A.; Levy, H.; Zlotkin-Rivkin, E.; Melamed-Book, N.; Tal, N.; Lev, D.; Yeshua, T.; Fedosyeyev, O.; Aroeti, B.; Lewis, A. Live Cell Near-Field Optical Imaging and Voltage Sensing with Ultrasensitive Force Control. *Opt. Express* **2017**, *25* (11), 12131. https://doi.org/10.1364/OE.25.012131.

(172) Wang, X.; Zhong, J.-H.; Zhang, M.; Liu, Z.; Wu, D.-Y.; Ren, B. Revealing Intermolecular Interaction and Surface Restructuring of an Aromatic Thiol Assembling on Au(111) by Tip-Enhanced Raman Spectroscopy. *Anal. Chem.* **2016**, *88* (1), 915–921. https://doi.org/10.1021/acs.analchem.5b03588.

(173) Sun, J.-J.; Su, H.-S.; Yue, H.-L.; Huang, S.-C.; Huang, T.-X.; Hu, S.; Sartin, M. M.; Cheng, J.; Ren, B. Role of Adsorption Orientation in Surface Plasmon-Driven Coupling Reactions Studied by Tip-Enhanced Raman Spectroscopy. *J. Phys. Chem. Lett.* **2019**, *10* (10), 2306–2312. https://doi.org/10.1021/acs.jpclett.9b00203.

(174) Huang, S.-C.; Ye, J.-Z.; Shen, X.-R.; Zhao, Q.-Q.; Zeng, Z.-C.; Li, M.-H.; Wu, D.-Y.; Wang, X.; Ren, B. Electrochemical Tip-Enhanced Raman Spectroscopy with Improved Sensitivity Enabled by a Water Immersion Objective. *Anal. Chem.* **2019**, *91* (17), 11092–11097. https://doi.org/10.1021/acs.analchem.9b01701.

(175) Chen, Z.; Jiang, S.; Kang, G.; Nguyen, D.; Schatz, G. C.; Van Duyne, R. P. Operando Characterization of Iron Phthalocyanine Deactivation during Oxygen Reduction Reaction

Using Electrochemical Tip-Enhanced Raman Spectroscopy. *J. Am. Chem. Soc.* **2019**, *141* (39), 15684–15692. https://doi.org/10.1021/jacs.9b07979.

(176) Jiang, S.; Chen, Z.; Chen, X.; Nguyen, D.; Mattei, M.; Goubert, G.; Van Duyne, R. P. Investigation of Cobalt Phthalocyanine at the Solid/Liquid Interface by Electrochemical Tip-Enhanced Raman Spectroscopy. *J. Phys. Chem. C* **2019**, *123* (15), 9852–9859. https://doi.org/10.1021/acs.jpcc.9b00513.

(177) Kurouski, D.; Mattei, M.; Van Duyne, R. P. Probing Redox Reactions at the Nanoscale with Electrochemical Tip-Enhanced Raman Spectroscopy. *Nano Lett.* **2015**, *15* (12), 7956–7962. https://doi.org/10.1021/acs.nanolett.5b04177.

(178) Kang, G.; Yang, M.; Mattei, M. S.; Schatz, G. C.; Van Duyne, R. P. *In Situ* Nanoscale Redox Mapping Using Tip-Enhanced Raman Spectroscopy. *Nano Lett.* **2019**, *19* (3), 2106–2113. https://doi.org/10.1021/acs.nanolett.9b00313.

(179) Bao, Y.-F.; Cao, M.-F.; Wu, S.-S.; Huang, T.-X.; Zeng, Z.-C.; Li, M.-H.; Wang, X.; Ren, B. Atomic Force Microscopy Based Top-Illumination Electrochemical Tip-Enhanced Raman Spectroscopy. *Anal. Chem.* **2020**, *92* (18), 12548–12555. https://doi.org/10.1021/acs.analchem.0c02466.

(180) Sabanés, N. M.; Elizabeth, A.; Pfisterer, J. H. K.; Domke, K. F. The Effect of STM Parameters on Tip-Enhanced Raman Spectra. *Faraday Discuss.* **2017**, *205*, 233–243. https://doi.org/10.1039/C7FD00164A.

(181) Wu, D.-Y.; Li, J.-F.; Ren, B.; Tian, Z.-Q. Electrochemical Surface-Enhanced Raman Spectroscopy of Nanostructures. *Chem. Soc. Rev.* **2008**, *37* (5), 1025. https://doi.org/10.1039/b707872m.

(182) Touzalin, T.; Dauphin, A. L.; Joiret, S.; Lucas, I. T.; Maisonhaute, E. Tip Enhanced Raman Spectroscopy Imaging of Opaque Samples in Organic Liquid. *Phys. Chem. Chem. Phys.* **2016**, *18* (23), 15510–15513. https://doi.org/10.1039/C6CP02596J.

(183) Huang, S.-C.; Wang, X.; Zhao, Q.-Q.; Zhu, J.-F.; Li, C.-W.; He, Y.-H.; Hu, S.; Sartin, M. M.; Yan, S.; Ren, B. Probing Nanoscale Spatial Distribution of Plasmonically Excited Hot Carriers. *Nat. Commun.* **2020**, *11* (1), 4211. https://doi.org/10.1038/s41467-020-18016-4.

(184) Braun, K.; Hauler, O.; Zhang, D.; Wang, X.; Chassé, T.; Meixner, A. J. Probing Bias-Induced Electron Density Shifts in Metal–Molecule Interfaces via Tip-Enhanced Raman Scattering. *J. Am. Chem. Soc.* **2021**, *143* (4), 1816–1821. https://doi.org/10.1021/jacs.0c09392.

(185) Taguchi, A.; Yu, J.; Verma, P.; Kawata, S. Optical Antennas with Multiple Plasmonic Nanoparticles for Tip-Enhanced Raman Microscopy. *Nanoscale* **2015**, *7* (41), 17424–17433. https://doi.org/10.1039/C5NR05022G.

(186) Domke, K. F.; Pettinger, B. Studying Surface Chemistry beyond the Diffraction Limit: 10 Years of TERS. *ChemPhysChem* **2010**, *11* (7), 1365–1373. https://doi.org/10.1002/cphc.200900975.

(187) Kharintsev, S.; Alekseev, A.; Loos, J. Etchant-Based Design of Gold Tip Apexes for Plasmon-Enhanced Raman Spectromicroscopy. *Spectrochim. Acta. A. Mol. Biomol. Spectrosc.* **2017**, *171*, 139–143. https://doi.org/10.1016/j.saa.2016.07.048.

(188) Billot, L.; Berguiga, L.; de la Chapelle, M. L.; Gilbert, Y.; Bachelot, R. Production of Gold Tips for Tip-Enhanced near-Field Optical Microscopy and Spectroscopy: Analysis of the Etching Parameters. *Eur. Phys. J. Appl. Phys.* **2005**, *31* (2), 139–145. https://doi.org/10.1051/epjap:2005049.

(189) Boyle, M. G.; Feng, L.; Dawson, P. Safe Fabrication of Sharp Gold Tips for Light Emission in Scanning Tunnelling Microscopy. *Ultramicroscopy* **2008**, *108* (6), 558–566. https://doi.org/10.1016/j.ultramic.2007.08.012.

(190) *Standard Potentials in Aqueous Solution*; Bard, A. J., Ed.; Monographs in electroanalytical chemistry and electrochemistry; Dekker: New York, NY, 1985.

(191) Williams, C.; Roy, D. Fabrication of Gold Tips Suitable for Tip-Enhanced Raman Spectroscopy. *J. Vac. Sci. Technol. B Microelectron. Nanometer Struct.* **2008**, *26* (5), 1761. https://doi.org/10.1116/1.2981078.

(192) Huh, T. W.; Han, G.; Ban, W. J.; Ahn, H.-S. Efficient Fabrication of Gold Tips by Electrochemical Etching for Tip-Enhanced Raman Spectroscopy. *Int. J. Precis. Eng. Manuf.* **2017**, *18* (2), 221–226. https://doi.org/10.1007/s12541-017-0028-1.

(193) Weber, W. H.; Merlin, R. *Raman Scattering in Materials Science*; Springer Series in Materials Science; Springer Berlin Heidelberg, 2013.

(194) Martin Sabanes, N. Electrochemical Tip-Enhanced Raman Spectroscopy : Development and Applications, Johannes Gutenberg-Universität Mainz, 2018. https://doi.org/10.25358/OPENSCIENCE-2654.

(195) Gjonaj, B.; Johnson, P.; Bonn, M.; Domke, K. F. Index Mismatch Aberration Correction over Long Working Distances Using Spatial Light Modulation. *Appl. Opt.* **2012**, *51* (33), 8034. https://doi.org/10.1364/AO.51.008034.

(196) Kanoufi, F. Electrochemistry and Optical Microscopy. *ArXiv Prepr. ArXiv210912322* **2021**.

(197) Stadler, J.; Schmid, T.; Zenobi, R. Nanoscale Chemical Imaging Using Top-Illumination Tip-Enhanced Raman Spectroscopy. *Nano Lett.* **2010**, *10* (11), 4514–4520. https://doi.org/10.1021/nl102423m.

(198) Schuster, R.; Kirchner, V.; Allongue, P.; Ertl, G. Electrochemical Micromachining. *Science* **2000**, *289* (5476), 98–101. https://doi.org/10.1126/science.289.5476.98.

(199) de Abril, O.; Gündel, A.; Maroun, F.; Allongue, P.; Schuster, R. Single-Step Electrochemical Nanolithography of Metal Thin Films by Localized Etching with an AFM Tip. *Nanotechnology* **2008**, *19* (32), 325301. https://doi.org/10.1088/0957-4484/19/32/325301.

(200) Fan, X.-Y.; Nouchi, R.; Yin, L.-C.; Tanigaki, K. Effects of Electron-Transfer Chemical Modification on the Electrical Characteristics of Graphene. *Nanotechnology* **2010**, *21* (47), 475208. https://doi.org/10.1088/0957-4484/21/47/475208.

(201) Hartig, P.; Rappich, J.; Dittrich, T. Engineering of Si Surfaces by Electrochemical Grafting of *p* -Nitrobenzene Molecules. *Appl. Phys. Lett.* **2002**, *80* (1), 67–69. https://doi.org/10.1063/1.1430265.

(202) Mantha, R.; Taylor, K. E.; Biswas, N.; Bewtra, J. K. A Continuous System for Fe ^{0} Reduction of Nitrobenzene in Synthetic Wastewater. *Environ. Sci. Technol.* **2001**, *35* (15), 3231–3236. https://doi.org/10.1021/es0014943.

(203) Chen, Y.; Xiong, L.; Wang, W.; Zhang, X.; Yu, H. Efficient and Selective Electro-Reduction of Nitrobenzene by the Nano-Structured Cu Catalyst Prepared by an Electrodeposited Method via Tuning Applied Voltage. *Front. Environ. Sci. Eng.* **2015**, *9* (5), 897–904. https://doi.org/10.1007/s11783-015-0782-1.

(204) Zhao, L.-B.; Chen, J.-L.; Zhang, M.; Wu, D.-Y.; Tian, Z.-Q. Theoretical Study on Electroreduction of *p* -Nitrothiophenol on Silver and Gold Electrode Surfaces. *J. Phys. Chem. C* **2015**, *119* (9), 4949–4958. https://doi.org/10.1021/jp512957c.

(205) Zhu, T.; Yu, H. Z.; Wang, Y. C.; Liu, Z. F. Irreversible Adsorption and Reduction of *p* -Nitrothio-Phenol Monolayers on Gold: Electrochemical *in Situ* Surface Enhanced Raman Spectroscopy. *Mol. Cryst. Liq. Cryst. Sci. Technol. Sect. Mol. Cryst. Liq. Cryst.* **1999**, *337* (1), 241–244. https://doi.org/10.1080/10587259908023422.

(206) Touzalin, T.; Joiret, S.; Maisonhaute, E.; Lucas, I. T. Complex Electron Transfer Pathway at a Microelectrode Captured by *in Situ* Nanospectroscopy. *Anal. Chem.* **2017**, *89* (17), 8974–8980. https://doi.org/10.1021/acs.analchem.7b01542.

(207) Thomas, M.; Mühlig, S.; Deckert-Gaudig, T.; Rockstuhl, C.; Deckert, V.; Marquetand, P. Distinguishing Chemical and Electromagnetic Enhancement in Surface-Enhanced Raman Spectra: The Case of *Para* -Nitrothiophenol: Distinguishing Chemical and Electromagnetic Enhancement in Surface-Enhanced Raman Spectra. *J. Raman Spectrosc.* **2013**, *44* (11), 1497–1505. https://doi.org/10.1002/jrs.4377.

(208) Gao, P.; Gosztola, D.; Weaver, M. J. Surface-Enhanced Raman Spectroscopy as a Probe of Electroorganic Reaction Pathways. 1. Processes Involving Adsorbed Nitrobenzene, Azobenzene, and Related Species. *J. Phys. Chem.* **1988**, *92* (25), 7122–7130. https://doi.org/10.1021/j100336a018.

(209) Miao, P.; Ma, Y.; Sun, M.; Li, J.; Xu, P. Tuning the SERS Activity and Plasmon-Driven Reduction of *p* -Nitrothiophenol on a Ag@MoS $_{2}$ Film. *Faraday Discuss.* **2019**, *214*, 297–307. https://doi.org/10.1039/C8FD00139A.

(210) Dong, B.; Fang, Y.; Chen, X.; Xu, H.; Sun, M. Substrate-, Wavelength-, and Time-Dependent Plasmon-Assisted Surface Catalysis Reaction of 4-Nitrobenzenethiol Dimerizing to *p* , *p ′*-Dimercaptoazobenzene on Au, Ag, and Cu Films. *Langmuir* **2011**, *27* (17), 10677–10682. https://doi.org/10.1021/la2018538.

(211) Capitao, D. Formation Électro-Assistée de Monocouches Auto-Assemblées Sur or. Suivi in Situ et Effets Du Potentiel Appliqué à l'électrode Sur Le Mécanisme de Formation. PhD Thesis, 2016.

(212) Cyr, A.; Huot, P.; Marcoux, J.-F.; Belot, G.; Laviron, E.; Lessard, J. The Electrochemical Reduction of Nitrobenzene and Azoxybenzene in Neutral and Basic Aqueous Methanolic Solutions at Polycrystalline Copper and Nickel Electrodes. *Electrochimica Acta* **1989**, *34* (3), 439–445. https://doi.org/10.1016/0013-4686(89)87023-9.

(213) López, I.; Cesbron, M.; Levillain, E.; Breton, T. Diazonium Grafting Control through a Redox Cross-Reaction: Elucidation of the Mechanism Involved When Using 2,2-

Diphenylpicrylhydrazyl as an Inhibitor. *ChemElectroChem* **2018**, *5* (8), 1197–1202. https://doi.org/10.1002/celc.201701331.

(214) Merlen, A.; Plathier, J.; Ruediger, A. A near Field Optical Image of a Gold Surface: A Luminescence Study. *Phys. Chem. Chem. Phys.* **2015**, *17* (33), 21176–21181. https://doi.org/10.1039/C4CP05000B.

(215) Wong, E. H. J.; May, G. L.; Wilde, C. P. Oxidative Desorption of Thiols as a Route to Controlled Formation of Binary Self Assembled Monolayer Surfaces. *Electrochimica Acta* **2013**, *109*, 67–74. https://doi.org/10.1016/j.electacta.2013.07.072.

(216) Madzharova, F.; Heiner, Z.; Kneipp, J. Surface-Enhanced Hyper Raman Spectra of Aromatic Thiols on Gold and Silver Nanoparticles. *J. Phys. Chem. C* **2020**, *124* (11), 6233–6241. https://doi.org/10.1021/acs.jpcc.0c00294.

(217) *The Handbook of Infrared and Raman Characteristic Frequencies of Organic Molecules*, Nachdr.; Lin-Vien, D., Ed.; Academic Press: San Diego, 2006.

(218) Schrader, B. *Raman/Infrared Atlas of Organic Compounds*; Wiley, 1996.

(219) Gruger, A.; Le Calvé, N.; Dizabo, P.; Fillaux, J. Spectres de Vibration Du Trans-Azobenzène et de Quelques Dérivés Isotopiques. *J. Chim. Phys.* **1972**, *69*, 291–298. https://doi.org/10.1051/jcp/1972690291.

(220) Xu, J.-F.; Luo, S.-Y.; Liu, G.-K. Different Behaviors in the Transformation of PATP Adsorbed on Ag or Au Nanoparticles Investigated by Surface-Enhanced Raman Spectroscopy – A Study of the Effects from Laser Energy and Annealing. *Spectrochim. Acta. A. Mol. Biomol. Spectrosc.* **2015**, *143*, 35–39. https://doi.org/10.1016/j.saa.2015.02.039.

(221) Kim, K.; Kim, K. L.; Shin, D.; Choi, J.-Y.; Shin, K. S. Surface-Enhanced Raman Scattering of 4-Aminobenzenethiol on Ag and Au: PH Dependence of b_2 -Type Bands. *J. Phys. Chem. C* **2012**, *116* (7), 4774–4779. https://doi.org/10.1021/jp211730r.

(222) Menanteau, T.; Dias, M.; Levillain, E.; Downard, A. J.; Breton, T. Electrografting via Diazonium Chemistry: The Key Role of the Aryl Substituent in the Layer Growth Mechanism. *J. Phys. Chem. C* **2016**, *120* (8), 4423–4429. https://doi.org/10.1021/acs.jpcc.5b12565.

(223) Lu, M.; He, T.; Tour, J. M. Surface Grafting of Ferrocene-Containing Triazene Derivatives on Si(100). *Chem. Mater.* **2008**, *20* (23), 7352–7355. https://doi.org/10.1021/cm8007182.

(224) Steffenhagen, M.; Latus, A.; Trinh, T. M. N.; Nierengarten, I.; Lucas, I. T.; Joiret, S.; Landoulsi, J.; Delavaux-Nicot, B.; Nierengarten, J.-F.; Maisonhaute, E. A Rotaxane Scaffold Bearing Multiple Redox Centers: Synthesis, Surface Modification and Electrochemical Properties. *Chem. - Eur. J.* **2018**, *24* (7), 1701–1708. https://doi.org/10.1002/chem.201705245.

(225) Pavlishchuk, V. V.; Addison, A. W. Conversion Constants for Redox Potentials Measured versus Different Reference Electrodes in Acetonitrile Solutions at 25°C. *Inorganica Chim. Acta* **2000**, *298* (1), 97–102. https://doi.org/10.1016/S0020-1693(99)00407-7.

(226) Brooksby, P. A.; Downard, A. J. Multilayer Nitroazobenzene Films Covalently Attached to Carbon. An AFM and Electrochemical Study. *J. Phys. Chem. B* **2005**, *109* (18), 8791–8798. https://doi.org/10.1021/jp046095z.

(227) *Handbook of Solvents*; Elsevier, 2014. https://doi.org/10.1016/C2013-0-13246-1.

(228) Toccafondi, C.; Picardi, G.; Ossikovski, R. Molecular Bending at the Nanoscale Evidenced by Tip-Enhanced Raman Spectroscopy in Tunneling Mode on Thiol Self-Assembled Monolayers. *J. Phys. Chem. C* **2016**, *120* (32), 18209–18219. https://doi.org/10.1021/acs.jpcc.6b03443.

(229) Mazurkiewicz, J.; Mearns, F. J.; Losic, D.; Weeks, L.; Waclawik, E. R.; Rogers, C. T.; Shapter, J. G.; Gooding, J. J. Cryogenic Cleavage Used in Gold Substrate Production. *J. Vac. Sci. Technol. B Microelectron. Nanometer Struct.* **2002**, *20* (6), 2265. https://doi.org/10.1116/1.1518968.

(230) Himori, S.; Nishitani, S.; Sakata, T. Control of Potential Response to Small Biomolecules with Electrochemically Grafted Aryl-Based Monolayer in Field-Effect Transistor-Based Sensors. *Langmuir* **2019**, *35* (10), 3701–3709. https://doi.org/10.1021/acs.langmuir.9b00085.

(231) High Resolution XPS of Organic Polymers: The Scienta ESCA300 Database (Beamson, G.; Briggs, D.). *J. Chem. Educ.* **1993**, *70* (1), A25. https://doi.org/10.1021/ed070pA25.5.

(232) Dutta, P.; Pernites, R. B.; Danda, C.; Advincula, R. C. SPR Detection of Dopamine Using Cathodically Electropolymerized, Molecularly Imprinted Poly-p-Aminostyrene Thin Films. *Macromol. Chem. Phys.* **2011**, *212* (22), 2439–2451. https://doi.org/10.1002/macp.201100365.